Bandgap engineering of multi-junction solar cells using nanostructures for enhanced performance under concentrated illumination

Alexandre William Walker

Thesis submitted to the

Faculty of Graduate and Postdoctoral Studies in partial fulfillment of the requirements

for the Doctorate in Philosophy degree in Physics

Department of Physics
Ottawa-Carleton Institute for Physics
University of Ottawa

Abstract

This doctorate thesis focuses on investigating the parameter space involved in numerically modeling the bandgap engineering of a GaInP/InGaAs/Ge lattice matched multi-junction solar cell (MJSC) using InAs/InGaAs quantum dots (QDs) in the middle sub-cell. The simulation environment – TCAD Sentaurus – solves the semiconductor equations using finite element and finite difference methods throughout well-defined meshes in the device to simulate the optoelectronic behavior first for single junction solar cells and subsequently for MJSCs with and without quantum dots under concentrated illumination of up to 1000 suns' equivalent intensity. The MJSC device models include appropriate quantum tunneling effects arising in the tunnel junctions which serve as transparent sub-cell interconnects. These tunneling models are calibrated to measurements of AlGaAs/GaAs and AlGaAs/AlGaAs tunnel junctions reaching tunneling peak current densities above 1000 A/cm^2.

Self-assembled InAs/GaAs quantum dots (QDs) are treated as an effective medium through a description of appropriate generation and recombination processes. The former includes analytical expressions for the absorption coefficient that amalgamates the contributions from the quantum dot, the InAs wetting layer (WL) and the bulk states. The latter includes radiative and non-radiative lifetimes with carrier capture and escape considerations from the confinement potentials of the QDs. The simulated external quantum efficiency was calibrated to a commercial device from Cyrium Technologies Inc., and required 130 layers of the QD effective medium to match the contribution from the QD ground state. The current – voltage simulations under standard testing conditions (1

kW/cm^2, T=298 K) demonstrated an efficiency of 29.1%, an absolute drop of 1.5% over a control structure. Although a 5% relative increase in photocurrent was observed, a 5% relative drop in open circuit voltage and an absolute drop of 3.4% in fill factor resulted from integrating lower bandgap nanostructures with shorter minority carrier lifetimes. However, these results are considered a worst case scenario since maximum capture and minimum escape rates are assumed for the effective medium model. Decreasing the band offsets demonstrated an absolute boost in efficiency of 0.5% over a control structure, thus outlining the potential benefits of using nanostructures in bandgap engineering MJSCs.

A summary of the Ph.D. experience:

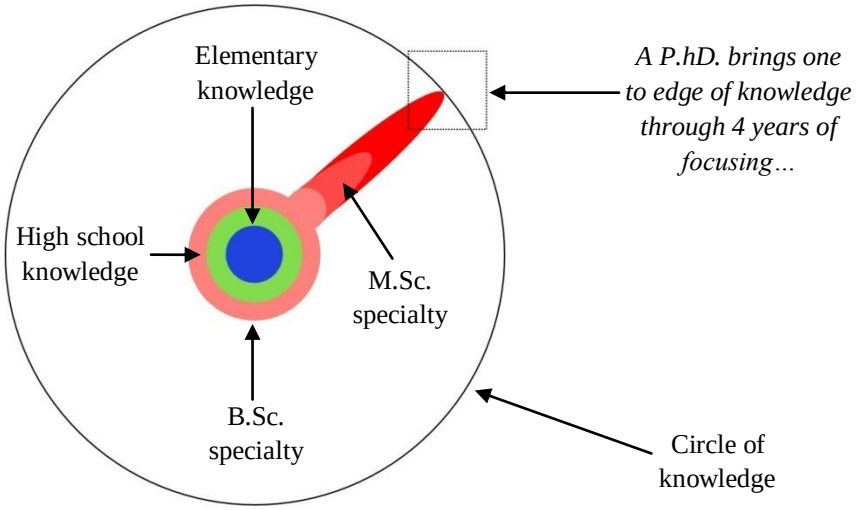

But one should not forget the Ph.D. in the context of the bigger picture:

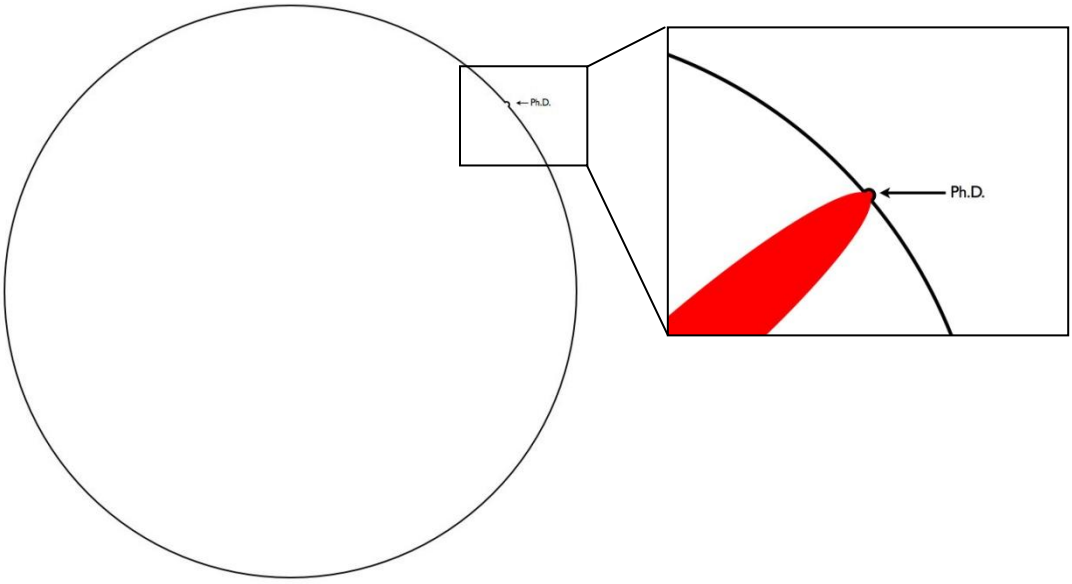

And that we stand on the shoulder of giants.

Statement of Originality

The results presented in this thesis were obtained during the period of the author's Ph.D. research project under the supervision of Dr. Karin Hinzer, except where otherwise noted. To the best of the author's knowledge, these results are original. These include:

1. The modeling of AlGaAs/AlGaAs, AlGaAs/GaAs, GaAs/GaAs and AlGaAs/InGaP tunnel junctions using TCAD Sentaurus,
2. Development of nonlocal tunneling models to reproduce the valley current in measured current – voltage characteristics of AlGaAs/GaAs and AlGaAs/AlGaAs tunnel junctions using TCAD Sentaurus,
3. Modeling of AlGaAs/GaAs and AlGaAs/AlGaAs tunnel junction-limited multi-junction solar cell behaviour as a function of concentration,
4. Development of analytical expressions for the absorption coefficient of InAs quantum dots and the associated wetting layer (in conjunction with Ph. D. candidate Olivier Thériault),
5. Modeling of quantum dot enhanced InGaP/InGaAs/Ge multi-junction solar cells using an effective medium with carrier dynamics considerations under standard testing conditions and under concentrated illumination.

The tunnel junctions used to calibrate the TCAD Sentaurus based models were grown and fabricated by Cyrium Technologies Inc., as well as Sherbrooke University. These were characterized at the University of Ottawa by Gitanjali Kolhatkar and Olivier Thériault. The external quantum efficiencies and current – voltage characteristics measured at the University of Ottawa of quantum dot multi-junction solar cells were performed by Olivier

Thériault and the author. The commercially available first generation quantum dot enhanced cells (QDEC) were supplied by Cyrium Technologies Inc.

The work outlined in this thesis led to the following papers and conference proceedings:

1. **A. W. Walker**, O. Thériault, J. F. Wheeldon, K. Hinzer. "The effects of absorption and recombination in quantum dot multi-junction solar cell device efficiency," *Journal of Photovoltaics*, **3**(3), pp. 1118-1124, 2013; DOI: 10.1109/JPHOTOV.2013.2257920.
2. **A. W. Walker**, O. Thériault, M. Wilkins, J. F. Wheeldon, K. Hinzer. "Nonlocal tunneling models and the simulation of tunnel junction limited multi-junction solar cells under concentration," *Journal of selected topics in quantum electronics: Numerical Simulation of Optoelectronic Devices*, **19**(5), p. 4000508 (8 pages), 2013; DOI: 10.1109/JSTQE.2013.2258140.
3. G. Kolhatkar, J. F. Wheeldon, C. E. Valdivia, **A. W. Walker**, S. Fafard, A. Turala, A. Jaouad, R. Arès, V. Aimez, and K. Hinzer. "Current-voltage measurements within the negative differential resistance region of AlGaAs/AlGaAs tunnel junctions for high concentration photovoltaic," *International Journal of Nanoscience*, **11**(4), p. 1240014 (6 pages), 2012.
4. J. F. Wheeldon, C. E. Valdivia, **A. W. Walker**, G. Kolhatkar, A. Jaouad, A. Turala, B. Riel, D. Masson, N. Puetz, S. Fafard, R. Ares, V. Aimez, T. J. Hall, K. Hinzer. "Performance comparison of AlGaAs, GaAs and InGaP tunnel junctions for concentrated multijunction solar cells," *Progress in Photovoltaics: Research and Applications.* **19**, pp. 442-452, 2011. DOI: 10.1002/pip.1056.
5. B. Paquette, M. DeVita, G. Kolhatkar, A. Turala, A. Boucherif, J. F. Wheeldon, **A. W. Walker**, O. Thériault, K. Hinzer, C. E. Valdivia, S. G. Wallace, S. Fafard, V. Aimez and R. Arès. "Chemical Beam Epitaxy Growth of AlGaAs/GaAs Tunnel Junctions using Trimethyl Aluminum for Multijunction Solar Cells," Conference proceeding from the *9th International Conference on Concentrating Photovoltaics*, Miyazaki, Japan, April 15-17 2013. [Oral]

6. O. Thériault, **A. Walker**, J. F. Wheeldon, K. Hinzer. "Effects of quantum dot layers on the behaviour of mulit-junction solar cell operation under concentration," *AIP Conference Proceedings*, **1477**, pp. 20-23, 2012. DOI: http://dx.doi.org/10.1063/1.4753824. [Oral]
7. **A. W. Walker**, J. F. Wheeldon, O. Thériault, M. D. Yandt, K. Hinzer. "Temperature dependent external quantum efficiency simulations and experimental measurement of lattice matched quantum dot enhanced multi-junction solar cells," Poster and proceeding from the *37th IEEE Photovoltaics Specialist Conference*, pp. 000564-000569, Seattle, WA, USA, June 19-24 2011. DOI: 10.1109/PVSC.2011.6186018. [Poster]
8. J. F. Wheeldon, **A. Walker**, C. E. Valdivia, S. Chow, O. Thériault, R. Beal, M. Yandt, F. Proulx, D. Masson, B. Riel, D. McMeekin, N. Puetz, S. G. Wallance, V. Aimez, R. Ares, T. J. Hall, S. Fafard, K. Hinzer. "Efficiency measurements and simulations of GaInP/InGaAs/Ge quantum dot solar cells at up to 1000-suns under flash and continuous concentration," *AIP Conference Proceedings*, 1407, pp. 220-223, 2011. DOI: http://dx.doi.org/10.1063/1.3658331. [Poster]
9. O. Thériault, J. F. Wheeldon, **A. W. Walker**, P. Bitar, M. D. Yandt, C. E. Valdivia, K. Hinzer. "Temperature-dependent external quantum efficiency of quantum dot enhanced multi-junction solar cells," *AIP Conference Proceedings*, **1407**, pp. 50-53, 2011. DOI:http://dx.doi.org/10.1063/1.3658293. [Poster]
10. J. F. Wheeldon, C. E. Valdivia, **A. Walker**, G. Kolhatkar, D. Masson, B. Riel, S. Fafard, A. Jaouad, A. Turala, R. Ares, V. Aimez, T. J. Hall, K. Hinzer. "GaAs, AlGaAs and InGaP Tunnel Junctions for Multi-Junction Solar Cells Under Concentration: Resistance Study," *AIP Conference Proceedings*, **1277**, pp. 28-31, 2010. DOI: http://dx.doi.org/10.1063/1.3509213. [Poster]
11. **A. W. Walker**, J. F. Wheeldon, C. E. Valdivia, G. Kolhatkar, K. Hinzer. "Simulation, modeling and comparison of III-V tunnel junction designs for high efficiency metamorphic multi-junction solar cells," *Proceedings of SPIE*, 7750, 77502X, 2010. DOI: 10.1117/12.872882. [Oral]
12. G. Kolhatkar, J.F. Wheeldon, C.E. Valdivia, **A. Walker**, S. Fafard, A. Turala, A. Jaouad, R. Ares, V. Aimez and K. Hinzer. "Time-dependent analysis of

AlGaAs/AlGaAs tunnel junctions for high efficiency multi-junction solar cells," *Proceedings of SPIE*, 7750, 77502S, 2010. DOI: 10.1117/12.872886. [Oral]

13. O. Thériault, A.J. SpringThorpe, J.F. Wheeldon, C.E. Valdivia, **A. Walker**, B.J. Riel and K. Hinzer. "Study of InGaAs/GaAs quantum dot saturation level for the design of concentrated multi-junction solar cells," *Proceedings of SPIE*, 7750, 77502T, 2010. DOI: 10.1117/12.872892. [Oral]
14. G. Arbez, J. Wheeldon, **A. Walker**, K. Hinzer, H. Schriemer. "Modeling and simulation of triple junction solar cells," *Proceedings of SPIE* 7750, 775032, 2010, Niagara Falls, Canada, 2010. DOI: 10.1117/12.876131. [Oral]
15. J. F. Wheeldon, C. E. Valdivia, **A. Walker**, G. Kolhatkar, T. J. Hall, K. Hinzer, D. Masson, S. Fafard, A. Jaouad, A. Turala, R. Arès, V. Aimez. "AlGaAs Tunnel Junction for High Efficiency Multi-Junction Solar Cells : Simulation and Measurement of Temperature-Dependent Operation," Proceeding from the *34th IEEE Photovoltaic Specialist Conference*, Philadelphia, PA, 135, 2009. DOI: 10.1109/PVSC.2009.5411723. [Poster]

<u>The above work has led to the following manuscripts presently in preparation</u>:

1. **A. W. Walker,** O. Thériault, J. F. Wheeldon, K. Hinzer. "Positioning and doping effects of quantum dot multi-junction solar cells," Submitted to *Progress in Photovoltaics: Research and Applications*, August 2013.
2. **A. W. Walker**, O. Thériault, J. F. Wheeldon, K. Hinzer. "The Dependence of Multi-Junction Solar Cell Performance on the Number of Quantum Dot Layers," Submitted to *IEEE Journal of Quantum Electronics*, September 2013.
3. **A. W. Walker**, O. Thériault, J. F. Wheeldon, K. Hinzer. "Carrier dynamics in quantum dot enhanced multi-junction solar cells under high concentration" Submitted to *IEE Journal of Photovoltaics*, July 2013.
4. **A. W. Walker,** F. Bouchard, K. Hinzer. "An alternative triple-junction solar cell design composed of GaInP/InGaAs/Cu(In,Ga)Se_2," In preparation for submission to *Progress in Photovoltaics: Research and Applications*, October 2013.

Portions of these results also contributed to the following work:

1. **A. W. Walker**, O. Theriault, J. F. Wheeldon, K. Hinzer. "Bandgap engineering of multi-junction solar cells using nanostructures for enhanced performance under concentration," Ottawa-Carleton Institute for Physics seminars, May 2013. [Oral]
2. M. Wilkins, **A. Walker**, J. F. Wheeldon, G. Arbez, H. Schriemer, K. Hinzer. "Design constraints of p-i-n GaAs/InGaAsN dilute nitride sub-cells for 3- and 4- junction solar cell applications under concentrated illumination," Conference proceeding from the *39th IEEE Photovoltaics Specialist Conference*, Tampa, Florida, USA, June 16-21 2013. [Poster]
3. G. Arbez, **A. Walker**, M. Wilkins, J. F. Wheeldon, K. Hinzer, and H. Schriemer. "4 Junction Dilute Nitride Solar Cell Optimization: Comparing Current Matching Approaches in Detailed Balance Algorithms," Conference proceeding from the *39th IEEE Photovoltaics Specialist Conference*, Tampa, Florida, USA, June 16-21 2013. [Poster]
4. P. Sharma, J. F. Wheeldon, **A. W. Walker**, H. Schriemer, and K. Hinzer, "Optimization of Finger Spacing for Concentrator Photovoltaic Cells under Non-Uniform Illumination using SPICE," Conference (SPIE) proceeding from the *15th Photonics North Conference*, June 3-5, 2013, Ottawa, ON, Canada. [Oral]
5. F. Bouchard, **A. Walker**, K. Hinzer. "Modeling of single crystalline Cu(In,Ga)Se2 single junction solar cell grown on a GaAs substrate," Conference (SPIE) proceeding from the *15th Photonics North Conference*, Ottawa, ON, Canada, June 3-5, 2013. [Oral]
6. M. D. Yandt, J. F. Wheeldon, J. Cook, R. Beal, **A. W. Walker**, O. Thériault, H. Schriemer, T.J. Hall and K. Hinzer. "Estimating Cell Temperature In A Concentrating Photovoltaic System," *AIP Conference Proceedings*, **1477**, pp. 172-175, 2012. DOI: http://dx.doi.org/10.1063/1.4753861. [Poster]
7. S. Schicho, M. Wilkins, A. Turala, A. Jaouad, A. Boucherif, **A. Walker**, J. F. Wheeldon, K. Hinzer, R. Arès, V. Aimez. "Effect of Ge Substrate Thinning on CPV Solar Cell Performance," Conference proceeding from the *8th International Conference on Concentrating Photovoltaic Systems*, Toledo, Spain, 2012. [Poster]
8. **A. W. Walker**, A. Coathup, O. Thériault, H. M. Myers, J. F. Wheeldon, S. Park, Z. Mi, I. Shih, K. Hinzer. "Modeling Cu(In,Ga)Se2 solar cells for applications in multi-

junction solar cell technologies," *Next Generation Solar Photovoltaics Canada National Scientific Conference*, Montreal, QC, Canada, 2012. [Oral]

The experience of the author using TCAD Sentaurus also contributed to the following studies conducted on down-conversion processes for photovoltaics presented at the following conferences:

1. A. Gabr, **A. Walker**, J. F. Wheeldon, T. J. Hall, R. N. Kleiman, and K. Hinzer. "Numerical Modeling of Silicon Nanocrystal Down-Shifting Layers for Enhanced Photovoltaic Efficiency," Poster and proceeding from the *39th IEEE Photovoltaics Specialist Conference*, Tampa, Florida, USA, June 16-21 2013.
2. A. M. Gabr, R. M. Beal, **A. Walker**, J. F. Wheeldon, J. Sacks, R. M. Savidge, T. J. Hall, R. N. Kleiman, K. Hinzer. "Modeling Down-Conversion and Down-Shifting for Photovoltaic Applications," Proceeding from the *38th IEEE Photovoltaics Specialist Conference*, Austin, TX, USA, June 3-8 2012, pp. 000048-000052. DOI: 10.1109/PVSC.2012.6317566. [Poster]
3. J. Sacks, R. M. Savidge, A. Gabr, **A. Walker**, R. Beal, J. Wheeldon, A. P. Knights, P. Mascher, K. Hinzer, R. N. Kleiman. "Quantum Efficiency Measurements of Down-Shifting Using Silicon Nanocrystals for Photovoltaic Applications," Proceeding at the *38th IEEE Photovoltaics Specialist Conference*, Austin, TX, USA, June 3-8 2012, pp. 000092-000096. DOI: 10.1109/PVSC.2012.6317575. [Poster]
4. M. Gabr, **A. Walker**, R. Beal, J.F. Wheeldon, J. Sacks, R.M. Savidge, T.J. Hall, R.N. Kleiman, and K. Hinzer. "Optimization of down-converters for photovoltaics applications," *NanoOntario Conference*, London, ON, Canada, October 2011. [Poster]

The author also contributed to work on intermediate band solar cells through the following abstracts:

1. J. J. Krich, **A. W. Walker**. "Modeling intermediate band solar cells: a roadmap to high efficiency," Abstract submitted to the *Conference on Physics, Simulation, and Photonic*

Engineering of Photovoltaic Devices III, SPIE West, San Fransisco, California, USA, 1-6 February 2014.

2. J. J. Krich, M. Nesrallah, N. Rogers, **A. W. Walker**. "Intermediate band photovoltaic device modeling," Abstract and oral presentation at the *Fourth National Scientific Conference for Photovoltaics Canada - Next Generation Solar*, Hamilton, ON, Canada, May 8-10 2013.
3. J. J. Krich, **A. W. Walker**. "Roadmap for high efficiency intermediate band solar cells," Abstract submitted to the *International Conference on Nanoscience and Technology (ChinaNano)*, Beijing, China, September 5-7, 2013.

Lastly, the work of the author led to the publication of an application note available to all Canadian universities associated with CMC Microsystems to understand how to simulate a simple *p-n* junction:

1. **A. W. Walker**, J. F. Wheeldon, O. Thériault, G. Arbez, K. Hinzer. "Understanding Synopsys TCAD Sentaurus by Simulating a P-N Junction." CMC Application Note, 2010.

Part of this work was performed as part of the Semiconductors Using Nanostructures for Record Increases in Solar-Cell Efficiency (SUNRISE) project supported by NSERC, the Photovoltaic Innovation network (PVIN) funded by NSERC, MRI, CFI and CRC. The author would like to thank the University of Ottawa and OGS for financial support and CMC Microsystems for the licensing of TCAD Sentaurus.

Acknowledgements

I would like to deeply and sincerely thank my supervisor, Dr. Karin Hinzer, for giving me this unique opportunity to do research in the field of photovoltaics. Her exceptional enthusiasm, strong support and research guidance was truly invaluable. Karin's resourcefulness led me to work on several different projects during my Ph.D. research, which gave me unparalleled experience working collaboratively with other research groups. I cannot thank Karin enough for this research opportunity, which also allowed me to travel to several international conferences and make important connections within the field of photovoltaics. This significantly assisted in my future post-doctoral position at Fraunhofer ISE in Freiburg, Germany. Karin was also an excellent teacher and proof-reader during my time writing and presenting my research. She strongly motivated me to participate in two projects within the NSERC funded Photovoltaic Innovation Network (PVIN), which was a wonderful learning experience with respect to project management. I would also like to thank Dr. Henry Schriemer for his expert advice in research direction and scientific writing.

I would like to sincerely thank Dr. Jeffrey F. Wheeldon for his keen intellect in research direction and focus, his helpful feedback in my scientific writing, and his numerous contributions to my research on multi-junction solar cells during his time as a post-doctoral fellow with the SUNLAB. He, Olivier Thériault and I made a formidable theoretical physics team which strongly influenced my research throughout my entire Ph.D. I am very grateful to Olivier Thériault for all of his helpful discussions throughout my graduate studies, since our research was closely tied together.

With respect to the use of TCAD Sentaurus, I would like to thank Gilbert Arbèz, Jeffrey F. Wheeldon and Matthew Wilkins for very useful discussions on the operation and troubleshooting of the software. I would like to thank Keith White and Jacques Sincennes from the IT group at the University of Ottawa who managed all of the software and servers, as they provided very helpful troubleshooting assistance on maintaining and managing the simulation software. Lastly, I would like to thank Linda Daugherty, Hugh Pollitt-Smith, Jessica Zhang and Lindsay Geoffrey from CMC Microsystems for managing the license servers, assisting with troubleshooting of the software, assisting with the application note, and most importantly, making TCAD Sentaurus and COMSOL available to the SUNLAB.

I would like to thank Mark Yandt and Ahmed Gabr for very useful discussions, insightful ideas and general brainstorming on the topic of photovoltaics. I would also like to thank Anna Trojna for her excellent proofreading of my thesis in her transition into a post-doctoral fellow with the Sunlab.

Finally, I would like to thank my parents for their strong support during the course of my graduate studies.

Table of Contents

Abstract i
Statement of Originality iv
Acknowledgements xi
Table of Contents xiii
List of Figures xvii
List of Tables xxv
List of Symbols and Acronyms xxvii

Chapter 1: Introduction 1
1.1. Multi-Junction Solar Cells 1
1.2. Modeling and Simulation of Advanced Photovoltaic Devices 5
1.3. Overview 8

Chapter 2: Semiconductor Properties 12
2.1. Crystal Structure and Energy Bands 12
2.2. Equilibrium Carrier Concentrations 15
2.2.1. Intrinsic carrier concentrations 16
2.2.2. Extrinsic carrier concentrations 20
2.3. Carrier Transport 24
2.3.1. Continuity Equations and Poisson's Equation 25
2.3.2. Drift and Diffusion 26
2.3.3. Minority Carrier Diffusion Lengths 29
2.3.4. Thermionic Emission and Tunneling 30
2.4. Recombination Mechanisms 32
2.4.1. Auger 32
2.4.2. Radiative 34
2.4.3. Shockley-Read-Hall (SRH) 35
2.4.4. Effective Lifetime of Minority Carriers 38
2.5. Generation and Absorption Characteristics 38
2.6. Heterostructures and Quantum Confinement 44
2.6.1. Heterostructures and Lattice Considerations 44
2.6.2. Quantum Structures, Energy Eigenvalues and Density of States 45
2.6.3. Quantum Dot and Quantum Well Absorption Characteristics 48
2.6.4. Altered Carrier Dynamics in Quantum Dot/Well Systems ... 50

Chapter 3: Simulations of Semiconductor *p-n* Junctions & Solar Cells 55
3.1. Qualitative Analysis of a *p-n* Junction in Equilibrium 55
3.2. Simulating a Perturbed *n-p* Junction using TCAD Sentaurus 58

3.2.1. Device Structure, Contacts and Numerical Mesh Generation 59
3.2.2. Simulation Details in *Sentaurus Device* 63
3.2.2.1. Input Files, Electrodes and Physical Models 63
3.2.2.2. Mathematical Methods and Convergence Criteria 64
3.2.2.3. Solving the System of Equations 69
3.2.2.4. Output of Simulation 71
3.2.3. Simulation Results and Analysis 72
3.3. Ideal Diode Equations for Diodes and Solar Cells 76
3.4. Simulating a Solar Cell in TCAD Sentaurus 81
3.4.1. Standard Illumination Spectrum 82
3.4.2. Transfer Matrix Method 83
3.4.3. Changes to Solar Cell Geometry due to Illumination 87
3.4.4. Quantum Efficiency Simulations 92
3.4.5. *J-V* and *P-V* Simulations and Results 96
3.5. Simulation of Other Solar Cell Material Systems as a Comparison 100
3.5.1. Properties of Si, GaInP, GaAs, Ge and Cu(In,Ga)Se_2 101
3.5.2. Material System-Specific Solar Cell Designs 104
3.5.3. Solar Cell Simulation Results 106
3.5.4. Ideal Solar Cell Behaviour – The Shockley Limit 108

Chapter 4: Multi-Junction Solar Cells 111
4.1. Motivation and Concepts of Concentrated Photovoltaics 111
4.1.1. Detailed Balance Predictions 115
4.2. Simulations of III-V based Multi-Junction Solar Cells 119
4.2.1. Tunnel Junctions 119
4.2.1.1. Qualitative Description 119
4.2.1.2. Nonlocal Tunneling Models 122
4.2.1.2.1. Band-to-Band Tunneling 122
4.2.1.2.2. Trap Assisted Tunneling 126
4.2.1.3. Simulation of Tunnel Junctions 128
4.2.2. Simulation Methods and Results of MJSC Sub-Cells and Full Structure 136
4.2.3. External and Internal Quantum Efficiencies 142
4.2.4. Broadband Anti-Reflection Coatings 144
4.2.5. Simulation Results 152
4.3. Concentrated Illumination 154
4.3.1. Effects on Performance 154
4.3.2. Limitations 157
4.3.2.1. Series Resistance 157
4.3.2.2. Temperature 158
4.3.2.3. Tunnel Junction Limited MJSC Perfomance 164

Chapter 5: QD Enhanced Multi-Junction Solar Cells 173
5.1. Literature Review on InAs/GaAs Quantum Dots and Wells 174

5.1.1. Growth Techniques for the Refinement of Structural and Optical Properties of Nanostructures 176
5.1.1.1. InAs QDs 176
5.1.1.2. InGaAs QWs 177
5.1.2. Optical Properties of QD: Band Structure and Corresponding Absorption Properties 178
5.1.2.1. Band structure 178
5.1.2.2. Absorption properties 179
5.1.3. Recombination Lifetimes 181
5.1.3.1. Radiative 181
5.1.3.2. Non-radiative 182
5.1.4. Carrier Dynamics 183
5.1.5. Thermionic Emission Theory for Quantum Structures 187
5.1.6. QD and QW Device Characteristics 188
5.1.7. Literature Review Conclusions 188
5.2. Modeling a QD Enhanced Multi-Junction Solar Cell 190
5.2.1. Quantum Dot and Quantum Well Absorption 191
5.2.2. Carrier Dynamics 195
5.2.2.1. Effective Band Offset Model 196
5.2.2.2. Quantum Well Scattering Formalism 201
5.2.3. Recombination Lifetimes in the QD Effective Medium 203
5.3. Simulating the QD MJSC 205
5.3.1. Structure 205
5.3.2. Effective Band Offset Model 206
5.3.2.1. External Quantum Efficiency 206
5.3.2.2. Current – Voltage Characteristics 208
5.3.3. Quantum Well Scattering Formalism 212
5.3.3.1. External Quantum Efficiency 212
5.3.3.2. Current – Voltage Characteristics 215
5.3.4. Performance Optimization of the QD Enhanced MJSC 217
5.3.5. Performance of QD Enhanced MJSC as a function of concentration 223
5.3.6. Positioning and Doping Effects of QD layers within the InGaAs Sub-Cell 228
5.4. Conclusions and Limitations of the Models 235

Chapter 6: Conclusions and Future Work 240

References 244

Appendix A: Simple Supplementary Calculations 259
A-1. A Motivating Argument for Solar
A-2. Comparing Concentrating Solar Power to Concentrating Photovoltaics

Appendix B: Sample Sentaurus Device Command File 264

Appendix C: Detailed Derivations 270
C-1. Detailed Derivation of QD Absorption Characteristics
C-2. Detailed Derivation of QW Absorption Characteristics
C-3. Approximating Carrier Escape and Capture using Bulk Thermionic Emission

List of Figures

Fig. 1-1. a) Lattice matched multi-junction solar cell, b) standard illumination spectrum, and c) semiconductor material bandgap vs. lattice constant. (p. 2)

Fig. 1-2. NREL efficiency roadmap. (p. 3)

Fig. 2-1. Illustration of direct and indirect energy-momentum diagrams. (p. 14)

Fig. 2-2. a) Simple energy band diagram of a semiconductor, and b) Illustration of a semiconductor's density of states. (p. 15)

Fig. 2-3. Fermi-Dirac distribution for various temperatures. (p. 16)

Fig. 2-4. Illustration of the ionization of dopant atoms. (p. 20)

Fig. 2-5. Illustration of the graphical method of determining the Fermi level of a semiconductor. (p. 22)

Fig. 2-6. A comparison between Boltzmann and Fermi-Dirac statistics near the degenerate point of a semiconductor. (p. 23)

Fig. 2-7. Random motion of an electron due to scattering off lattice atoms. (p. 27)

Fig. 2-8. An illustration of thermionic emission as a current transport process. (p. 30)

Fig. 2-9. An illustration of quantum tunneling of electrons as a current transport process. (p. 31)

Fig. 2-10. Illustration of Shockley-Read-Hall recombination processes. (p. 35)

Fig. 2-11. Electron and hole effective minority carrier lifetimes in GaAs according to SRH, radiative and Auger processes. (p. 38)

Fig. 2-12. Absorption coefficients of various semiconductor materials. (p. 43)

Fig. 2-13. Semiconductor bandgap energy as a function of lattice constant. (p. 45)

Fig. 2-14. Density of states for bulk and quantum structures. (p. 48)

Fig. 2-15. Carrier dynamics in an InAs/GaAs quantum dot/well system. (p. 51)

Fig. 3-1. Schematic of carrier concentrations, electric field and potential energy profiles of a *p-n* junction. (p. 56)

Fig. 3-2. Energy band profile of a semiconductor *p-n* junction. (p. 57)

Fig. 3-3. TCAD Sentaurus simulation tool flow. (p. 60)

Fig. 3-4. Structure in terms of a) doping and b) meshing as simulated in TCAD Sentaurus. (p. 62)

Fig. 3-5. Illustration of the spatial discretization of the device domain used in the box discretization method. (p. 64)

Fig. 3-6. Newton's root finding algorithm. (p. 66)

Fig. 3-7. Schematic of the quasi-stationary command used in Sentaurus Device's command file. (p. 70)

Fig. 3-8. Simulated current – voltage characteristics of example GaAs *p-n* junction using TCAD Sentaurus. (p. 72)

Fig. 3-9. a) Simulated energy band diagram and b) carrier concentrations at equilibrium. (p. 73)

Fig. 3-10. a) Simulated energy band diagram and b) carrier concentrations at a forward bias of 1 V. (p. 73)

Fig. 3-11. a) Simulated energy band diagram and b) carrier concentrations at a forward bias of 2 V. (p. 73)

Fig. 3-12. a) Simulated energy band diagram and b) carrier concentrations at a reverse bias of 1 V. (p. 74)

Fig. 3-13. a) Structure of a simple GaAs based solar cell with shading effects, and b) equivalent circuit of such a solar cell with parasitic resistances. (p. 77)

Fig. 3-14. Simulated external quantum efficiency of a GaAs solar cell overlapped with the normalized photon flux. (p. 79)

Fig. 3-15. a) Current – voltage and power – voltage characteristics according to the single diode model of a solar cell, b) with various series resistances and c) with various shunt resistsances. (p. 80)

Fig. 3-16. Standard extraterrestrial AM0 and terrestrial global (AM1.5G) and direct (AM1.5D) spectra. (p. 82)

Fig. 3-17. Illustration of the transfer matrix method which considers forward and backward propagating waves. (p. 84)

Fig. 3-18. a) Simulated GaAs solar cell structure, b) meshing strategy and c) a close-up near the contact area to consider the effects of shadowing. (p. 88)

Fig. 3-19. Simulated energy band diagram of the GaAs solar cell with front and back surface fields. (p. 89)

Fig. 3-20. a) Refractive indices and b) extinction coefficients of various anti-reflection coating materials, and c) the simulated reflectivity profiles for various anti-reflection coating deisgns. (p. 91)

Fig. 3-21. Simulated external and internal quantum efficiencies, as well as the external and internal spectral responses of the GaAs solar cell with Si_3N_4 anti-reflection coating and AlGaAs front and back surface fields. (p. 94)

Fig. 3-22. a) Effects of minority carrier SRH lifetime and b) base thickness on the simulated EQE of the example GaAs solar cell. (p. 95)

Fig. 3-23. Simulated optical generation profile of the GaAs solar cell for various design considerations. (p. 97)

Fig. 3-24. Simulated current – voltage of the GaAs solar cells for various design considerations. (p. 98)

Fig. 3-25. Simulated energy band diagrams of the GaAs solar cell at a) short circuit, b) maximum power and c) open circuit. (p. 100)

Fig. 3-26. a) Real and b) complex refractive indices of Si, AlInP, GaInP, AlGaAs, GaAs, Ge and $CuIn_{0.8}Ga_{0.2}Se_2$. (p. 101)

Fig. 3-27. a) Electron and b) hole mobilities of Si, AlInP, GaInP, AlGaAs, GaAs, Ge and $CuIn_{0.8}Ga_{0.2}Se_2$ as a function of doping. (p. 102)

Fig. 3-28. a) Electron and b) hole recombination lifetimes of Si. (p. 102)

Fig. 3-29. a) Electron and b) hole recombination lifetimes of GaInP. (p. 103)

Fig. 3-30. a) Electron and b) hole recombination lifetimes of Ge. (p. 103)

Fig. 3-31. a) Electron and b) hole recombination lifetimes of $CuIn_{0.8}Ga_{0.2}Se_2$. (p. 103)

Fig. 3-32. Simulated EQE for the solar cells composed of Si, GaInP, GaAs, Ge and $CuIn_{0.8}Ga_{0.2}Se_2$ according to the designs outlined in tables 3-5, 3-6, 3-3, 3-7 and 3-8 respectively. (p. 106)

Fig. 3-33. Simulated *J-V* characteristics of the various solar cell designs for Si, GaInP, GaAs, Ge and $CuIn_{0.8}Ga_{0.2}Se_2$. (p. 107)

Fig. 3-34. a) Plot of J_{sc} as a function of E_g, and b) V_{oc} as a function of E_g based on the simulations shown in Fig. 3-33. (p. 108)

Fig. 3-35. Theoretical efficiency of a solar cell as a function of its semiconductor bandgap according to detailed balance argument (etaOpt), with the simulated efficiencies of the solar cells composed of Ge, Si, $CuIn_{0.8}Ga_{0.2}Se_2$, GaAs and GaInP for comparison. (p. 109)

Fig. 4-1. Lattice matched multi-junction solar cell design composed of InGaP/InGaAs/Ge with the standard illumination spectrum to outline the separation of photon energies absorbed by the inter-connected sub-cells of the multi-junction solar cell. (p. 112)

Fig. 4-2. Ideal efficiency contour plots of the 3JSC under 1 sun concentration predicted by detailed balance for a fixed bottom sub-cell bandgap of 0.67 eV with the top and middle sub-cell bangaps varied. (p. 116)

Fig. 4-3. Ideal efficiency contour plots of the 3JSC under 1 sun concentration predicted by detailed balance for a fixed middle sub-cell bandgap of 1.42 eV with the top and bottom sub-cell bangaps varied. (p. 118)

Fig. 4-4. Schematic energy band diagrams of an ideal tunnel junction as a function of bias. (p. 120)

Fig. 4-5. Schematic illustrating the different tunneling processes within local and nonlocal frameworks. (p. 122)

Fig. 4-6. Simulation of an AlGaAs/GaAs tunnel junction whose structure is outlined in Table 4-1 to calibrate the various tunneling models. (p. 131)

Fig. 4-7. Experimental *J-V* curve of an AlGaAs/GaAs tunnel junction on a semi-log scale to outline the different regions of current contributions. (p. 133)

Fig. 4-8. Simulated *J-V* curve of an AlGaAs/AlGaAs tunnel junction as depicted in Table 4-2 on a linear scale in a) and on a semi-log scale in b) as compared to the experimentally measured data. (p. 134)

Fig. 4-9. Simulated structure of an InGaP/InGaAs/Ge multi-junction solar cell. (p. 137)

Fig. 4-10. Equivalent circuit diagram of a multi-junction solar cell with tunnel junctions and virtual contacts to extract the behaviour of the individual components (sub-cells and tunnel junctions). (p. 138)

Fig. 4-11. Simulated *J-V* characteristics of the individual sub-cells of the multi-junction solar cells. (p. 140)

Fig. 4-12. Simulated external and internal quantum efficiencies for the InGaP/InGaAs/Ge multi-junction solar cell corresponding to Table 4-3. (p. 144)

Fig. 4-13. Comparison of reflectivity profiles for three anti-reflection coatings. (p. 146)

Fig. 4-14. a) Simulated internal quantum efficiency of the top InGaP sub-cell and b) the middle InGaAs sub-cell for various InGaP bandgaps. (p. 148)

Fig. 4-15. Surface contour plots of a) calculated top and middle sub-cell short circuit current densities and b) the solar weighted reflectance as a function of the top (Si_3N_4) and bottom (SiO_2) anti-reflection coating layer thicknesses. (p. 149)

Fig. 4-16. Simulated optimized minimum sub-cell short circuit current density as a function of InGaP bandgap. (p. 151)

Fig. 4-17. Simulated a) current – voltage and b) power – voltage characteristics of the InGaP/InGaAs/Ge multi-junction solar cell with a Si_3N_4/SiO_2 anti-reflection coating. (p. 152)

Fig. 4-18. Simulated a) current – voltage and b) power – voltage characteristics of the InGaP/InGaAs/Ge multi-junction solar cell at 1 sun, 2 suns and 3 suns intensity. (p. 156)

Fig. 4-19. Simulated a) short circuit current density b) open circuit voltage, c) fill factor (*FF*) and d) efficiency (η) as a function of concentration *X*. (p. 156)

Fig. 4-20. Simulated a) J_{sc} b) V_{oc}, c) fill factor (*FF*) and d) efficiency (η) as a function of concentration X for various series resistances. (p. 158)

Fig. 4-21. Absorption coefficient of GaAs over temperature using a simple Varshi-based absorption model. (p. 161)

Fig. 4-22. Simulated EQE of the lattice matched MJSC as a function of temperature. (p. 162)

Fig. 4-23. Simulated a) J_{sc}, b) V_{oc}, c) *FF* and d) efficiency (η) as a function of concentration for various temperatures. (p. 163)

Fig. 4-24. Simulated V_{oc} temperature coefficient as a function of temperature. (p. 164)

Fig. 4-25. Simulated *J-V* characteristic of an AlGaAs/GaAs tunnel junction with contributions from the nonlocal band-to-band and trap assisted tunneling, where $J_{peak} \sim J_{sc}(X=500)$. (p. 165)

Fig. 4-26. Simulated forward and reverse biased a) *J-V* and b) *P-V* characteristics of a standard InGaP/InGaAs/Ge MJSC at 300 K under the AM1.5D spectrum (900

W/cm^2) concentrated by a factor of 500 with and without limitations from the bottom AlGaAs/GaAs TJ. (p. 167)

Fig. 4-27. A close up of the simulated energy band diagram of the AlGaAs/GaAs TJ within the MJSC at a) J_{peak} within the direct tunneling regime, and b) J_{peak} in the excess current. (p. 169)

Fig. 4-28. Simulated a) efficiency of the ideal and TJ limited MJSC over concentration for the three AlGaAs/GaAs TJs illustrated (b) for low, medium and high J_{peak} considerations, and b). For the medium Jpeak scenario, the efficiency for forward and reverse sweeps is illustrated to show the effects of the hysteresis on the efficiency. (p. 170)

Fig. 4-29. Simulated a) ideal and TJ limited MJSC efficiency over concentration for three AlGaAs/GaAs TJs illustrated in (b) for low, medium and high J_{valley} considerations. (p. 171)

Fig. 5-1. Different relaxation processes in InAs/GaAs QD. (p. 183)

Fig. 5-2. a) Geometry of the effective medium which includes the InAs wetting layer (WL) and quantum dot (QD). b) Approximate energy band alignment in an InAs/InGaAs heterostructure. (p. 191)

Fig. 5-3. The absorption coefficient contributions from the bound states of the QD and WL, the continuum states of above the confined potential (InAs) and finally, bulk InGaAs. (p. 194)

Fig. 5-4. a) Simulated energy levels and density of states of the QD, WL (or QW) and bulk as a function of energy above the CB (at 0 eV) using a QD radius of 18 nm and a height of 5.2 nm with a WL thickness of 2 nm, and compared to the effective medium DOS, b) the log (base 10) of the electron concentration as a function of Fermi energy computed using the DOS (shown in a) computed using equation (2.2.2) compared to the electron concentration predicted by equation (2.2.7) using the best fit effective conduction band DOS of 3.3×1014 cm^{-3}. The inset plot shows the residual of equations (2.2.2) and (2.2.7) each integrated over all Fermi energies as a function of effective DOS. The optimal N_c from this inset plot is used in b. (p. 199)

Fig. 5-5. Energy band diagram (left) and density of states (right) schematics of the effective medium a) within the effective band offset model, b) within the quantum well scattering formalism, and c) the most realistic depiction of the energy band diagram and density of states of an InAs QD within an InGaAs matrix based on the literature review. (p. 202)

Fig. 5-6. Simulated external quantum efficiency (EQE) of a QD enhanced MJSC with 130 layers of 56 meV band offset QDs compared to experimental measurements on a Cyrium QDEC. (p. 207)

Fig. 5-7. Simulated *J-V* curves of four MJSC structures with (1) an *n-p* middle sub-cell without QD, (2) *n-i-p* middle sub-cell without QD, (3) *n-i-p* sub-cell with 130 layers of QD (0 meV band offset) and (4) *n-i-p* sub-cell with 130 layers of QD (56 meV effective band offsets). Inset plot shows a close-up of the V_{oc}. (p. 209)

Fig. 5-8. a) Simulated external quantum efficiency (EQE) of a QD enhanced MJSC with 65 layers QDs as a function of carrier scattering time within the quantum well scattering formalism and compared to experimental measurements on a Cyrium QDEC® and b) dependence of the EQE at 920 nm as a function of carrier scattering time. (p. 213)

Fig. 5-9. Simulated *J-V* curves of the QD enhanced MJSC structures with 65 layers of QD using the quantum well scattering formalism for a scattering time of 1×10^{-12} s at and compared to two control structures (*n-p* and *n-i-p* with an intrinsic thickness of 0.65 μm) and lastly to the QD enhanced MJSC with 130 layers of QD modeled using the 56 meV effective band offsets. (p. 216)

Fig. 5-10. Simulated external quantum efficiency curves of a QD enhanced MJSC with increasing number of layers of QD in the intrinsic region of the middle sub-cell where the QD are described using the quantum well scattering formalism with scattering times of 1 ps for electrons and holes respectively. The contribution from the WL and QD show linear increases in EQE magnitude, and leads to an unphysical result for over 120 QD layers. (p. 218)

Fig. 5-11. a) Increase in responsivity of the middle sub-cell in terms of EQE due to the addition of QD layers for band offsets given by scenario (2). The photon flux is normalized. b) J_{sc}, c) V_{oc}, d) *FF* and e) efficiency as a function of QD layers for QD enhanced MJSC described using effective band offset scenarios (1)-(6) as summarized in Table 5-6, and compared to a control MJSC structure which has an intrinsic region increasing by 10 nm for each QD layer added. (p. 220)

Fig. 5-12. Simulated *J-V* metrics (J_{sc}, V_{oc}, *FF* and η) of a QD enhanced MJSC as a function of concentration for control structures (*n-p* and *n-i-p* for the middle sub-cell) and the QD enhanced MJSC described using the effective band offset approach with 0 meV and 56 meV (with traps) and lastly, a QD enhanced MJSC structure as described using the QW scattering formalism (as a comparison). (p. 224)

Fig. 5-13 Simulated *J-V* metrics (J_{sc}, V_{oc}, *FF* and η) of a QD enhanced MJSC as a function of concentration for the QD enhanced MJSC described using the effective band

offset with traps using the 6 scenarios outlined in Table 5-6, namely (1) 0 meV of effective band offsets, (2) 6.7 meV, (3) 13.4 meV, (4) 26.8 meV, (5) 40.2 meV and (6) 56 meV. (p. 227)

Fig. 5-14. Simulated *J-V* curves of the QD enhanced MJSC structures with 110 layers of QD using the effective band offset approach (6.7 meV) with traps where the QD are positioned in the a) emitter, b) intrinsic region, and c) base. These results are compared to a control structure (*n-i-p* in the middle sub-cell with an intrinsic thickness of 1.1 μm). (p. 229)

Fig. 5-15. Simulated energy band diagrams of four structures at equilibrium and at an applied bias of V=2.3 V: a) a control MJSC structure with no QD in the *n-i-p* middle sub-cell, and three QD enhanced MJSC structures each with 110 layers of QD using 6.7 meV of effective band offsets with traps, where the QD are positioned in the b) the intrinsic region, c) the emitter, and d) the base. (p. 231)

Fig. 5-16. a) Simulated *J-V* curves of a QD enhanced MJSC with 110 layers of QD as a function of intrinsic doping level for the InGaAs spacer and the QD layers. The QD are described using 6.7 meV of effective band offset with traps. The *J-V* metrics are then given as a function of intrinsic background doping for b) J_{sc}, c) V_{oc}, d) *FF* and e) efficiency. (p. 234)

Fig. A-1. Theoretical CSP efficiency as a function of receiver temperature for various concentration ratios based on equation (1). (p. 261)

Fig. C-1. Schematic energy band diagram of the QD potential (of thickness LQD) surrounded by barrier layers to demonstrate the current densities in and out of the potential due to thermionic emission. (p. 281)

List of Tables

Table 3-1. Structural details of simulated GaAs *n-p* junction. (p. 63)

Table 3-2. Equations fitting into the box discretization method given by equation (3.2.4). (p. 65)

Table 3-3. Structural details of simulated GaAs solar cell with ARC and front and back surface fields. (p. 90)

Table 3-4. Simulated *J-V* metrics of the GaAs solar cell with and without ARC, with and without FSF and BSF. (p. 98)

Table 3-5. Structural details of simulated Si solar cell with ARC and a front surface field, based on [98]. (p. 105)

Table 3-6. Structural details of simulated GaInP solar cell with ARC and front and back surface fields, based on [99]. (p. 105)

Table 3-7. Structural details of simulated Ge solar cell with ARC and a front surface field, influenced by [100]. (p. 105)

Table 3-8. Structural details of simulated $CuIn_{0.2}Ga_{0.8}Se_2$ solar cell with ARC and front surface field, based on [101]. (p. 105)

Table 3-9. Simulated *J-V* metrics of the Si, GaInP, GaAs, Ge and Cu(In,Ga)Se2solar cells, including the bandgap of these materials. (p. 107)

Table 4-1. Tunnel junction structure used in the simulation based on [121]. (p. 130)

Table 4-2. Tunnel junction structure used in the simulation based on a structure grown by Cyrium Technologies [21]. (p. 136)

Table 4-3. Standard multi-junction solar cell structure composed of InGaP/InGaAs/Ge. (p. 137)

Table 4-4. Simulated *J-V* metrics of the lattice matched (LM) MJSC compared to values published in the literature for a LM MJSC and a lattice mismatched (LMM) MJSC, all of which are corrected for an incident spectrum of 900 W/m^2 at 25^0 C, where "*" implies the J_{sc} was corrected for the incident spectrum total power from 1000 W/m^2 to 900 W/m^2, with the V_{oc}, *FF* and efficiency remaining intact. (p. 154)

Table 5-1. Summary of QD and QW solar cell properties. (p. 189)

Table 5-2. Parameters adopted for COMSOL and Sentaurus absorption coefficient calculations. (p. 195)

Table 5-3. QD enhanced multi-junction solar cell structure composed of InGaP/InGaAs/Ge. (p. 205)

Table 5-4. Summary of simulated solar cell characteristics under 1 sun illumination (1 kW/m^2, AM1.5D) at 300 K according to the effective band offset model. (p. 209)

Table 5-5. Summary of simulated QD enhanced MJSC characteristics under 1 sun illumination (1 kW/m^2, AM1.5D) at 300 K corresponding to Fig. 5-9 for various QD models. (p. 217)

Table 5-6. Summary of effective band offset scenarios explored during the optimization study of the QD enhanced MJSC as a function of QD layers. (p. 221)

Table 5-7. Summary of simulated QD enhanced MJSC characteristics under 1 sun illumination (1 kW/m^2, AM1.5D) at 300 K corresponding to Fig. 5-14. (p. 230)

Table C-1. Parameters used to compute carrier escape and capture lifetimes using equations (C.3.10). (p. 280)

List of Symbols and Acronyms

AM – Air Mass

ARC – Anti-reflection coating

B2B – Band-to-band

BSF – Back surface field

CBO – Conduction band offset

$\vec{D}$ – Electric displacement field

$D_{n,p}$ – Diffusion constant

E – Energy

E_A – Acceptor energy level

E_C – Conduction band energy

E_D – Donor energy level

E_F – Fermi energy

E_g – Bandgap

E_i – Intrinsic energy level

ε – Dielectric constant

EQE – External quantum efficiency

ESR – External spectral response

E_v – Valence band energy

$\mathcal{F}_n$ – Fermi-Dirac integral of order n

FF – Fill factor ($= J_{mp}V_{mp}/J_{sc}V_{oc}$)

FSF – Front surface field

G – Generation

g_D – Donor impurity degeneracy

g_A – Acceptor impurity degeneracy

H – Hamiltonian

$\vec{H}$ – Magnetic field

h – Planck's constant

$\hbar$ – Reduced Planck's constant

IQE – Internal quantum efficiency

ISR – Internal spectral response

$\vec{J}$ – Current density

J_{peak} – Peak tunneling current density

J_{sc} – Short circuit current density

J_{mp} – Maximum power point current density

J_{valley} –Valley tunneling current density

$\vec{k}$ – Wave vector

κ – Extinction coefficient

k_B – Boltzmann constant

LM – Lattice matched

LMM – Lattice mismatched

m^* - carrier effective mass

μ – Carrier mobility

μ_B – Magnetic permeability

MJSC – Multi-junction solar cell

MPP – Maximum power point

η – Efficiency

n – Electron concentration

n_i – Intrinsic carrier concentration

n_s – Refractive index

N_A – Acceptor concentration

N_c – Effective density of states in the conduction band

N_D – Donor concentration

N_v – Effective density of states in the valence band

N(E) – Density of states

NDR – Negative differential resistance

$\vec{p}$ – Carrier momentum

p – Hole concentration

P – Power density

q – Electronic charge

QD – Quantum dot

QDEC – Quantum Dot Enhanced Cell

QW – Quantum well

V_{oc} – Open circuit voltage

V_{mp} – Maximum power point voltage

σ - Conductivity

SRH – Shockley-Read-Hall

STC – Standard Testing Conditions

R(E) – Reflectivity as a function of energy

R - Recombination

τ_{scat} – Scattering lifetime

τ – Minority carrier lifetime

T_i – Transmission coefficient

T – Temperature

TAT – Trap assisted tunneling

TJ – Tunnel junction

VBO – Valence band offset

WL – Wetting layer

WR – World record

Chapter 1: Introduction

1.1. Multi-junction Solar Cells

The state-of-the-art in photovoltaic (PV) devices is multi-junction solar cell (MJSC) technology, which is at the forefront of photovoltaic device efficiencies reported in the literature with efficiencies of 37.7% under standard testing conditions (STC) [1] – defined as 25°C measured under the global AM1.5 spectrum of 1000 W/m^2 – and 44% under concentrated illumination of ~400 suns measured at a cell temperature of 25°C [2],[3]. MJSCs are composed of multiple monolithically stacked *n-p* junctions connected in series via tunnel junctions in order to harvest different regions of the solar spectrum, as outlined in the top left and right panels of Fig. 1-1. The nature of the series connected sub-cells results in a large open circuit voltage. At the same time, it introduces a significant constraint to the design of the device since the overall photocurrent is limited by the sub-cell which generates the least photocurrent. An optimal MJSC design is therefore one where each sub-cell produces a similar current; this optimization problem is referred to as current matching. The problem is augmented further by the limited choice of lattice matched materials that produce similar photocurrents within a multi-junction solar cell (see the bottom panel of Fig. 1-1 for the well known bandgap as a function of lattice constant plot for semiconductors). Some semiconductor epitaxial growth methods use lattice mismatched materials to overcome these limitations, such as metamorphic multi-junction solar cells, which are capable of reaching >40% efficiency under concentration [4],[5],[6]. These structures are designed to exploit a more optimal combination of inherent bandgap materials than lattice matched material

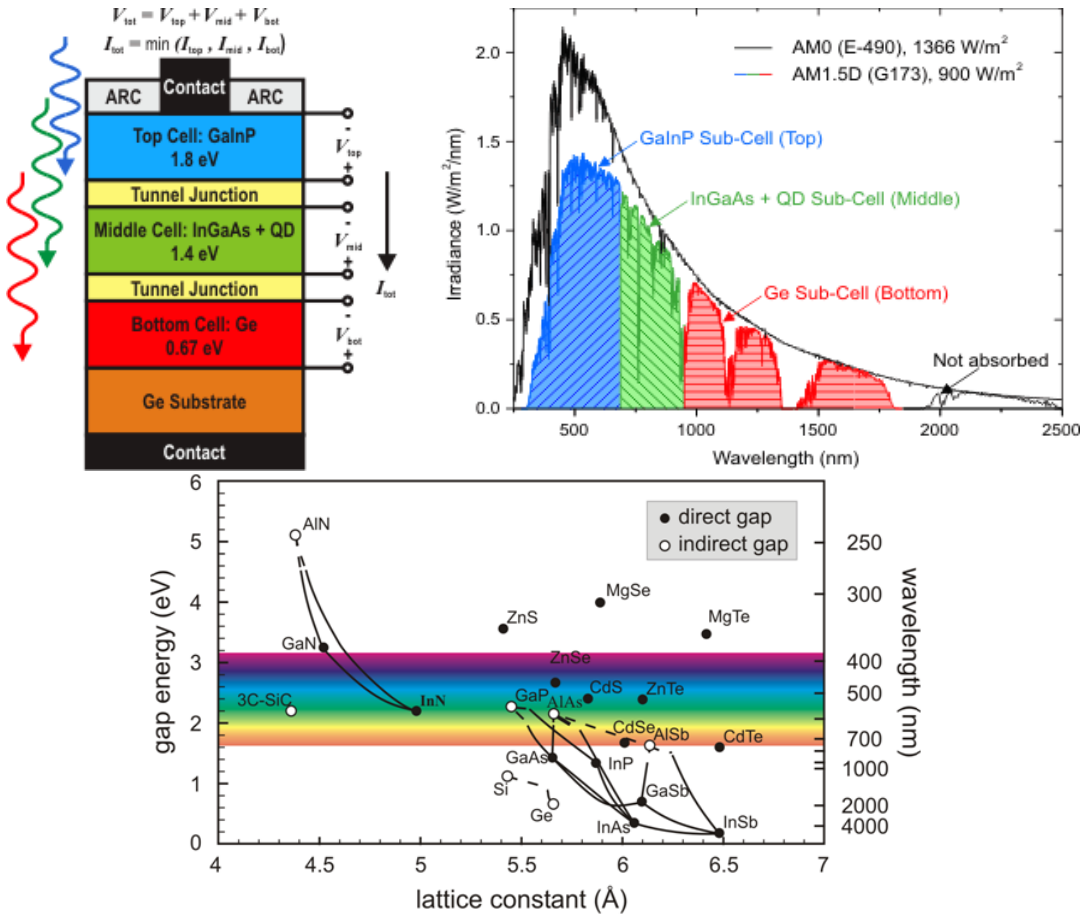

Figure 1-1. Top left: Example lattice matched multi-junction solar cell design composed of GaInP/InGaAs/Ge. Top right: the standard illumination spectrum to outline the photon energies absorbed by each sub-cell [retrieved from: http://sunlab.site.uottawa.ca/ on July 31st, 2012; courtsey of Christopher Valdivia]. Bottom: Plot of bandgap as a function of lattice constant for important semiconductors known to date [retrieved from: http://gorgia.no-ip.com/phd/html/thesis/phd_html/node4.html on July 31st, 2012; courtesy of Simone Montanari.]

systems. However, there are intricate complexities in growing such lattice mismatched heterojunction structures due to the important strain considerations, such as optimizing graded metamorphic buffer layers [7] or growing a cell in an inverted manner [8]. Regardless of the disadvantages for either lattice matched or metamorphic material systems, properly designed multi-junction solar cells can collect a greater portion of the visible spectrum in comparison to single junction solar cells. Furthermore, since an electron must effectively absorb three photons to progress through each sub-cell and complete the circuit of the MJSC, the overall photo-voltage is significantly greater than single junction devices.

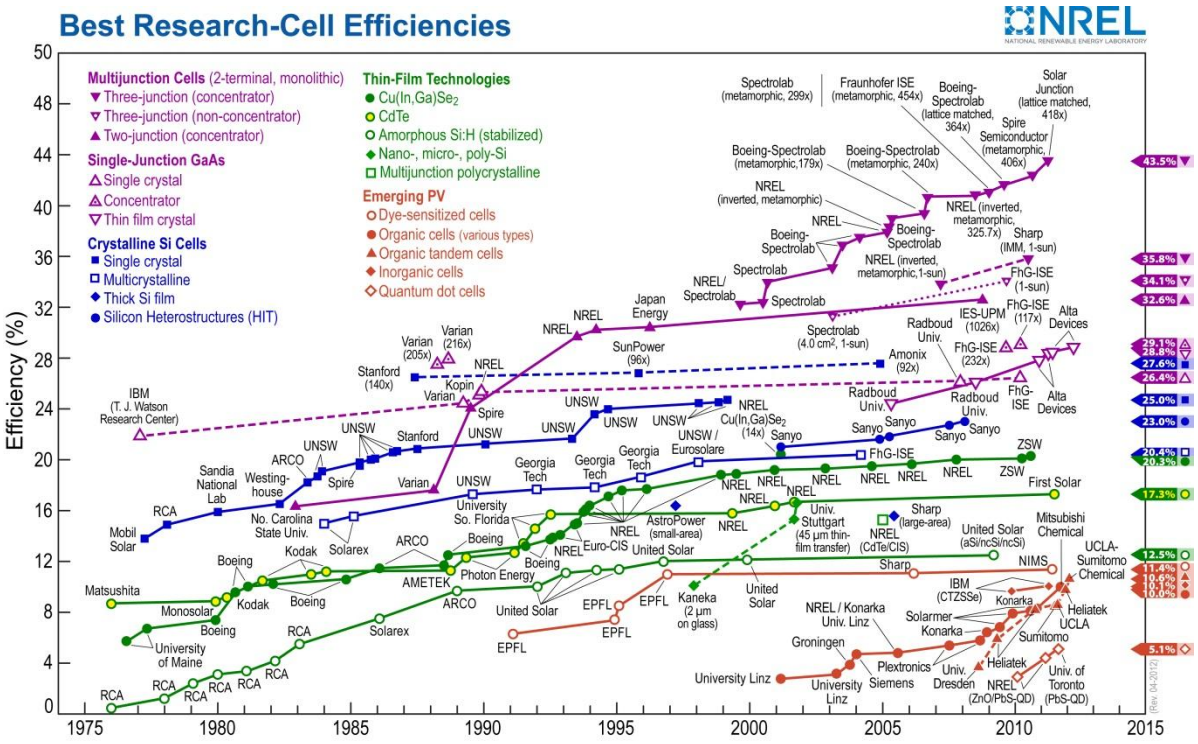

Figure 1-2. Efficiency roadmap of best research-cell efficiencies as a function of time, with the current world records outlined on the right axis. [Retrived from: www.nrel.gov/, on July 31st, 2012; courtesy of L.L. Kazmerski, National Renewable Energy Laboratory (NREL), Golden, CO.]

Presently, multi-junction solar cells mostly include dual and triple junction solar cells and it is expected that quadruple and quintuple junction cells will produce higher performing devices in the near future [9]. Originally designed for space applications due to their high performing radiation hard materials coupled to an environment where high costs were not a pressing issue, multi-junction solar cells have been a hot topic of research and development for large scale energy generation for terrestrial applications as outlined in Fig. 1-2 for the past four decades. Multi-junction solar cells are central to this thesis and are discussed in detail in chapter 4, including topics such as ideal efficiencies, important designs considerations such as tunnel junctions, and performance effects due to concentration and temperature.

Figure 1-2 illustrates the evolution of MJSC in comparison to other PV device architectures, including gallium arsenide (GaAs) single junction solar cells, silicon (Si) solar cells, thin film technologies including I-III-VI semiconductors such as $Cu(In,Ga)Se_2$ and CdTe, and emerging technologies such as organic solar cells, dye sensitized solar cells, and lastly, quantum dot solar cells. Quantum dot and/or quantum well solar cells are devices which focus on enhancing the performance of a standard solar cell through the use of these nanostructures. The benefits arise from extending the range of absorption from the solar cell to lower photon energies than the bandgap of the composing material by exploiting the optical properties of the nanostructures. This exploitation can work quite beautifully to increase the photocurrent of a solar cell as shown theoretically [10],[11] and experimentally [12],[13],[14],[15],[16]. However, an overall boost in efficiency is difficult to achieve in practice due to the voltage drop incurred when nanostructures with lower bandgaps are integrated within a bulk device [12],[13],[14]. Minimizing the open circuit voltage drop is heavily dependent on various strain compensation strategies such as strain compensation layers [14],[15]. It was shown only recently that modulation (or δ-) doped InAs quantum dots (i.e. 2-6 electrons per dot) within a single junction GaAs solar cell outperformed a single GaAs solar cell with undoped (or unmodulated) quantum dots (14.0% vs. 9.3%, respectively) [16]. Primarily due to their potential in enhancing the power conversion efficiency of a solar cell, quantum dot solar cells are still a hot topic of research in the photovoltaic community.

The concept of nanostructure enhancement to photovoltaic devices has significant potential when extrapolated to multi-junction solar cells. This is indicated in the top left panel of Fig. 1-1 where the middle sub-cell composed of InGaAs incorporates InAs quantum

dots grown within the bulk material. Since current matching is one of the most important challenges of lattice matched multi-junction solar cell design, the proposal of bandgap engineering using nanostructures such as quantum dots or quantum wells allows for designers to fine-tune the absorption range of each sub-cell and therefore maximize the photocurrent of the complete device. This idea has been the focus of experimental studies such as [17], and is currently available as a commercial device offered by Cyrium Technologies Inc. [18]. However, the modeling and simulation of such advanced devices remains to be explored in depth in the literature. This forms the central focus of this thesis: modeling and simulating nanostructure enhancements in multi-junction solar cell designs for improved device performance under concentrated illumination. Before going into the overview of this thesis, however, a brief discussion is given on the importance of approaching this problem via modeling and simulation.

1.2. Modeling and Simulation of Advanced Photovoltaic Devices

The efficiency map illustrated in Fig. 1-2 illustrates the complexity of the field of research in photovoltaics. The material systems that are exploited in some of the most advanced device architectures, such as multi-junction solar cells, are complicated in terms of growth dynamics, the physical processes occurring within these interacting optoelectronic sub-systems (i.e. sub-cells), and are expensive to grow and fabricate. This makes device design and troubleshooting a multifaceted problem in the area of research and development. For example, the top sub-cell material of triple junction solar cells is $Ga_xIn_{1-x}P$ the bandgap of which can vary between 1.8 and 1.9 eV at room temperature depending on the ordering of group III atoms (Ga and In) in the crystal lattice, which depends on growth parameters such as substrate temperature and orientation [19]. This material property, combined with the

overall thickness of this sub-cell and the design of the anti-reflection coating can all be used to current match the top and middle sub-cells for optimal device performance [19]. The optical transfer function of concentrating optics (i.e. the transmission of the incident spectrum onto the active area of the solar cell) can also be an important factor in this current matching problem. Furthermore, the integration of nanostructures for added control over the photocurrent of the middle sub-cell drastically increases the parameter space that is fundamental in optimizing the MJSC for maximal performance. This can become a costly issue from an experimental standpoint in an industrial research and development environment. Furthermore, since devices are composed of a multitude of inter-connected components (such as tunnel junctions, etalon effects and shading due to metallic contacts). The misbehaviour of devices under illumination and bias can often be difficult to understand, and thus require sophisticated modeling tools. For these reasons, the modeling and simulation of state-of-the-art devices allows for a cost-effective approach to design optimization, whilst also giving insight into troubleshooting device behaviour.

Modeling and simulation has proven quite useful in the design of tunnel junctions, which are essential components in multi-junction solar cells (for details, see sections 2.3.4 and 4.2.1). Since the measurement of tunneling devices such as tunnel diodes (or Esaki diodes) are unstable due in part to the negative differential resistance region [20] and in part to the measurement setup [21], the modeling and simulation of these stand-alone devices gives great insight into their operation and optimization [20],[22],[23]. From the perspective of equivalent circuit and/or distributed resistance models of multi-junction solar cells, tunnel junctions are often described as small resistances in series with its adjacent sub-cells [24],[25]. However, understanding the effects and optimization of tunnel junction designs

within multi-junction solar cells under concentrated illumination requires a more in-depth analysis based on energy band alignment and accurate tunneling models. For these reasons, tunnel junctions have received significant interest in the photovoltaic community. Various numerical modeling environments have been used to study and design stand-alone tunnel junction devices and as components within multi-junction solar cells, such as Silvaco by Atlas [26], Crosslight [27], and TCAD Sentaurus (Synopsys, Mountain View, California, USA) [20],[22],[23],[28],[29]. TCAD Sentaurus has been benchmarked by the semiconductor industry over the past 20 years. For two landmark publications outlining its benchmarking for PV based on its numerical engine, see [30],[31].

The design optimization of next generation photovoltaic devices such as quadruple junction solar cells and quantum dot enhanced multi-junction solar cells can also be investigated with these types of semiconductor device simulation packages. Although an important consideration for any modeling work is the appropriate calibration to experimental designs and their associated material properties, both of which are non-trivial, the benefits of developing such models can greatly assist in advancing the fundamental understanding of the physical processes involved, identifying critical parameters that influence these processes, and ultimately enhancing the performance of next generation PV devices. For example, embedding quantum dots within a solar cell leads to an increased photocurrent but a decreased open circuit voltage, which leads to an optimization problem that inherently depends on a number of quantum dot parameters such as the density of quantum dots per layer, the number of quantum dot layers, the shape and sizes of the dots (and thus energy level configurations), etc. At the time of this thesis work, known MJSC devices structures were not available to the author to assist in the calibration of the developed models.

1.3. Overview

The central focus of the thesis is understanding the photovoltaic effect in multi-junction solar cells with a focus on advancing these devices through bandgap engineering for performance improvements under concentrated illumination. **Chapter 2** gives a brief description of essential semiconductor properties and semiconductor carrier transport theory. It also describes basic quantum structures such as quantum wells and quantum dots in terms of density of states, energy levels, absorption characteristics and carrier dynamics. **Chapter 3** adopts the theory of Chapter 2 through the semiconductor device simulation software package TCAD Sentaurus by Synopsys to model and simulate semiconductor *p-n* junctions. Initially, *p-n* junctions are discussed in equilibrium before discussing perturbations to the system via an applied bias and/or illumination using energy band diagrams and current – voltage characteristics. The latter perturbation requires the computation of reflection, transmission and absorption throughout the structure, which is performed using the transfer matrix method (TMM). Other important photovoltaic concepts such as minority carrier diffusion lengths are also introduced. The chapter then focuses on the simulation of solar cells with basic guidelines on solar cell design, such as setting up appropriate meshing throughout the structure to account for shadowing and lateral currents. The mathematical methods within the numerical environment are also discussed along with convergence criteria. With these considerations in mind, the simulation results of single junction solar cells for various material systems (ex. GaAs and Si) are discussed. From this point, the impact of realistic design features such as anti-reflection coatings as well as front and back surface fields are discussed. The simulated performance of each material system is compared to data reported in the literature as a quasi-justification of the models for these

realistic solar cell designs. The final brief study included in this chapter compares the ideal performance of single junction solar cells based on detailed balance arguments to the simulated characteristics of the various material systems, i.e. outlining efficiency as a function of bandgap to illustrate the effects of including non-ideal losses in the solar cells such as non-radiative recombination.

Chapter 4 focuses on modeling and simulating multi-junction solar cells. First, the motivation and fundamental concepts of these devices are discussed. The ideal predicted efficiencies based on detailed balance arguments are then introduced as a method of designing these structures, which also serves as an introduction to an important material system for multi-junction solar cells based on lattice matching requirements: the GaInP/InGaAs/Ge MJSC structure. An alternative metamorphic design is also discussed comparatively to address the issue of optimal bandgap combinations and current matching constraints. Modeling and simulating MJSC using TCAD Sentaurus requires the methodologies from chapter 3 to be extrapolated in order to account for multiple *p-n* junctions connected in series via tunnel junctions. However, a significant portion of the focus of this chapter is placed on accurately modeling and simulating tunnel junctions, which are vital components to the operation of multi-junction solar cells. The most realistic tunneling models (band-to-band and trap assisted) are discussed analytically and then used to simulate the performance of these structures as stand-alone devices and as components within the multi-junction solar cells. Since MJSCs are intended for concentrated illumination, their effects on performance under standard testing conditions are explored based on the performance metrics of the device, i.e. current density – voltage (*J-V*) and external quantum efficiency (EQE) characteristics. However, the limitations of

concentration due to effects such as series resistance, temperature and lastly, tunnel junctions are also discussed with respect to the performance metrics. The latter two studies are important in developing appropriate thermal management strategies for MJSCs on carriers, and achieving minimum doping levels for adequate tunnel junction performance at high concentration respectively.

The enhancement potential of nanostructures (such as quantum dots and quantum wells) coupled to multi-junction solar cells is the topic of **chapter 5,** which forms the central hypothesis of this thesis: how bandgap engineering of multi-junction solar cell materials using nanostructures can enhance device performance under concentrated illumination. A literature review on the growth, energy level tuning, absorption and carrier dynamics in InAs/GaAs quantum dots is given to outline the relationship between important physical processes introduced by the nanostructures to the semiconductor equations of interest. This gives rise to the key section of this thesis: modeling quantum dots in the numerical simulation environment TCAD Sentaurus. The models are discussed in terms of absorption and confinement of carriers to describe the effects of carrier capture and escape. The overall effects are studied in terms of photovoltaic performance metrics based on varying the confinement conditions. A few parameter studies are then performed including the positioning and doping effects of the quantum dots and spacer layers. Lastly, the optimization of a QD enhanced MJSC is given to outline the highest efficiency achievable based on the developed, calibrated QD models. **Chapter 6** concludes the thesis with the impact of the work presented as well as limitations in the developed models.

Lastly, for the interest of the reader, a motivating argument for solar cells is included in Appendix A-1, as well as a comparative analysis on the theoretical efficiency of

harnessing the sun's energy via concentrating solar thermal power in A-2. Appendix B contains an example Sentaurus Device command file which is important to users interested in learning how Sentaurus can model solar cells. Lastly, Appendix C contains important derivations for the analytical absorption coefficient of quantum dots and quantum wires used in chapter 5. Appendix C also contains a detailed derivation of retrieving carrier escape and capture terms in the carrier continuity equations when bulk thermionic emission theory is used to describe these effects. This justifies its use as a first approximation to modeling a quantum dot effective medium in chapter 5.

Chapter 2: Semiconductor Properties

Semiconductors are materials with conductive properties in between conductors and insulators as indicated by the name. These conductive properties are manipulated through the controlled integration of impurities during the growth of the elemental compounds, a process known as doping. The doping influences several sets of material properties including low-field carrier mobilities, carrier concentrations, recombination processes, etc. In tertiary and quaternary semiconductor alloys, such as $Ga_xIn_{1-x}P$ and $(Al_{1-}xGa_x)_yIn_{y-1}P$, the atomic compositions add another degree of control in dictating specific material properties such as material bandgap. Exploiting the material properties of semiconductors has led to modern day devices based on the *p-n* junction, such as diodes and light emitting diodes, transistors, photodiodes, infrared lasers and solar cells. Below is a brief overview of semiconductor properties in order to develop more advanced concepts useful in understanding photovoltaic devices.

2.1. Crystal Structure and Energy Bands

Semiconductor properties depend on the elements that compose the semiconductor and the way these elements bind together to form crystal structures. Some of the most important semiconductors, such as silicon and gallium arsenide, form nearly perfect crystalline structures with repeating patterns of atoms arranged in a specific configuration to form a lattice with long-range order and symmetry. A unit cell within a lattice is the most basic repeating pattern. Simple examples of unit cells include: simple cubic, body centered cubic

and face centered cubic. However, real semiconductors do not typically form such simple crystal structures. For example, silicon and germanium form a diamond cubic structure which contains 8 atoms in a unit cell. The semiconductor gallium arsenide forms the zinc blende structure where two inter-penetrating face centered cubics of gallium atoms and arsenic atoms blend together. For more details on crystal structures and reciprocal lattices, see for example Ashcroft and Mermin [32].

The unit cell of a semiconductor establishes the periodicity of the atomic potentials of the lattice, where the periodicity is expressed as $\vec{V}(\vec{r} + \overrightarrow{r_n}) = \vec{V}(\vec{r})$ for any Bravais lattice vector $\overrightarrow{r_n} = n_1\overrightarrow{a_1} + n_2\overrightarrow{a_2} + n_3\overrightarrow{a_3}$ for any $\{n_i\}$. This periodic potential is extremely important in solving the single-particle Schrödinger equation. The solution to the wavefunction for a single particle within such a periodic potential takes the form of the Bloch function $\psi_{n,k}(\boldsymbol{r})$ as [32]

$$\psi_{n,k}(\boldsymbol{r}) = u_{n,k}(\boldsymbol{r}) \cdot e^{i\boldsymbol{k}\cdot\boldsymbol{r}} \tag{2.1.1}$$

where $\boldsymbol{k}$ represents the wavevector of the carrier, n is the index of the energy band and represents the n^{th} solution for the given wavevector, and $u_{n,k}(\boldsymbol{r})$ is the periodic Bloch function that modulates the electronic plane wave given as $e^{i\boldsymbol{k}\cdot\boldsymbol{r}}$; the periodicity of the Bloch function is the same as the atomic potentials in the lattice. The energy eigenvalues of the Bloch functions, $E_n(\boldsymbol{k})$, represent the allowed energy levels within the semiconductor which depends highly on the wavevector $\boldsymbol{k}$. These energies are periodic in the reciprocal space associated with the unit cell geometry, which is called the first Brillouin zone. As a result of symmetry considerations, solving for these energies as a function of the wavevector $\boldsymbol{k}$ gives the energy-momentum (E-k) diagram of the semiconductor. This energy band structure can

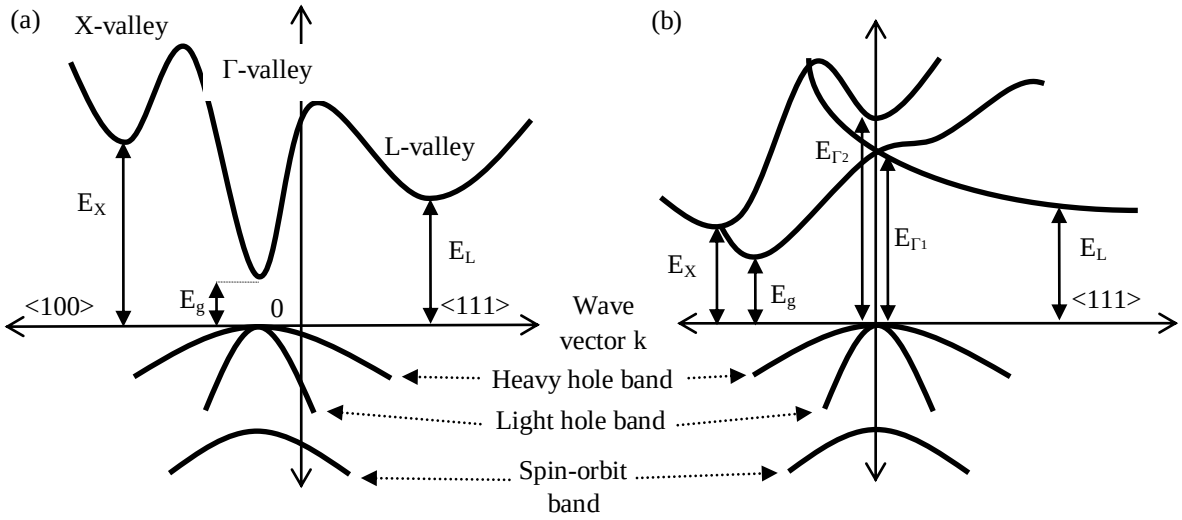

Figure 2-1. a) Illustration of direct energy-momentum (E-k) diagram (GaAs) and b) indirect energy-momentum diagram (Si). Source: NSM database.

be computed using a number of numerical methods, including the tight-binding method [1], the augmented plane wave method [32], the pseudopotential method [32] and the **k·p** perturbation method [33] to name a few. Direct and indirect energy-momentum diagrams are illustrated in Fig. 2-1. An assumption for the remainder of the thesis is that only direct transitions are considered for III-V materials (thus silicon is an exception).

In order for valence electrons to be considered "free", they must gain enough energy to hop into the conduction band where available electronic states exist. The separation in energy between the top of the valence band and the bottom of the conduction band is defined as the energy bandgap, which is specific to the semiconductor material and is one of the most important properties in semiconductor physics. The presence of the energy bandgap is essential in understanding semiconductor physics and concepts such as free carrier concentrations, quasi-Fermi levels and carrier dynamics within a semiconductor. A summary of basic processes within semiconductor band theory is given in Fig. 2-2a, which outlines the edges of the conduction and valence bands as a function of position, the minimum energy required to release an electron from the bottom of the conduction band to

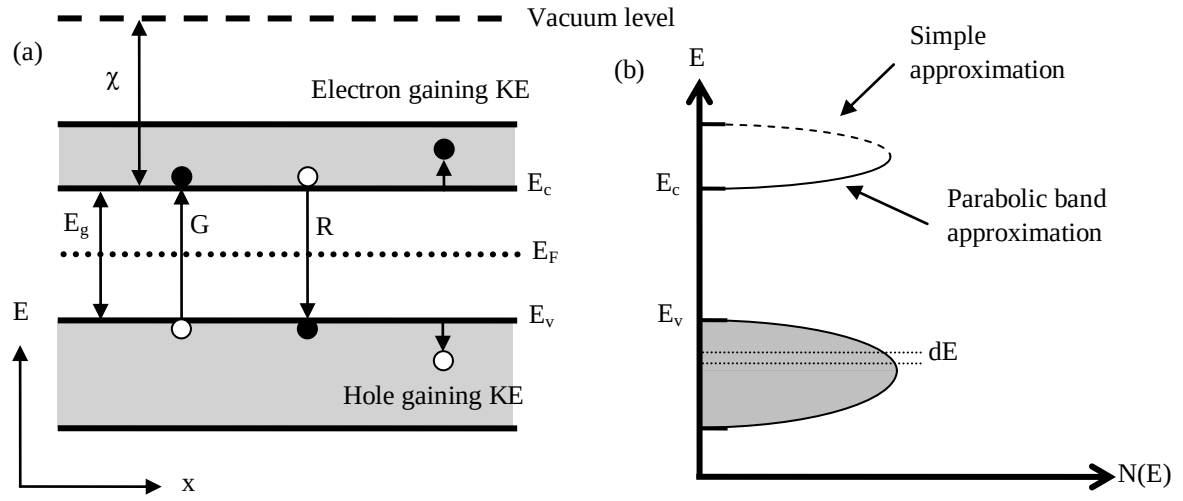

Figure 2-2. a) Simple energy band diagram of a semiconductor with bandgap E_g separating the conduction and valence bands, with the Fermi level near the middle of the bandgap. Typical semiconductor processes such as generation (G), recombination (R) and electrons and holes gaining kinetic energy are outlined with arrows. The electron affinity (χ) is also outlined. b) Corresponding illustration of the density of electronic states (*N(E)*) as a function of energy, where the filled area represents the carriers in the valence band, and empty represents available electronic states in the conduction band.

vacuum (known as the electron affinity, χ), generation (G) and recombination (R) processes, and the Fermi level (E_F) near the middle of the bandgap which is typical of intrinsically pure semiconductors. Figure 2-2b illustrates the associated occupied and unoccupied number of states in each band as a function of energy, where *N(E)* is the density of states at a specific energy *E* (a topic discussed in the next section), and dE is a small energy interval which is useful when considering the density of states and equilibrium carrier concentrations, as discussed below.

2.2. Equilibrium Carrier Concentrations

Carrier concentrations in semiconductors are fundamental in dictating the overall resistivity (or conductivity) of the material. The higher the concentration of free carriers, the higher the conductivity of the material, as given by

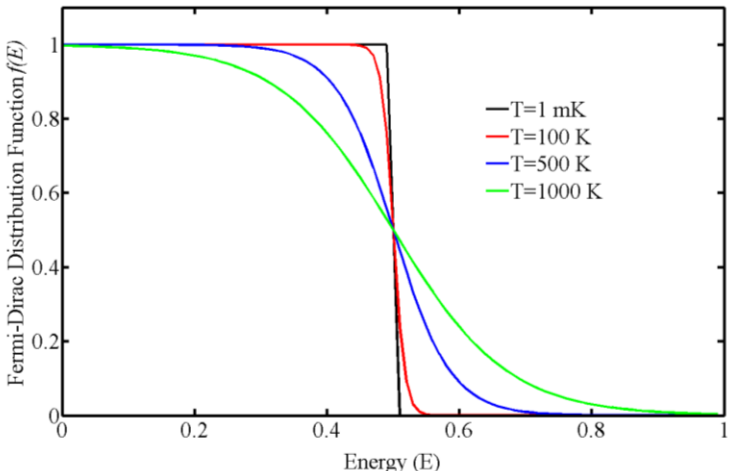

Figure 2-3. Fermi-Dirac distribution function for various temperatures, where the Fermi level is located at an energy E_F=0.5 (in arbitrary units).

$$\sigma = q(\mu_n n + \mu_p p) = \frac{1}{\rho} \tag{2.2.1}$$

where σ is the conductivity (ρ being the resistivity), $\mu_{n,p}$ are the carrier mobilities for electrons (n) and holes (p), and n and p are the free electron and hole concentrations respectively. By free, it is implied that electrons (holes) are in the conduction (valence) band of the material. Carriers can become free through thermal excitation, photo-excitation, carrier injection, or through doping (i.e. extrinsic carriers).

2.2.1. Intrinsic carrier concentrations

In practice, typical defect concentrations in intrinsic semiconductors are on the order of 1×10^{15} cm^{-3} to 1×10^{16} cm^{-3}, which is orders of magnitude smaller than the average density of atoms within the structure (comparable to Avogadro's number). Although some defect densities as low as 1×10^{13}-1×10^{14} cm^{-3} have been reported in the literature for research grade materials [34], such low values are not typically seen in semiconductor devices. Ignoring the effects of defects, intrinsic carrier concentrations can be calculated based on statistical thermodynamic arguments for fermions, which are summarized below.

The number of electrons occupying energy levels within the conduction band can be expressed as the product of the total number of available electronic states and the probability of having a fermion occupy a state at an energy *E*, integrated over the possible energy levels in the conduction band. This is expressed as

$$n = \int_{E_c}^{\infty} N(E) f(E) dE \tag{2.2.2}$$

where *N(E)* is the density of states and *f(E)* is the Fermi-Dirac distribution function, given as

$$f(E) = \frac{1}{1+\exp[(E-E_F)/kT]} \tag{2.2.3}$$

where E_F is the Fermi energy level, defined as the highest energy level occupied by electrons at zero Kelvin, *k* is Boltzmann's constant, and *T* is the temperature in Kelvin. Figure 2-3 illustrates the Fermi-Dirac distribution function as a function of energy for various temperatures. This figure demonstrates that the probability of a carrier occupying a state at energy *E* below that of the Fermi energy (E_F=0.5 in this example) is unity for a temperature close to 0 K (0.001 K in this numerically computed example). For energies above the Fermi energy, the probability drops to zero. However, as the temperature increases, the Fermi-Dirac distribution distorts such that fermions can occupy states above the Fermi energy solely due to thermal excitation (or phonon interaction).

To calculate carrier concentrations according to equation (2.2.2), certain assumptions must be made on the density of states *N(E)*. The first is to approximate the bands as parabolic near the band edges, where a Taylor series of the energy dependence on wavevector is taken to second order with respect to $\boldsymbol{k}$. This is known as the parabolic band approximation, and is given by

$$E(k) = E_c + \frac{\hbar^2 k^2}{2m^*}, \tag{2.2.4}$$

where m^* represents the density of states effective mass of the electrons and $\hbar$ is Planck's constant. This density of states effective mass is a parameter obtained from the band structure by

$$\frac{1}{m^*} = \frac{1}{\hbar^2}\frac{\delta^2 E_c(k)}{\delta k^2}. \tag{2.2.5}$$

The density of states effective mass is typically taken as a single value corresponding to the edge of the conduction band (or valence band for holes). However, it is actually a tensor depending on the crystal wavevector in reciprocal space. For our purposes, the effective mass at the Γ-point is sufficient. Using the parabolic band approximation given in equation (2.2.4) and the Pauli Exclusion Principle, one can approximate the number of available states per unit crystal volume. Although the derivation is not shown here, it can be shown that the bulk density of states for the conduction band can be expressed as

$$N_c(E) = \frac{\sqrt{2}m_e^{*3/2}}{\pi^2\hbar^3}\sqrt{E - E_c}. \tag{2.2.6}$$

Based on equations (2.2.6) and (2.2.2), one simply needs to integrate the Fermi-Dirac function with the density of states to obtain the expression for the carrier concentration, given as

$$n = N_c \frac{2}{\sqrt{\pi}} F_{1/2}\left(\frac{\mathrm{E_F - E_c}}{\mathrm{kT}}\right) \tag{2.2.7}$$

where N_c is the effective density of states in the conduction band given by $N_c = 2\left(\frac{2\pi m_e^* kT}{h^2}\right)^{3/2}$, and $F_{1/2}$ represents the Fermi-Dirac integral of order ½ given by

$$F_{1/2}\left(\frac{\mathrm{E_F - E_c}}{\mathrm{kT}}\right) = \int_{E_c}^{\infty} \frac{[(\mathrm{E - E_c})/kT]^{1/2}}{1+\exp[(\mathrm{E - E_c})/kT]}\frac{dE}{kT}. \tag{2.2.8}$$

This integral can be approximated using Boltzmann statistics for intrinsic semiconductors where the Fermi level is far from both the conduction and valence band edges, which gives

$$n = N_c \exp\left(\frac{\mathrm{E_F - E_c}}{\mathrm{kT}}\right). \quad (2.2.9)$$

Similarly for the concentration of holes,

$$p = N_v \exp\left(\frac{\mathrm{E_v - E_F}}{\mathrm{kT}}\right), \quad (2.2.10)$$

where N_v is the effective density of states in the conduction band given by $N_v = 2\left(\frac{2\pi m_h^* kT}{h^2}\right)^{3/2}$. The density of states effective mass of the hole in the valence band is typically expressed as $m_h^* = \left({m_{lh}^*}^{3/2} + {m_{hh}^*}^{3/2}\right)^{2/3}$, where m_{lh}^* and m_{hh}^* are the light and heavy hole masses respectively. For electrons, the effective mass can be computed based on transverse and longitudinal electron masses. In an intrinsic semiconductor, Boltzmann's approximation to equation (2.2.8) is excellent. As a result of using equations (2.2.9) and (2.2.10), one can solve for the Fermi level for the intrinsic semiconductor

$$\mathrm{E_F} = \mathrm{E_i} = \frac{\mathrm{E_c + E_v}}{2} + \frac{kT}{2} ln\left(\frac{N_v}{N_c}\right). \quad (2.2.11)$$

The final important parameter for intrinsic semiconductors is the intrinsic carrier concentration n_i, representative of the electron carrier concentration due to thermal excitation, which is by definition also equal to the hole concentration in the valence band. This intrinsic carrier concentration can be expressed as

$$n_i = N_c \exp\left(\frac{\mathrm{E_i - E_c}}{\mathrm{kT}}\right) = N_v \exp\left(\frac{\mathrm{E_v - E_i}}{\mathrm{kT}}\right) = \sqrt{N_c N_v} \exp\left(-\frac{\mathrm{E_g}}{\mathrm{2kT}}\right), \quad (2.2.12)$$

where we use $E_g = E_c - E_v$. This can be generalized even further as

$$n_i = 4.9 \times 10^{15} \left(\frac{m_e^* m_h^*}{m_0}\right)^{3/4} T^{3/2} \exp\left(-\frac{\mathrm{E_g}}{\mathrm{2kT}}\right). \quad (2.2.13)$$

Equation (2.2.13) states that the product of the electron and hole concentration remains fixed in a material at a given temperature. This is the mass-action law, and is expressed as

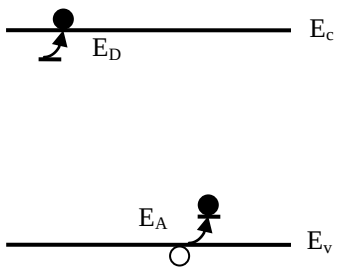

Figure 2-4. Process of ionizing dopant atoms to donate electrons into the conduction band or accept valence electrons. Each contributes extrinsic carriers to the lattice.

$$pn = N_c N_v \exp\left(-\frac{\mathrm{E_g}}{\mathrm{kT}}\right) = {n_i}^2. \tag{2.2.14}$$

2.2.2. Extrinsic carrier concentrations

A doped semiconductor can contain a mixture of donor and/or acceptor impurities to add free carriers to the system and dominate the intrinsic carrier concentration. The former gives rise to an *n*-type semiconductor as dopant atoms donate electrons to the lattice, whereas the latter results in a *p*-type semiconductor as dopant atoms accept electrons from the lattice, which is equivalent to the donation of holes. In both scenarios, these donated and accepted carriers are referred to as extrinsic carriers. Figure 2-4 illustrates the energy band structure of doped semiconductors. It outlines the fact that for dopant atoms to donate or accept electrons, these atoms must be ionized. In other words, for a donor atom to give up its electron to the lattice, the electron must gain a certain amount of thermal energy (given by $\mathrm{E_D}$) to be excited to the conduction band. Similarly, for an acceptor atom to accept an electron (and donate a hole to the lattice), an electron from the valence band must be excited into the acceptor state through thermal excitation, where this ionization energy is given by E_A. The total number of ionized donors can be expressed as

$$N_D^+ = \frac{N_D}{1+g_D \exp[(E_F - E_D)/kT]}, \tag{2.2.15}$$

Where g_D is the ground-state degeneracy of the donor impurity level (equal to 2 due to spin degeneracy). Similarly, the ionized acceptor concentration can be expressed as

$$N_A^- = \frac{N_A}{1+g_A \exp[(E_A - E_F)/kT]}. \quad (2.2.16)$$

The ground-state degeneracy of acceptor atoms is 4 in this case due to the double degeneracy of the defect state for heavy and light holes, which are also degenerate in spin. The defect state can then be described by a by a linear superposition of the 4 degenerate VB states.

When doping is considered in the semiconductor, the Fermi level moves away from the intrinsic energy of the semiconductor due to the modified carrier concentration, although this depends on the ionization level of the dopant atoms. One can determine the Fermi level based on charge neutrality conditions, given as

$$n + N_A^- = p + N_D^+. \quad (2.2.17)$$

When a material is predominantly doped *n*-type, however, this charge neutrality can be simplified as $n \approx N_D^+$, if the donor impurity concentration is larger than the intrinsic carrier concentration. This gives us the following transcendental equation

$$N_c \exp\left(\frac{\mathrm{E_F - E_c}}{\mathrm{kT}}\right) = \frac{N_D}{1+2\exp[(E_F - E_D)/kT]}. \quad (2.2.18)$$

Equation (2.2.18) cannot be solved analytically. In order to determine the Fermi level of a doped semiconductor, one must solve this equation numerically based on the parameter set corresponding to the semiconductor; this includes knowing N_D, E_D, N_C and the temperature T. For example, let us consider an *n*-type GaAs semiconductor sample at room temperature where the dopant atoms are tellerium (Te) with a donor level 0.03 eV below the conduction band and a donor concentration of 1×10^{17} cm^{-3}. Figure 2-5 illustrates the graphical method of determining the Fermi level, which is the intersection of the ionized donor concentration

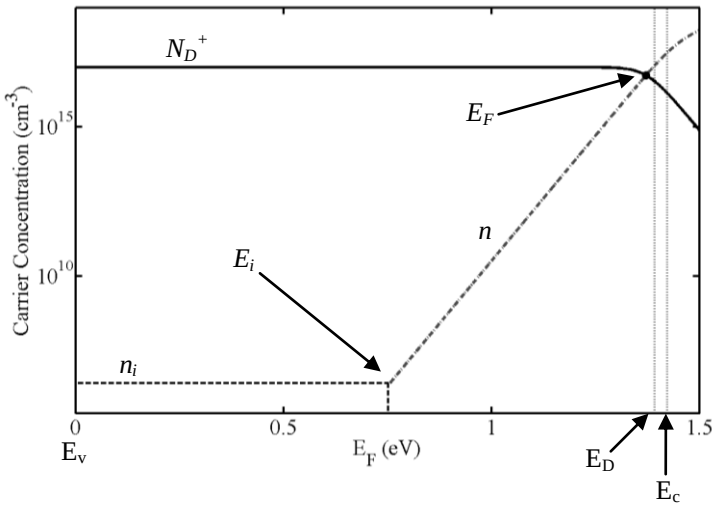

Figure 2-5. Illustration of the graphical method of determining the Fermi level for an *n*-type GaAs sample doped at 1×10^{17} cm^{-3} at T = 300 K using Te dopant atoms. E_i represents the Fermi level for intrinsically pure GaAs.

N_D^+ and the carrier concentration n. According to these calculations, 53% of the donor atoms are ionized at room temperature, resulting in a carrier concentration on the order of 5.3×10^{16} cm^{-3}. In such a doped semiconductor, one can observe the Fermi level has moved much closer to the conduction band. Similarly, *p*-type semiconductors have Fermi levels closer to the valence band.

In an *n*-type semiconductor, the electron concentrations are significantly higher than the thermal equilibrium intrinsic electron concentration. Since the mass-action law $pn = {n_i}^2$ is valid at equilibrium, the hole concentration is greatly reduced, since $p = \frac{{n_i}^2}{N_D}$. For these reasons, the electrons are considered majority carriers, and holes are minority carriers. One can see that according to equation (2.2.1), the conductivity increases significantly since $n \approx N_D \gg n_i$. At high temperatures, the intrinsic carrier concentrations become comparable to the dopant concentration(s), and eventually dominate the carrier concentrations. In these scenarios, the neutrality condition cannot be simplified, and the resulting system of equations becomes more complex. One can also consider both types of dopant atoms in the

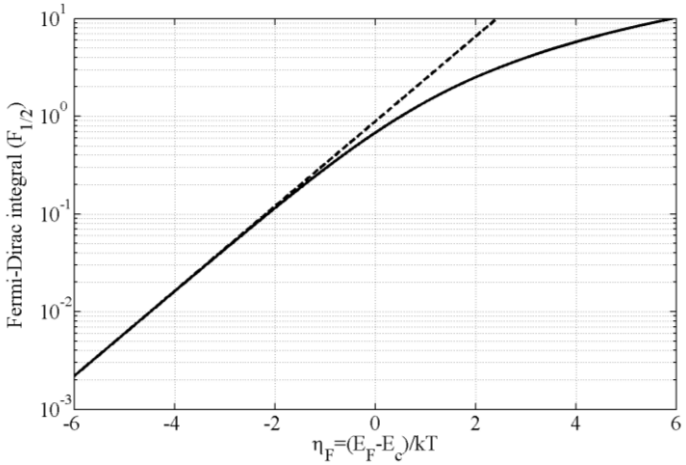

Figure 2-6. Fermi-Dirac integral as a function of Fermi energy (solid line), including the Boltzmann approximation (dashed line).

neutrality condition in compensated semiconductors. For more details on these scenarios, see section 1.4 of [35]. The information of the carrier concentration can be obtained from resistivity measurements as a function of inverse temperature, which yields great insight into extrinsic and intrinsic regimes of a semiconductor.

However, in highly doped semiconductors, the Boltzmann approximation may not necessarily hold. This depends on the proximity of the Fermi level to the conduction band to describe the carrier concentrations. Consider again the Fermi-Dirac integral given by equation (2.2.8), where $\eta_F = (E_F - E_c)/kT$. Figure 2-6 shows the numerically computed Fermi-Dirac integral compared to the Boltzmann approximation given by

$$F_{1/2}\left(\frac{\mathrm{E_F}-\mathrm{E_c}}{\mathrm{kT}}\right) = \frac{\sqrt{\pi}}{2}\exp\left(\frac{\mathrm{E_F}-\mathrm{E_c}}{\mathrm{kT}}\right). \tag{2.2.19}$$

Figure 2-6 illustrates that the Boltzmann approximation fails if $\eta_F > -1$. This situation corresponds to when the doping concentration N_D or N_A are close to the effective density of states N_c and N_v. For these reasons, Fermi statistics are of vital importance in simulating carrier concentrations in semiconductor devices, especially when doping levels are quite high, such as in tunnel junctions (see chapter 4). Heavy doping also has effects on the

overall bandgap, as the donor and/or acceptor states introduced into the bandgap form tails under the conduction band (or above the valence band), which reduces the bandgap. Alternatively, for degenerate semiconductors, the Burstein-Moss shift can occur since the Fermi level is within the conduction band such that carriers excited to the conduction band need to enough energy to be promoted to an unoccupied region of the conduction band. This effectively increases the bandgap. Such bandgap normalization effects cannot always be explicitly treated in modeling, however, as empirical data is not always reliable.

2.3. Carrier Transport

The previous section discussed notions of semiconductors in thermodynamic equilibrium. When semiconductors are under an external perturbation, such as under light biasing or carrier injection from an external voltage, the semiconductor's equilibrium is disturbed. However, if these perturbations are only slightly disturbing the equilibrium, and are not changing too quickly, then the population of carriers relaxes to a state of quasi-thermal equilibrium. It is a good approximation due to the extremely fast intraband relaxation processes (picosecond to femtosecond) compared to interband recombination (millisecond to nanosecond). Another important aspect that is introduced in this section is the split population of electrons and holes under these types of perturbations. For these reasons, the Fermi level are split into two quasi-Fermi levels, one for electrons in the conduction band and one for holes in the valence band. Below, basic semiconductor transport theory is outlined starting from Maxwell's equations, followed by generation and recombination processes and concluded by a brief introduction to quantum structures.

2.3.1. Continuity Equations and Poisson's Equation

Starting from Maxwell's equations, one can derive the relevant semiconductor equations of interest in current semiconductor transport theory. These are given respectively as

$$\nabla \times \vec{E} = 0 \tag{2.3.1}$$

$$\nabla \times \vec{H} = \vec{J} + \frac{\delta \vec{D}}{\delta t} \tag{2.3.2}$$

$$\nabla \cdot \vec{D} = \rho, \qquad \nabla \cdot \vec{B} = 0 \tag{2.3.3}$$

where $\vec{E}$ is the applied electric field, $\vec{H}$ is the magnetic field (related to $\vec{B}$ using the relation $\vec{B}=\mu\vec{H}$, where μ is the magnetic permeability of the material), $\vec{J}$ is the conduction current density, $\vec{D}$ is the electric displacement field given as $\vec{D} = \varepsilon\vec{E}$ (where ε is the dielectric permittivity of the material), and ρ is the free charge density. As a result of equation (2.3.1), one can express the electric field as the gradient of a scalar electrostatic potential field φ as $\vec{E} = -\nabla\varphi$. Applying equation (2.3.4) with Gauss' law given by equation (2.3.3) and using the relation $\vec{D} = \epsilon\vec{E}$, assuming isotropic materials, one obtains Poisson's equation, given as

$$\nabla \cdot (\epsilon\nabla\varphi) = \rho = q(p - n + N_D^+ - N_A^-), \tag{2.3.4}$$

where the free charge density ρ is given by the sum of free electron and hole concentrations n and p as well as the ionized impurity concentrations N_A^- and N_D^+. Equation (2.3.4) dictates the resulting electric field responsible for separating charged carriers in *p*-*n* junctions, as discussed in chapter 3. The next set of important equations are the continuity equations, which are derived using Ampère's law (equation 2.3.2) coupled with the fundamental property of any vector: $\nabla \cdot (\nabla \times H) = 0$. Together, they give

$$\nabla \cdot \left(\nabla \times \vec{H}\right) = 0 = \nabla \cdot \vec{J} + \frac{\delta(\nabla \cdot D)}{\delta t} = \nabla \cdot \vec{J} + \frac{\delta \rho}{\delta t}. \tag{2.3.5}$$

Equation (2.3.5) can also be expressed as

$$0 = \nabla \cdot \vec{J} + q\frac{\delta}{\delta t}(p - n + N_D^+ - N_A^-). \tag{2.3.6}$$

Since the conduction current density J is a contribution of electron and hole current densities respectively, one can separate equation (2.3.6) into its constituent components, given as

$$0 = \nabla \cdot \vec{J}_n - q\frac{\delta n}{\delta t}, \qquad 0 = \nabla \cdot \vec{J}_p + q\frac{\delta p}{\delta t}, \tag{2.3.7}$$

where it is assumed the ionized acceptor and donor concentrations are constant over time. In perturbed semiconductor materials, however, the generation and recombination of free carriers through various scattering processes (such as carrier-phonon, carrier-photon and carrier-carrier) are important to consider in balancing equations (2.3.7) such that the net change in carrier densities over time is zero, or

$$\frac{\delta n}{\delta t} = \frac{1}{q}\nabla \cdot \vec{J}_n + G_n - R_n = 0, \qquad \frac{\delta p}{\delta t} = -\frac{1}{q}\nabla \cdot \vec{J}_p + G_p - R_p = 0. \tag{2.3.8}$$

The equations above represent the fundamental carrier continuity equations in semiconductors and are set to zero to represent a static quasi-equilibrium system. The generation and recombination parameters are discussed in the next section. Prior to this, however, the current equations in semiconductors must be introduced corresponding to diffusion and drift forces.

2.3.2. Drift and Diffusion

Free carriers initially experience a random walk type of motion in the material. This random motion is associated with the scattering of carriers off lattice atoms in the structure as shown in Fig. 2-7, and results in no net motion due to the randomness of this process. The average thermal velocity associated with this random motion can be expressed as $v_{th} = \sqrt{3kT/m}$ where the behaviour of carriers can be approximated using the ideal gas law

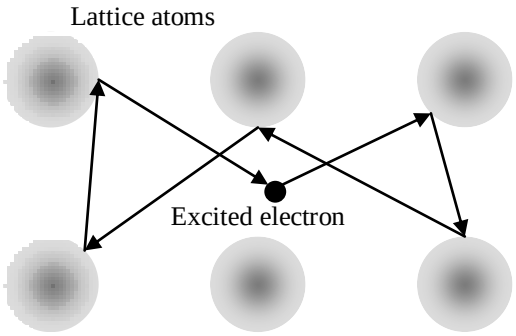

Figure 2-7. Random motion of an electron due to scattering by lattice atoms.

according to the equipartition theorm from statistical mechanics. Since carriers incur no net motion, this type of process does not contribute to current. In the event that carriers are generated non-uniformly in the structure (due to a local injection of carriers or non-uniform illumination), a gradient in carrier concentration is formed which results in a diffusion process. The flux of carriers due to this gradient is governed by Fick's law, expressed as

$$\left.\frac{dn}{dt}\right|_x = D_n \frac{d^2 n}{dx^2} \tag{2.3.9}$$

where D_n is the diffusion constant given by $D_n = {}^1\!/_3\, v_{th}^2 \tau_{scat}$ where τ_{scat} is the average scattering time of carriers off lattice atoms. The flux of carriers results in a diffusion current which is given by

$$J_{n,diff}(\boldsymbol{r}) = qD_n \nabla n, \qquad J_{p,diff}(\boldsymbol{r}) = -qD_p \nabla p. \tag{2.3.10}$$

The diffusion coefficients can be related to the mobility of carriers through the Einstein relations, valid for nondegenerate semiconductors, given as

$$\mu_n = \frac{qD_n}{kT}, \qquad \mu_p = \frac{qD_p}{kT}. \tag{2.3.11}$$

In the presence of an electric field, which could be due to the application of a voltage or the built-in electric field in a *p-n* junction (see chapter 3), another type of motion is introduced: drift. It is found that in low electric fields, the drift velocity of carriers is proportional to the electric field through carrier mobility, or $v_{drift} = \mu E$, where μ represents the mobility of the carrier in units of $cm^2\ V^{-1}\ s^{-1}$ for an electric field given in units of V/cm.

For higher electric fields, the velocity typically overshoots before a saturation of the drift velocity is observed. In this section, we will assume a low electric field. The mobility is a very important property of carriers in a semiconductor and depends on phonon scattering, ionized impurity scattering and carrier-carrier scattering. Each contribution to the mobility can be derived theoretically (see for example section 1.5.1 of chapter 1 in [35]) and added together according to Matthiessen's rule (based on adding rates together), given by

$$\frac{1}{\mu} = \frac{1}{\mu_{lattice}} + \frac{1}{\mu_{phonons}} + \frac{1}{\mu_{carrier-carrier}}. \tag{2.3.12}$$

Qualitatively speaking, the mobility can be expressed based on the mean free time between scattering processes, τ_{scat}, giving the expression

$$\mu = \frac{q\tau_{scat}}{m^*} = \frac{q\lambda}{\sqrt{3kTm^*}}, \tag{2.3.13}$$

where λ represents the mean free path, given by $\lambda = v_{th}\tau_{scat}$. Since the mobility is inversely proportional to the effective mass of the carrier, electron mobilities are larger than hole mobilities since $m_h^* > m_e^*$ in most semiconductor materials. In numerical simulation environments, however, the mobility of carriers is typically expressed empirically as a function of doping or impurity concentration, which will be discussed in chapter 3. The resulting drift current can be expressed as

$$J_{drift}(\boldsymbol{r}) = \sigma E(r) = q\big(\mu_n n + \mu_p p\big)E. \tag{2.3.14}$$

Combining the drift current with the diffusion current given by equations (2.3.10) gives the final set of drift-diffusion current densities, given as

$$J_n(\boldsymbol{r}) = qD_n\nabla n + q\mu_n En, \quad J_p(\boldsymbol{r}) = -qD_p\nabla p + q\mu_p Ep. \tag{2.3.15}$$

Lastly, it is important to note that the total current density through a material or device is the sum of equations (2.3.15). These two equations, combined with the continuity equations (2.3.8) and Poisson's equation (2.3.4) form the basic semiconductor physics equations.

2.3.3. Minority Carrier Diffusion Lengths

In the context of photovoltaics, carriers that are generated through photon absorption will diffuse through the material according to a characteristic length scale. One can study this by substituting the current equations (2.3.15) into the continuity equations (2.3.8) in one dimension (say along the *x*-direction),

$$D_n \frac{d^2n}{dx^2} + \mu_n E \frac{dn}{dx} + \mu_n n \frac{dE}{dx} + G_n - R_n = 0,$$

$$D_p \frac{d^2p}{dx^2} + \mu_p E \frac{dp}{dx} + \mu_p p \frac{dE}{dx} + G_p - R_p = 0. \quad (2.3.16)$$

where E is the electric field. The above equations can be greatly simplified to reveal the concept of minority carrier diffusion lengths, if one carrier type greatly exceeds the other, in which case the recombination terms are approximated as $R_n \approx (n - n_0)/\tau_n$. Furthermore, if the electric field is zero or constant, such as in the neutral regions away from the depletion region, then equation (2.3.16) can be re-written for electrons as

$$\frac{d^2n}{dx^2} + \frac{G_n}{D_n} - \frac{(n-n_0)}{L_n^2} = 0, \quad (2.3.17)$$

and for holes as

$$\frac{d^2p}{dx^2} + \frac{G_p}{D_p} - \frac{(p-p_0)}{L_p^2} = 0, \quad (2.3.18)$$

where L_n and L_p are the minority carrier diffusion lengths for electrons and holes respectively, as given by $L_{n,p} = \sqrt{D_{n,p}\tau_{n,p}}$. It represents the average distance a minority carrier will diffuse prior to a recombination event. When considering strictly diffusion in one dimension, equation (2.3.17) reduces to

$$D_n \frac{d^2n}{dx^2} = \frac{(n-n_0)}{\tau_n}, \quad (2.3.19)$$

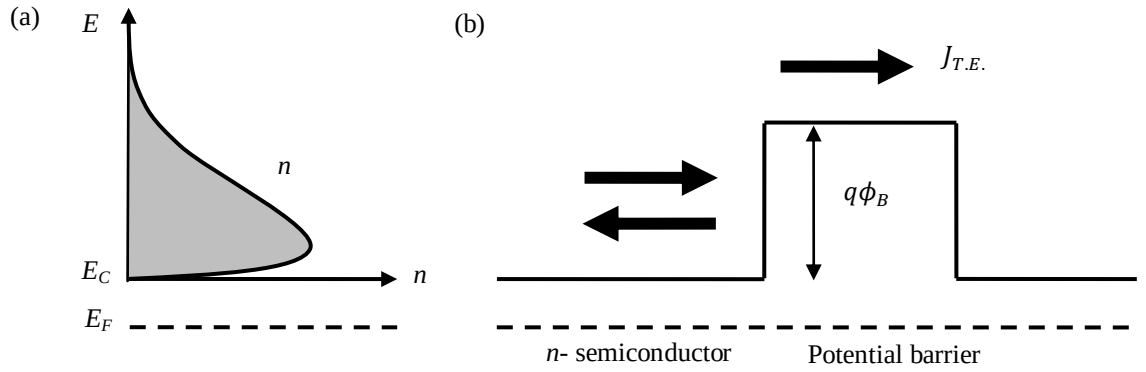

Figure 2-8. a) Electron concentration as a function of energy above the conduction band edge according to the overlap between density of states and the Fermi-Dirac distribution function, and b) the energy band diagram demonstrating the potential barrier for the carriers, and an illustration of currents from carriers with energies below (reflected) and above (J_{TE}) the potential barrier. The latter contributes to the thermionic emission current density. Figures adopted based on [35].

which has the solution of the form $\exp\left(\pm x/\sqrt{D\tau}\right)$.

2.3.4. Thermionic Emission and Tunneling

The last forms of current transport mechanisms important in semiconductor physics are thermionic emission over potential barriers and quantum tunneling of carriers through potential barriers. These two forms of current are typically secondary to the drift and diffusion components to the current. However, these currents are essential in describing the behaviour of modern photovoltaic devices.

Thermionic emission arises from the Fermi-Dirac statistics in that non-zero carrier concentrations exist at any finite energy above the conduction band edge. This process is summarized in Fig. 2-8. The theory for thermionic emission is derived in typical semiconductor textbooks such as in section 3 of chapter 3 of [35]. The form of the current density resulting from this standard derivation, which does not depend on the shape of the barrier, can be expressed as

$$J_{T.E.} = A^* T^2 \exp\left(-\frac{q\phi_B}{kT}\right), \tag{2.3.20}$$

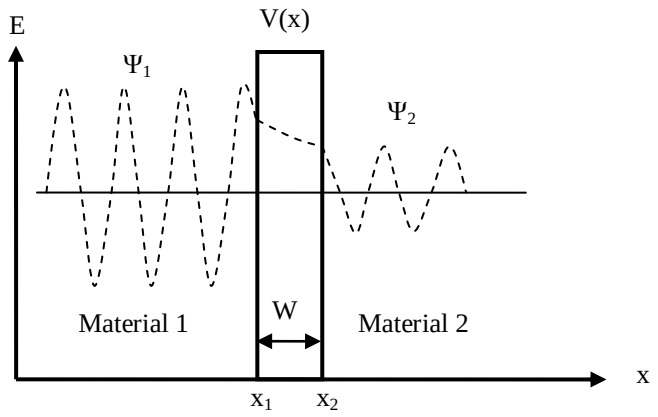

Figure 2-9. Quantum tunneling of an electronic wavefunction Ψ_1 through a rectangular potential barrier and recovering a plane wave Ψ_2 of decreased amplitude due to the exponential decay within the potential barrier. Figure adopted based on [35].

where ϕ_B is the potential barrier and A^* is the effective Richardson constant, given as

$$A^* = \frac{4\pi q m^* k^2}{h^3}. \tag{2.3.21}$$

Quantum tunneling, on the other hand, is a more complex phenomenon. According to quantum mechanics, electrons can be represented by a wavefunction and therefore possess wave-like and particle-like behaviour. The particle-like behaviour of an electron presented by a potential barrier results in the thermionic emission current presented earlier. However, the wave-like nature of the wavefunction gives rise to a finite probability of the wavefunction existing on the other side of the potential barrier. This is illustrated in Fig. 2-9, where a traveling wave strikes a potential barrier that is thin enough such that the exponential wavefunction of the electron within the barrier does not decay to zero before the barrier is terminated. The general theory of quantum tunneling depends on the potential barrier, and requires an approximation to the Schrödinger equation to solve for the electronic wavefunctions of the electron outside and inside the potential barriers. This approximation is based on separating the wavefunction into its amplitude and phase components and assuming that the amplitude varies slowly compared to its phase counter-part, or vice versa.

This allows the second derivative of the wavefunction in Schrödinger's equation to simplify greatly; this is known as the WKB approximation. In this scenario, the potential *V(x)* is assumed not to vary rapidly, which gives the following tunneling probability [35]

$$T = \frac{|\Psi_2|^2}{|\Psi_1|^2} \approx \exp\left[-2\int_{x_1}^{x_2}|k(x)|dx\right] \approx \exp\left[-2\int_{x_1}^{x_2}\sqrt{\frac{2m^*}{\hbar^2}(V(x)-E)}\,dx\right]. \quad (2.3.22)$$

The resulting tunneling current density can be expressed as

$$J_t = \frac{qm^*}{2\pi^2\hbar^3}\int f_1(E)N_1(E)T[1-f_2(E)]N_2(E)dE. \quad (2.3.23)$$

where $f_1(E)$ and $f_2(E)$ are the Fermi-Dirac distribution functions for regions 1 and 2 respectively, and $N_1(E)$ and $N_2(E)$ are the density of states in regions 1 and 2 respectively.

2.4. Recombination Mechanisms

Recombination is an integral component of semiconductors, and plays a central role in the current – continuity equations of semiconductors. Once an electron-hole pair is generated due to phonon or photon scattering, this electron-hole pair diffuses in the material until it experiences a recombination event. There exist three main recombination mechanisms: 1) Auger, 2) radiative, and 3) Shockley-Read-Hall (SRH), where this latter mechanism is non-radiative. These are discussed in more detail below, including an example for electron and hole lifetimes in GaAs as a function of impurity doping.

2.4.1. Auger

Auger recombination is a two-step process whereby an electron in the CB recombines with a hole in the VB by transfering its kinetic energy to another electron through an elastic scattering process. The electron newly excited electron then releases its extra kinetic energy through phonon scattering, thereby releasing heat. However, since this

is a three particle process, the Auger recombination rate is proportional to the third power of carrier concentrations, and is only important when carrier concentrations are very high. The recombination rate can be expressed as [36]

$$R_{Aug} = \left(C_n n + C_p p\right)(np - n_{i,eff}^2) \tag{2.4.1}$$

where n and p are carrier concentrations, $n_{i,eff}$ is the effective intrinsic carrier concentration given as $n_{i,eff} = n_i \exp\left({E_{bgn}}/{2kT}\right)$ where E_{bgn} is a bandgap narrowing term, C_n and C_p are temperature dependent coefficients given as

$$C_n(T) = \left(A_{A,n} + B_{A,n}\left(\frac{T}{T_0}\right) + C_{A,n}\left(\frac{T}{T_0}\right)^2\right)\left[1 + H_n \exp\left(-\frac{n}{N_{0,n}}\right)\right] \tag{2.4.2}$$

$$C_p(T) = \left(A_{A,p} + B_{A,p}\left(\frac{T}{T_0}\right) + C_{A,p}\left(\frac{T}{T_0}\right)^2\right)\left[1 + H_p \exp\left(-\frac{p}{N_{0,p}}\right)\right] \tag{2.4.3}$$

where $T_0 = 300\ K$, A_A, B_A and C_A are material specific parameters for electrons (n) and holes (p) respectively, and H is a parameter used in empirically modeling the decreasing Auger coefficients at high injection levels based on the reference doping concentration N_0. This mechanism is usually important in materials of low bandgap and when highly doped, or at high temperature. The Auger recombination rate can be rearranged to give

$$R_{Aug} = C_n\left(n^2 p - n n_{i,eff}^2\right) + C_p\left(np^2 - p n_{i,eff}^2\right) \tag{2.4.4}$$

which can be described as contributions from two different mechanisms: 1) a two electron collision followed by a recombination with a hole, and 2) a two hole collision followed by a recombination with an electron. Equation (2.4.4) can be simplified for the lifetime of an electron in a p-type material for band-to-band Auger recombination, expressed as

$$\tau_{n,Aug} = \frac{1}{C_p N_A^2}, \tag{2.4.5}$$

where N_A is the acceptor doping concentration (assuming 100% ionization). Similarly, the Auger recombination lifetime of a hole in an *n*-type material is given by

$$\tau_{p,Aug} = \frac{1}{C_n N_D^2}, \tag{2.4.6}$$

where N_D is the donor concentration.

2.4.2. Radiative

Radiative recombination is an inevitable process in semiconductor devices whereby electrons spontaneously recombine with a hole through the emission of a photon. The radiative recombination rate follows the equation [36]

$$R_{\text{Radiative}} = B_{\text{rad}} \left(\frac{T}{T_{par}}\right)^{\alpha} (np - n_i^2) \tag{2.4.7}$$

where B_{rad} is a material dependent radiative recombination coefficient with units of cm^{-3}/s, T_{par} is typically 300 K which serves as a reference temperature to scale to temperature T, and α is a material dependent parameter. Re-arranging equation (2.4.7) gives the electron radiative lifetime, which depends on the acceptor concentration, since the electrons are minority carriers

$$\tau_{n,Rad} = \frac{1}{B_{rad} N_A} \tag{2.4.8}$$

Similarly for holes,

$$\tau_{p,Rad} = \frac{1}{B_{rad} N_D} \tag{2.4.9}$$

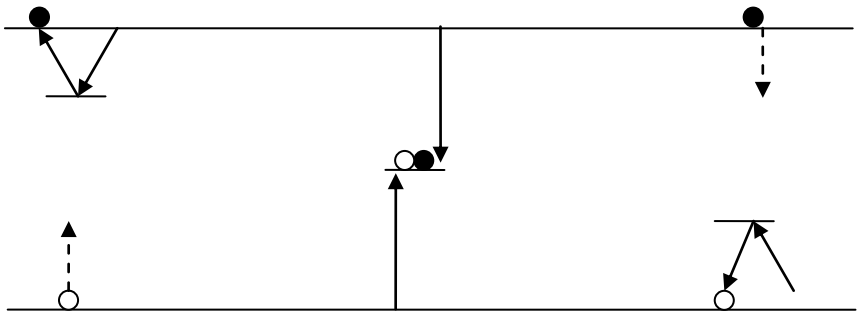

Figure 2-10. SRH recombination events through traps, shown in steps: (a) shows an electron (filled circle) being trapped and detrapped without recombination, (b) shows a recombination of an electron with a hole (empty circle) in a trap located in the middle of the bandgap, and (c) shows hole trapping and detrapping.

where N_A and N_D are the acceptor and donor concentrations respectively. The material dependent parameter B_{rad} can be calculated according to an ideal blackbody emitter as [37]

$$B_{Rad} = \frac{1}{n_i^2}\frac{2\pi}{\mathrm{h}^3 c^2}\int_0^\infty n_s^2 \alpha(E) E^2 \exp\left(-{}^{E}/_{kT}\right) dE \qquad (2.4.10)$$

where n_s is the refractive index of the material. However, modeling radiative recombination typically utilizes B_{rad} as a material dependent parameter.

2.4.3. Shockley-Read-Hall (SRH)

Shockley-Read-Hall (SRH) recombination is a non-radiative process. It involves electrons recombining with holes in deep trap levels within the forbidden bandgap (or vice versa, holes recombining with electrons trapped in deep defect levels). A carrier can be 'captured' by a trap, and subsequently released by phonon scattering. However, if the trap captures another carrier of the opposite polarity prior to the first carrier being thermally released, these two recombine non-radiatively. This is illustrated in Fig. 2-10 which shows three scenarios related to SRH recombination. The net recombination rate according to this process can be described by [36]

$$R_{net}^{SRH} = \frac{np - \gamma_n \gamma_p n_i^2}{\tau_{n,SRH}(p + \gamma_p p_t) + \tau_{p,SRH}(n + \gamma_n n_t)}, \tag{2.4.11}$$

where n_t and p_t are the electron and hole densities when the quasi Fermi levels are equal to the defect level, as given below

$$n_t = n_i \exp\left(\frac{E_{\text{trap}}}{kT}\right), \qquad p_t = n_i \exp\left(\frac{-E_{\text{trap}}}{kT}\right) \tag{2.4.12}$$

where E_{trap} is the energy difference between the defect (or trap) level and the intrinsic level, and γ_n and γ_p are Fermi functions of η_n and η_p (recall $\eta = (E - E_c)/kT$), as given below

$$\gamma_n = \frac{n}{N_C} \exp(-\eta_n), \qquad \gamma_p = \frac{p}{N_V} \exp(-\eta_p) \tag{2.4.13}$$

$$\eta_n = \frac{E_{F,n} - E_C}{kT}, \qquad \eta_p = \frac{E_V - E_{F,p}}{kT} \tag{2.4.14}$$

According to equation (2.4.11), the defect energy levels play an important role in calculating the SRH recombination rate. As a conservative approach in the simulations, E_{trap} is typically set to the intrinsic level for maximum SRH recombination. Furthermore, the minority carrier lifetimes will also play an important role in the overall recombination rate. These can be defined based on trap cross-sectional areas and trap densities within the semiconductor; however, these are difficult to measure. For these reasons, the minority carrier lifetimes are modeled empirically based on doping and temperature dependent equations as follows:

$$\tau_{dop}(N_A + N_D) = \tau_{min} + \frac{\tau_{max} - \tau_{min}}{1 + \left(\frac{N_A + N_D}{N_{ref}}\right)^{\gamma}}, \tag{2.4.15}$$

where N_A+N_D is the sum of acceptor and donor concentrations, where one typically dominates the other in a doped material, τ_{min}, τ_{max} N_{ref} and the exponent γ are material

constants. The temperature dependence of the SRH minority carrier lifetime is calculated using the temperature dependent relation below

$$\tau(T) = \tau_{dop}\left(\frac{T}{300}\right)^{\alpha}. \tag{2.4.16}$$

Typically, the minority carrier lifetimes can be simplified to

$$\tau = \frac{\tau_{max}}{1+\left(\frac{N}{N_{ref}}\right)^{\gamma}}. \tag{2.4.17}$$

Another important process within standard Shockley-Read-Hall recombination theory is surface recombination. This type of process is described in a manner very similar to bulk SRH theory introduced above, with the exception that this recombination takes place at an interface. As a result, it is no longer bulk SRH but a 2 dimensional recombination process which becomes important when considering heterointerfaces such as metal-semiconductor or semiconductor-semiconductor interfaces. The expression for surface recombination takes the form

$$R_{srv}^{SRH} = \frac{np-n_i^2}{(p+p_{int})/_{S_p}+(n+n_{int})/_{S_n}}, \tag{2.4.18}$$

where n_{int} and p_{int} are the trap densities along the interface in equation, given by

$$n_{int} = n_i \exp\left(\frac{E_{\text{trap}}}{kT}\right), \qquad p_{int} = n_i \exp\left(\frac{-E_{\text{trap}}}{kT}\right) \tag{2.4.19}$$

and s_p and s_n are the surface recombination velocities expressed in units of cm/s. These are highly dependent on the impurity concentration at the interface and can be expressed as

$$s = s_0\left[1 + s_{ref}\left(\frac{N}{N_{ref}}\right)^{\gamma}\right], \tag{2.4.20}$$

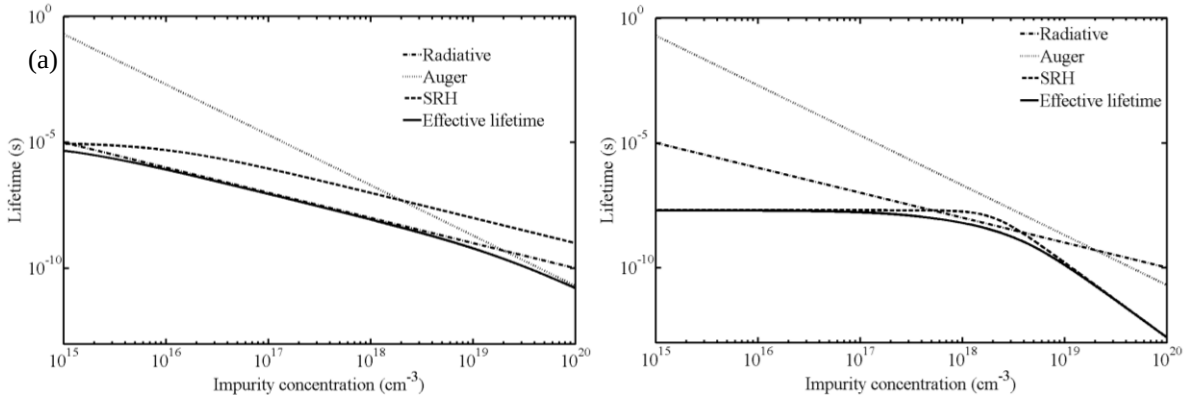

Figure 2-11. a) Electron lifetimes in p-type GaAs, which is dominated by radiative processes, and b) hole lifetime in n-type GaAs which is mostly dominated by SRH processes [39].

where the parameters above are highly dependent on the materials and growth methods. For example, the surface recombination velocities are normally on the order of 1-100 cm/s for GaInP/GaAs and GaInP/AlGaInP interfaces [38]. However, for unpassivated surfaces, the surface recombination velocity can be as high as 10^6 cm/s [39].

2.4.4. Effective Lifetime of Minority Carriers

The overall effective lifetime of a minority carrier can be expressed similar to the Matthiessen rule, as given by

$$\frac{1}{\tau} = \frac{1}{\tau_{rad}} + \frac{1}{\tau_{SRH}} + \frac{1}{\tau_{Auger}}. \tag{2.4.18}$$

Figure 2-11 displays the minority carrier lifetime dependence on impurity concentration for *n*- and *p*-type GaAs, where *p*-type GaAs is dominated by radiative recombination [40]. The SRH lifetimes are adopted from [41], whereas Auger parameters are adopted from [42].

2.5. Generation and Absorption Characteristics

In solar cells, photogeneration is the most important photo-excitation process to consider, where free carriers are generated as a result of photon interaction, or light

absorption. It is important to note that other photo-excitation mechanisms exist, such as photons absorbed by already free carriers (a process known as free carrier absorption), photons absorbed to generate phonons, and lastly, photons absorbed to excite electrons between localized states. However, free carrier absorption and phonon generation are only important at low photon energies (much smaller than the bandgap material). For energies close to the bandgap, interband transitions are dominant.

Photogeneration can be described microscopically according to the quantum mechanical description of transition probabilities. The overall transition rate of carriers being excited from an initial electronic state $|i\rangle$ at an energy E_i to a final state $|f\rangle$ at an energy E_f can be described using Fermi's Golden Rule, given by [43]

$$R_{i\to f} = \frac{2\pi}{\hbar}|\langle i|H'|f\rangle|^2 \delta\big(E_f - E_i - E\big) f_i(E_i)\left(1 - f_f\left(E_f\right)\right) \tag{2.5.1}$$

where $R_{i\to f}$ is the overall transition probability per unit time, H' is the perturbed Hamiltonian describing light-matter interactions, f_i is the Fermi-Dirac probability of a state being occupied at energy E_i, and $(1\text{-}f_f)$ represents the probability the state at energy E_f is unoccupied. The reverse process, radiative recombination, can also be described by a very similar expression. The net difference between absorption and emission (or radiative recombination) represents the net overall transition rate for a specific energy of photons $R_{net}(E)$, which must be integrated over all wavevectors of initial and final states for a specific energy. This requires the initial and final density of states as a function of wavevector, $g_i(k_i)$ and $g_f(k_f)$ respectively, and is given by [43]

$$R_{net}(E) = \frac{2\pi}{\hbar}\iint \left|H_{if}\right|^2 \delta\big(E_f - E_i - E\big)\big(f_i\big(E_i(k_i)\big) - f_f\left(E_f\left(k_f\right)\right)\right)$$
$$\times\, g_i(k_i)\, g_f(k_f) d^3k_i d^3k_f. \tag{2.5.2}$$

Expression (2.5.2) can be further simplified when considering the perturbed component of the Hamiltonian involving the initial and final states using the dipole approximation, which can be given as

$$\left|H_{if}\right|^2 = \frac{q^2}{m^2}\frac{|E_0^2|}{4\omega^2}|P_{cv}|^2, \tag{2.5.3}$$

where m is the rest mass of an electron, E_0 is the amplitude of the incident electromagnetic field, ω is the angular frequency of the incident field, and P_{cv} is the dipole matrix element given as

$$P_{cv} = \left|\langle v, k_i|\epsilon \cdot \hat{p}|c, k_f\rangle\right|, \tag{2.5.4}$$

where $\hat{p}$ is the momentum operator, and ϵ the polarisation vector. Combining equations (2.5.4) and (2.5.3) with (2.5.2) gives the overall net rate of photon absorption

$$R_{net}(E) = \frac{2\pi}{\hbar}\frac{q^2E_0^2\hbar^2}{4m_0^2E}\iint |P_{cv}|^2\,\delta(E_c - E_v - E)(f_v\big(E_v(k_v)\big) - f_c\big(E_c(k_c)\big)$$
$$\times\, g_v(k_i)\, g_c(k_f)d^3k_i d^3k_f. \tag{2.5.5}$$

Assuming the conduction and valence bands are empty and full respectively (or $f_v\big(E_v(k_i)\big) = 1$ and $f_c\big(E_c(k_f)\big) = 0$ respectively), and considering the rate at which the electromagnetic field is giving up its energy to the semiconductor material (see appendix C-1), the absorption coefficient can be expressed as

$$\alpha(E) = A\iint |P_{cv}|^2\,\delta(E_c - E_v - E)\cdot g_v(k_v)\, g_c(k_c)d^3k_v d^3k_c, \tag{2.5.6}$$

where $A = \frac{q^2\pi\hbar}{n_s c\varepsilon_0 m_0^2 E}$, n_s is the refractive index of the material for a given wavelength, ε_0 is the permittivity of free space, and c is the speed of light. In equation (2.5.6), the product of the valence and conduction band density of states can be grouped together to form the joint

density of states. For direct bandgap semiconductors, the bulk absorption coefficient can be shown to give

$$\alpha(E) = \alpha_0\sqrt{E - E_g}, \tag{2.5.7}$$

where α_0 is a material dependent parameter. For indirect bandgap semiconductors, the joint density of states follows a different dependence on energy, and the bulk absorption coefficient is highly dependent on the availability of phonons of appropriate energy to satisfy the interband transitions. It can be shown that the absorption coefficient follows the proportionality given by

$$\alpha(E) \propto \left(E - E_g\right)^2. \tag{2.5.8}$$

For more details on how to use Fermi's Golden Rule for photovoltaic materials, see chapter 4 of [43].

The photogeneration process can also be described macroscopically by the absorption coefficient, which represents the attenuation of incident intensity by the propagation of light through a material. Such a relation can be given by

$$\frac{dI}{dx} = -\alpha I \tag{2.5.9}$$

where I is the intensity of the light at a specific depth x, and α is the absorption coefficient. One can integrate equation (2.5.9) to obtain the Beer-Lambert law (assuming uniform absorption), which is given as

$$I(x) = I_o \exp\left(-\int_0^x \alpha(E, x')dx'\right) \tag{2.5.10}$$

where I_o is the incident intensity. The absorption coefficient, $\alpha(E, x)$, is related to the imaginary component of the refractive index of the material, as given by

$$\alpha(\lambda) = \frac{4\pi\kappa}{\lambda} \tag{2.5.11}$$

where k is the imaginary part of the complex refractive index, and referred to as the extinction coefficient and λ is the wavelength of the incident light, associated to its energy via $E = hc/\lambda$. The complex refractive index is typically given as $n = n_r + i\kappa$, and where the real part, n_r, indicates the phase speed of the wave. Both n_r and k are related to the dielectric constant of the material through the well known relations

$$n = \sqrt{\frac{\sqrt{\epsilon_1^2+\epsilon_2^2}+\epsilon_1}{2}}, \qquad \kappa = \sqrt{\frac{\sqrt{\epsilon_1^2+\epsilon_2^2}-\epsilon_1}{2}}, \tag{2.5.12}$$

where ϵ_1 and ϵ_2 are the real and imaginary components of the dielectric constant, as given by $\epsilon = \epsilon_1 + i\epsilon_2$. The following relationships hold as well

$$\epsilon_1 = n^2 - k^2, \qquad \epsilon_2 = 2n\kappa. \tag{2.5.13}$$

Assuming semiconductors are homogeneous, isotropic, and optically linear materials, one can readily describe their optical characteristics through their n and κ values. The origin of the extinction coefficient comes from the fact that the incident radiation decays along the z-direction according to a characteristic decay length scale of $\lambda/2\pi\kappa$, which gives rise to the aforementioned absorption coefficient in units of inverse length. Figure 2-12 illustrates the absorption coefficient for various semiconductor materials of interest in this thesis. The absorption edge, defined where the absorption coefficient drops, corresponds to the energy of the bandgap of the semiconductor material. One can observe that direct bandgap materials such as GaInP [44], GaAs [44], and Cu(In,Ga)Se_2 [45], have large absorption coefficients and sharp edges compared to indirect bandgap materials, Si [46] and Ge [44]. InAs's bandgap is close to 3.5 μm and has a strong absorption coefficient [44] through the visible spectrum wavelengths due to the high density of states at these energies. These absorption coefficients are extremely useful in computing the total generation rate in each respective

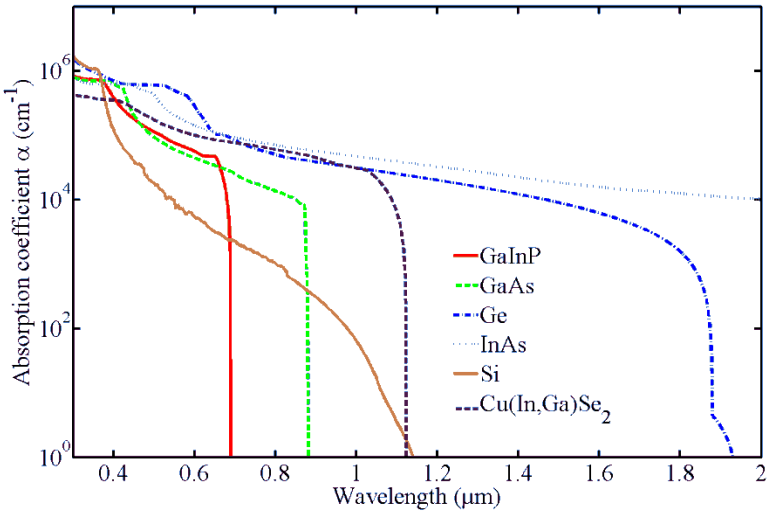

Figure 2-12. Absorption coefficients for various semiconductor materials in the wavelength range of interest (i.e. 300 to 2000 nm), where the molar fraction of Cu(In,Ga)Se_2 is x=0.2.

material. Furthermore, the refractive index profile of each material as a function of wavelength is valuable in determining the reflectivity and transmittance of light at various heterointerfaces typically found in modern photovoltaic devices. A simple calculation of the photogeneration rate at a position z for a photon energy E is done using the following equation

$$g(E,z) = \left(1 - R_{reflection}(E)\right)\alpha(E)b_s(E)\exp\left[-\int_0^z \alpha(E,x')\,dx'\right], \qquad (2.5.15)$$

where $R_{reflection}(E)$ is the reflection coefficient and $b_s(E)$ is the photon flux. Note that the reflection should consider any internal reflection from interfaces within a structure. Equation (2.5.15) must then be integrated over all photon energies to compute the total generation rate at a position z. This calculation is revised within the transfer matrix method discussion of section 3.4.2 of chapter 3.

2.6. Semiconductor Heterostructures and Quantum Confinement

2.6.1. Heterostructures and Lattice Considerations

Semiconductor heterostructures are junctions formed between two different semiconductor materials, which include examples such as Type-I (or straddling), Type-II (or staggered) and Type-III (or broken-gap) heterojunctions. These are outlined nicely in Fig. 34 of [35]. The difference in material bandgaps in such heterostructures allows for many interesting phenomena to be observed, such as structures which exhibit quantum confinement. Prominent examples include $Al_{1-x}Ga_xAs/GaAs$ quantum well devices. The exploration of heterostructures, however, is highly dependent on the epitaxial growth of high quality crystal structures that are lattice matched. This constraint allows for certain material groups to be epitaxially grown together, although lattice mismatched materials can be grown using highly specific strain management conditions such as strain compensation layers. Figure 2-13 illustrates some elemental and binary semiconductor compounds in terms of energy bandgap and lattice constant. A notable example of a widely used heterojunction is GaAs/AlGaAs, which is nearly perfect in terms of lattice constant. When growing heterojunction structures, the epitaxial layer initially adopts the lattice constant of the substrate material. As the strain builds up, this layer eventually transforms to a more relaxed state with a lattice constant closer to its energetically favourable state. The lattice mismatch between two materials is defined as

$$\Delta \equiv \frac{|a_{sub} - a_{epi}|}{a_{epi}}, \tag{2.6.1}$$

where a_{epi} and a_{sub} are the lattice constants of the epitaxial layer and of the substrate respectively. A critical thickness has been determined empirically beyond which the

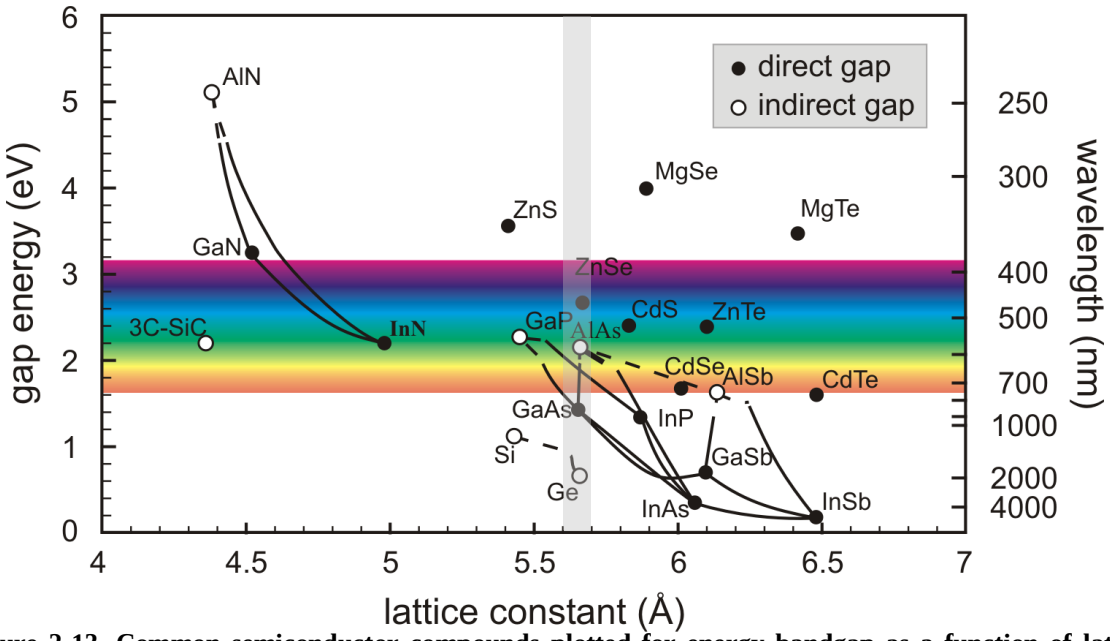

Figure 2-13. Common semiconductor compounds plotted for energy bandgap as a function of lattice constant. The light grey rectangle outlines the common lattice matching combination between $Ga_{0.51}In_{0.49}P/In_{0.01}Ga_{0.99}As$/Ge used in multi-junction solar cells. From [47].

formation of dislocation densities begins. This parameter takes the form

$$t_c \equiv \frac{a_{epi}^2}{2|a_{sub}-a_{epi}|}. \tag{2.6.2}$$

Not only are the bandgaps and lattice constants of various semiconductor materials different, but their respective electron affinities also need to be considered in designing heterojunctions. Since GaAs and $Ga_{0.51}In_{0.49}P$ are closely lattice matched to Ge (<1% lattice mismatch), the growth of high quality crystalline $Ga_{0.51}In_{0.49}P$ on GaAs and on Ge has been an important material combination for modern photovoltaic devices.

2.6.2. Quantum Structures, Energy Eigenvalues and Density of States

An important consideration in heterojunctions is the difference in electron affinities of the two materials, which leads to differences in energy band alignment (Types I, II and III heterostructures). Coupling two heterojunctions together can thus lead to the formation of potential barriers for carriers in one or both electronic bands. Returning to the notable

example of an AlGaAs/GaAs heterojunction, one can extend this to an AlGaAs/GaAs/AlGaAs double heterojunction to form a quantum well (QW). In such a configuration, carriers in the GaAs layer can become confined in one-dimension (1D) due to the potential barriers of the AlGaAs layers while remaining free along the other 2-dimensions. In this scenario, if the thickness of the GaAs layer is small enough, quantization effects become important. Within the confinements of such a 1D potential well, the carrier wavefunctions exist in bands at discrete energy eigenvalues, which can be compared to continuous wavefunctions in bulk materials where carriers are free to diffuse or drift in any direction. A simplification to the quantum well problem is the infinite potential well, where it is easily shown that the electronic wavefunctions go to zero at the potential barrier. The analytical solution to the electronic energy eigenvalues is given as

$$E_n = \frac{\hbar^2 \pi^2 n^2}{2m^* L^2}, \tag{2.6.3}$$

where L is the thickness of the QW, and n is the nth eigenenergy and nth solution to the Schrödinger equation. The fact that energies take on discrete values gives rise to quantized density of states, which can be shown to be

$$N(E) = \frac{m^*}{\pi \hbar^2 L} \sum_n \Theta(E - E_n), \tag{2.6.4}$$

where $\Theta(E)$ is the Heaviside function (or step function). Figure 2-14a and b illustrate bulk and quantum well density of states respectively. Realistically, quantum wells have finite potential barriers, which give rise to an exponential decay of the wavefunction within each potential barrier. This results in non-analytical equations to describe the resulting energy eigenvalues. The solution to these can be obtained numerically using multi-physics modeling tools such as COMSOL [48], using approximate analytical models [49] or using graphical methods [50]. The former is used in solving for quantum well energy eigenvalues

corresponding to the wetting layer of the InAs/GaAs material system with strain considerations in chapter 5. For details on the transcendental equations describing the finite potential well, see chapter 3 of [33].

When carriers are confined in 2D, the resulting quantum structure is referred to as a quantum wire. The resulting density of states takes the form

$$N(E) = \frac{1}{\pi L_x L_y}\sqrt{\frac{2m^*}{\hbar^2}}\sum_{n_x n_y}\sqrt{\frac{1}{E-E_{n_x}-E_{n_y}}}, \tag{2.6.5}$$

where L_x and L_y are the dimensions of confinement and the ideal energy eigenvalues (for infinite potential barriers) are given as

$$E_{n_x,n_y} = \frac{\hbar^2\pi^2}{2m^*}\left(\frac{n_x^2}{L_x^2}+\frac{n_y^2}{L_y^2}\right). \tag{2.6.6}$$

The last example of a quantum structure is the quantum dot (QD), whereby carriers are confined in all 3D. The density of states and resulting energy eigenvalues for an ideal cubic structure are given as

$$N(E) = \frac{g_s}{L_x L_y L_z}\delta\left(E - E_{n_x} - E_{n_y} - E_{n_z}\right), \tag{2.6.7}$$

$$E_{n_x,n_y,n_z} = \frac{\hbar^2\pi^2}{2m^*}\left(\frac{n_x^2}{L_x^2}+\frac{n_y^2}{L_y^2}+\frac{n_z^2}{L_z^2}\right), \tag{2.6.8}$$

respectively, where g_s is the spin degeneracy (typically 2), and $\delta(E)$ is the Dirac delta function. A summary of the density of states for each type of structure is given in Fig. 2-14. It is important to note that these are for ideal quantum structures; the eigenenergies of real quantum structures deviate from these ideal predictions primarily due to the finite potential barriers that confine carriers. Although analytical approximations to more realistic eigenenergies have been described in the literature for quantum wells [49],[50] and quantum dots [51], COMSOL is capable of predicting more accurate eigenenergies using numerical

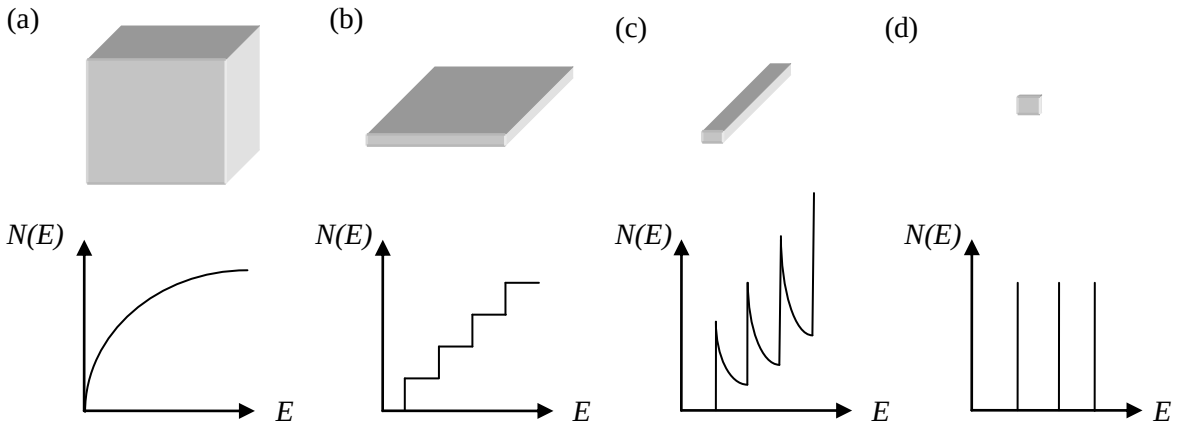

Figure 2-14. a) Bulk, b) quantum well, c) quantum wire and d) quantum dot structures with associated density of states.

methods specifically for quantum well and quantum dot systems [48].

2.6.3. Quantum Dot and Quantum Well Absorption Characteristics

The absorption characteristics of quantum dots and quantum wells can be computed theoretically according to equation (2.5.6). One requires two important parameter sets, however. The first is the joint density of states, which is very similar to the density of states of each nanostructure in the previous section with the exception that the effective masses of both electrons and holes must be considered as one reduced effective mass. The second is the dipole matrix element, which depends on the overlap integral between the initial and final wavefunctions representative of free carriers in the conduction and valence bands. In a nanostructure, however, carriers are no longer free, and one must consider the bound initial and final wavefunctions in the nanostructure. Let us consider the example of a quantum well of thickness *L*. The absorption coefficient can be expressed as

$$\alpha(E) = \frac{q^2\pi\hbar}{n_s c\varepsilon_0 m_0^2 E}\int |P_{cv}|^2 \delta(E_c - E_v - E')\, jDOS(E')dE'. \qquad (2.6.9)$$

Equation (2.6.9) agrees with equation (2.5.6) since the joint density of states represents the range of energies relevant to the conduction and valence band wave vectors involved in

interband transitions, and thus simplifies to a single integration constant over energy rather than a double integration over both initial and final wave vectors. For a quantum well, the joint density of states ($jDOS(E)$) can be expressed as equation (2.6.4) with the exception that the effective mass must be replaced to a reduced effective mass, or

$$jDOS_{QW}(E) = \frac{\mu}{\pi\hbar^2 L}\sum_n \Theta\left(E - E_g - E_n\right) \tag{2.6.10}$$

where the reduced effective mass μ is given by

$$\frac{1}{\mu} = \frac{1}{m_e^*} + \frac{1}{m_h^*}. \tag{2.6.11}$$

The dipole matrix element P_{cv} in equation (2.5.6) can be expressed as the bulk dipole matrix element reduced by the overlap between the n^{th} bound initial and final envelope wavefunctions in the QW. Let us introduce the optical matrix element $M_{QW}^2 = \left|\left\langle \Psi_{e,n} \middle| \Psi_{h,n} \right\rangle\right|^2$, where $\Psi_{e,n}$ is the n^{th} electron wavefunction and $\Psi_{h,n}$ is the n^{th} hole wavefunction. To compute this matrix element, one must solve for the bound wavefunctions in the quantum well, which can be performed in COMSOL using appropriate potential barriers and effective masses [48]. Putting equations (2.6.10) and (2.6.9) together gives

$$\alpha_{QW}(E) = A_\alpha \frac{\mu|P_{cv}|^2}{\pi\hbar^2 L}\sum_n M_{QW}^2 \Theta\left(E - E_g - E_n\right), \tag{2.6.12}$$

where we made the substitution $A_\alpha = \frac{q^2\pi\hbar}{n_s c\varepsilon_0 m_0^2 E}$. According to equation (2.6.12), the absorption characteristics take on the form of the quantum well density of states. One should note that this derivation does not consider exciton effects which are assumed negligible at temperatures above room temperature since the exciton binding energy is on the order of a few meV. Considering these effects would result in an extra resonance in the absorption characteristics centered at an energy lower than the confined energy levels given by the exciton binding energy. For an example of this, see [30].

The QD absorption characteristic also follows a similar derivation. It can be shown that the absorption coefficient of a QD can be given as

$$\alpha_{QD}(E) = A_{\alpha}|P_{cv}|^2 \sum_n M_{QD}^2 \delta\big(E - E_g - E_n\big). \tag{2.6.13}$$

Equation (2.6.13) dictates the absorption of a single QD. In a real QD system, for example, the InAs/GaAs material system, the sizes of the quantum dots are distributed according to a Gaussian distribution. For a good example on the derivation of the absorption coefficient for spherical quantum dots, see [52]. This results in a broadening of the absorption spectrum. A further broadening is due to thermal effects. Chapter 5 derives the absorption characteristics of QD and QW in the InAs/GaAs material systems representative of typical sizes and energy levels.

2.6.4. Altered Carrier Dynamics in Quantum Dot/Well Systems

The confinement of carriers in quantum dot and quantum well systems results in localized carrier wavefunctions within the potentials of the nanostructure. Due to the localized nature of bound wavefunctions, these carriers do not contribute to current within a semiconductor device. The current arises due to the free (or unbound) carriers in the conduction and valence bands. Figure 2-15 illustrates this by outlining bound energy levels within a quantum well and the processes that relate to the exchange of carriers between bound localized states and unbound delocalized states. Thermionic emission over the bound states is used to model bulk current density (J_{TE}).

As a result, for bound carriers to contribute to the current of the device, they must first escape the confinement region. This can be mediated through carrier-phonon scattering, which is typically modeled using thermionic emission theory. However, the thermionic emission theory outlined in section 2.3.4 is for bulk materials and thus adopts bulk density

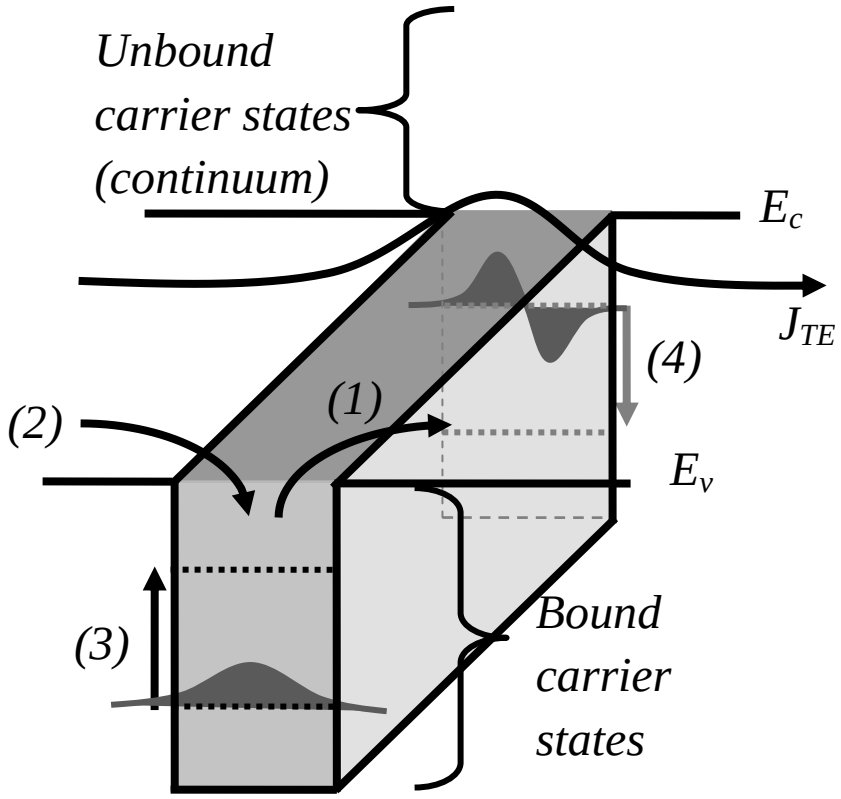

Figure 2-15. Carrier dynamics in a quantum well, where the processes represent: 1) carrier escape from bound to unbound states, 2) carrier capture from unbound to bound states, 3) intraband carrier-phonon scattering (excitation) between bound states, and 4) intraband carrier-phonon scattering (relaxation) between bound states. Thermionic emission current dictates the bulk current density flowing over the bound states, labelled as J_{TE}.

of states. In quantum wells, the density of states is quantized, which leads to a deviation from bulk thermionic emission theory [53]. A different theory must therefore be developed to consider the escape as well as the capture of carriers out of and into the quantum well DOS respectively. This approach requires two separate sets of carrier number densities: that of bound and unbound carriers. This introduces two new quasi-Fermi levels which are fundamental in describing both populations of carriers.

Fortunately, semiconductor laser theory has developed such an approach over the past decade [54],[55],[56],[57],[58]. Although similarities exist between quantum well lasers and quantum well solar cells, important differences still exist such as maximizing generation

within solar cells whereas quantum well laser design focuses on optimizing stimulated emission (a form of radiative recombination). Stephen M. Ramey and Rahim Khoie applied this type of theory to develop modified continuity equations [59] as

$$\frac{\delta n}{\delta t} = \frac{1}{q}\nabla \cdot J_n + G_{bulk} - R_{bulk} + \frac{n_{QW}}{\tau_{esc}} - \frac{n_{bulk}}{\tau_{cap}} = 0 \,, \tag{2.6.14a}$$

$$\frac{\delta p}{\delta t} = -\frac{1}{q}\nabla \cdot J_p + G_{bulk} - R_{bulk} + \frac{p_{QW}}{\tau_{esc}} - \frac{p_{bulk}}{\tau_{cap}} = 0 \,, \tag{2.6.14b}$$

where n_{QW} and p_{QW} are the bound electron and holes densities within the quantum well, and τ_{esc} and τ_{cap} are the escape and capture times respectively for electrons and holes. In order for equations (2.6.14) to reach a quasi-equilibrium system, one must introduce a supplementary set of continuity equations for bound carriers

$$\frac{\delta n_{QW}}{\delta t} = G_{QW} - R_{QW} + \frac{n_{bulk}}{\tau_{cap}} - \frac{n_{QW}}{\tau_{esc}} = 0, \tag{2.6.15a}$$

$$\frac{\delta p_{QW}}{\delta t} = G_{QW} - R_{QW} + \frac{p_{bulk}}{\tau_{cap}} - \frac{p_{QW}}{\tau_{esc}} = 0. \tag{2.6.15b}$$

In semiconductor laser simulation packages, a net capture rate which encompasses carrier-phonon and carrier-carrier scattering has been described in the literature [57]. This net capture rate acts as a source for bound carriers and a drain for the unbound (or continuum) carriers from the point of view of a laser. The opposite perspective would then be true for a photovoltaic device, where carriers escaping the bound modes of the quantum well add to the current of the device (therefore a source) and carriers captured by the bound modes remove from the current of the device (therefore a drain). This generalized net capture rate can be obtained by integrating the 2D and 3D density of states for the well and bulk respectively with the Fermi-Dirac distribution functions and a scattering probability over all energy ranges including the bound states [57]. It can be expressed as

$$C_{cap} = (1 - e^{\eta_{QW} - \eta_{bulk}}) \left(1 - \frac{n_{QW}}{N_{QW}}\right) \frac{n_{bulk}}{\tau}, \quad (2.6.16)$$

where $\eta_{QW} = \left(-E_{F,QW} - E_c\right)/kT$ and $\eta_{bulk} = \left(-E_{F,bulk} - E_c\right)/kT$ contain the quasi-Fermi levels of the QW and bulk regions respectively, $N_{QW} = \int_{E_{QW}}^{E_c} DOS_{QW}(E)dE$ represents the 2D density of states of the QW, and τ represents the net capture time representative of carrier-carrier and phonon scattering.

Expression (2.6.16) can be simplified if one considers a shallow quantum well, where only a certain range of phonon energies can satisfy the scattering mechanisms. In this type of scenario, elastic scattering via acoustic phonon and/or carrier-carrier scattering is more important than inelastic scattering (i.e. optical phonon scattering) [56]. The transition probability between unbound and bound states in general depends explicitly on wavefunction interference and phase-space reduction [54]. The former effect arises due to the asymmetric nature of the potential barrier (such the effects of the electric field in the active region of the cell, or can be a consequence of asymmetric strain in the QW) whereby the wavefunction of the unbound carrier can reflect several times off the potential barriers of the well (generally occurs more readily on the larger potential barrier due to the asymmetry). Such multiple reflection series must be considered in determining the net capture rates as these processes affect the wavefunction of the carriers. The latter effect, phase-space reduction, arises due to the scattering of carriers near the potential barrier that does not lead to carrier capture. This notion reflects the phase coherence of carriers and amplitude loss during propagation over the potential barrier of the well. Note that the phase of a single particle wavefunction does not have any meaning by itself. It becomes important when considering the scattering of two particles of different phase. For example, unbound (or free) carriers can scatter off other carriers or phonons near the potential well without being

captured. This scattering process leads to a change in carrier phase during its propagation in the unbound states of the well, whereby the state of the carrier changes from one state to another; its previous state becomes filled by another carrier of different phase until a steady-state equilibrium is reached between unbound carriers such that the rate of carriers filling in the initial state is nearly equal to the rate at which carriers scatter out of their initial state. This process toward steady-state leads to the notion of phase decoherence, which has been shown to affect the transmission, reflection and capture processes important in quantum well based devices [54]. Phase decoherence is a similar notion to the spin relaxation time T_2 commonly adopted in nuclear magnetic resonance studies.

Considering these notions, the net capture rate has been shown to be expressed as

$$C_{cap,elasic} = \left(\frac{\mathcal{F}_{1.5}(\eta_{bulk})}{\mathcal{F}_{0.5}(\eta_{bulk})} - \frac{\mathcal{F}_{1.5}(\eta_{QW})}{\mathcal{F}_{0.5}(\eta_{QW})}\right)\frac{n_{bulk}}{\tau}, \tag{2.6.17}$$

where $\mathcal{F}_{1.5}$ represents the Fermi-Dirac integral of order 1.5. Setting the Fermi-Dirac integral to order 1 accounts only for phase space reduction, and order 0.5 is the simplest approximation whereby the energy dependence of the scattering rate is not considered. An advantage of this formalism is the explicit specification of a scattering time, which is unique to the carrier type. The derivation of equations (2.6.16) and (2.6.17) are not given here as they result from two high level quantum well laser simulation papers (Ref. [56] and [57] respectively).

Chapter 3: Simulations of Semiconductor *p-n* Junctions & Solar Cells

Armed with a foundation in fundamental semiconductor properties from chapter 2, the features and characteristics of semiconductor *p-n* junctions are investigated initially from an analytical standpoint, and subsequently using the finite element and finite difference methods offered by the Technology Computer Aided Design (TCAD) Sentaurus engine. From this point, the simulated current – voltage characteristics, external quantum efficiency profiles and energy band diagrams of semiconductor *p-n* junctions and single junction solar cells are discussed. The final focus of this chapter is on designing a *p-n* junction for photovoltaic purposes in terms of the benefits of anti-reflection coatings and front and back surface fields on performance. A comparison of solar cell performance is also given for various material systems such as silicon, gallium arsenide (GaAs), gallium indium phosphide ($In_{1-x}Ga_xP$), germanium (Ge) and copper indium gallium diselenide ($Cu(In,Ga)Se_2$).

3.1. Qualitative Analysis of a *p-n* Junction in Equilibrium

As two semiconductors of opposite polarity (*n*- and *p*-type) contact each other, a built-in electric field is formed at the *p-n* junction. A diffusion current of majority carriers is generated, which is then balanced by a drift current to form a thermodynamic equilibrium. This thermodynamic equilibrium implies that at any given time, each of these currents is

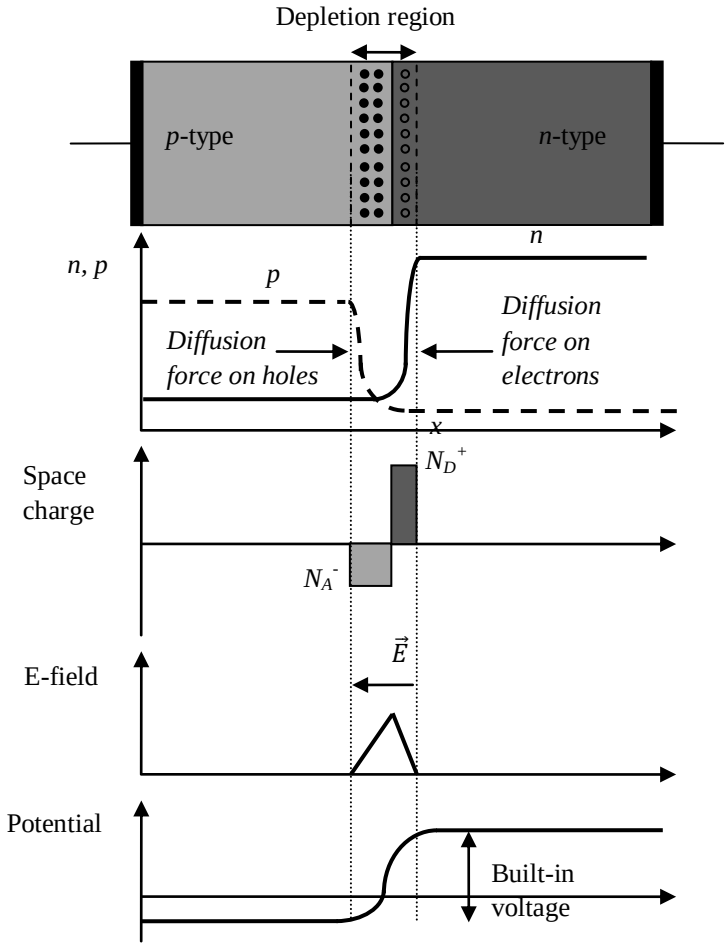

Figure 3-1. Schematic diagrams of a *p-n* junction and its carrier concentration, space charge, electric field and potential profiles.

non-zero, but the net current is very close to zero. In this thermodynamic equilibrium, a space charge region (or depletion region) is formed as illustrated in Fig. 3-1. The depleted volume on either side of the junction can be estimated by making use of the depletion approximation (all carriers are depleted within a finite volume from the interface). Under this approximation, one can show using Poisson's equation for 100% ionization of dopant atoms that the depleted widths on either side of an ideal junction are given by [60]

$$w_p = \frac{1}{N_A}\sqrt{\frac{2\epsilon_s V_{bi}}{q\left(\frac{1}{N_A}+\frac{1}{N_D}\right)}} \qquad w_n = \frac{1}{N_D}\sqrt{\frac{2\epsilon_s V_{bi}}{q\left(\frac{1}{N_A}+\frac{1}{N_D}\right)}} \tag{3.1.1}$$

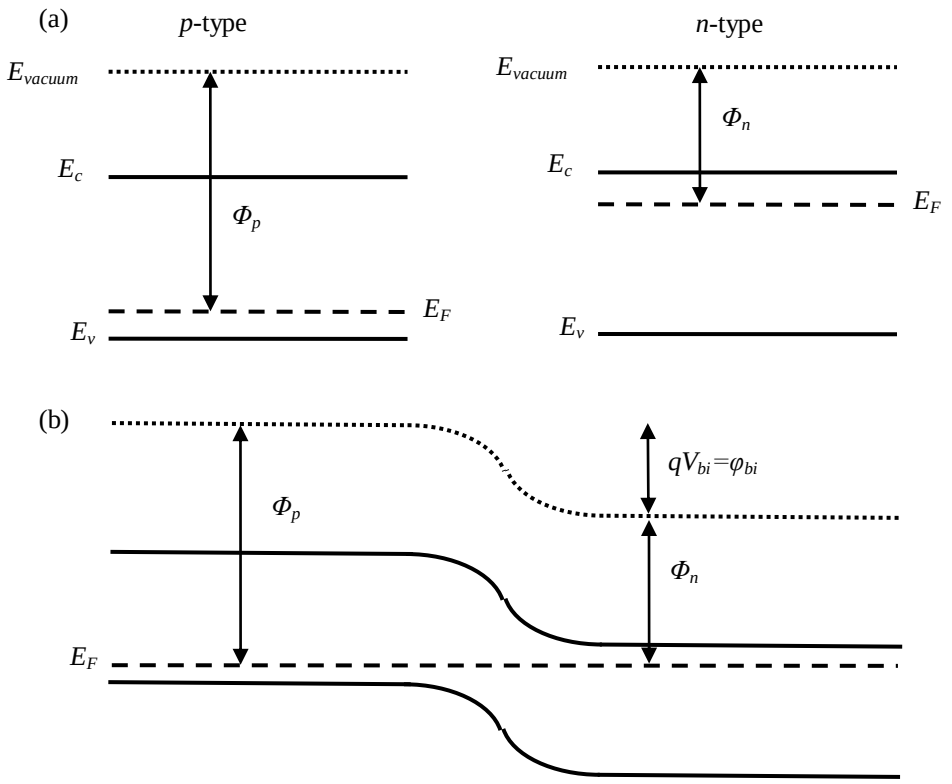

Figure 3-2. a) energy band profile of standalone *p*- and *n*-type semiconductors, and b) the resulting equilibrium energy band diagram of a p-n junction.

where w_p and w_n represent the widths into the *p*- and *n*-regions from the perfect junction that are depleted of carriers respectively, and $qV_{bi}=\varphi_{bi}$ is the built-in potential of the *p-n* junction. Equation (3.1.1) shows that the larger the doping concentration of one side of the *p-n* junction, the smaller the depletion width is on that side. The built-in voltage at equilibrium is highly dependent on the doping levels N_A and N_D of the materials, as these dictate the Fermi levels within each material away from the intrinsic level. To gain a better understanding of this built-in voltage, one must investigate the energy band diagram of the *p-n* junction, which is illustrated in Fig. 3-2. In this figure, an important observation is that the quasi-Fermi level is constant throughout the device, which represents a net current flow of zero. One can show that this built-in voltage, for a homojunction, can be expressed as [60]

$$V_{bi} = \frac{1}{q}\left(\Phi_p - \Phi_n\right) = \frac{1}{q}\left[\mathrm{E}_{F,n} - \mathrm{E}_{F,p}\right], \tag{3.1.2}$$

where Φ_p and Φ_n are the work function of holes and electrons respectively. In a homo-junction, equation (3.1.2) can be simplified using equations (2.2.9) and (2.2.10) re-arranged in terms of the intrinsic level, which gives

$$V_{bi} = \frac{kT}{q} ln\left(\frac{N_A N_D}{n_i^2}\right). \tag{3.1.3}$$

The metallic contacts on either side of the junction must be carefully selected in order to produce ohmic contacts with low resistance rather than creating Schottky contacts. The former results in minimal resistance at the interface, whereas the latter results in potential barriers due to differences in the metal and the semiconductor work functions. For more details on the analytical descriptions of *p-n* junctions in equilibrium, see for example, chapter 6 of [35]. Energy band diagrams similar to Fig. 3-2 will be considered to assist in describing the behaviour of *p-n* junction-based photovoltaic devices.

3.2. Simulating a Perturbed *n-p* Junction using TCAD Sentaurus

The above analysis for a *p-n* junction applies to a system in thermodynamic equilibrium, which allows for a great simplification of the equations dictating carrier concentrations. When the system is perturbed, however, a vital assumption is that the system quickly reaches quasi-equilibrium. Within this approximation, one can assume that the equations describing semiconductor carrier concentrations under equilibrium are valid. This is an excellent approximation considering intraband relaxation is orders of magnitude faster than interband relaxation [35]. This section investigates the numerical simulation and analysis of a perturbed *n-p* junction making use of this assumption; it is simulated over a *p-n* junction since *n-p* junctions will form the multi-junction solar cells studied in chapters 4 and

5. More specifically, the behaviours of an *n-p* junction under bias in the dark and under illumination are discussed using TCAD Sentaurus. The simulation details, such as device structure, contacts, meshing and physical models, are discussed in section 3.2.1. The numerical methods for solving the partial differential equations (PDE's) representative of the semiconductor equations of interest are discussed in 3.2.2. The simulation results, analysis and data extraction are then discussed in 3.2.3. Section 3.2 can thus be used as a basic introduction to TCAD Sentaurus, with specific examples of code given in Appendix B. A systematic description of the simulation tool flow is useful to understand how to model semiconductor devices and the Sentaurus framework; this tool flow is illustrated in Fig. 3-3. For readers interested in learning how to use TCAD Sentaurus to model and simulate a simple *p-n* junction, see [61]; chapter 6 of [35] includes a good analytical analysis of modeling *p-n* junctions.

3.2.1. Device Structure, Contacts and Numerical Mesh Generation

A simple device geometry can be defined using TCAD Sentaurus' *Epi* tool, which dictates global variables such as the *X* and *Y* geometry of the structure as well as each epitaxial layer's material information such as doping, thickness, tertiary or quaternary molar fraction (*nX_epi.tcl*), along with the preliminary meshing strategy corresponding to the epitaxial stack (*nX_epi.scm*). The structure and meshing are then imported into the Sentaurus *Structure Editor* (SDE) which generates the structure grid using matrices with appropriate boundary conditions (i.e. with or without contacts) and the meshing information using a built-in tool (called the Sentaurus *Mesh Generator*); the output is in a "tdr" format (*grid_msh.tdr,* see Fig. 3-3*)* and is an input into the Sentaurus Device simulator (*SDevice*). The second output file from the *Epi* tool (i.e. the *nX_epi.tcl)* is imported into the Sentaurus

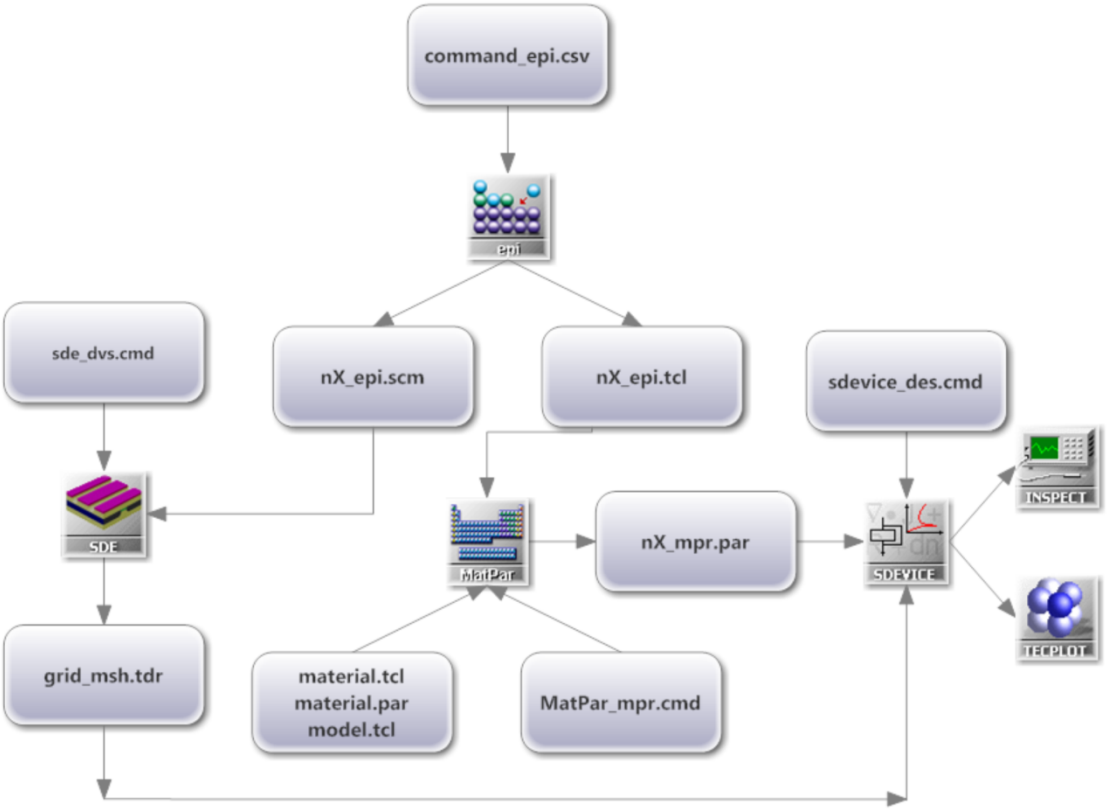

Figure 3-3. TCAD Sentaurus simulation tool flow.

MatPar tool, which generates the final material parameter files (*mpr.par*) which are imported into the *SDevice* simulation using material-specific model files (*material.tcl*; *model.tcl; material.par*). These final parameter files contain all the relevant material properties such as bandgap, density of states, electron and hole effective masses, doping dependent mobilities, optical properties, recombination lifetimes, etc. The details of important parameters for semiconductor materials relevant to this thesis are discussed in section 3.5.1.

A case study to outline the overall steps is discussed using a GaAs *n-p* junction simulated with two highly doped layers on either side of the junction to ensure the contacts are ohmic, as seen in Table 3-1. Charge neutrality and equilibrium are assumed at such

contacts, as given by equations (2.2.17) and (2.2.14) respectively. This assumes the carrier concentrations across the metal-semiconductor are at equilibrium, and implies the metal to be at equilibrium. The simulation assumes the contacts have negligible series resistance and interface recombination by default, although these assumptions can be modified. For boundaries without contacts, the edges are considered reflective with the conditions expressed as

$$\epsilon \nabla \varphi = 0, \tag{3.2.1}$$

$$\overrightarrow{J_n} \cdot \hat{n} = 0, \qquad \overrightarrow{J_p} \cdot \hat{n} = 0. \tag{3.2.2}$$

This inhibits current from flowing across the edges of the structure.

Figure 3-4a illustrates the simulated device geometry with the aforementioned highly doped layers above and below the junction, the ultra-thin contacts at the top and bottom of the structure (not easily visible), and the white horizontal lines outlining the depletion region. Fig. 3-4b outlines the generated numerical mesh required to accurately solve the Poisson, electron and hole current-continuity equations at all mesh vertices (defined as the intersection of mesh lines) within the structure using appropriate boundary conditions. The mesh is generated using the Sentaurus Mesh tool [62] based on a Delaunay algorithm that strictly forbids vertices to lie within the circumcircle of any triangle formed by the set of vertices within the boundaries of the structure. The adopted mesh strategy for this *p-n* junction is uniformly graded along the *X* axis, and graded along the *Y* axis according to a ratio which controls the mesh spacing away from the interfaces. This meshing strategy is used to define finely spaced vertices near interfaces where physical phenomena must be characterized accurately, since the solutions to the Poisson, electron and hole current-continuity exhibit large variations near the junction. An increase in mesh spacing in the bulk

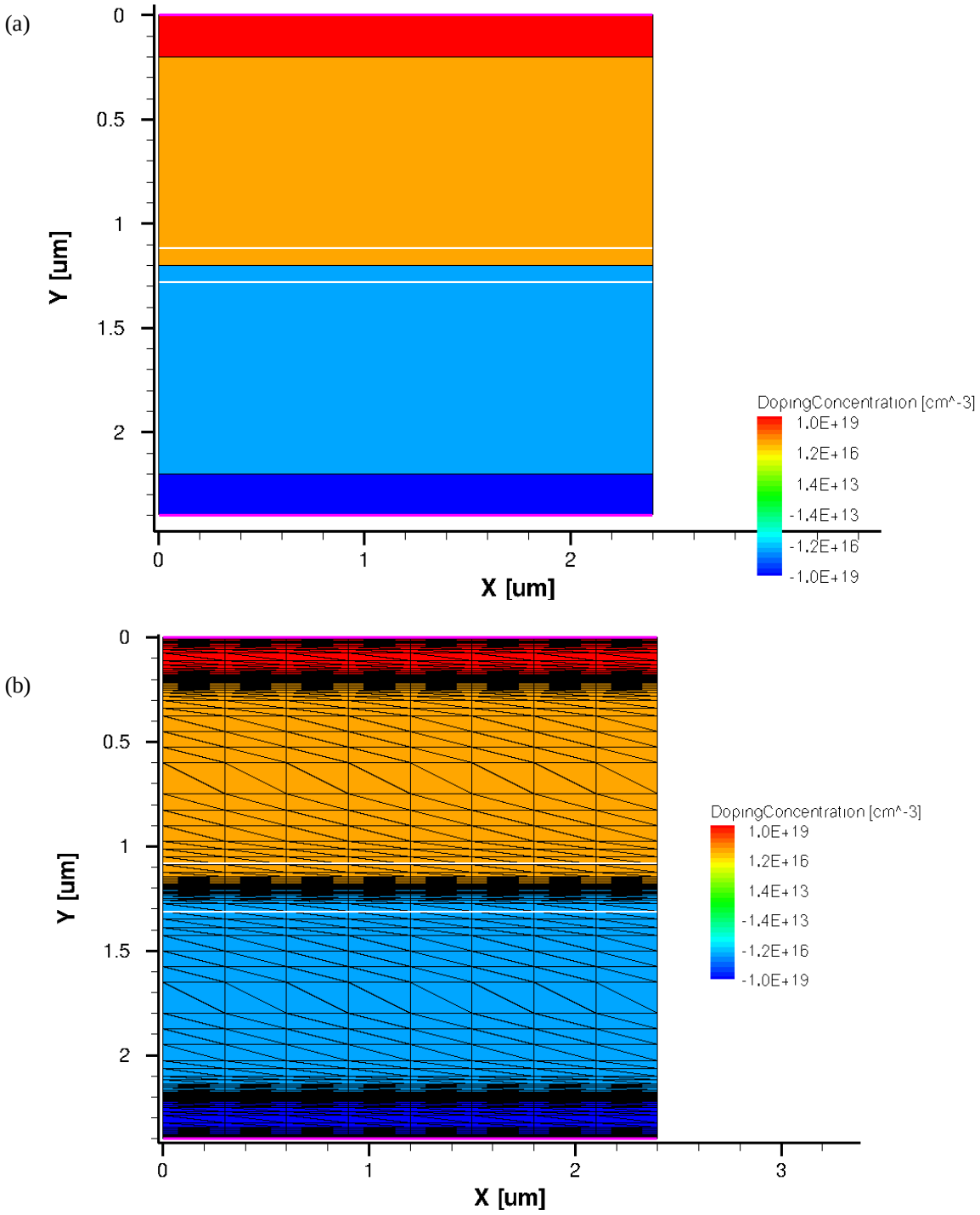

Figure 3-4. a) Simulated vertical GaAs *p-n* junction with highly doped *n*+ and *p*+ layers below and above the top and bottom contacts respectively, where the white lines outline the depletion region, and b) the generated mesh according to a multi-box refinement strategy for the same structure. These figures were generated using the TCAD Sentaurus tool *Tecplot*.

regions of the material minimizes computational time and memory since the solutions are

generally smooth. The advantage of a multi-box refinement strategy compared to uniform meshing strategies is a balance between a finely spaced mesh (increases computational time) and a larger spaced mesh (decreases computational time). For more details on these types of mesh strategies and their implementation within Sentaurus' tools, see [62] and [63]. This meshing strategy is based on grid continuation, and is discussed concisely in section II-D of [64].

Table 3-1. Structural details of simulated GaAs *n-p* junction.

Layer	Material	Thickness (μm)	Doping (cm^{-3})
n-cap	GaAs:Si	0.2	1×10^{19}
n-side	GaAs:Si	1	1×10^{17}
p-side	GaAs:P	1	1×10^{17}
p-cap	GaAs:P	0.2	1×10^{19}

3.2.2. Simulation Details in *Sentaurus Device*

3.2.2.1. Input Files, Electrodes and Physical Models

Sentaurus Device (*SDevice*) is the numerical simulation tool which makes use of the grid and mesh information as well as all material parameters in order to simulate the behaviour of the device of interest; it is essentially the heart of TCAD Sentaurus simulations. The command file of this tool contains the most important simulation-specific information, such as which files to import (grid, mesh, material parameters, etc), boundary conditions of the electrodes (such as initial voltages, distributed resistances, Schottky barriers, etc), keywords that activate physical models within the semiconductor equations (such as activating radiative recombination), mathematical solver-specific parameters, and output plot data. For a simple *n-p* junction, the important physical phenomena must be specified in the global *Physics* section (see Appendix B-1), and include such keywords as

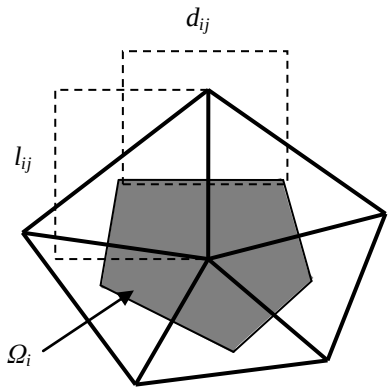

Figure 3-5. Illustration of the spatial discretization of the device domain used in the box discretization method. This illustrates the mesh vertices and edges between vertices. Based on Figure 110 in [63].

Fermi, temperature, an area factor to consider the third dimension of the device, bandgap narrowing effects due to doping, recombination mechanisms (doping dependent SRH, radiative and Auger), doping dependent mobilities, thermionic emission, tunneling phenomena, quantum well scattering, etc. The aforementioned keywords activate the relevant physical equations and models within the set of semiconductor equations as outlined in chapter 2. For details on the specific keywords, their implementation and related equations, see Part II of the *SDevice* user guide [65].

3.2.2.2. Mathematical Methods & Convergence Criteria

The set of coupled nonlinear partial differential equations (PDE's, i.e. the Poisson, electron and hole continuity equations) are solved using a box discretization approach that make use of both finite difference and finite element methods [64],[66],[67]. The method, illustrated in Fig. 3-5, discretizes and parameterizes the PDE's into smaller elemental equations and integrates them within a test volume (determined based on the mesh density) such as to discretize the terms to first order; this allows for the approximation of the behaviour of the equations in smaller localized regions of the device. Position dependent

scalar data such as the electrostatic potential and carrier concentrations serve as inputs into the PDE's. The discretization of the continuity equation

$$\nabla \cdot \vec{J} + R = 0, \tag{3.2.3}$$

where R represents the net recombination rates (multiplied by carrier charge), is performed as

$$\sum_{j \neq i} \kappa_{ij} \cdot j_{ij} + \mu(\Omega_i) \cdot r_i = 0, \tag{3.2.4}$$

where κ_{ij} is a dimensional parameter, j_{ij} is a vector representing the flux across the edge between nodes *i* and *j*, $\mu(\Omega_i)$ a volume parameter around node *i* (see Fig. 3-5), and r_i is the coordinate of the node *i* in the device. Equation (3.2.4) therefore represents how SDevice numerical discretizes the continuity equation to solve it over the mesh. For example, in 1D, κ_{ij} represents the inverse of the box length, or $1/l_{ij}$, and $\mu(\Omega_i) = l_{ij}$. Conversely, in 2D, κ_{ij} represents the proportionality of the box length to the box width, or d_{ij}/l_{ij}, and $\mu(\Omega_i) = d_{ij} \times l_{ij}$. Figure 3-5 illustrates the box discretization method graphically and corresponds to equation (3.2.4). Table 3-2 outlines the equations representing j_{ij} and r_i in equation (3.2.4), where the function B is the Bernoulli function given as $B(x) = x/(e^x - 1)$. The solution to the assembly of equations outlined in Table 3-2 is performed

Table 3-2. Equations fitting into the box discretization method given by equation (3.2.4).

Equation	j_{ij}	r_i
Poisson	$\epsilon(u_i - u_j)$	$-\rho_i$
Electron current-continuity	$\mu_n \left(n_i B(u_i - u_j) - n_j B(u_j - u_i)\right)$	$R_i - G_i + \frac{dn_i}{dt}$
Hole current-continuity	$\mu_p \left(p_j B(u_j - u_i) - p_i B(u_i - u_j)\right)$	$R_i - G_i + \frac{dp_i}{dt}$

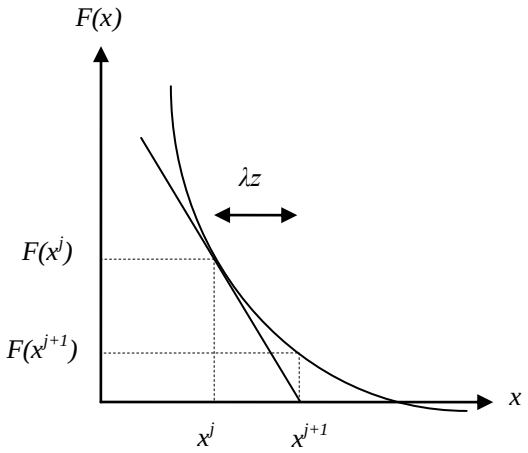

Figure 3-6. Illustration of Newton's method of root finding.

element-wise such that the parameters u, n and p (potential, electron and hole concentrations respectively) can be varied at each element of the mesh. The discretized terms of the PDE's are then grouped into the global set of equations, whereby the solutions to the equations are obtained across the full domain of the device using a Newton-like solver until the convergence criteria are met for a specific boundary condition (such as a voltage at the contacts); this gives the final potential and carrier concentrations throughout the structure. These data can then be used to compute the current – voltage characteristics as a function of voltage or the current at zero bias for a specific wavelength. The Newton-like solver is discussed thoroughly in [64] and described concisely below.

For a system of equations given as *F(x)=0* (representative of the electron and hole continuity equations and Poisson's equations), the Newton-like solver adopts the following formalism:

$$\vec{F}(\vec{x}) + \vec{F}'(\vec{x})\vec{x} = 0, \tag{3.2.5}$$

$$\vec{x}^{\,j} - \vec{x}^{\,j+1} = \lambda\vec{z}, \tag{3.2.6}$$

where λ is chosen based on the criteria that $\left\|\vec{F}_{j+1}(\vec{x}^{\,j+1})\right\| < \left\|\vec{F}_j(\vec{x}^{\,j})\right\|$ but that λ is as close to unity as possible, where $\vec{F}_j$ represents the j^{th} Newton iteration in solving the set of equations represented by *F(x)*. Efficient computation of the Jacobian matrix (i.e. $\vec{F}'(\vec{x})$) is crucial in these calculations. The residual error of equation (3.2.5), hereafter referred to as *Rhs*, must be calculated at each step of the calculation to verify whether the system of equations has converged. The general process of Newton's method is illustrated in Fig. 3-6. One possible criterion for convergence is that the norm of the *Rhs* is less than unity. A more reasonable yet simple convergence criteria, however, is that the relative error of the variables of interest (i.e. carrier concentrations and potential) is within a certain tolerance, such as $\left\|\frac{\lambda\vec{z}}{x}\right\| < \varepsilon_r$, where ε_r is a relative error typically given as $\varepsilon_r = 10^{-\gamma}$; the parameter γ is a parameter specified within the global *Math* section of the *SDevice* command file and is typically 5 or 7 depending on the type of simulation. In other words, the Newton iterations stop if the relative error for the variable of interest is within 10^{-5} or 10^{-7} compared to the step size $\lambda\vec{z}$. The above convergence criteria typically apply for large *x*. In the case that the system is being solved for very small changes in *x*, the step sizes λz must be compared to some reference value x_{ref} rather than the step size to ensure numerical stability. In *SDevice*, the convergence criteria in such cases is expressed as

$$\frac{1}{\varepsilon_r}\frac{1}{N}\sum_{e,i}\frac{|x(e,i,j)-x(e,i,j-1)|}{|x(e,i,j)|+x_{ref}(e)} < 1, \qquad (3.2.7)$$

where $x(e,i,j)$ represents the solution to equation *e* (Poisson, electron, hole) at a node *i* after a Newton iteration *j*, *N* represents the total number of nodes in the system multiplied by the number of equations. Lastly, $x_{ref}(e)$ is a reference value that ensures numeric stability even

for very small or zero values for $x(e,i,j)$ such that the equations are solved to an accuracy on the order of $x(e,i,j)\varepsilon_r$. Equation (3.2.7) can be rewritten in a more generalized form as

$$\frac{1}{\varepsilon_r}\left\|\frac{\lambda z}{x^j+x_{ref}}\right\| < 1, \quad \text{or as} \quad \left\|\frac{\lambda \bar{z}}{\varepsilon_r \bar{x}^j+\varepsilon_A}\right\| < 1 \tag{3.2.8}$$

where $\bar{x}^j = x^j/x^*$ and $\bar{z} = z/x^*$, with x^* a normalization constant that depends on the equation of interest. Take for example the electron and hole current-continuity equations: the default normalization factor is the intrinsic carrier concentration of the material. For Poisson's equation, the normalization constant is the thermal voltage equal to 25.8 mV at a temperature 298 K. However, the second formulation of equation (3.2.8) considers an absolute error ε_A, which can also be set in the global *Math* section for each equation (i.e. override; typical values are unity for electron and hole equations). The absolute error is related to the relative error given by

$$\varepsilon_A = \varepsilon_r \frac{x_{ref}}{x^*}. \tag{3.2.9}$$

The global *Math* section also specifies important keywords such as *derivates* and *extrapolate*. These ensure *SDevice* calculates full derivatives (relevant to calculating the Jacobian matrix), and extrapolates the solutions of the previous two calculations as the initial guess for the next calculation respectively. One also sets the minimum number of iterations to solve the system of equations in the device for each iteration of the Newton-solver before Bank-Rose damping is activated [64],[68], which enforces a damping factor to the step size for the solutions to the PDEs. This is useful when Newton's method is converging only for very small step sizes. This method has been shown to successfully apply to semiconductor device modeling [69]. Non-linear solver-oriented keywords are also specified in this section, such as controlling the size of the residual error of the equations through the parameter *RhsMin*, or setting the maximum factor the residual error can increase

in a single Newton iteration through the parameter *RhsFactor*. Since solving the set of semiconductor equations is the most time consuming component of the simulation, thread parallelization is used to accelerate the calculations on shared memory computers. It is typically set as the maximum (computer dependent) for more sophisticated simulations with non-local meshes and more complex calculations (see for example multi-junction solar cell simulations in chapter 4). For more details on the global *Math* section and the corresponding mathematical methods, see parts II and IV of [65], as well as the example *Math* section for simulating a simple *p-n* solar cell in Appendix B-5.

3.2.2.3. Solving the System of Equations

The global *Solve* section specifies the type of simulation, such as a transient or quasistationary simulation, along with which equations to solve. Within each type of simulation, one must specify the step sizes such as the initial, maximum, minimum sizes and factors incrementing or decrementing the step sizes between successful and unsuccessful iterations respectively. See Appendix B-7 for the example of simulating the *p-n* junction. The simulation initially solves the Poisson equation using Netwon's method with Bank-Rose damping at all mesh vertices of the structure for the initial conditions specified at the electrodes (typically *V=0*). The solution gives rise to the electrostatic potential of the device, based on the distribution of carriers. This in turn gives rise to an energy band diagram at equilibrium with no currents flowing at the contacts. These solutions are then used as the initial guess in solving the set of coupled equations given by the Poisson, electron and hole continuity equations, solved using the Newton-like solver. The solutions give carrier concentrations coupled to the electrostatic potential, which are used to compute the total current densities flowing throughout the full structure using drift and diffusion with

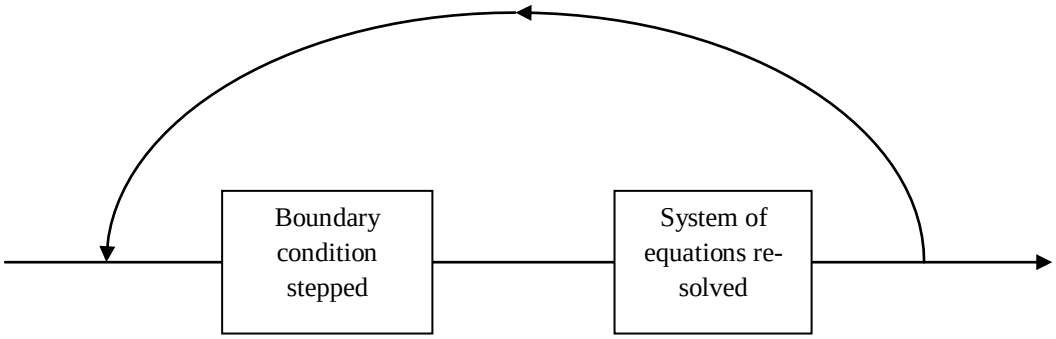

Figure 3-7. Schematic of the quasi-stationary command, where the system of equations is solved iteratively using finite element methods.

thermionic emission at heterointerfaces. One can solve these equations in a single iteration of the Newton solver if the initial guess is expected to result in convergence, such as in a simple system like the *p-n* junction. However, more complicated structures such as multi-junction solar cells require differential methods to ramp to the final set of solutions. The set of equations are typically solved using finite difference simulation (transient) using the trapezoidal rule/backward differentiation formulation or the simpler backward Euler method in order to ramp the initial guess to the final solution.

Once these equations are solved at all mesh points in the structure for the initial conditions specified, a quasi-stationary simulation solves the same system of equations from one boundary condition to another through a parameter ramp, for example, a voltage ramp between the initial condition of 0 V to a final condition of 2 V. The process of a quasi-stationary simulation can be schematically understood through the illustration in Fig. 3-7, where the system of equations is solved initially for the set of initial conditions, at which point the simulation enters the loop depicted by Fig. 3-7 where the boundary condition is stepped and the system of equations is re-solved iteratively. The initial, minimum and maximum step sizes (Δt) are constraints on the steps of this parameter ramp relative to a normalized goal of $t=1$, starting from $t=0$. In other words, the ramping abides by the

following parameter mapping: $V(t) = V_0 + t(V_1 - V_0)$ where $V(t)$ is the voltage at a time step t, V_0 is the initial voltage and V_1 is the final user-defined voltage. For example, for a voltage ramp from 0 to 2 V, an initial step size of 0.1 represents 10 steps in the voltage ramp at 0.2 V increments, assuming the system of equations converge at each step. In the case that convergence does not occur at one step, the step size is decreased based on the *decrement* factor until the system of equations is solved.

The parameter ramping can also be performed in a wavelength ramp, as in section 3.4.4 for the simulation of the external quantum efficiency. One last important note on the contents of the global *Solve* section is specifying at what point of the simulation the user wishes to output the plot parameters (i.e. recombination, generation, carrier concentrations, potentials, etc). For example, one may wish to investigate the energy band diagram or the recombination rates throughout the structure at one or several biases. For solar cells, this is useful in studying the behaviour of the device at its short circuit current density, at its maximum power point, or at its open circuit voltage.

3.2.2.4. Output of Simulation

The simulation is successful once the *Epi*, *SDE*, *MatPar* and *SDevice* tools run without errors and convergence issues. The simulation of *SDevice* generates plot files containing the current at all contacts within the structure and the plot parameters in a spatially resolved dataset (in TDR format). Current plots are normally viewed using the graphical tool called *Inspect*, which can be used to easily export current – voltage characteristics for a voltage ramp, or external quantum efficiencies for a wavelength ramp. Post-processing can be performed using Matlab for example. TDR files, on the other hand, contain plot variable datasets at all mesh points of the structure which are mainly loaded and studied using a

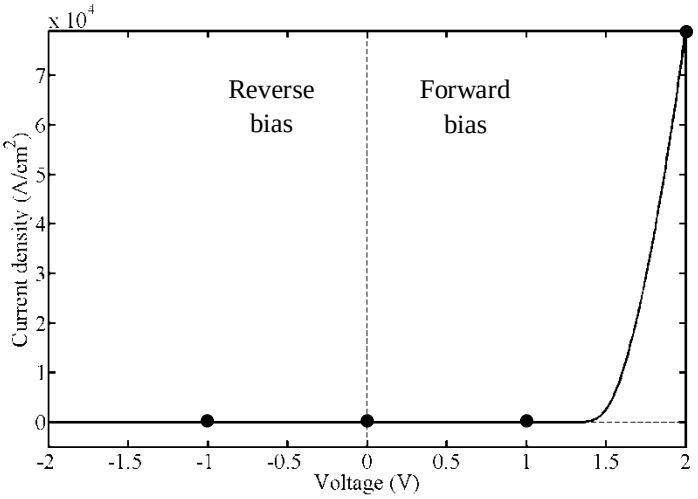

Figure 3-8. Simulated current density - voltage characteristics of the *p-n* junction, outlined with four black circles to identify the biases at which the energy band diagrams and carrier concentration profiles are extracted for analysis in section 3.2.3.

specially designed tool to read TDR datasets, such as the *Tecplot* tool (see Fig. 3-4b; note that newer versions of Sentaurus include *SVisual* to replace *Tecplot*). These plot variables are outlined in Appendix B-4. Although not used in this case study, SPICE based circuit components can be integrated into the simulation environment relative to the electrodes of the device through the global *System* section (see chapter 3 of [65]). As such, parasitic resistances such as series and shunt resistances can be added to the *n-p* junction.

3.2.3. Simulation Results and Analysis

The simulated current – voltage characteristic of the perturbed GaAs *p-n* junction, whose structure is illustrated in Fig. 3-4, are shown in Fig. 3-8. It illustrates the basic function of a semiconductor diode: a forward bias allows current to flow, whereas a reverse bias does not. Although the ideal diode equation predicts this type of behaviour, understanding this functionality in more detail requires energy band diagrams and carrier concentration profiles through the device for various degrees of perturbation. These are outlined in Fig. 3-9 to 3-12 for equilibrium conditions (or 0 V bias), a forward bias of 1 V, a

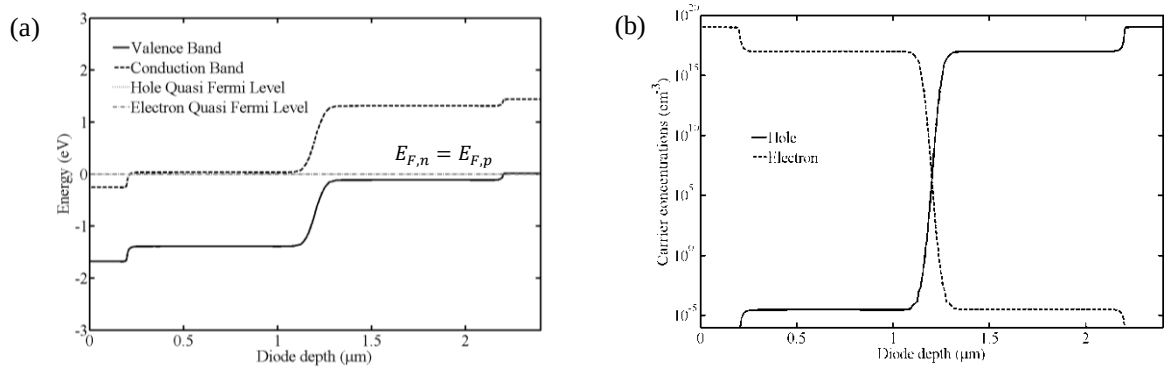

Figure 3-9. a) Simulated energy band diagram at equilibrium (0 V applied bias), and b) carrier concentration profile.

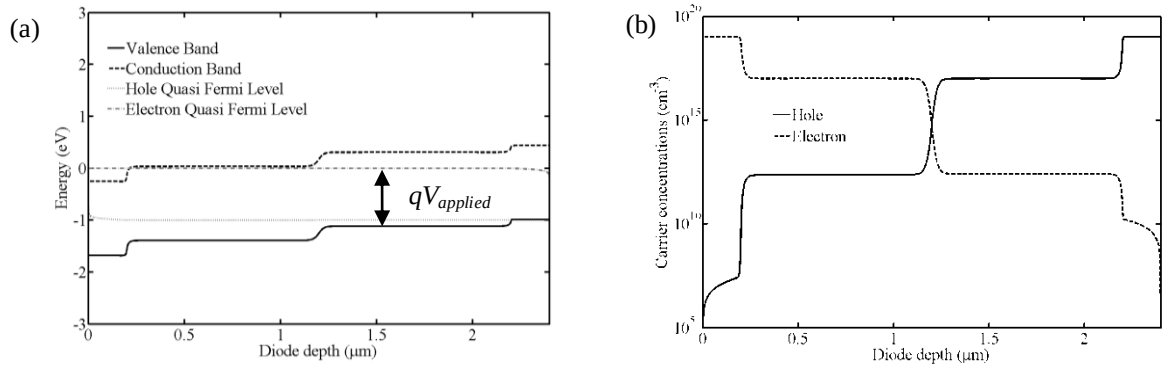

Figure 3-10. a) Simulated energy band diagram at a forward bias of 1 V, and b) carrier concentration profile.

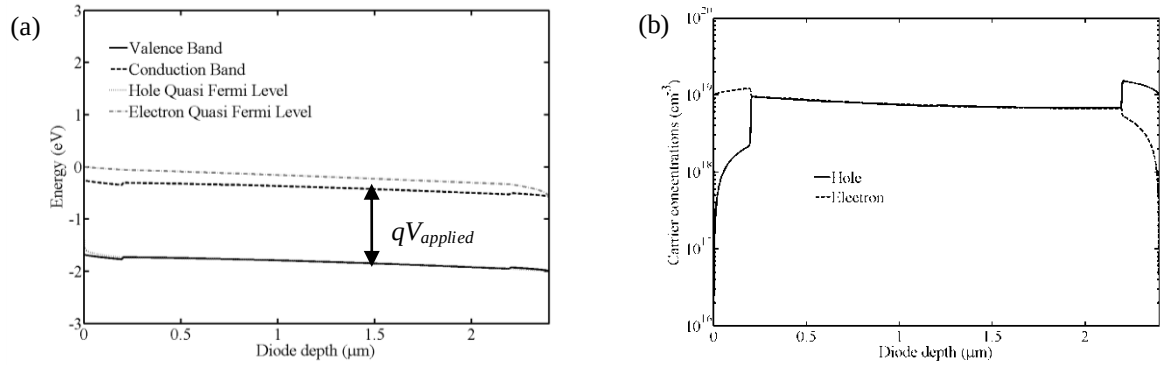

Figure 3-11. a) Simulated energy band diagram at a forward bias of 2 V, and b) carrier concentration profile.

forward bias of 2 V and a reverse bias of -2 V respectively, and are discussed below. Details on the ideal diode equation are discussed in section 3.3.

The energy band diagram of the *p-n* junction in equilibrium (at an applied bias of V=0 V) is illustrated in Fig. 3-9a, which shows the electron and hole quasi-Fermi levels super-

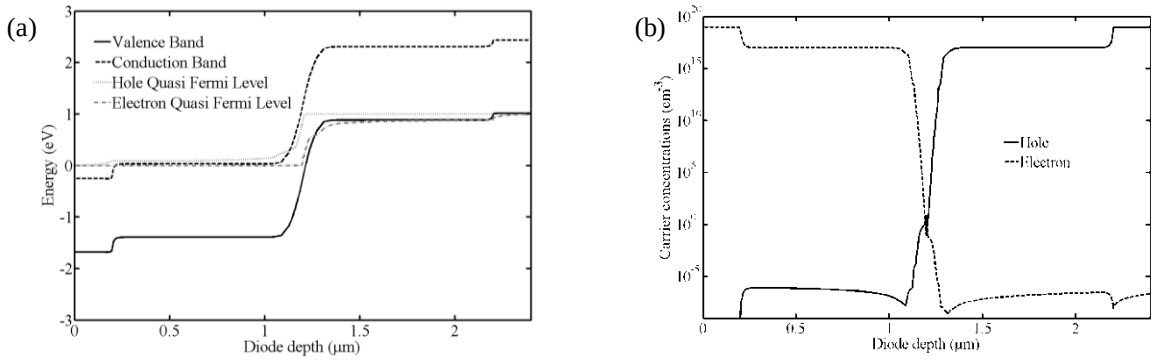

Figure 3-12. a) Simulated energy band diagram at a reverse bias of -1 V, and b) carrier concentration profile. The hole concentration on the *n*-side within the depletion region is not smooth perhaps due to lack of precision in the simulation.

imposed and constant throughout the whole device. This implies, as mentioned previously in section 3.1, that no net current is flowing through the device. The corresponding carrier concentrations are illustrated in Fig. 3-9b. For the *n*-region (corresponding to a diode depth of 0 to 1.2 μm), the majority carriers are electrons, with its minority carriers being holes at concentrations orders of magnitude lower than the intrinsic carrier concentrations as given by equation (2.2.14). On the *p*-side, the majority carriers are holes, with electrons being the minority carriers. Near the junction (depth of 1.2 μm), one can observe the depletion region, where majority carrier concentrations drop by several orders of magnitude. The carrier concentration profiles are symmetric about the interface of the *p*-*n* junction due to the equal doping concentrations of both sides of the junction.

The application of a bias to the junction results in the injection of carriers via the contacts. Consequently, the carrier concentrations of the device become perturbed from their equilibrium and no longer abide by equation (2.2.14). Instead, the carrier concentrations can be expressed as

$$pn = {n_i}^2 \exp\left(\frac{qV}{kT}\right), \tag{3.2.10}$$

where V is the applied bias. Equation (3.2.10) manifests itself through the separation of the quasi-Fermi levels within the device equivalent to qV, as seen in Fig. 3-10a. Two important supplementary consequences of equation (3.2.10) include: 1) the minority carrier concentrations vary logarithmically as a function of the applied bias, and 2) the built-in potential diminishes as a function of the forward bias, which manifests itself as a reduced potential barrier for the majority carriers. Consequently, the reduction in V_{bi} reduces the overall depletion width, as expected from equation (3.1.1).

An increasing applied voltage (V>1.5V) leads to the built-in potential vanishing entirely such that no potential barrier exists for majority carriers. In this regime, an exponential current flows through the device, as shown in the simulated *J-V* characteristics of Fig. 3-8. A large power is dissipated by the diode based on the equation $P=V\cdot I$. At such biases, the energy band diagram becomes heavily distorted with respect to Figs. 3-9 and 3-10, as illustrated in Fig. 3-11a. The injection of majority carriers becomes so large that two important phenomena can be observed. First, the electron quasi-Fermi level is significantly above the conduction band edge, which results in radiative recombination. In other words, the diode becomes luminescent, and behaves as a light emitting diode (LED). Second, the minority carrier concentrations become comparable to the majority carrier concentration, as seen in the low doping regions of Fig. 3-11b (0.2 to 2 microns).

In the reverse bias regime, the built-in potential increases as a function of applied bias. The energy band diagram and the corresponding carrier concentrations are illustrated in Fig. 3-12a and 3-12b respectively. The potential barrier for majority carriers inhibits the flow of current through the device, and therefore explains the current – voltage characteristics of Fig. 3-8. The depletion width increases in this scenario as a result of the increased built-in

potential. The minority carrier concentrations drop by orders of magnitude as a result of equation (3.2.10). Only when the applied bias reaches the breakdown voltage of the diode that one will observe avalanche breakdown. However, it is not considered in this simulation since this type of breakdown typically occurs at larger reverse biases, and is also not a physical effect activated with the *SDevice* environment. For details on avalanche breakdown as described in Sentaurus Device, see chapter 13 of [65].

3.3. Ideal Diode Equation for Diodes and Solar Cells

Prior to studying the simulation of a *p*-*n* junction as a solar cell, a simpler approach to understanding a solar cell is discussed using the ideal diode equation offset by a photocurrent. Solar cells are devices that exploit the photovoltaic effect: an optoelectronic phenomenon where the absorption of incident photons of energy larger than the material's bandgap induces a quantum mechanical transition of electrons from the valence band to the conduction band. This transition results in the generation of electron-hole pairs, a process called photo-excitation. These photo-excited carriers diffuse within the material until a recombination event takes place, whereby an excited electron returns to the valence band by recombining with a hole. However, if these electron-hole pairs can be separated via an electric field prior to a recombination event, they can contribute to the photocurrent of the solar cell. A photovoltage is generated as a result of this photon induced current (or short circuit current) when a load is applied to the solar cell to extract work from the excited electrons. Once they complete the circuit, these carriers return to the opposite contact of the solar cell where a final recombination event occurs.

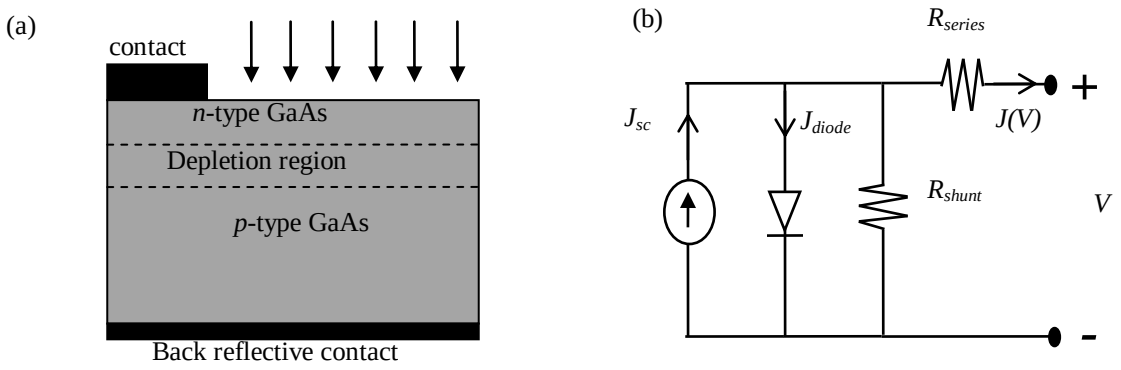

Figure 3-13. a) Structure of a GaAs *p-n* junction illuminated by light (arrows). b) Equivalent circuit of a solar cell with parasitic resistances where the solar cell acts as a current source in parallel with a diode and a shunt resistance R_{shunt}, all of which are in series with a resistance R_{series}.

An example of a solar cell is a semiconductor diode composed of *n*- and *p*-type GaAs as illustrated in Fig. 3-13a. An equivalent circuit representing a solar cell is illustrated in Fig. 3-13b. The *n*- and *p*-type layers form a depletion region in equilibrium which acts as the electric field to separate the photo-excited charges and contribute to a photocurrent. A solar cell's current – voltage (*J*-*V*) characteristics are the standard method for measuring its performance under illumination and bias. These *J*-*V* characteristics can be understood using the ideal diode equation, offset by a photocurrent given as [70]

$$J(V) = J_{SC} - J_0\left(e^{\left(qV/nkT\right)} - 1\right). \tag{3.3.1}$$

The first term, J_{SC}, is the short circuit current density of the diode due to the incident light, which represents a current source in an equivalent circuit of an illuminated solar cell (see Fig. 3-13b). The second term is the ideal diode equation of a diode in the dark, which represents the forward biased diode current, where J_0 is the saturation current (or dark current) due to recombination processes occurring within the diode. Further variables and constants include the elementary charge *q*, the applied voltage *V*, an ideality factor *n* which ranges between 1 and 2 depending on the primary method of recombination taking place (1

for radiative and 2 for non-radiative recombination), Boltzmann's constant k and the temperature T in Kelvins. Including the effects of parasitic resistances to equation (3.3.1) gives

$$J(V) = J_{SC} - J_0\left(e^{\left(q[V+JAR_s]/nkT\right)} - 1\right) - \frac{V+JAR_S}{R_{shunt}}, \tag{3.3.2}$$

where A is the cross-sectional area of the cell.

A first step in understanding equations (3.3.1) or (3.3.2) is the photocurrent, which is highly dependent on the incident photon flux density (or solar irradiance) and the design of the solar cell. The J_{sc} can be expressed using this incident photon flux density as well as the external quantum efficiency, which represents the probability of a photon of a specific energy to photo-excite a carrier which is collected at the contacts to finally contribute to the circuit. This relationship is given below as [71]

$$J_{SC} = q\int b_s(E)EQE(E)dE, \tag{3.3.3}$$

where $b_s(E)$ is the incident spectral photon flux density, which represents the total number of photons incident on a unit area per unit time in the energy range E to $E+dE$, and $EQE(E)$ is the external quantum efficiency of the cell, defined as the ratio of the number of electron-hole pairs that contribute to the J_{sc} divided by the total number of photons incident on the cell at energy E. The EQE of any cell is intricately related to the bandgap of the materials composing the solar cell as well as its design. The integral given in equation (3.3.3) is typically computed over the entire range of incident photon energies, typically in the range of 300-2000 nm.

Figure 3-14 demonstrates the EQE of an example GaAs solar cell overlaid with the normalized incident photon flux. The details of the simulated EQE are discussed in more

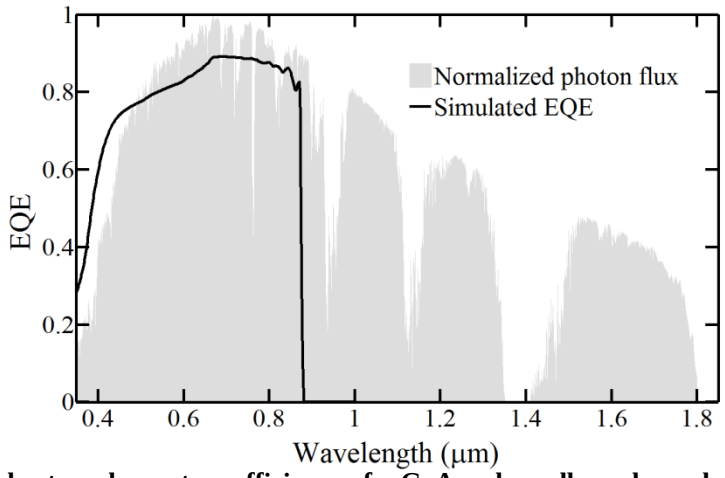

Figure 3-14. Simulated external quantum efficiency of a GaAs solar cell overlapped with the normalized photon flux.

detail in section 3.5.4, whereas the photon flux is described in section 3.4.1. The corresponding short circuit current density for this type of cell is calculated to be 0.0256 A/cm^2 according to equation (3.3.3). As a side note, one can observe the range of photons that are not absorbed by the cell (wavelengths longer than ~880 nm), which outlines an important loss mechanism that ultimately limits the performance of any single junction solar cell. A good review on fundamental losses in solar cells is given in [72].

Having computed the first term of equation (3.3.2), one can then plot the *J-V* characteristics of this solar cell and the corresponding power density – voltage (*P-V*) characteristics according to $P = J \cdot V$. This is illustrated in Fig. 3-15a using the following values: the short circuit current density computed earlier of J_{SC} = 0.0256 A/cm^2, a saturation current density of J_0 = 8×10^{-11} A/cm^{-2}, an ideality factor of 2, nearly ideal parasitic resistances (R_s=0 Ω, R_{shunt}=1×10^{10} Ω), and a temperature of 300 K. The overall efficiency of this device is computed based on the maximum power generated by the device (21 mW/cm^2 at a voltage of 0.83 V) and gives an efficiency of 21% since the incident power that generates this photocurrent is approximately 100 mW/cm^2 based on a standard spectrum (see section 3.4.1). Two important parameters are also of great merit to the study of

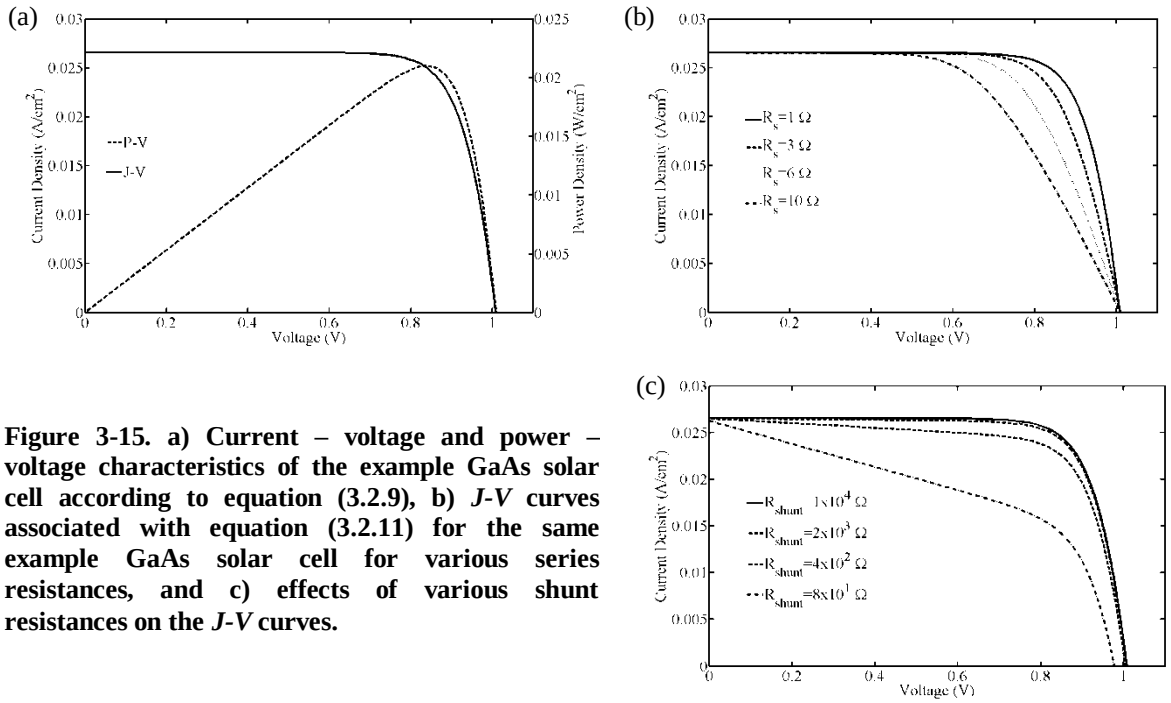

Figure 3-15. a) Current – voltage and power – voltage characteristics of the example GaAs solar cell according to equation (3.2.9), b) *J-V* curves associated with equation (3.2.11) for the same example GaAs solar cell for various series resistances, and c) effects of various shunt resistances on the *J-V* curves.

photovoltaics. The first is the open circuit voltage, V_{oc}, defined as the applied voltage required to balance the short circuit current density and the dark current density. It can be determined analytically by re-arranging equation (3.3.1) as

$$V_{OC} = \frac{nkT}{q} ln\left(\frac{J_{SC}}{J_0} + 1\right). \tag{3.3.4}$$

Evaluating equation (3.3.4) for the GaAs solar cell example gives V_{oc}=1.01 V. This equation also shows that the open circuit voltage (V_{oc}) increases logarithmically as the J_{sc}, which is an important notion for concentrated illumination applications. However, an increase in recombination current (or J_0) will result in a decrease in V_{oc}. The last figure of merit with solar cell performance is the fill factor (*FF*), or "square-ness" of the *J-V* curve. This metric is computed as the ratio of the maximum power and the power associated with the short circuit current density and open circuit voltage, or

$$FF = \frac{P_{MAX}}{J_{SC}V_{OC}} = \frac{J_{MPP}V_{MPP}}{J_{SC}V_{OC}}, \tag{3.3.5}$$

This parameter is representative of the area of the maximum power rectangle compared to the total area of the J_{sc}-V_{oc} rectangle. The *FF* related to this example is 79%. The reported *J-V* metrics are in agreement with typical values reported in the literature for a single junction GaAs cell, although the fill factor is generally on the order of 85% [71]. Comparatively, the highest reported efficiency of a GaAs cell is 28.8% [73]. Lastly, figures 3-15b and 3-15c demonstrate the effects of series and shunt resistance on the *J-V* characteristics of the same GaAs solar cell.

3.4. Simulating a Solar Cell in TCAD Sentaurus

Since inorganic solar cells are typically designed as *p-n* junctions, the transition from the previous section of simulating a *p-n* junction to this section is straightforward, especially with an understanding of the ideal diode equation and a simple GaAs solar cell. The essential features that must be added to the analysis of section 3.3 include an incident illumination spectrum and the computation of the optical generation of electron-hole pairs which contributes to the continuity equations (2.3.8) from chapter 2. First, the standard illumination spectrum must be integrated into the Sentaurus tool flow (see Fig. 3-3). The transfer matrix method (TMM) is then used to model the propagation of light intensities through the solar cell's epitaxial stack of semiconductor layers. The TMM calculates transmission, reflectance at all interfaces of the device as well as absorption in every layer for all wavelengths of interest. This calculation produces reflectivity and free carrier generation profiles which allow the user to perform two types of simulations. The first is a wavelength parameter ramp, which gives rise to the internal and external quantum efficiencies (EQE) discussed in section 3.4.4. Section 3.4.4 also discusses the effects of solar

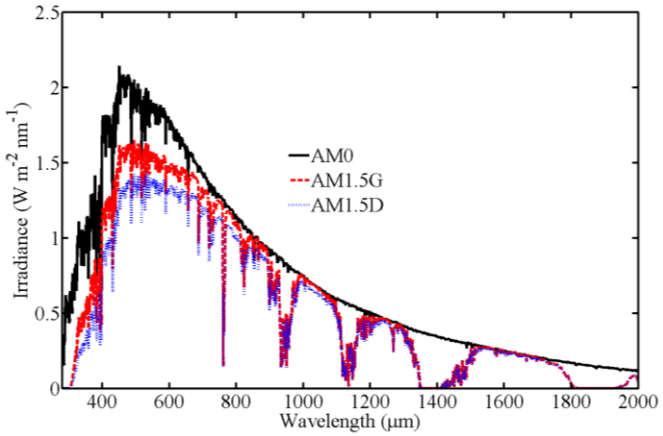

Figure 3-16. Standard extraterrestrial AM0 and terrestrial global (AM1.5G) and direct (AM1.5D) spectra.

cell design on the shape and magnitude of the EQE. The second is a voltage ramp that gives rise to the current – voltage characteristics, similar to the previous section, which is discussed in section 3.4.5.

3.4.1. Standard Illumination Spectrum

The terrestrial illumination spectrum is highly dependent on the atmospheric conditions, the time of day, the location, and a variety of other factors such as temperature and aerosol content. For these reasons, a standard spectrum is often used to predict the performance of a solar cell; this standard spectrum is crucially important in comparing the performance metrics of spectrally sensitive photovoltaic devices such as multi-junction solar cells. Two current standard spectra exist based on the ASTM G173-03 for both direct normal spectral irradiance and global spectral irradiance [74]. The direct normal spectrum is a component of the global spectrum, which considers a field of view of 180° with respect to the tilted surface. They are often referred to as the AM1.5D and AM1.5G spectra respectively, where AM represents the air mass value, defined as $1/\cos\theta$ where θ is the angle of inclination of the sun. The AM1.5G illumination spectrum is higher in magnitude than the AM1.5D since it considers both diffuse light and direct light. Figure 3-16 illustrates these

spectra along with the standard extraterrestrial spectrum, referred to as AM0, where the units of the incident spectrum are in watts per square meter per nanometer of bandwidth. The total intensity of each spectrum is close to 1300 W/m^2, 1000 W/m^2 and 900 W/m^2 for the AM0, AM1.5G and AM1.5D respectively. Sentaurus Device, however, requires an intensity profile rather than an irradiance spectrum. An intensity profile has the advantage over an irradiance profile in that the resolution need not be every nanometer since the specified intensity represents the total irradiance for a range of wavelengths. This can therefore reduce the computational time of the generation profile using the Beer-Lambert law.

3.4.2. Transfer Matrix Method (TMM)

Within the transfer matrix method, monochromatic plane waves of electromagnetic radiation of an arbitrary polarization are incident on a material stack at an arbitrary angle. The materials are isotropic, homogenous and optically linear, with the layers parallel to each other. Within these assumptions, each material can be characterized by a complex refractive index $\tilde{n}_j = (n_j + k_j)\cos\Theta_j$ for transverse electric polarization (TE) and by $\tilde{n}_j = (n_j + k_j)/\cos\Theta_j$ for transverse magnetic polarization (TM), where n_j represents the index of refraction of the j^{th} material, k_j the extinction coefficient, and Θ_j is the complex counterpart of the angle of refraction based on Snell's law ($n_0 \cdot sin\Theta_0 = n_j \cdot sin\Theta_j$). The absorption coefficient, α, for a specific wavelength of light, λ, is expressed as $\alpha_j = 4\pi k_j/\lambda$ for the j^{th} material layer. The refractive index and extinction coefficients are dimensionless values, whereas the resulting absorption coefficient has dimensions of inverse length. The propagation of light at a depth z_j through a material with absorption coefficient α_j can be modeled using the transfer matrix:

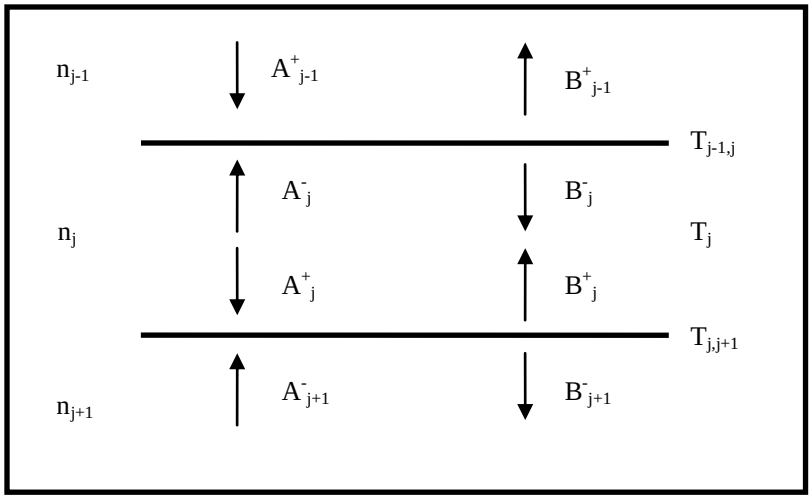

Figure 3-17. Illustration of the transfer matrix method showing forward and backward propagating waves due to transmission and reflectance at various interfaces. The matrix T_j is used to compute the absorption through a material layer using the Beer-Lambert law.

$$T_j(z_j) = \begin{bmatrix} \exp\left(i\alpha_j z_j\right) & 0 \\ 0 & \exp\left(-i\alpha_j z_j\right) \end{bmatrix}, \tag{3.4.1}$$

where z_j is the thickness of the j^{th} layer, and α_j is the wavelength dependent absorption coefficient. The absorption of light is computed using the Beer-Lambert law, usually expressed as $\cos(\alpha_j z_j)$ while ignoring the complex component, which is why the off-angle components are zero. The propagation of light at a material interface consisting of *j* and *j+1* layers can be modeled by the transfer matrix:

$$T_{j,j+1} = \frac{1}{2\tilde{n}_j} \cdot \begin{bmatrix} \tilde{n}_j + \tilde{n}_{j+1} & \tilde{n}_j - \tilde{n}_{j+1} \\ \tilde{n}_j - \tilde{n}_{j+1} & \tilde{n}_j + \tilde{n}_{j+1} \end{bmatrix}, \tag{3.4.2}$$

Consider the following example representative of a multiple heterojunction in Fig. 3-17. The top layer has a refractive index of n_{j-1} incident with a forward wave amplitude of $A^{\pm}_{j+1}$ and backward wave amplitude of $B^{\pm}_{j-1}=0$. These waves will transfer to the next layer with a refractive index n_j through the transfer matrix $T_{j-1,j}$ according to the following calculation:

$$\begin{bmatrix} B_j^+ \\ A_j^+ \end{bmatrix} = T_{j,j+1} \cdot \begin{bmatrix} A_{j+1}^- \\ B_{j+1}^- \end{bmatrix}. \tag{3.4.3}$$

Once in the layer, the light is absorbed by the material according to the transfer matrix T_j:

$$\begin{bmatrix} A_j^- \\ B_j^- \end{bmatrix} = T_j(z_j) \cdot \begin{bmatrix} B_j^+ \\ A_j^+ \end{bmatrix}. \tag{3.4.4}$$

Finally, the light will then transfer from the j^{th} material to the $j\text{-}1^{th}$ material in the following way:

$$\begin{bmatrix} B_{j-1}^+ \\ A_{j-1}^+ \end{bmatrix} = T_{j-1,j} \cdot \begin{bmatrix} A_j^- \\ B_j^- \end{bmatrix}. \tag{3.4.5}$$

The light intensity can then be calculated at a depth z from an interface, say the interface *(j,j+1)*, for both cases of polarization, as:

$$I_{(TE,TM)}(z) = \frac{\mathcal{R}e(Z_j)}{\mathcal{R}e(Z_0)} \left\| T_j(z) \cdot \begin{bmatrix} A_j^- \\ B_j^- \end{bmatrix} \right\|^2, \tag{3.4.6}$$

where the total intensity is the sum of both the transverse electric (TE) and transverse magnetic (TM) contributions, $I(z) = I_{TE}(z) + I_{TM}(z)$. For solar cell applications, the absorption of light for each wavelength propagating in a material can be calculated and related to the generation rate of electron-hole pairs, G_0^{opt}, as

$$G_0^{opt}(\lambda) = \alpha(\lambda)\eta_{QE} \frac{I(z)}{\hbar c/\lambda}. \tag{3.4.7}$$

This calculation depends on the absorption coefficient α(λ), on the photon energy $E = \hbar c/\lambda$ (which simply transforms the intensity of light into a photon flux), on the depth of light propagation into the layer, *z*, on the unitless quantum yield for that wavelength, η_{QE} (typically assumed to be 1), and lastly, on the light intensity *I(z)*. Equation (3.4.7) implicitly considers the losses of light intensity due to reflection since it is considered within *I(z)*. Typically, η_{QE}=1 for wavelengths greater than 450 nm, and is greater than unity for

wavelengths shorter than 450 nm due to the high energy of the photon in comparison to the bandgap of the material. An example for a wavelength dependence on the quantum efficiency for wavelengths shorter than 450 nm is $\eta_{QE} = 1 + 33.5(0.45\mu m - \lambda[\mu m])$, although this is ignored in the simulation. Integrating equation (3.4.7) over all photon energies gives the total generation rate at a particular depth *d*.

For UV light, generated electron-hole pairs will possess kinetic energy on the order of 1 eV or more. Since drift-diffusion equations only consider carriers in thermal equilibrium, these hot carriers must thermalize to the lattice temperature through phonon scattering; as a result, photogenerated carriers diffuse within a few diffusion lengths from the original location of generation. To take this process into account, the generation rate G_0^{opt} is weighted with a Gaussian function and a stepwise constant function to cut off the Gaussian (reduces computational time), as given below:

$$c(x) = \begin{cases} \frac{1}{2\lambda_{sp}} & -\lambda_{sp} \le z \le \lambda_{sp} \\ 0 & \text{otherwise.} \end{cases},$$

$$g(x) = \frac{1}{\lambda_{sp}\sqrt{\pi}} \exp\left[-\left(\frac{x}{\lambda_{sp}}\right)^2\right], \tag{3.4.8}$$

where the characteristic length scale λ_{sp} is based on a random walk model given by $\lambda_{\mathrm{sp}} = \sqrt{\frac{2}{3}\mathrm{N_{ph}}}\,\lambda_{\mathrm{ph}}$, where λ_{ph} is the average mean free path for phonon scattering ($\lambda_{ph} =$ 5.5 nm), and N_{ph} is the number of phonons involved in the thermalization process given by

$$\mathrm{N_{ph}} = \frac{1}{2}\frac{\hbar\omega - \mathrm{E_{gap}} - (\eta-1)\langle \mathrm{E_{imp}} \rangle}{\langle E_{\mathrm{ph}} \rangle}. \tag{3.4.9}$$

In the expression above, the bandgap is given by E_{gap}, $\langle E_{imp} \rangle$=1.5 eV is the average impact ionization energy for silicon, and $\langle E_{ph} \rangle$=0.054 eV is the phonon energy. Both of the weight functions are normalized,

$$\int_{-\infty}^{+\infty} c(x)\,dx = \int_{-\infty}^{+\infty} g(x)\,dx = 1. \qquad (3.3.10)$$

The convolution of G_0^{opt} with both weight functions gives a modified G^{opt} as

$$G^{opt}(z) = \left(\int_0^{+\infty} G_0^{opt}(x) w(z - x')\,dx'\right) + (1-\beta)\int_0^{+\infty} G_0^{opt}(x) w(z + x')\,dx' \qquad (3.4.11)$$

where β is a loss factor due to carriers diffusing out of the layer through a random walk process, z is the depth of the active layer, and w is one of the weight functions specified above. Equation (3.4.11) is equivalent to equation (2.5.15) of chapter 2 with the exception of the weight functions. The resulting optical generation profile is used in computing the generation terms of the continuity equations (2.3.8) as a function of vertical position throughout the solar cell (i.e. at all vertices of the mesh). For details on how the optical generation is activated in Sentaurus, see Appendix B-1.

3.4.3. Changes to Solar Cell Geometry due to Illumination

The illumination of a solar cell naturally requires light to be transmitted into the solar cell. However, the structure of the *p-n* junction illustrated in Fig. 3-4 consists of top and bottom contacts that cover the entire device. Although these contacts are transparent in the simulation environment, it does not reflect a realistic solar cell device geometry which considers shading from the top contacts. In some cases, such as Cu(In,Ga)Se_2 solar cell, which consists of a transparent conductive oxide (TCO) typically composed of zinc oxide (ZnO), the aforementioned device geometry is realistic. For cases in which a metallic grid covers the top surface of the solar cell, shading becomes an important consideration as it induces lateral currents to the top contacts. The device geometry must therefore be altered to consider this; this subsequently effects the generation of the mesh, since it must be refined in both the *x*- and *y*- directions to accurately simulate the behaviour of lateral currents. Fig. 3-18 illustrates the updated device geometry which shows a front contact to induce 5%

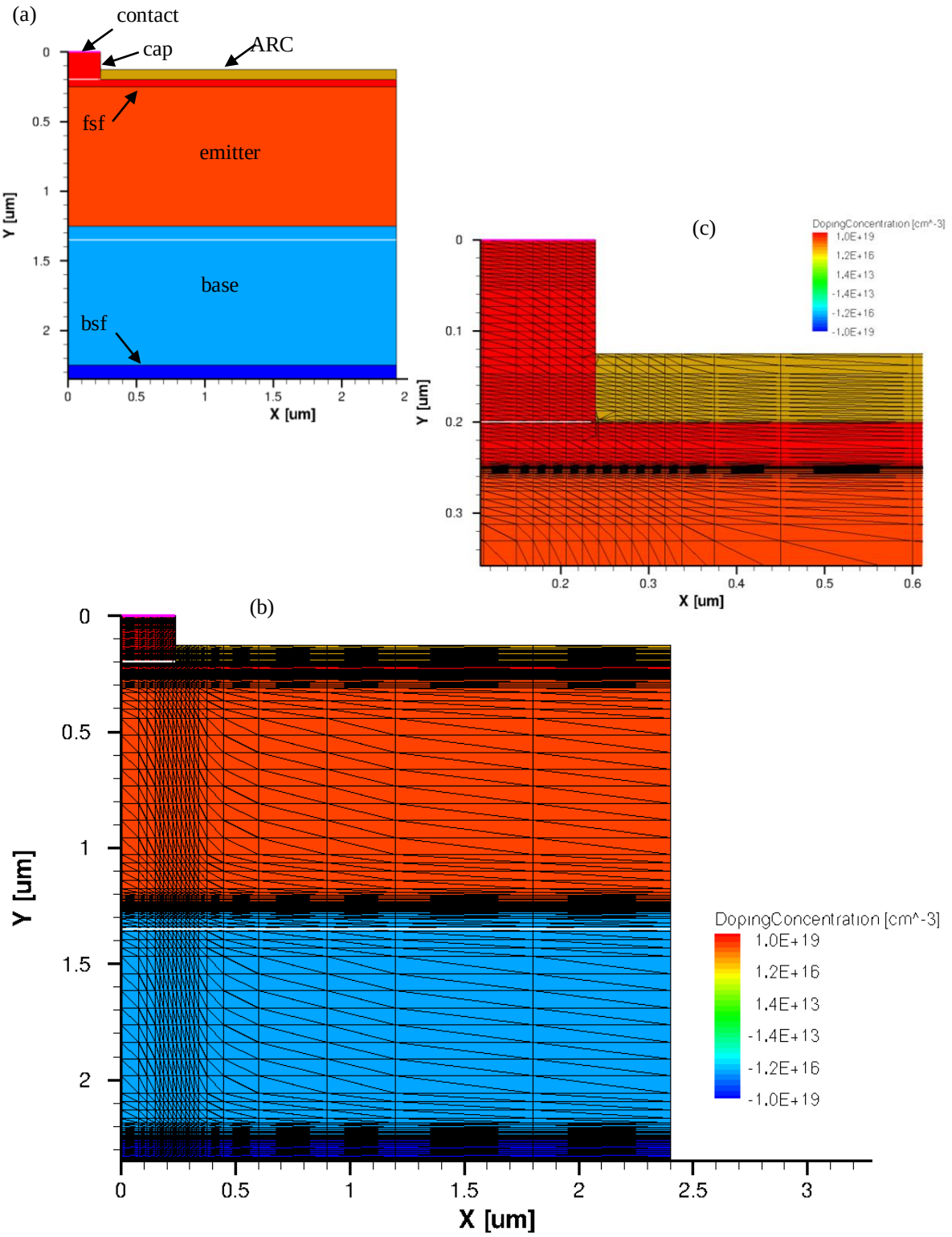

Figure 3-18. a) Simulated GaAs solar cell structure with shadowing considerations (5%), an anti-reflection coating (ARC) composed of Si_3N_4 and front and back surface fields composed of $Al_{0.3}Ga_{0.7}As$, b) meshing of the structure, and c) close-up of the mesh near the contact.

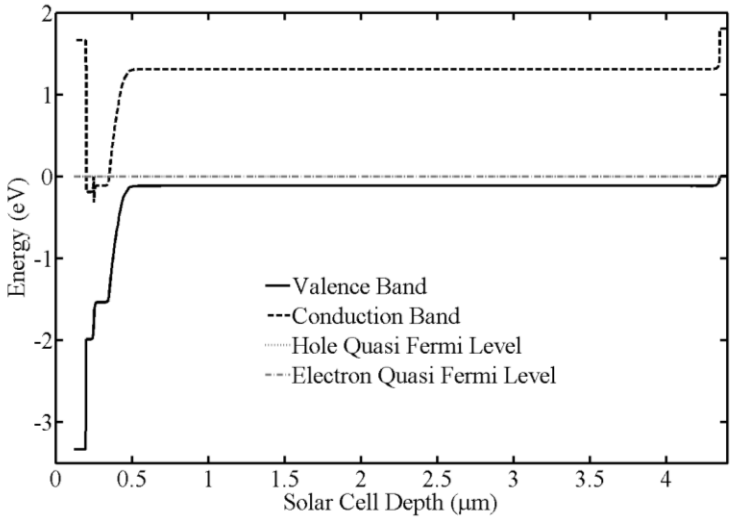

Figure 3-19. Simulated energy band diagram of a GaAs solar cell with front and back surface fields composed of $Al_{0.3}Ga_{0.7}As$ at equilibrium to outline the potential barriers of these layers at a cross-section along the Y-axis at X=2 μm. The energy bands begin at a depth of 0.12 μm to outline the ARC (with high bandgap) as the cross-section does not intersect the contact and cap layers.

shadowing losses. Furthermore, the structure also demonstrates the implementation of front and back surface fields composed of $Al_xGa_{1-x}As$ (FSF and BSF respectively), which are good in minimizing surface recombination due to their higher bandgap relative to GaAs. The bandgap of $Al_xGa_{1-x}As$ at room temperature is 1.798 eV according to $Eg(x) = 1.424 + 1.247x$ where x is the molar fraction of Al [75]. Front and back surface fields produce potential barriers for the minority carriers to prevent them from reaching the front and back interfaces of the cell where surface recombination is important. The simulated energy band diagram at short circuit (Fig. 3-19) illustrates these effects; their effects on the *J-V* characteristics are studied in the next section. Higher bandgap materials such as $Ga_xIn_{1-x}P$ can also be used as front and back surface. An anti-reflection coating (ARC) is also used to minimize reflectivity across the wavelength range of interest, discussed shortly. The details of the structure are outlined in Table 3-3 based on the cell design in [37], where a thin emitter is used at a higher doping compared to a thicker base of lower doping due to diffusion length considerations. The nature of the doping atoms (Te, Si, P and C) is based on

the ability to highly dope GaAs based materials, which is entirely dependent on ionization energy (see Fig. 10 of [35]). This cell geometry is representative of a unit cell which is repeated along the *x-y* plane. Extrapolating the simulation results of one unit cell as representative of a complete solar cell assumes edge effects are minimal. It is important to note that radiative recombination acts solely as a loss mechanism in the continuity equations. The simulation does not account for the emitted photons from this process.

The anti-reflection coating (ARC) such as one composed of Si_3N_4 or SiO_2, minimizes reflectivity over a range of wavelengths. The optimal refractive index of an ARC is based on the geometric mean of the refractive index of the surrounding media, or $n_{ARC} = \sqrt{n_0 n_1}$ [37], where n_0 and n_1 are the refractive indices of the materials above and below respectively ($n_0=1$ to represent that of air). The refractive index and extinction coefficient of Si_3N_4, SiO_2 and other known ARC materials are illustrated in Fig. 3-20a and b respectively. The refractive index of GaAs is illustrated in Fig. 3-26. Although the reflectivity is calculated using the TMM, it can be shown analytically that, for normal incidence, it is given by [37]

$$R = \frac{(n_0-n_1)^2+(n_0 n_1/n_{ARC}-n_{ARC})^2 tan^2(\delta_1)}{(n_0+n_1)^2+(n_0 n_1/n_{ARC}+n_{ARC})^2 tan^2(\delta_1)} \quad (3.4.12)$$

Table 3-3. Structural details of simulated GaAs solar cell with ARC and front and back surface fields.

Layer	Material	Thickness (μm)	Doping (cm^{-3})
ARC	Si_3N_4	0.08	-
n-cap	GaAs:Te	0.2	1×10^{19}
n-FSF	$Al_{0.3}Ga_{0.7}As$:Te	0.05	1×10^{19}
n-emitter	GaAs:Si	0.1	3×10^{18}
p-base	GaAs:P	4	1×10^{17}
p-BSF	$Al_{0.3}Ga_{0.7}As$:C	0.05	1×10^{19}

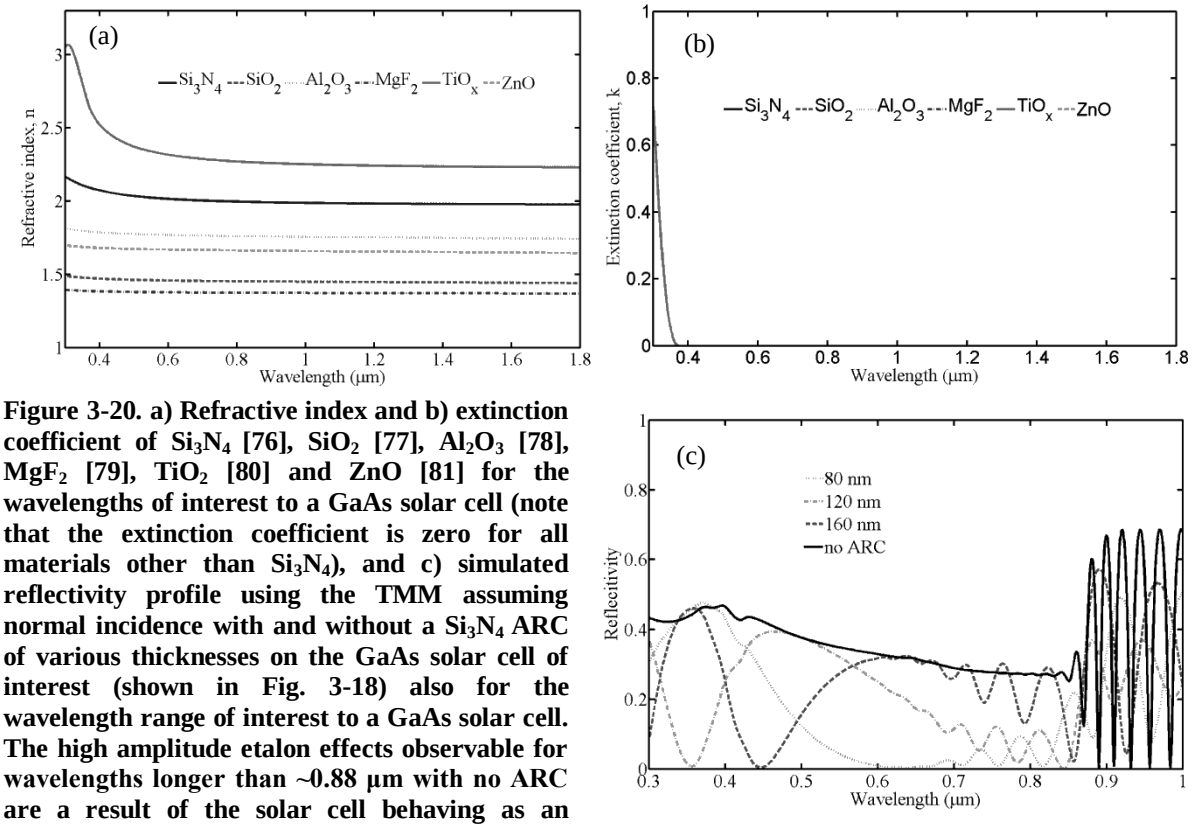

Figure 3-20. a) Refractive index and b) extinction coefficient of Si_3N_4 [76], SiO_2 [77], Al_2O_3 [78], MgF_2 [79], TiO_2 [80] and ZnO [81] for the wavelengths of interest to a GaAs solar cell (note that the extinction coefficient is zero for all materials other than Si_3N_4), and c) simulated reflectivity profile using the TMM assuming normal incidence with and without a Si_3N_4 ARC of various thicknesses on the GaAs solar cell of interest (shown in Fig. 3-18) also for the wavelength range of interest to a GaAs solar cell. The high amplitude etalon effects observable for wavelengths longer than ~0.88 μm with no ARC are a result of the solar cell behaving as an optical cavity, which induces constructive and destructive interference at long wavelengths.

where δ_1 is the phase shift occurring to the incident light at the semiconductor/ARC interface, given by $\delta_1 = 2\pi n_1 d_{ARC}/\lambda$ where d_{ARC} is the thickness of the ARC. The reflectivity according to equation (3.4.12) reaches its minimum when $\delta_1 = \pi/2$, which first occurs when $d_{ARC} = \lambda/4$. To demonstrate the effects of an ARC on a solar cell using the TMM within Sentaurus, a single layer Si_3N_4 ARC is deposited on the solar cell illustrated in Fig. 3-18, and the simulated reflectance for normal incidence is illustrated in Fig. 3-20c for various thicknesses of this ARC as well as a comparison with no ARC. Any thickness of the ARC results in lower overall reflectivity across the wavelength range of interest for the GaAs solar cell compared to the reflectivity without an ARC. It is also observed that different thicknesses result in different wavelengths where the minimum in the reflectivity occurs, as one would expect based on equation (3.4.12). Although the ARC is not optimized, a

thickness of 80 nm is adopted for further simulations as the minimum in reflectivity lies in the range of 600-700 nm which is useful for GaAs solar cells. For more details on the physics of ARC, see section 9.3.2 of [37].

3.4.4. Quantum Efficiency Simulations

The external quantum efficiency (EQE) of a solar cell measures the probability that an incident photon of energy E will generate an electron-hole pair that is collected at the electrodes. The calculation of the EQE is based on the definition of quantum efficiency: the ratio of the number of carriers collected at the electrodes for one particular wavelength with the total number of incident photons of that wavelength. Analytically, this is expressed as

$$EQE(\lambda) = \frac{\left({}^{Jsc}/_{q}\right)}{{}^{I}/_{E_{ph}}}\ , \tag{3.4.13}$$

where J_{sc} is the short circuit current density, typically expressed in A/m^2, q is the electronic charge – the ratio therefore giving the number of carriers collected at the electrodes per unit area per second – I is the incident intensity in units of W/m^2 and E_{ph} is the energy of the photon. Re-arranging gives

$$EQE(\lambda) = hc\frac{\left({}^{Jsc}/_{q}\right)}{I\cdot\lambda}\qquad , \tag{3.4.14}$$

where the substitution $E_{ph} = hc/\lambda$ was performed. As a result, the simulated J_{sc} at intensity I for a specific wavelength λ reveals the external quantum efficiency.

The simulation of the EQE is carried out as follows: a quasi-stationary simulation is performed where the wavelength is ramped to determine the photocurrents collected at the contacts at each wavelength. The internal quantum efficiency (IQE) is intricately related to the EQE through the reflectivity. Since the IQE does not consider reflectivity, it is always greater than the EQE. The TMM computes the total reflectivity profile, which can therefore

be used to compute the IQE from the EQE. However, an equivalent calculation can be performed with the use of the optical generation profile within the solar cell at a particular wavelength. The integral of the optical generation over the device thickness represents the photocurrent for a QE of unity (i.e. all carriers due to generation are being collected, thus a perfect photocurrent). The ratio of the short circuit current by the photocurrent gives the internal quantum efficiency, and is expressed as

$$IQE(\lambda) = \frac{J_{sc}}{J_{ph}} = \frac{J_{sc}}{qA\int G^{opt}(z)dz} \tag{3.4.15}$$

where A is the cross-sectional area of the device in order to obtain a current density. Two other very closely related parameters are the internal spectral responsivity (ISR) and external spectral responsivity (ESR). These are typically expressed in Amps per Watt (A/W), and are given analytically as

$$ISR(\lambda) = IQE(\lambda)\frac{q}{E_{ph}} = IQE(\lambda)\frac{q\lambda}{hc}, \tag{3.4.16}$$

$$ESR(\lambda) = EQE(\lambda)\frac{q}{E_{ph}} = EQE(\lambda)\frac{q\lambda}{hc} \quad , \tag{3.4.17}$$

respectively. The simulated EQE, IQE, ISR and ESR of the aforementioned GaAs solar cell are illustrated in Fig. 3-21. The EQE demonstrates a relatively low response in the UV due in part to the reflectivity of the ARC, but also due to the high levels of recombination occurring in the emitter. The magnitude of the EQE at wavelengths longer than 550 nm increases to 70% and beyond primiarly due to the vicinity of the generated electron-hole pairs to the depletion region coupled to the relatively long diffusion lengths of electrons in the lowly doped based. It is also in part due to the storng effects of the back surface field of the device. A more detailed study on the effects of ARC and both FSF and BSF layers is conducted in section 3.4.5. The IQE is, as expected, greater than the EQE at every

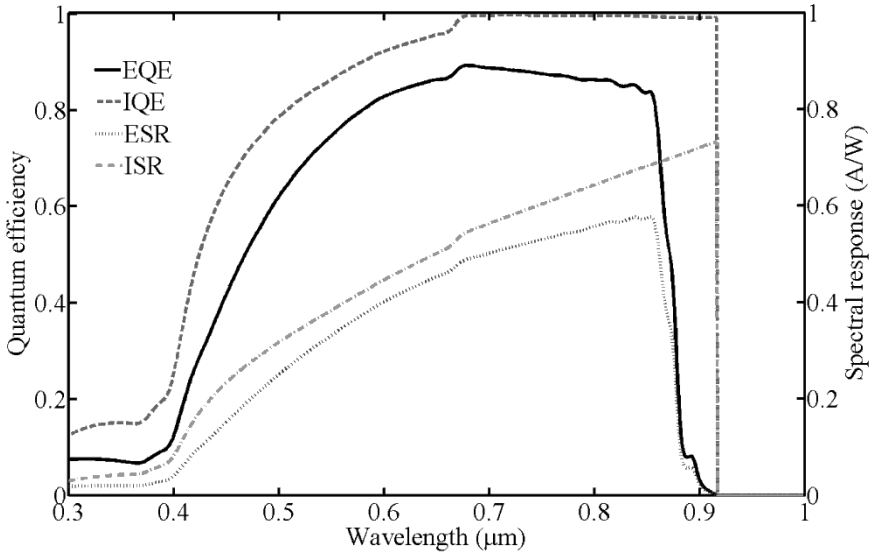

Figure 3-21. Simulated EQE, IQE, ISR and ESR of the GaAs solar cell with the ARC and with front and back surface fields as outlined in Fig. 3-18 and specified in Table 3-3. The IQE (and therefore ISR) are cut-off to zero as soon as the extinction coefficient of GaAs goes to zero (close to 0.917 μm).

wavelength. Based on definition, the ISR and ESR are similar in shape to the IQE and EQE respectively, which also shows these are increasing functions for increasing wavelength, since they are simply the IQE and EQE divided by photon energy respectively. Interestingly, the IQE remains non-zero for wavelengths longer than 0.88 μm compared to the EQE, which decays quickly after this wavelength. This is due to a drastically reduced absorption coefficient near this cut-off wavelength, but it does not go to absolute zero until 0.917 μm. In this thesis, only the EQE will be discussed as it is the most common attribute used in the photovoltaic community to describe the response of a solar cell to incident illumination.

One worthy issue to address with a quantum efficiency simulation is that for a highly resolved IQE simulation, the photon current J_{ph} can be non-zero for wavelengths where the absorption coefficient is indeed zero. This non-physical result is due to a cubic spline interpolation performed by Sentaurus Device on the optical parameters n and κ during the wavelength ramp. The interpolated extinction coefficients become non-zero, and therefore

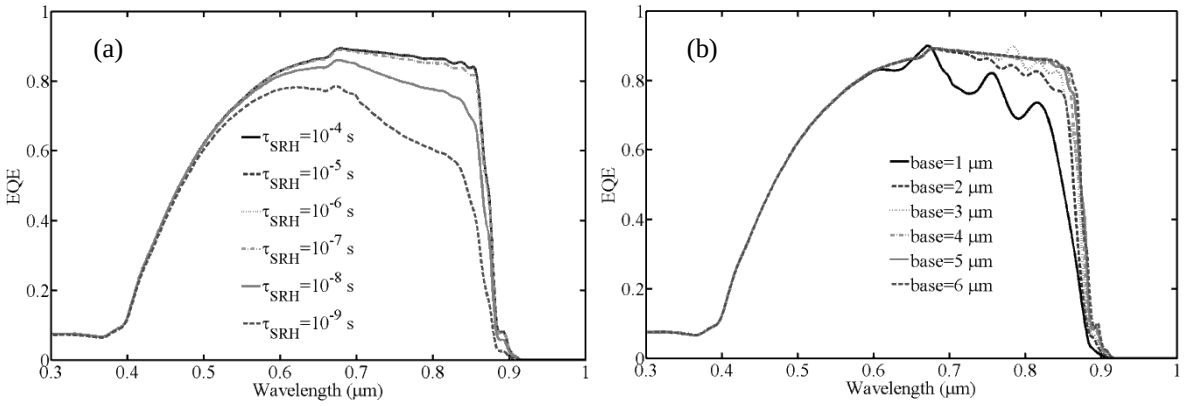

Figure 3-22. Effect of a) minority carrier SRH lifetime, and b) base thickness s on the simulated EQE of the GaAs solar cell of interest.

predict very small photon currents (on the order of 10^{-20} mA/cm^2) for wavelengths where no photon currents are expected, which is orders of magnitude larger than the dark current of the cell. The result of this non-physical photon current gives extremely large values of IQE, which are non-physical.

Recombination of minority carriers through Shockley-Read-Hall (SRH) processes has a significant effect on the EQE, as shown in Fig. 3-22a which outlines the effects of minority carrier recombination lifetime for SRH processes on the EQE of the GaAs solar cell. Reducing the minority carrier lifetime leads to a decreased diffusion length which implies that carriers generated far from the depletion region experience a reduction in carrier collection probability, which should ultimately reduce the J_{sc}. These effects are expected to be greatest in the long and short wavelength ranges of the EQE, since these are the wavelengths that are preferentially absorbed furthest from the depletion region of the cell. Figure 2-12 illustrates how long wavelengths have a relatively weaker absorption coefficient and are therefore absorbed deeper in the base, i.e. further from the depletion region. Shorter wavelengths, on the other hand, correspond to a very high absorption coefficient and

therefore are absorbed very close to the surface of the material. For carriers generated in the depletion region of the cell, on the other hand, a reduction in lifetime makes very little difference to the magnitude of the EQE, as can be seen by wavelengths that are preferentially absorbed at a depth corresponding to the depletion width (0.67 - 0.86 microns); note this is doping and therefore design dependent. The minority carrier SRH lifetimes for GaAs were only modified in this short study to outline its pronounced effects on the EQE. The lifetimes for GaAs assume the values expressed in Fig. 2-11. Figure 3-22b illustrates that for an increased base thickness, the EQE in the long wavelength range increases since these are the wavelengths which have the lowest absorption coefficient. Furthermore, the oscillations in the EQE for a base thickness of 1 μm increasingly disappear for increasing thickness. Based on these simulation results, a base thickness of 4 microns is adopted for later simulations since this thickness absorbs 99% of the light.

3.4.5. *J-V* and *P-V* Simulations and Results

The incident spectrum on the solar cell gives rise to a generation profile specific to the solar cell design, which describes the total number of electron-hole pairs generated at a specific depth for all wavelengths. Figure 3-23 illustrates the simulated generation profile using the TMM for the epitaxial stack shown in Fig. 3-18. It is used to compute the short circuit current density of the cell by solving the Poisson, electron and hole current-continuity equations in Sentaurus Device with no applied bias. Once this is solved, a voltage ramp is conducted within a quasi-stationary command similar to the steps carried out in section 3.2.2. With no parasitic resistances, the simulated current – voltage (*J-V*) characteristics of the GaAs solar cell are illustrated in Fig. 3-24 for various design modifications as given by:

Design A: an *n-p* cell with an ARC and FSF/BSF

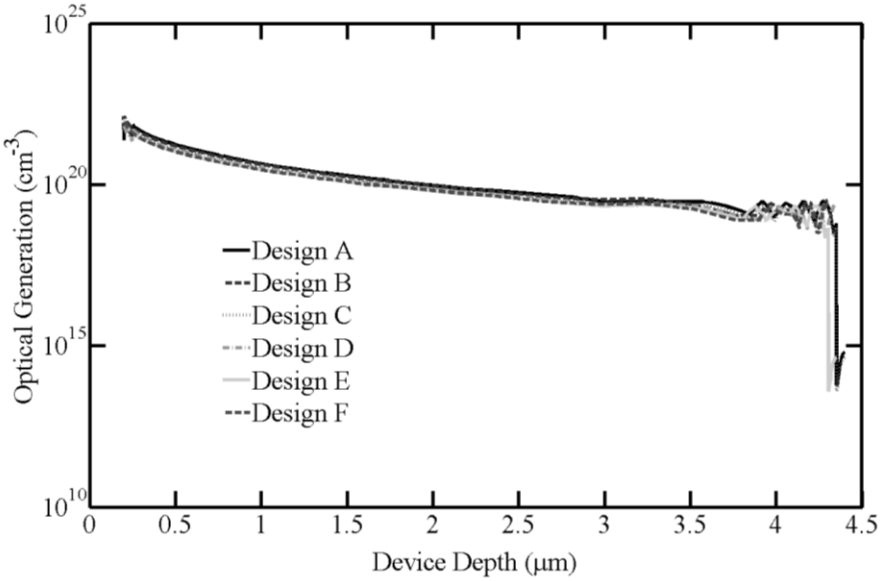

Figure 3-23. Simulated optical generation profile of the various GaAs solar cell designs illuminated by the AM1.5D spectrum. Each design encompasses different layers, which results in different profiles. For example, only three designs consist of an AlGaAs BSF, which results in the observable drop in optical generation close to a depth of 4.4 μm. Furthermore, different oscillatory behaviors are observed for various designs due to slight changes in the total optical cavity thickness from design to design.

Design B: an *n-p* cell with an ARC but no FSF/BSF

Design C: an *n-p* cell with a FSF and a BSF but no ARC

Design D: an *n-p* cell with a FSF but no ARC and no BSF

Design E: an *n-p* cell with a BSF but no ARC and no FSF

Design F: an *n-p* cell with no ARC and without FSF/BSF

The ARC in this solar cell design is composed of Si_3N_4. The corresponding *J-V* metrics, namely the J_{sc}, V_{oc}, *FF* and efficiency η, are given in Table 3-4. The simulated V_{oc} and *FF* metrics for design A are reasonable compared to typical values reported in the literature as well as the results from the ideal diode equation from section 3.3, although fall short compared to the world record (WR) GaAs solar cell produced by Alta Devices [3]. An improved agreement could hypothetically be obtained by replacing the AlGaAs barrier layers with a higher bandgap material, such as GaInP, and by increasing carrier lifetimes

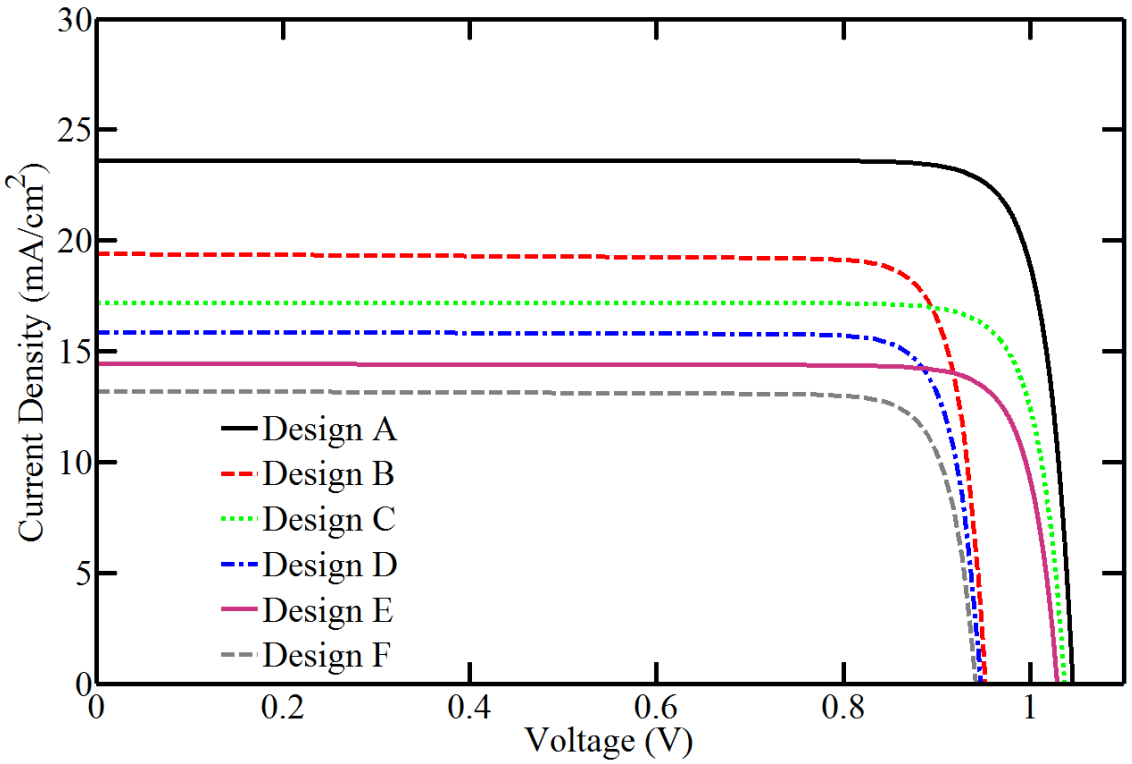

Figure 3-24. Simulated current-voltage characteristics of a GaAs solar cell with and without ARC and fsf/bsf.

within the material (representative of higher quality GaAs). Interestingly, the world record is for a thin GaAs solar cell that exploits photon recycling effects, which are not modeled in Sentaurus. Photon recycling effectively increases the radiative lifetime of minority carriers,

Table 3-4. Simulated *J-V* metrics of the GaAs solar cell with and without ARC, FSF and BSF.

Cell Design	J_{sc} (mA/cm^2)	V_{oc} (V)	FF (%)	P_{max} (mW/cm^2)	η (%)
Design A	23.6	1.05	87.2	21.5	21.5
Design B	19.4	0.95	86.5	16.0	16.0
Design C	17.2	1.04	86.9	15.5	15.5
Design D	15.9	0.95	86.9	13.1	13.1
Design E	14.4	1.03	86.7	12.9	12.9
Design F	13.2	0.94	86.4	10.7	10.7
World Record [3]	29.7	1.11	88.5	28.8	28.8

and since the non- radiative lifetimes (mostly from SRH processes) are relatively long, the increased radiative lifetime has a pronounced effect on the V_{oc}. The J_{sc} and efficiencies are starkly different most likely due to differences in ARC designs, such as a larger number of layers composing the ARC. When the FSF and BSF are removed from the solar cell design (B), a noticeable decrease in both J_{sc} and V_{oc} are observed, with a corresponding degradation in *FF*. This arises from the lack of potential barriers reflecting minority carriers toward the depletion region, and thus the minority carrier diffusion lengths increase, which results in an increase in overall recombination rates. Design C simply demonstrates the strong effect of the ARC on the J_{sc}. Designs D and E outline how the FSF mostly impacts the J_{sc} and the BSF mostly impacts the V_{oc}. The former effect arises from the low EQE in the short wavelength range, which is impacted by the FSF, whereas the recombination rates in the emitter are already high due to the high doping of the emitter. The BSF has little impact on the Jsc since the EQE is relatively high in the long wavelength range. However, the BSF strongly impacts the V_{oc} since the recombination rates are low in

the base compared to the emitter. Thus, a potential barrier which repels minority carriers away from the back of the cell toward the depletion region will mitigate recombination and thus impact the V_{oc}. Lastly, design F demonstrates a bare *p-n* junction which will have poor J_{sc} and V_{oc} as a result of no ARC and no FSF/BSF layers.

The simulated energy band diagrams of the solar cell design consisting of an ARC and FSF/BSF are illustrated in Fig. 3-25a-c at J_{sc}, the maximum power point (*MPP*) and V_{oc} respectively. These are qualitatively similar to the energy band diagrams of the diode as a function of bias (see Figs. 3-9 to 3-12), with the exception that the quasi-Fermi levels are separated throughout the device due to the generation of electron-hole pairs. The separation

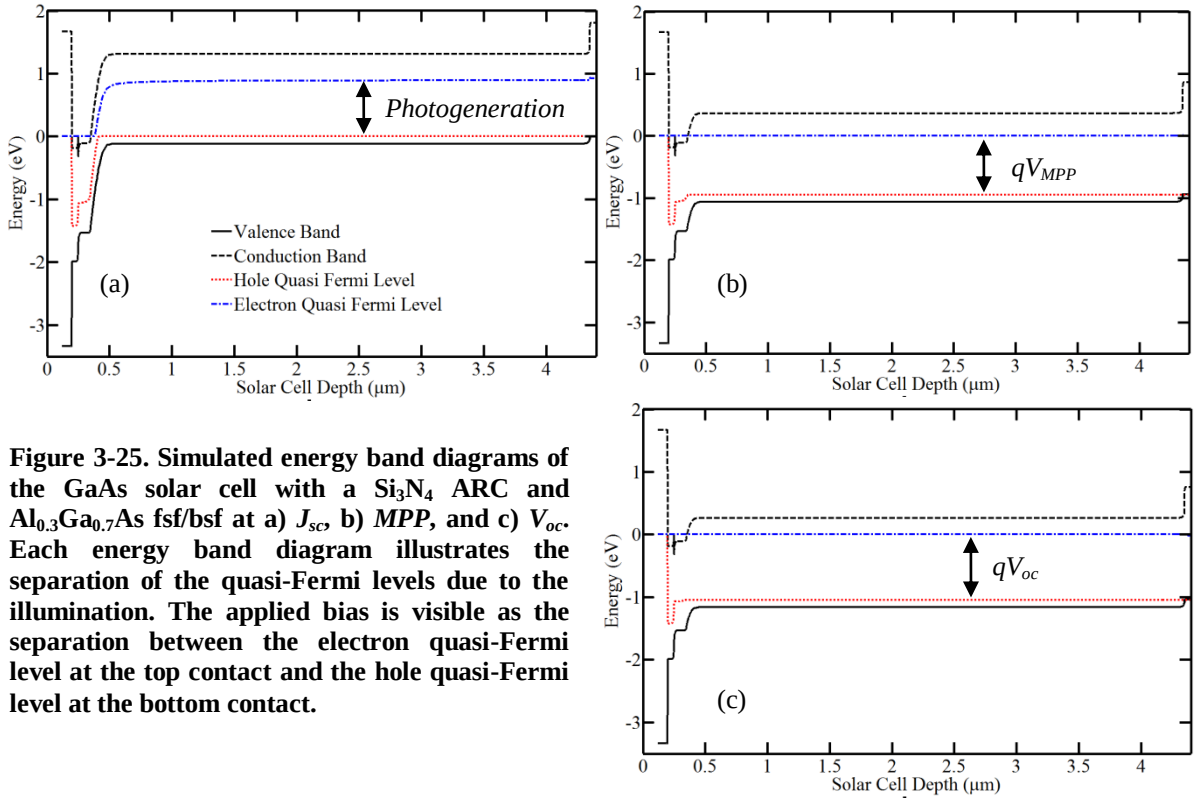

Figure 3-25. Simulated energy band diagrams of the GaAs solar cell with a Si_3N_4 ARC and $Al_{0.3}Ga_{0.7}As$ fsf/bsf at a) J_{sc}, b) *MPP*, and c) V_{oc}. Each energy band diagram illustrates the separation of the quasi-Fermi levels due to the illumination. The applied bias is visible as the separation between the electron quasi-Fermi level at the top contact and the hole quasi-Fermi level at the bottom contact.

of the quasi-Fermi levels between the top to bottom contacts is equivalent to the applied voltage.

3.5. Simulations of Other Solar Cell Material Systems as a Comparison

So far, the discussion of single junction solar cells has been focused on the well known III-V semiconductor GaAs. An interesting study can be conducted on the variation of solar cell performance by expanding this study to other material systems such as crystalline silicon (Si), gallium indium phosphide (GaInP), germanium (Ge) and copper indium gallium di-selenide ($CuIn_xGa_{1-x}Se_2$) to name a few. These materials are chosen based on the focus of this thesis, namely lattice matched multi-junction solar cells composed of GaInP/InGaAs/Ge, and with other high performing solar cell materials (Si and

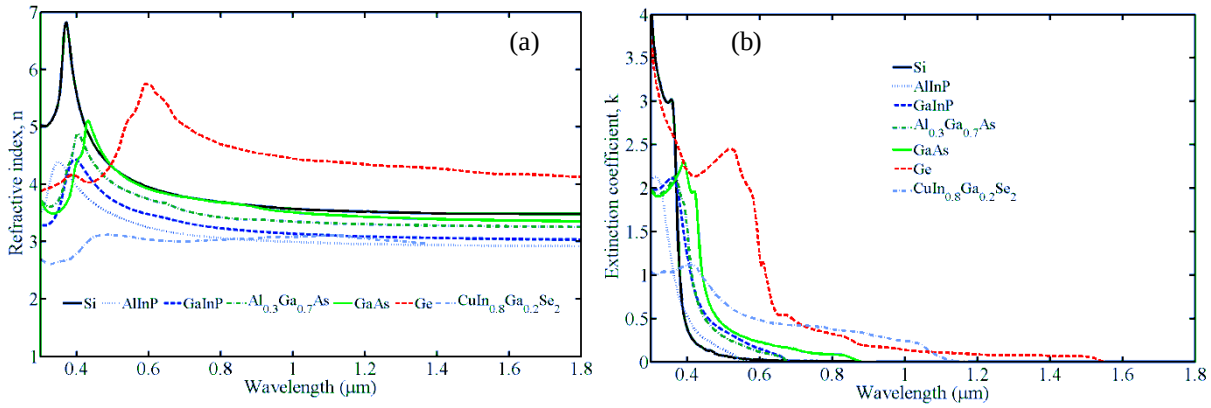

Figure 3-26. a) Real and b) complex components of the refractive index of Si [82], AlInP [83], GaInP [83], AlGaAs [84], GaAs [84], Ge [85] and $CuIn_{0.8}Ga_{0.2}Se_2$ [45].

Cu(In,Ga)Se_2). In order to understand the simulated *J-V* characteristics and EQE profiles, it is essential to first introduce the important properties of these materials, such as bandgap, optical characteristics, carrier mobilities and recombination lifetimes.

3.5.1. Properties of Si, GaInP, GaAs, Ge and Cu(In,Ga)Se_2

The bandgaps of Si, GaInP, GaAs, Ge and Cu(In,Ga)Se_2 are illustrated in Table 3-9. Their real and imaginary components of the refractive index are illustrated in Fig. 3-26a and b respectively. The extinction coefficients are representative of the absorption coefficients illustrated in Fig. 2-12 of Chapter 2. The carrier mobilities are illustrated in Figs. 3-27 for Si [86], AlInP [87], GaInP [87], $Al_{0.3}Ga_{0.7}As$ [88], GaAs [88], Ge [89], and $Cu(In_{0.8}Ga_{0.2})Se_2$ [90] respectively. Note the larger electron mobilities in GaAs compared to Si led to the use of GaAs for high electron mobility transistors (HEMT). The mobilities in $Cu(In_{1-x}Ga_x)Se_2$ have been reported as constant over hole carrier concentrations ranging from 10^{16} to 10^{19} cm^{-3} [90]. Lastly, the recombination lifetimes for these materials are illustrated in Figs. 3-28 to 3-31 (the lifetimes of carriers in GaAs are illustrated in Fig. 2-11).

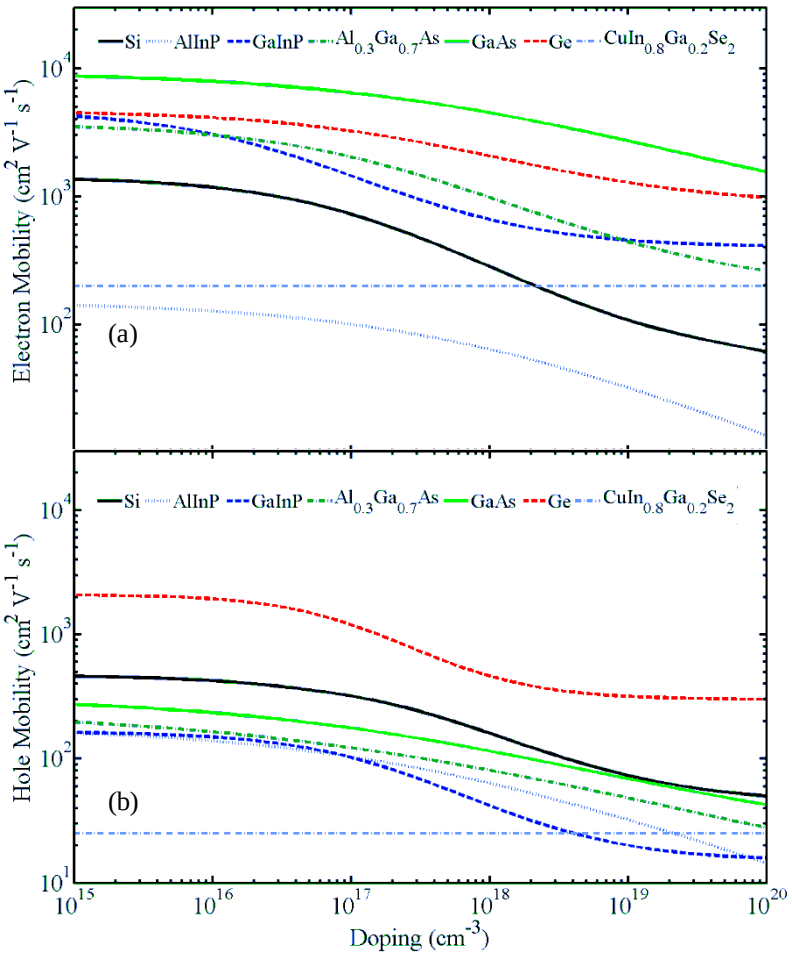

Figure 3-27. a) Electron and b) hole mobilities as a function of doping concentration for Si [86], AlInP, GaInP [87], AlGaAs [88], GaAs [88], Ge [89] and $CuIn_{0.8}Ga_{0.2}Se_2$ [90]. The AlInP mobilities were lowered in the actual simulations with respect to [87] based on internal discussions within the 4CPV project in collaboration with Sherbrooke University and Cyrium Technologies.

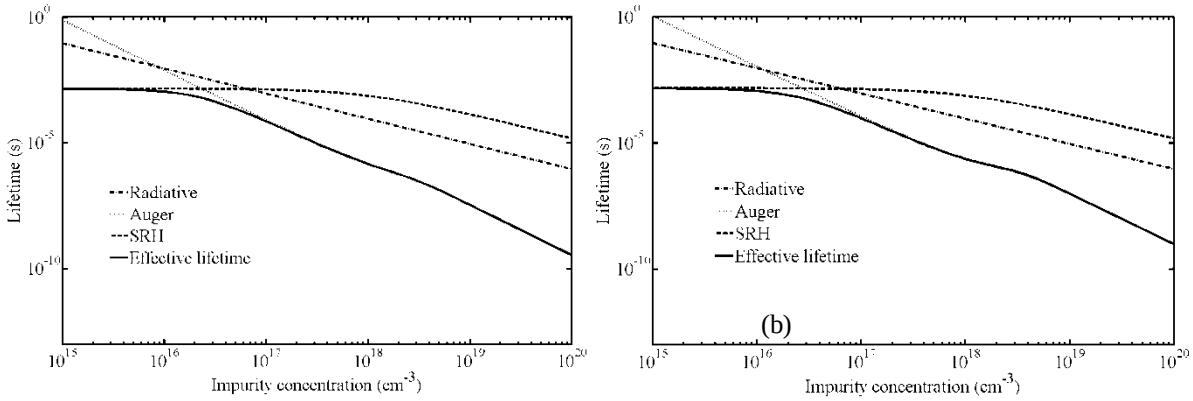

Figure 3-28. a) Electron and b) hole recombination lifetimes of Si for the three important recombination mechanisms (Auger [91], SRH [92] and radiative [93]).

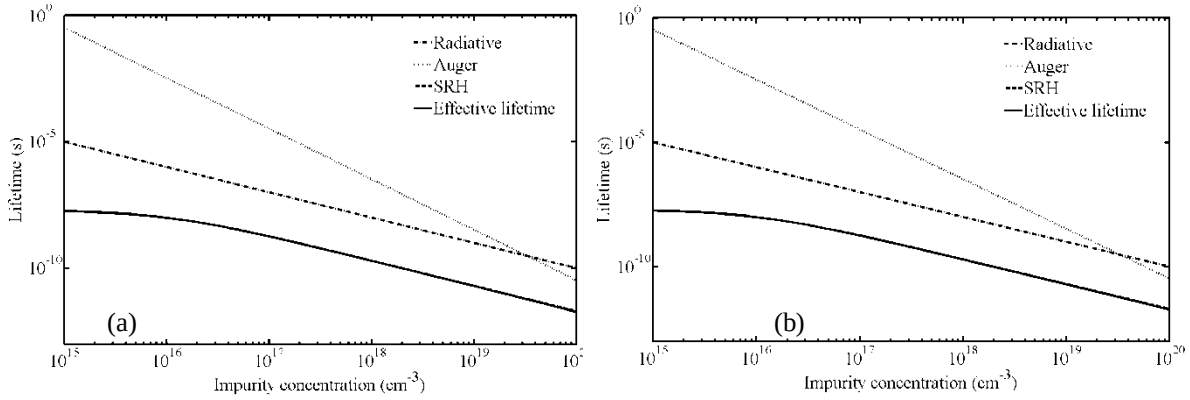

Figure 3-29. a) Electron and b) hole recombination lifetimes of GaInP for the three important recombination mechanisms (Auger [94], SRH [95] and radiative [94]).

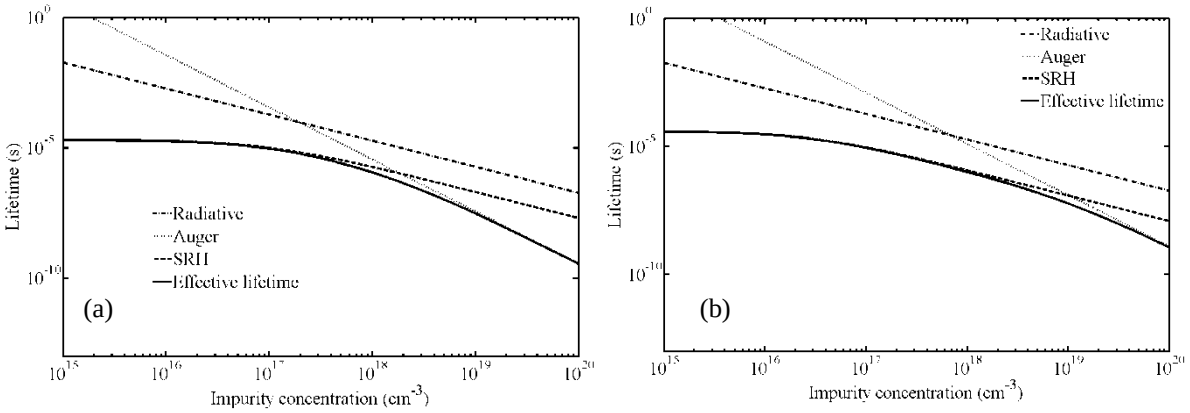

Figure 3-30. a) Electron and b) hole recombination lifetimes of Ge for the three important recombination mechanisms (Auger, SRH and radiative [96]).

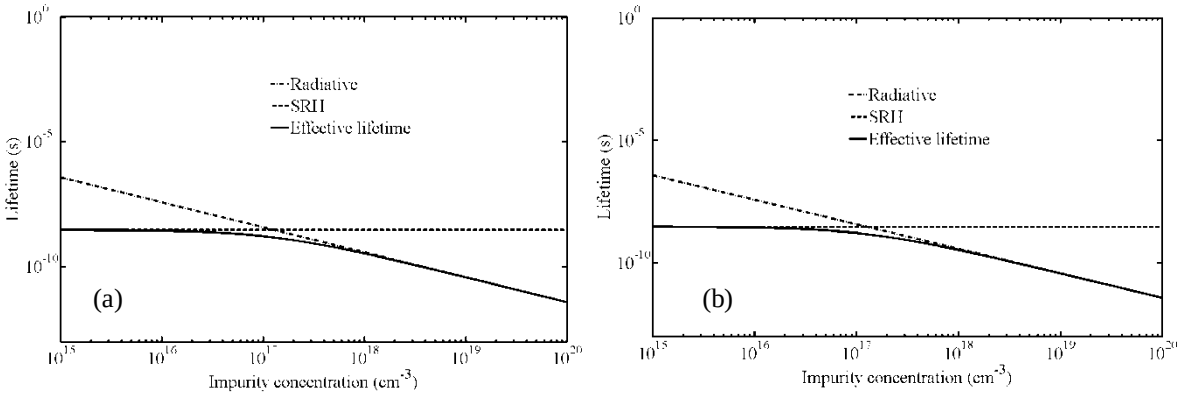

Figure 3-31. a) Electron and b) hole recombination lifetimes of $CuIn_{1-x}Ga_xSe_2$ for the two important recombination mechanisms (SRH and radiative [97]), as Auger has not been reported in the literature. The SRH lifetime is constant, similar to the mobility, due to a lack of available information in the literature.

3.5.2. Material System-Specific Solar Cell Designs

Armed with these material parameters, one can simulate the EQE and *J-V* characteristics for each of the material systems for a specific design. The designs of each solar cell are given in Tables 3-5 to 3-8 based on designs reported in the literature for Si [98], GaInP [99], Ge [100] and $CuIn_{0.2}Ga_{0.8}Se_2$ [101] solar cells. The latter material system, however, is different than the aforementioned III-V and IV semiconductor systems. This material is typically grown in its polycrystalline structure with a CdS emitter and a ZnO transparent conductive oxide (see Table 3-8). The bandgap of this I-III-VI ternary alloy can also be modified through the substitution of In with Ga, which gives the quaternary alloy $Cu(In_{1-x}Ga_x)Se_2$; in this case, the bandgap as $E_g(x) = 1.01 + 0.626x - 0.167x^2$ [102] at room temperature. The ability to control the bandgap of the solar cell material with a few assumptions on material parameters allows for a simple case study to compare Sentaurus simulation results to those using detailed balance limits of ideal solar cell (see section 3.5.4).

Table 3-5. Structural details of simulated Si solar cell with ARC and a front surface field, based on [98].

Layer	Material	Thickness (μm)	Doping (cm^{-3})
ARC	Si_3N_4	0.08	-
n-emitter	Si:B	0.15	1×10^{17}
p-base	Si:P	250	2×10^{16}
p-BSF	Si:P	3	1×10^{19}

Table 3-6. Structural details of simulated GaInP solar cell with ARC and front and back surface fields, based on [99].

Layer	Material	Thickness (μm)	Doping (cm^{-3})
ARC	Si_3N_4	0.05	-
n-cap	GaAs:Si	0.2	1×10^{19}
n-FSF	$Al_{0.51}In_{0.49}P$:Si	0.03	1×10^{19}
n-emitter	$Ga_{0.51}In_{0.49}P$:Si	0.08	1×10^{17}
p-base	$Ga_{0.51}In_{0.49}P$:Be	1.5	1×10^{17}
p-BSF	$Al_{0.51}In_{0.49}P$:Be	0.03	1×10^{19}

Table 3-7. Structural details of simulated Ge solar cell with ARC and a front surface field, based on [100].

Layer	Material	Thickness (μm)	Doping (cm^{-3})
ARC	Si_3N_4	0.06	-
n-cap	GaAs:Si	0.2	1×10^{19}
n-FSF	$Ga_{0.51}In_{0.49}P$: Si	0.25	1×10^{19}
n-emitter	Ge:As	0.06	1×10^{17}
p-base	Ge:Ga	160	1×10^{17}

Table 3-8. Structural details of simulated $CuIn_{0.2}Ga_{0.8}Se_2$ solar cell with ARC and front surface field, based on [101].

Layer	Material	Thickness (μm)	Doping (cm^{-3})
TCO/ARC	ZnO:Al	0.06	-
TCO/FSF	*i*-ZnO	0.2	1×10^{19}
n-emitter	CdS	0.1	1×10^{17}
p-base	$CuIn_{0.2}Ga_{0.8}Se_2$	3.5	1×10^{17}

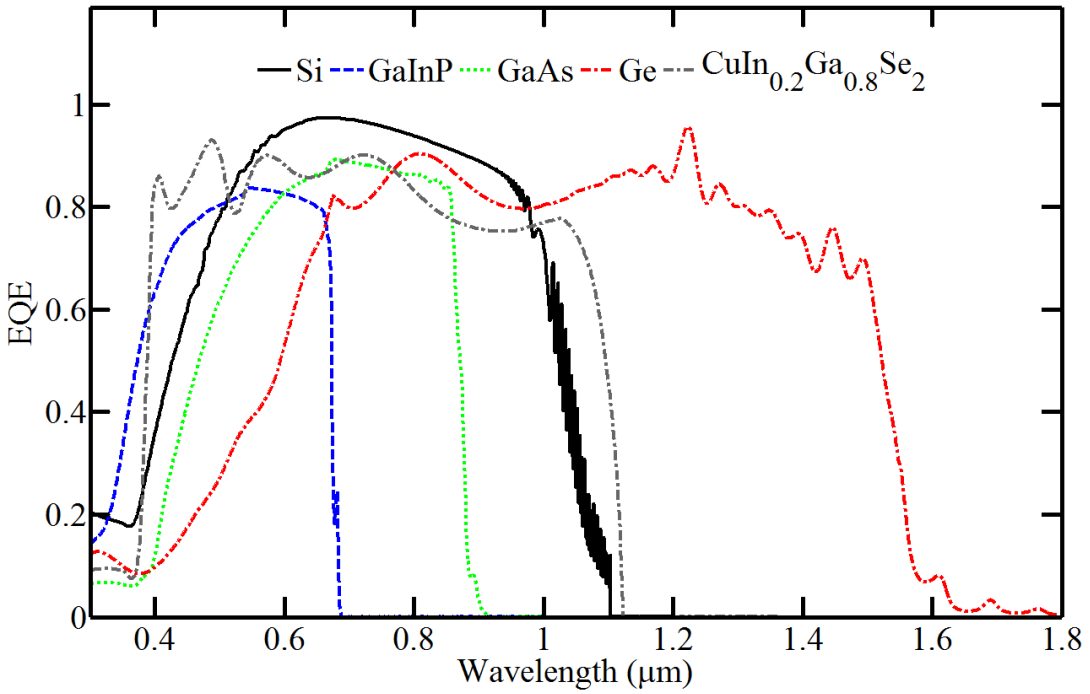

Figure 3-32. Simulated EQE for the solar cells composed of Si, GaInP, GaAs, Ge and Cu(In,Ga)Se_2 according to the designs outlined in tables 3-5, 3-6, 3-3, 3-7 and 3-8 respectively. The Ge EQE extends to 1.8 microns, whereas the Cu(In,Ga)Se_2 extends to 1.1 microns.

3.5.3. Solar Cell Simulation Results

Figure 3-32 illustrates the simulated EQE profiles of the solar cells for the Si, GaInP, GaAs, Ge and Cu(In,Ga)Se_2 material systems according to the designs given in Tables 3-5, 3-6, 3-3, 3-7 and 3-8 respectively. Each of these terminate close to the wavelength corresponding to the bandgap of its constituent material, similar to the absorption coefficients (see Fig. 2-12 in chapter 2). The silicon solar cell EQE demonstrates strong etalon effects beyond 1 μm. According to equation (3.3.3), a larger overlap between non-zero EQE and photon flux results in a larger J_{sc}. Since the range of non-zero EQE is largest for the smallest bandgap, one would expect a anti-correlation between J_{sc} and E_g. This is confirmed in the simulated *J-V* characteristics, which are displayed in Fig. 3-33, as well as Fig. 3-34a which shows the plot of J_{sc} vs. E_g. The corresponding *J-V* metrics are summarized in Table 3-9 for each solar cell design. Figure 3-34b shows the expected

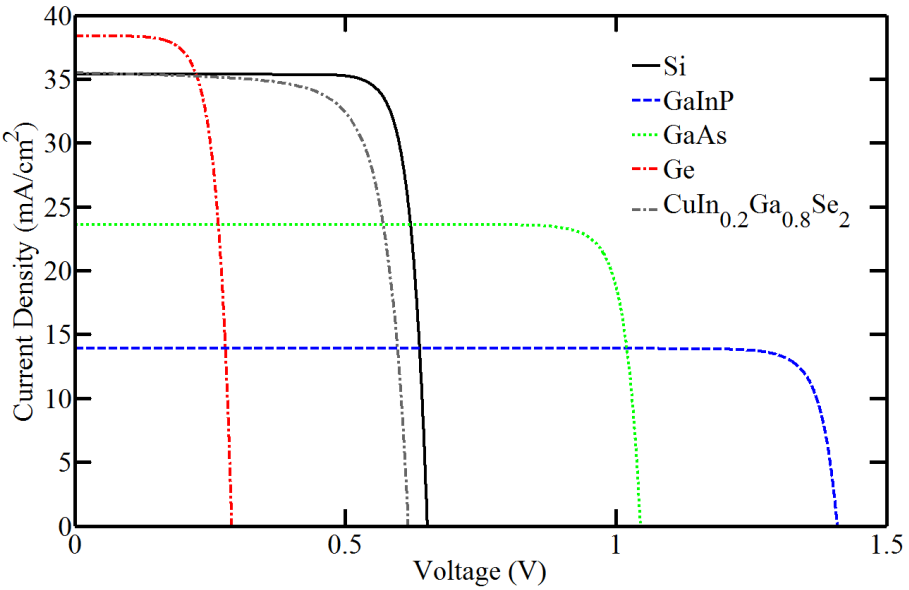

Figure 3-33. Simulated *J-V* characteristics for the solar cells composed of Si, GaInP, GaAs, Ge and $CuInSe_2$ according to the designs outlined in tables 3-5, 3-6, 3-3, 3-7 and 3-8 respectively.

positive correlation between E_g and V_{oc}. Note that the EQE and *J-V* metrics are not optimized for each solar cell structure. The goal of the exercise is to compare various solar cell material systems in order to appreciate a new comparison: ideal versus real solar cell efficiencies.

Table 3-9. Simulated *J-V* metrics of the Si, GaInP, GaAs, Ge and $Cu(In,Ga)Se_2$ solar cells, including the bandgap of these materials. Performances compared to world records (WRs).

Solar cell	E_g (eV)	J_{sc} (mA/cm^2)	V_{oc} (V)	FF (%)	η (%)
Si	1.13 [93]	35.4	0.652	83.2	19.2
WR [3]	*1.13*	*42.7*	*0.706*	*82.8*	*25.0*
GaInP	1.85 [99]	13.9	1.41	89.0	17.4
Ref [97]	*1.88*	*10.1*	*1.4*	*Not reported*	*Not reported*
Ge	0.66 [93]	38.4	0.290	71.6	7.98
Ref [98]	*0.66*	*45.8*	*0.245*	*59.6*	*6.7*
$CuIn_{0.2}Ga_{0.8}Se_2$	1.13 [102]	35.5	0.616	74.3	16.3
WR [3]	*Not reported*	*35.9*	*0.714*	*78.1*	*20.0*

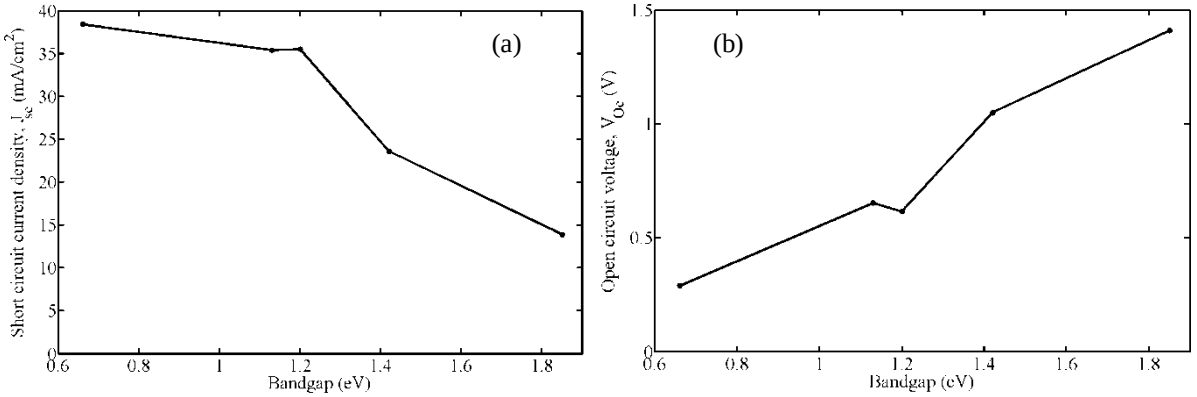

Figure 3-34. a) Plot of J_{sc} as a function of E_g, and b) V_{oc} as a function of E_g based on the simulations shown in Fig. 3-33.

3.5.4. Ideal Solar Cell Behaviour – The Shockley limit

Shockley and Queisser were the first to consider the inherent limitations of a simple *n-p* junction behaving as a solar cell in 1961 [103]. Their paper adopts the detailed balance principle, which is summarized concisely as follows. First, photons of energy greater than the bandgap are absorbed with a quantum efficiency of 1, and therefore sub-bandgap photons are completely transmitted). Second, the recombination current is dictated strictly according to radiative processes, and is the only consideration in the single diode characteristics of the solar cell. And third, carrier mobilities approach infinity for maximum diffusion lengths, which is a manifestation of QE=1 in equation (1.3.3). Equation (1.3.1) can be used to determine the overall efficiency of the solar cell. The consideration that radiative recombination is the only recombination process considered is a manifestation of the second law of thermodynamics. It implies the solar cell acts as a miniature blackbody radiator at room temperature to return to thermal equilibrium through the radiative emission of photons. Under this assumption, radiative recombination dictates the magnitude of the saturation current of the solar cell, and is computed as

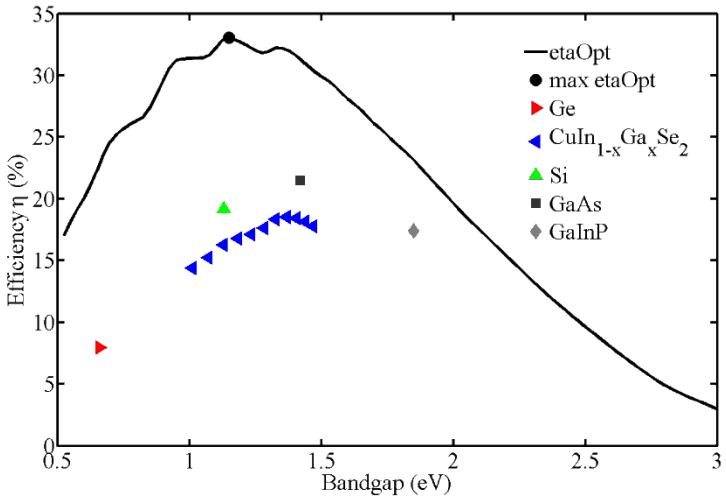

Figure 3-35. Theoretical efficiency of a solar cell as a function of its semiconductor bandgap according to detailed balance arguments (using the software *etaOpt* (Fraunhofer, Freiburg, Germany) [104]); the maximum efficiency is 33.0%. The wiggles correspond to dips in the standard AM1.5D spectrum. The simulated efficiencies of the solar cells composed of Ge, Si, $CuInGaSe_2$, GaAs and GaInP are shown for comparison. This figure was obtained using a revised version of the *etaOpt* program publicly available through the Fraunhofer website.

$$J_{rad} = \frac{2\pi q}{h^3 c^2}\left(n_o^2 - n_u^2\right)\int_{E_g}^{\infty} \frac{E^2}{\exp\left(\frac{E-qV}{kT}\right)-1}\,dE, \tag{3.4.18}$$

where n_o and n_u represent the refractive indices above and below the cell (default to 1 and 0 for air and a perfectly reflective back contact), E_g is the bandgap of the material, V is the applied voltage, and E is the energy of the emitted photons by the blackbody radiator as it is returning to thermal equilibrium.

The central idea explored by Shockley and Queisser is an optimization problem on solar cell efficiency based on one critical parameter: the energy bandgap of the semiconductor material composing the diode. The arguments and results contributed by Shockley and Queisser have been referenced enormously in the literature and established a foundation in photovoltaic theory. Figure 3-35 shows a reconstruction of their work: the ideal solar cell efficiency as a function of semiconductor bandgap using the AM1.5D spectrum normalized to 1000 W/cm^2. These results are super-imposed with the results of the

previous section on simulations of single junction solar cells for various materials. The Shockley-Queisser limit is observed to occur at a maximum of 33.0% for a semiconductor bandgap close to 1.15 eV; the closest real material to this bandgap is silicon. The simulated efficiencies (using Sentaurus), although not optimized, represent the various losses that are typical of real solar cell materials, such as SRH, reflection losses and a non-unity EQE. The detailed balance perspective does not consider these non-ideal loss mechanisms which typically arise from imperfections in the growth of the material as well as fabrication of the solar cell. It is important to note that these results do not consider concentrated illumination incident on the solar cell and are solely representative of single junction solar cell performance at room temperature.

Chapter 4: Multi-Junction Solar Cells

As mentioned in chapter 1, only a few material systems exist which have been shown to successfully illustrate the concept of a multi-junction solar cell (MJSC) for space applications, and recently, for terrestrial applications in concentrator photovoltaic (CPV) systems. In this chapter, the modeling and simulation of lattice matched MJSC composed of InGaP/InGaAs/Ge is explored by first describing the motivation of MJSC in the context of CPV, and then introducing the fundamental physical concepts required for the functionality of these devices, namely the degenerately doped *p-n* junctions called tunnel junctions which are used to connect the constituent sub-cells together, as discussed in section 4.2.1. Section 4.2.2 then discusses the simulation of the individual sub-cells comprising the MJSC. The external quantum efficiency is simulated in section 4.2.3 before progressing toward broadband anti-reflection coatings and full device simulations in 4.2.3 and 4.2.4 respectively. As partial validation of the models, a comparison between simulated and reported performances in the literature is also included. In section 4.3, the benefits and limitations of concentrated illumination for terrestrial MJSC applications are explored in terms of *J-V* metrics for the former, and series resistance, temperature and tunnel junction limitations for the latter.

4.1. Motivation and Concepts of Concentrated Photovoltaics

The motivation for the development of MJSC or tandem cells for application in concentrated photovoltaics is based on efforts to avoid the fundamental losses of single

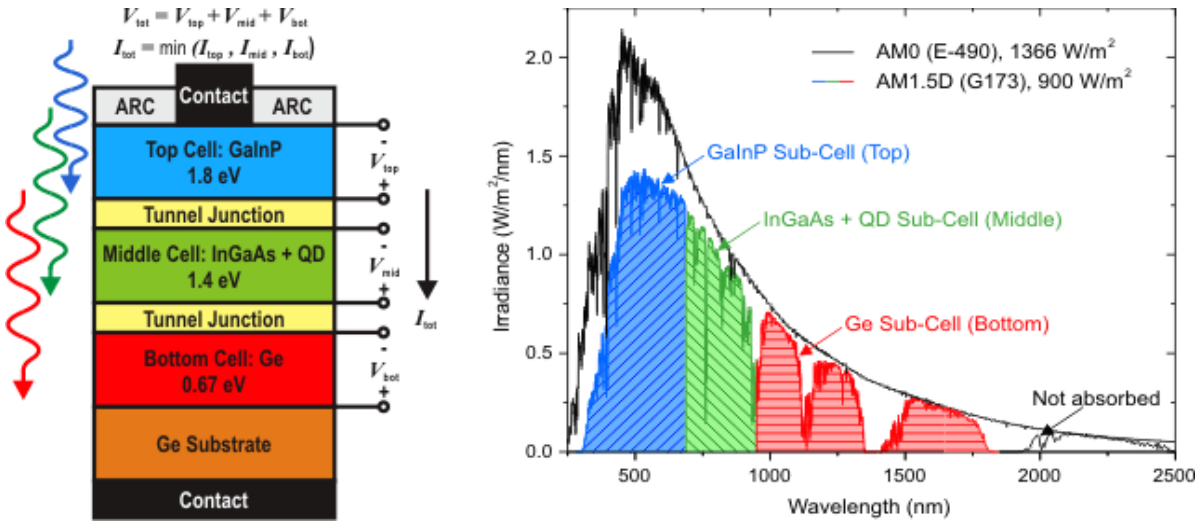

Figure 4-1. Lattice matched multi-junction solar cell design composed of GaInP/InGaAs/Ge combined with the standard illumination spectrum to outline the photon energies absorbed by each sub-cell [retrived from http://sunlab.site.uottawa.ca/ on July 31st, 2012; Courtsey of Christopher Valdivia].

junction solar cells, which consist primarily of thermalization and sub-bandgap losses. The former is due to the absorption of photon energies greater than the bandgap, whereby excited electrons scatter with phonons and subsequently relax to the lowest energy level of the conduction band (a process on the order of femto-seconds). The latter is due to the transparency of the semiconductor to photon energies below the bandgap, resulting in photons not being utilized at all. The concept of tandem cells is relatively straightforward in principle: the design features a high bandgap semiconductor *p-n* junction stacked on top of a lower bandgap semiconductor junction. In such a configuration, high energy photons are absorbed by the top junction (or sub-cell), whereas lower energy photons are transmitted through the top sub-cell and into the lower sub-cell. A third sub-cell is typically added based on the same principle to make a triple junction solar cell. An example of such a configuration is outlined in Fig. 4-1 for the standard GaInP/InGaAs/Ge triple junction solar cell; the separation of the incident spectrum to each sub-cell is also outlined in parallel. This type of tandem cell specifically consists of monolithically stacked series connected *p-n*

junctions that are epitaxially grown in a lattice matched configuration to minimize the formation of undesirable dislocations and other defects. Since these are connected in series, the photocurrent of the full device is limited by the sub-cell which generates the least current. Furthermore, the open circuit voltage of the device is approximately given by the sum of each sub-cell's open circuit voltage.

Two notions immediately become apparent for the design of such tandem devices with respect to the interconnection of sub-cells. The first is that these interconnections must be optically transparent to photon energies intended for lower sub-cells. The second is that these must be minimally resistive to large current densities. This second notion is even more important for design considerations in CPV applications, where the photocurrent scales linearly with the concentration of sunlight [105]. For example, a concentrator optic of geometric area 1000× the cell area will illuminate this cell with 100 W/cm^2. This requires the interconnection between sub-cells to conduct extremely high current densities on the order of 14 A/cm^2 [3],[20]. Tunnel junctions (TJ) are structures capable of satisfying these requirements when composed of high bandgap materials such as $Al_xGa_{1-x}As$ or $Ga_{0.51}In_{0.49}P$ which are lattice matched to Ge. These TJ are degenerately doped semiconductor *p-n* junctions that exploit the quantum mechanical phenomenon of tunneling [35], a topic discussed in more detail in section 4.2.1. For the moment, it is assumed that the TJ are ideal components of MJSC devices.

The concepts for multi-junction solar cells originate mainly from research and development for space applications such as powering satellites, since these types of devices are highly efficient in comparison to single junction devices. A drawback of MJSC devices is the high cost of the composing materials due to the combination of growth on germanium

substrates (for lattice matched devices) and the requirement of high crystal quality typically obtained through sophisticated epitaxial growth techniques such as molecular beam epitaxy (MBE), chemical beam epitaxy, metal-organic chemical vapour deposition (MOCVD) which is similar to metal oxide vapour phase epitaxy (MOVPE); atomic layer deposition is another technique primarily used in the microelectronics industry and not typically in PV. The high costs associated with these high efficiency devices were offset by their high energy density capacity for space applications. It was only recently that concentrators enabled the reduction of overall material volume that MJSC became a cost-effective approach for terrestrial energy production. One of the earliest reported publications on tandem devices originates from work by Jerry Olson and colleagues at the Solar Energy Research Institute, who reported a 27.3% efficient $Ga_{0.51}In_{0.49}P/In_{0.01}Ga_{0.99}As$ tandem solar cell under the standard AM1.5 spectrum [106]. This efficiency was a record at the time of its publication in 1990, and close to the theoretical maximum of 33% according to theoretical arguments with no concentration considered [106]. The progression of dual junction solar cells has progressed significantly since then, with the current world record efficiency closer to 30.3% under one sun illumination [107]. Under concentration, however, the current world record belongs to the Instituto de Energia Solar at the Universidad Politecnica de Madrid (IES-UPM), achieving an efficiency of 32.6% under 1026 suns (see the NREL PV technology roadmap illustrated in Fig. 1-2). A noteworthy point to make here regarding the importance of tunnel junctions in the advancement of dual junction solar cells regards a publication by Mingju Yang and his colleagues at the Toyota Technological Institute in Japan on investigating high efficiency InGaP/GaAs tandem solar cells under concentration [108]. The research group reported the efficiency as a function of concentration, which peaked at 31.2%

under 5.1 suns of AM1.5D, only to decrease sharply toward 25% at close to 7 suns illumination. The blame lies on the poor performance of their tunnel junction, which drastically reduced the fill factor of the cell.

The addition of a third cell to the aforementioned dual junction solar cell was the next step in obtaining higher power conversion efficiencies. In principle, the third junction targets wavelengths below the bandgap of the middle cell (~880 nm at room temperature for InGaAs), which would essentially add to the voltage output of the cell. According to Fig. 2-13, the most obvious lattice matched material candidate for the third sub-cell is germanium, with a bandgap of 0.67 eV. However, the photocurrent available between 880 nm and ~1800 nm (the bandgap of Ge) is quite large in comparison to the photocurrent available to the top two sub-cells, resulting in a significant current mismatch between sub-cells. The wasted current generates heat which deteriorates the performance of the PV device. Irrespective of this, the highest efficiencies reported in the literature correspond to the state-of-the-art research grade MJSC, such as the (now) standard MJSC composed of GaInP/InGaAs/Ge, where the middle sub-cell is composed of $In_{0.01}Ga_{0.99}As$ to be perfectly lattice matched to Ge. The current world record for such a device is 34.1% under one sun illumination according to AM1.5G spectrum with a J_{sc} of 14.7 mA/cm^2, a V_{oc} of 2.691 V and a fill factor of 86% [109]. This device has achieved even higher efficiencies under concentration, for example, 41.6% under 364 suns [109].

4.1.1. Detailed Balance Predictions

In order to achieve higher efficiencies for MJSC, different bandgap combinations must be considered in combination with improvements in epitaxial growth methods. Detailed balance arguments are very useful in predicting ideal efficiencies and giving

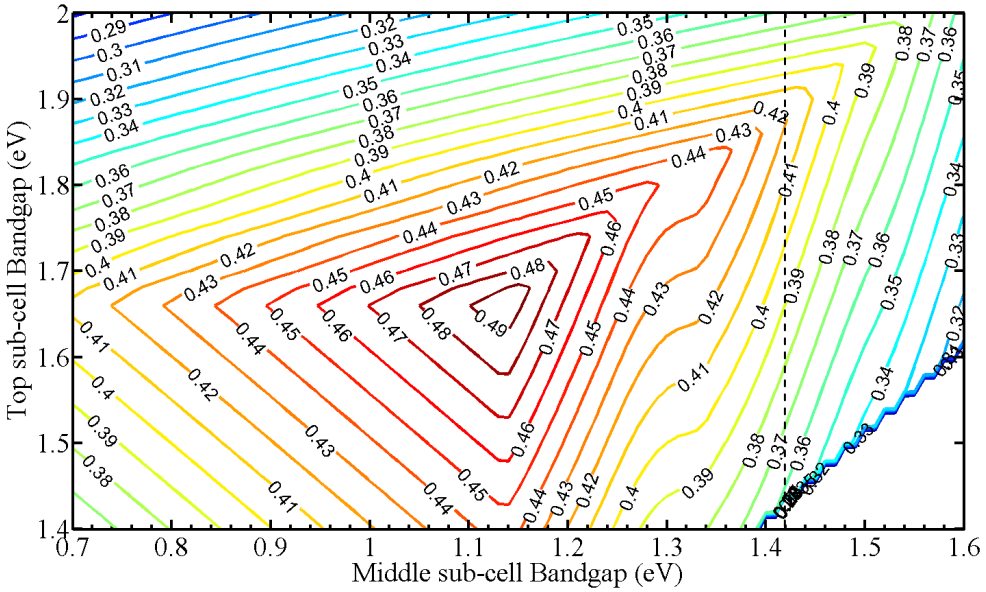

Figure 4-2. Ideal power-conversion efficiency contour plots of 3JSC under 1 sun concentration predicted by detailed balance for a fixed bottom sub-cell bandgap of 0.67 eV representative of Ge and varying the top and middle sub-cell bandgaps, where the vertical dashed line corresponds to the bandgap of InGaAs with 1% Indium.

experimentalists' direction for what material combinations could potentially achieve the next MJSC record efficiency. This argument is based on the detailed balance principle for each sub-cell of a MJSC using software called *etaOpt* [104] as introduced in section 3.5.4, in combination with the equivalent circuit perspective of series connected sub-cells (see Fig. 4-10). Two new assumptions are added to those discussed in section 3.5.4, and are outlined as follows: 1) sub-cells are connected in series through transparent non-resistive ohmic contacts, and 2) the current matching is performed by varying the transparency of the proper sub-cells (i.e. optimizing the thickness). Each sub-cell has a corresponding *J-V* characteristic based on its absorbed photon flux, which is added in series with the other interconnected sub-cells to produce an *J-V* characteristic of the full device that ultimately leads to a power conversion efficiency.

Figure 4-2 outlines the ideal contour efficiency plot of a triple junction solar cell whereby the third sub-cell bandgap is fixed to 0.67 eV to represent a sub-cell designed on a

germanium substrate, with the top sub-cell bandgap limited to values between 1.4 and 2.0 eV. Note that the possible bandgaps of $Ga_{0.51}In_{0.49}P$ ranges between 1.8 and 1.9 eV based on the ordering of InP and GaP lattice planes within the structure [99]. The bandgap can be increased to 2.1 eV based on the incorporation of Al to form the quaternary semiconductor alloy $(Al_xGa_{1-x})_{0.51}In_{0.49}P$ depending on the Al to Ga molar fraction ratio [110]. Furthermore, the middle sub-cell bandgap is varied between 1.90 and 1.42 eV based on the ternary alloy $Al_xGa_{1-x}As$ that is lattice matched to Ge (see lattice constant vs. energy band gap in Fig. 2-11). The resulting optimal combination is given as: 1.66/1.13/0.67 eV with an efficiency of 49.6% at one sun illumination and room temperature, with a J_{sc} of 21.1 mA/cm^2, a V_{oc} of 2.68 V and a fill factor of 87.2%. This bandgap combination, however, cannot be realized by lattice matched materials to Ge. Figure 4-2 also outlines the possible efficiencies for the $(AlGa)_{0.51}In_{0.49}P/In_{0.01}Ga_{0.99}As/Ge$ MJSC for the middle sub-cell bandgap at 1.42 eV (represented as a vertical dashed line), which approaches 42% for a top sub-cell bandgap close to 1.87 eV.

Alternatively, Fig. 4-3 investigates a different approach whereby the middle sub-cell has fixed bandgap of 1.42 eV, since III-V semiconductor based MJSC are typically designed with respect to GaAs. The same assumptions as above are adopted for the top sub-cell, which is hypothetically composed of a derivative of $AlGa_{0.51}In_{0.49}P$. The bottom sub-cell, however, has the complete freedom with respect to the bandgap based on the ternary lattice mismatched alloy of $In_xGa_{1-x}As$. The optimal bandgap combination in this case is 1.88/1.42/1.04 eV with an efficiency of 47.2%, a J_{sc} of 15.0 mA/cm^2, a V_{oc} of 3.50 V and a fill factor of 89.6% at one sun illumination and at room temperature. This material system can be realized using the ternary lattice mismatched material $In_xGa_{1-x}As$, which has the

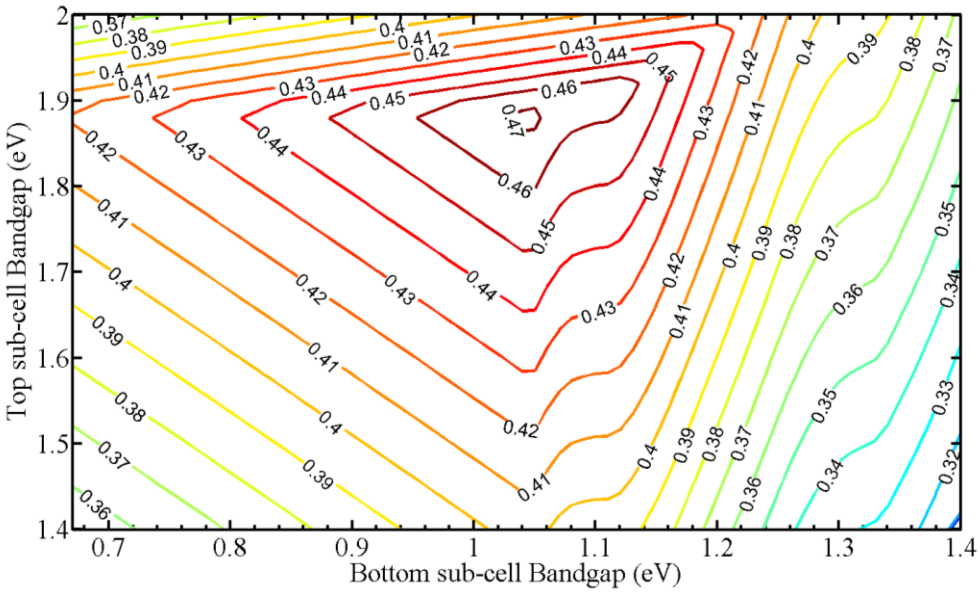

Figure 4-3. Ideal power-conversion contour plots of 3JSC under 1 sun concentration predicted by detailed balance for a fixed middle sub-cell of 1.424 eV representative of GaAs and varying the top and bottom sub-cell bandgaps.

appropriate bandgap for a molar fraction of x=0.28 and a lattice mismatch of 2.8%. One can also perform similar studies focusing on 4JSC, fixing the bottom Ge sub-cell bandgap to 0.67 eV and the second sub-cell to 1.42 eV (representative of $In_{0.01}Ga_{0.99}As$). However, these types of studies are not part of the focus of this thesis.

Although multi-junction solar cells are primarily composed of III-V semiconductors, alternative material systems based on amorphous silicon (a-Si) and nanocrystalline Si (nc-Si) are also studied as candidates for third generation photovoltaic cells. The advantage in these Si-based designs lies primarily in their reduced growth and manufacturing costs. A thin film triple junction solar cell comprising of a-Si/nc-Si/nc-Si has been demonstrated in the literature [111] by United Solar with an efficiency of 12.4% under STC, resulting in a J_{sc} of 8.96 mA/cm^2, a V_{oc} of 1.936 V and a fill factor of 71.5%. Tandem devices are thus key in advancing PV devices beyond the Shockley-Queisser limit of single junction devices, and are the mainstream avenue for pursuing the next generation of PV devices.

4.2. Simulations of III-V based Multi-Junction Solar Cells

The simulation of lattice matched MJSC composed of III-V semiconductors targets three steps: 1) simulating the behaviour of the tunnel junctions, 2) simulating the sub-cell *J-V* characteristics for current matching under STC, the external quantum efficiency of the device, and designing and implementing broadband anti-reflection coatings and gridlines, and lastly 3) simulating the full device *J-V* and *P-V* characteristics also under STC. These are the topics of the next few sections, which are discussed with a focus on performing these types of simulations using TCAD Sentaurus.

4.2.1. Tunnel Junctions

4.2.1.1. Qualitative Description

The concept of carriers tunneling across a potential barrier was introduced in section 2.3.4. For the purpose of simulating tunnel junctions (degenerately doped *n-p* junctions), however, a more physically rigorous approach is required which makes use of energy band theory to consider the elastic spatial transport of carriers across interfaces as a recombination process. The spatial component is typically labelled as a nonlocal tunneling process since carriers tunnel from one location to another (hence nonlocal), whereas tunneling between bands at the same physical location is considered local tunneling (see Fig. 3 of [22]). For tunnel junction applications within multi-junction solar cells, it is the nonlocal band-to-band tunneling current that is relevant, i.e. the tunneling of electrons from the conduction band of one side of the tunnel junction to the valence band of the other side (or a hole from the valence band of one side tunneling into the conduction band of the other side). To gain a qualitative understanding of how this occurs at the interface of degenerately doped *n-p*

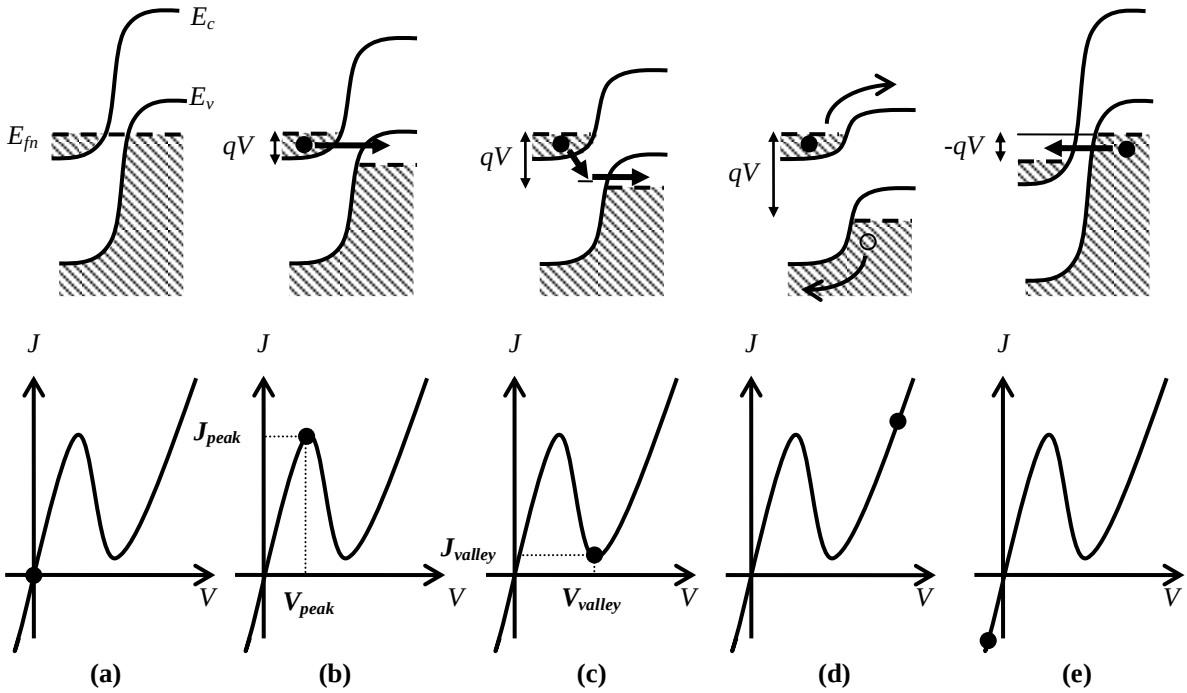

Figure 4-4. Schematic energy band alignment of a tunnel junction at a) thermal equilibrium, b) forward bias operating at the peak tunneling current, c) forward bias near the valley peak due to trap assisted tunneling, d) forward bias due to diffusion current resulting from thermionic emission of carriers, and e) reverse bias with increasing overlap between filled and available electronic states which results in large current densities tunneling through the tunnel diode (After Ref. [35]).

junctions as a function of applied bias, see Fig. 4-4.

At thermal equilibrium, no carriers can tunnel through the potential barrier since no occupied states exist on the degenerately doped *n*-side at an energy level where unoccupied states are available on the degenerately doped *p*-side. As a result, ideally no current flows through the device under zero applied bias, as seen in Fig. 4-4a. Upon the application of a forward bias, however, the bands on the *n*-side are shifted up by an amount equivalent to *qV*, resulting in current flowing through the tunnel junction due to the availability of unoccupied states on the *p*-side at the same energy as occupied states on the *n*-side. One can visualize the optimal region whereby bands with occupied states on the *n*-side and unoccupied states on the *p*-side are properly aligned. The applied bias which maximizes the overlap between these bands corresponds to the peak tunneling voltage V_{peak}; this leads to a peak current

tunneling density J_{peak} as seen in Fig. 4-4b. It is important to note that band to band tunneling (B2B) is maximized for carriers tunneling at a constant energy.

Increasing the forward bias further results in a region where the aforementioned bands do not overlap as seen in the energy band diagram of Fig. 4-4c. The tunneling between bands therefore reaches a minimum in terms of tunneling current, which is called the valley current or J_{valley} occurring at a valley voltage or V_{valley}, as seen in the current – voltage characteristics of Fig. 4-4c. A non-zero tunneling current flows at this bias due to the trap states existing within the forbidden bandgap which assist in carrier tunneling via phonon scattering [112], a formalism referred to as nonlocal trap-assisted tunneling (TAT). Figure 4-5 illustrates these differences as well as local tunneling. One can then see the resemblance of the local TAT process with the more familiar standard SRH process. The essential difference between the local TAT and SRH recombination is the effect of the strong electric field present in the TJ in the local TAT mechanism, which reduces the SRH recombination lifetime through the relation

$$\tau_{SRH,tunnel}(F) = \frac{\tau_{SRH}}{1+g(F)} \tag{4.3.1}$$

where F is the electric field and $g(F)$ is the field enhancement factor. This latter function can be computed through the Schenk formalism [113] or the Hurkx formalism [114]. However, neither of these two models are considered further since these do not properly explain any reasonable features of a tunnel junction, as reported by Hermle *et al*. [22]. This was also verified by the author using Sentaurus.

The final component of the forward biased tunnel junction *J-V* characteristic is the diffusion current which occurs in any forward biased diode. At high voltages, the carriers on the *n*-side can overcome the potential barrier at the junction due to thermal excitation since

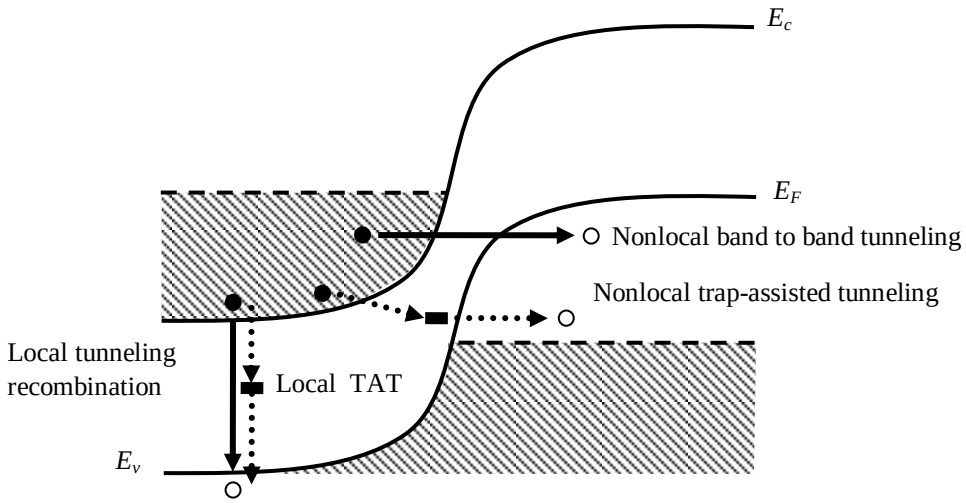

Figure 4-5. Schematic illustrating the differences between band to band tunneling (B2B) and trap-assisted tunneling (TAT) in a nonlocal framework, and the local tunneling recombination and local TAT.

the potential barrier is reduced, as seen in Fig. 4-4d. This results in very high current densities through the device. In the reverse bias regime of the tunnel junction, the band alignment continues to overlap as a function of voltage, which leads to an exponentially increasing tunneling current as seen in Fig. 4-4e. In order to reproduce the above qualitative descriptions of tunnel junctions, it is imperative that appropriate nonlocal tunneling models are adopted.

4.2.1.2. Nonlocal Tunneling Models

The nonlocality of the tunneling models is crucial to the accuracy of the simulated characteristics of the tunnel junctions, and is discussed below.

4.2.1.2.1. Band-to-Band Tunneling

The interband tunneling probability is based on an improved model of Ieong *et al.*'s work [115]. This model adopts the Wentzel-Kramers-Brillouin (WKB) approximation to compute the local wave numbers of carriers involved in the tunneling from a position r and energy ε as

$$\kappa_c(r,\varepsilon) = \sqrt{2m_c|E_c(r)-\varepsilon|}\ \Theta(E_c(r)-\varepsilon)/\hbar\ , \tag{4.3.2}$$

$$\kappa_v(r,\varepsilon) = \sqrt{2m_v|\varepsilon-E_v(r)|}\ \Theta(\varepsilon-E_v(r))/\hbar\ , \tag{4.3.3}$$

where m_c and m_v are the conduction band and valence band tunneling masses of the carriers involved in tunneling respectively, E_c and E_v are the conduction and valence band energies at a position r, and $\Theta(x)$ is the Heaviside function. This latter aspect of the equation ensures that the wave number is non-zero only when the potential energy of the carrier, ε, is below the conduction band and therefore within the forbidden bandgap of the tunnel junction. The tunneling mass is essentially a fitting parameter which scales the peak tunneling current of the TJ. Since the carriers start in the conduction band of the n++ material and tunnel through the bandgap into the valence band of the p++ material (and vice versa), a two band dispersion relation is used to compute the wave numbers of the carriers since the single band dispersion relation best represents the band structure at the edges of the conduction and valence bands. Within this framework, the wave numbers are both given by

$$\kappa = \frac{\kappa_c\kappa_v}{\sqrt{{\kappa_c}^2+{\kappa_v}^2}}\quad . \tag{4.3.4}$$

The wave number given by equation (4.3.4) then enters the calculation of the interband tunneling probability Γ_{cv} of a carrier at position l in the conduction band tunneling to position $u>l$ in the valence band given as

$$\Gamma_{cv}(u,l,\varepsilon) = T_{cv}(l,\varepsilon)\exp\left[-2\int_l^u \kappa(r,\varepsilon)dr\right]T_{cv}(u,\varepsilon). \tag{4.3.5}$$

Vice versa, the interband tunneling probability Γ_{vc} of a carrier at position l in the valence band tunneling to position $u>l$ in the conduction band

$$\Gamma_{vc}(u,l,\varepsilon) = T_{vc}(l,\varepsilon)\exp\left[-2\int_l^u \kappa(r,\varepsilon)dr\right]T_{vc}(u,\varepsilon), \tag{4.3.6}$$

where T_{cv} and T_{vc} are interface transmission coefficients that default to one. On the other hand, these can be computed using carrier velocities on either side of the tunneling interface using the relation [116]

$$T_{cv}(x,\varepsilon) = \frac{v_{-}(x,\varepsilon)\sqrt{v_{-}(x,\varepsilon)^2+16v_{+}(x,\varepsilon)^2}}{v_{+}(x,\varepsilon)^2+v_{-}(x,\varepsilon)^2}, \tag{4.3.7}$$

where $v_{-}(x,\varepsilon)$ is the velocity of the carrier at energy ε and position x on the side of the interface where the particle is moving freely in the conduction band, and $v_{+}(x,\varepsilon)$ is the velocity on the side of the tunneling barrier. These velocities are computed using the relation $v = \delta\varepsilon/\delta\hbar\kappa$ [117]. Based on the two band dispersion relation, the tunneling probabilities are the same, or $\Gamma_{cv}= \Gamma_{vc}$. It is important to note that references [114],[115],[116],[117] are based on calibrated models based on polycrystalline silicon-gate-metal-oxide semiconductor interfaces that are important for functional MOSFETs. It is assumed that these models are accurate within the framework of tunnel junctions.

The net recombination rate, given by the difference between the recombination rate of valence band electrons with energy ε at position u due to tunneling to the conduction band at point l (which is equivalent to the generation of holes at point u) and generation of electrons at point u due to tunneling from the conduction band at point l (or recombination of holes at point l), is then given as

$$R_{cv}(u,l,\varepsilon) - G_{cv}(u,l,\varepsilon) =$$

$$\frac{A_{cv}}{2qk_B}\vartheta\left[\varepsilon - E_v(u), \frac{dE_v}{du}(u)\right]\vartheta\left[\varepsilon - E_c(l), \frac{dE_c}{dl}(l)\right]\Gamma_{cv}(u,l,\varepsilon)\times$$

$$\left[T_p(u)+T_n(l)\right]\left[\left(1+\exp\left[\frac{\varepsilon-E_{F,p}(u)}{kT_p(u)}\right]\right)^{-1} - \left(1+\exp\left[\frac{\varepsilon-E_{F,n}(l)}{kT_n(l)}\right]\right)^{-1}\right], \tag{4.3.8}$$

where A_{cv} is the effective Richardson constant given by $A_{cv} = \sqrt{g_c g_v}A_o$ where g_c and g_v are scaling parameters and A_o is the Richardson constant for free electrons, T_n and T_p are

electron and hole temperatures, and $E_{F,n}$ and $E_{F,p}$ are the electron and hole quasi-Fermi levels respectively. The function ϑ is given by $\vartheta(x,y) = \delta(x)|y|\Theta(y)$ computes the shape of the potential barriers using the derivatives of the conduction and valence bands if and only if the carrier energy is equal to the valence band edge at position u with a positive gradient in the valence band, and the carrier has energy equal to the conduction band edge band at point l for a positive gradient in the conduction band. The reverse processes, or $R_{vc}(u,l,\varepsilon) - G_{vc}(u,l,\varepsilon)$, are analogous. The resulting current density through the tunneling region due to the process of electrons tunneling from points $u>l$ of the valence band to the conduction band at point l is given by

$$j_{cv}(l) = -q \int_l^{\infty} \int_{-\infty}^{\infty} [R_{cv}(r,l,\varepsilon) - G_{cv}(r,l,\varepsilon)]\, d\varepsilon dr. \tag{4.3.9}$$

The equations for the hole tunneling current are analogous.

Note that the simulation of tunnel junctions using the nonlocal band to band tunneling model requires a nonlocal mesh in the *SDevice* engine. This nonlocal mesh is comprised of lines that originate from the interface of the TJ and propagate in both directions away from this interface up to a specific length (typically the length of the degenerate TJ layer). These lines correspond to the tunneling paths of the carriers, and the lengths of these lines comprising the nonlocal mesh correspond to the integration limits of equations (4.3.5)-(4.3.9). Since the integration time is quite sensitive to the length of these lines, it is important to limit these lengths for computational time considerations. Typical execution time of a TJ simulation is on the order of 60 s. The code to activate such a nonlocal mesh is given in Appendix B-7 and is implemented within the Sentaurus Device command file's Math section. Note that this nonlocal mesh is a separate mesh from the full device mesh used to solve the relevant semiconductor equations. The mesh used in modeling the local

tunneling processes is the standard mesh. The total tunneling current and its contributions from electrons and holes can be visualized using the Tecplot (or SVisual) tool by specifying the key words *eBarrierTunneling* and *hBarrierTunneling* in the Plot section of the SDevice command file.

4.2.1.2.2. Trap Assisted Tunneling (TAT)

As mentioned previously, the local trap assisted tunneling models corresponding to Schenk and Hurkx models have been reported to fail in abrupt heterojunctions, primarily due to the strong electric field in combination with band offsets at the hetero-interface. In an effort to accurately simulate the valley current of a tunnel junction using trap assisted tunneling, a dynamic nonlocal model is required which considers the tunneling barrier shape similar to the aforementioned band-to-band model, whilst also considering the energy levels of the traps at different physical locations. Each trap location results in a different tunneling path for carriers, which is a straight path with a direction determined dynamically for each carrier according to the slope of energy band profile. The energies of the tunneling electron before and after are at the conduction level and at the defect (trap) level respectively, where the latter is expressed with respect to the intrinsic level of the semiconductor as

$$E_T(x) = E_{trap}(x) + E_{intrinsic}(x), \tag{4.3.10}$$

where E_{trap} defaults to 0 eV such that the trap level is at the intrinsic level. Furthermore, the formalism must consider that electrons can be emitted from (or captured by) the trap level during the tunneling.

The recombination rate of the nonlocal TAT must be integrated over all positions along a path of length l since electrons can be emitted or captured at any position along the path of the trap-assisted tunneling due to the traps. The net electron recombination according

to the nonlocal TAT at a position x is based on the Schenk [112] and Hurkx [113] formalisms for local TAT take the form

$$R_{net}^{TAT} = C_n \int_0^l \frac{\Gamma_c\big(x, E_c(0)\big)}{\tau_n(x)} \frac{T(0)+T(x)}{2\sqrt{T(0)T(x)}} \times$$

$$\left[\exp\left[\frac{E_{F,n}(0)-E_c(0)}{kT(0)}\right] f^p(x) - \exp\left[\frac{E_{F,p}(0)-E_c(0)}{kT(0)}\right] f^n(x)\right] dx \qquad (4.3.11)$$

where $\tau_n(x)$ represents the electron lifetime at a position x, $T(x)$ represents the temperature at x (assumed to be the same everywhere), $f^n(x)$ and $f^p(x)$ are the electron and hole occupation probabilities at the defect level respectively (based on the equilibrium condition of capture and emission from the traps along the path of integration), and C_n is a term related to the conduction band profile and effective density of states given by

$$C_n = |\nabla E_c(0)| \frac{N_c(0)}{kT(0)} \left[\exp\left[\frac{E_{F,n}(0)-E_c(0)}{kT(0)}\right] + 1\right]^{-\alpha}, \qquad (4.3.12)$$

where $N_c(0)$ is the effective density of states in the conduction band at position x, α=1, and lastly, the function $\Gamma_c(x,\varepsilon)$ is the tunneling probability computed using the WKB approximation and given as

$$\Gamma_c(x,\varepsilon) = W_c(x,\varepsilon)\exp\left(-2\int_0^x \kappa(x,\varepsilon)dr\right) \qquad (4.3.13)$$

where κ is the magnitude of the imaginary wave number based on equation (4.3.4), and $W_c(x,\varepsilon)$ is a weighting factor that is unity for the Hurkx nonlocal TAT model. For the Schenk nonlocal TAT model, it is given by

$$W_c(x,\varepsilon) = \frac{\hbar[E_c(x)-E_c(0)]\exp(0.5)W[\varepsilon-E_T(x)]}{4x[E_c(x)-E_T(0)]\sqrt{\pi m_c kT(x)}W[E_c(x)+kT(x)/2-E_T(x)]}, \qquad (4.3.14)$$

where m_c is the tunneling mass of the electrons, the function $W(\varepsilon)$ is given by

$$\mathrm{W}(\varepsilon) = \frac{1}{\sqrt{\chi}}\exp\left(\frac{\varepsilon}{2kT}+\chi\right)\left(\frac{z}{l+\chi}\right)^l, \qquad (4.3.15)$$

where $\chi = \sqrt{l^2 + z^2}$, $l = \varepsilon/\hbar\omega_o$, $z = S/\sinh(\hbar\omega_o/2kT)$, $\hbar\omega_o$ is the phonon energy and S is the Huang-Rhys constant. Recombination rates for holes are analogous. The Huang-Rhys constant is a factor which describes the coupling between a charged carrier and the longitudinal optical (LO) phonon at a localized state such as a trap. It has been shown experimentally that this coupling constant depends strongly on the type of trap involved in the transition [118] and can therefore be used as a fitting parameter to fit simulation to experiment. The net recombination rate is then integrated over energy to compute the overall current, similar to equation (4.3.9).

4.2.1.3. Simulation of Tunnel Junctions

The simulation of tunnel junctions is nontrivial in many ways due to the difficulties involved in calibrating the tunneling models to experimental data (namely J_{peak} and J_{valley}). Some of these difficulties include the several fitting factors present in the nonlocal tunneling models for both B2B and TAT such as the effective Richardson constants for electrons and holes for the B2B parameter set, the electron and hole B2B tunneling masses, and the electron and hole TAT tunneling masses along with the Huang-Rhys constant (also part of the TAT parameter set). The fitting factors for the B2B parameter set are used to obtain good agreement between the simulated and experimental peak tunneling currents, whereas the fitting factors for the TAT parameter set are used to obtain agreement between the simulated and experimental valley currents. Due to the large number of fitting parameters, the tunneling masses are assumed to be close to the carrier effective masses, even there is no consensus in the literature as to what these tunneling masses should be. For example, Hermle *et al.* use the tunneling masses to investigate their effects on the simulated current density – voltage characteristics [22]. Another difficulty in calibrating the models to

measurement is the unstable negative differential resistance (NDR) region of the tunnel junction *J-V* characteristic which results in nonlinear oscillations in the measurement [20],[21]. These oscillations also hide the peak tunneling current and result in a plateau due to averaging in the NDR. Although adding an appropriately valued shunt resistance can inhibit the oscillations and assist in recovering the full *J-V* characteristics [119], this technique is very sensitive to the overall resistance and is not always successful. Irrespective of these, the essential components of the tunnel junction's *J-V* characteristic can be reproduced based on the nonlocal tunneling models introduced in section 4.2.1.2, albeit using the tunneling masses and effective Richardson constants as fitting parameters to the tunneling peaks.

The initial structure of an III-V semiconductor tunnel junction is based on the $Al_xGa_{1-x}As$/GaAs material system outlined in Table 4-1 for a structure grown by Sherbrooke University. Buffer layers are typically used as adjacent layers to the degenerately doped *n++/p++* layers due to growth considerations and inhibiting outward doping diffusion [120]. The level of doping of the degenerate TJ layers allow for exponentially increasing peak tunneling current densities, as illustrated by a rigorous analytical approach to derive the tunneling peak density, J_{peak} as [35]

$$J_{peak} \propto \exp\left(-\frac{E_g^{3/2}}{\sqrt{N_{eff}}}\right) \tag{4.3.16}$$

where N_{eff} is the effective doping concentration of the tunnel junction given by $N_{eff} = N_a + N_d/N_aN_d$. Equation (4.3.16) implies that the lower the bandgap and the higher the effective doping concentration, the larger the peak tunneling current density. One would therefore expect a GaAs/GaAs based tunnel junction to operate at a higher J_{peak} than an AlGaAs/GaAs tunnel junction; however, the latter design has the advantage of requiring a

lower effective doping concentration to achieve a resistivity less than 10^{-4} $\Omega \cdot cm^2$ for 1 sun and 1500 sun applications [20]. As a result, these are expected to be easier to grow and are therefore the focus of this initial tunnel junction simulation study.

The simulations of the tunnel junction outlined in Table 4-1 are illustrated in Fig. 4-6 where the nonlocal band to band tunneling model tunneling masses are varied in (a) without nonlocal TAT considerations. The nonlocal B2B parameters are optimized to generate a similar J_{peak} to the measured data in (a) based on the experimentally measured *J-V* characteristic of the TJ outline in Table 4-1 with a J_{peak} close to 1500 A/cm^2. Note that the the aforementioned instability in the measurement setup does not allow the resolved measurement of the true experimental J_{peak}. Figure 4-6a shows that a decrease in electron or hole tunneling masses within the nonlocal B2B framework results in an increase in J_{peak}. The tunneling masses (in units of the electron mass) that generate a similar J_{peak} to experiment for GaAs are 0.085 and 0.34 for electrons and holes respectively, and 0.09 and 0.37 for AlGaAs. It is important to note that multiple solutions exist to fit the tunneling peak based on the four tunneling masses available.

Table 4-1. Tunnel junction structure composed of AlGaAs/GaAs based on [121].

Layer	Material	Doping (cm^{-3})	Thickness (μm)
Cap	n-GaAs:C	4×10^{18}	0.250
p++ TJ	p-$Al_{0.3}Ga_{0.7}As$:C	1×10^{20}	0.050
n++ TJ	n-GaAs:Te	2×10^{19}	0.050
n+ buffer	n-GaAs:Te	4×10^{18}	0.750

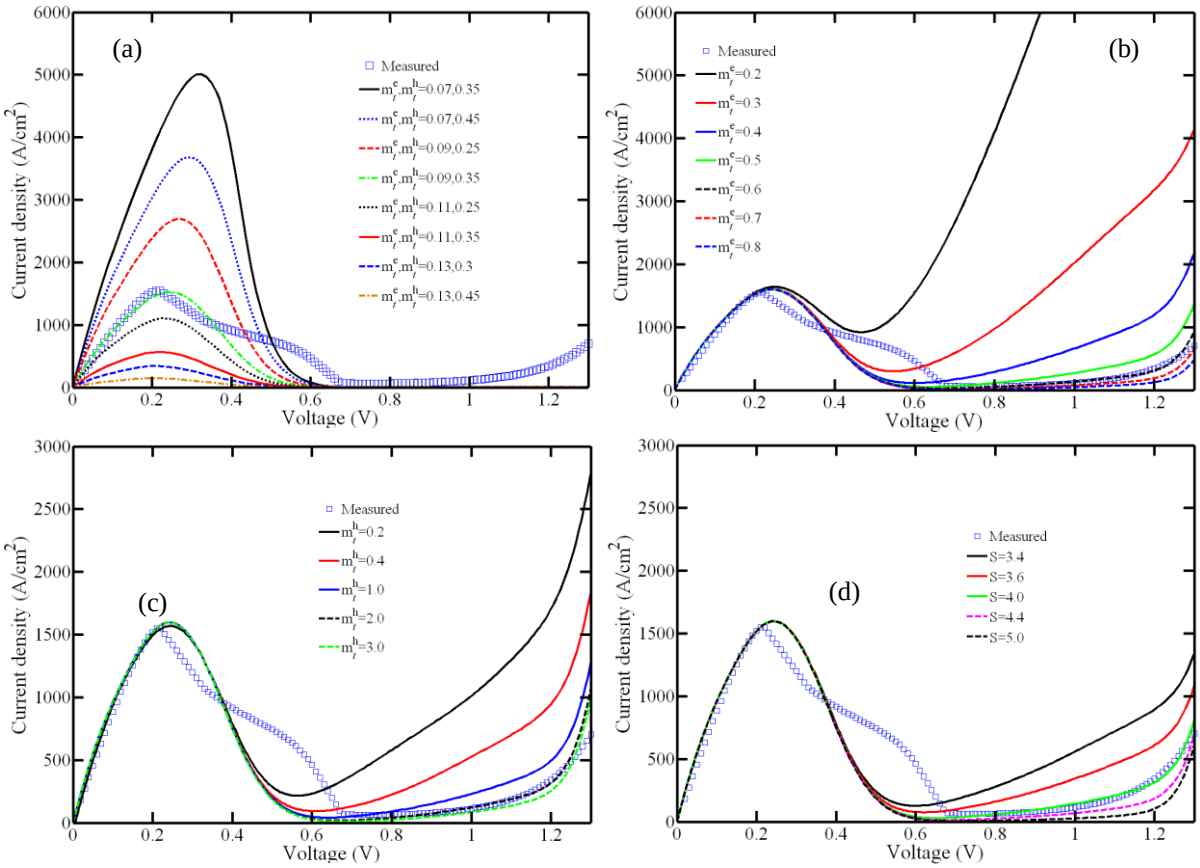

Figure 4-6. Simulation of the AlGaAs/GaAs tunnel junction depicted in table 4-1 to calibrate the nonlocal band to band tunneling masses of GaAs in (a) without nonlocal TAT effects. Using the B2B tunneling masses of 0.085 and 0.34 for electrons and holes respectively in GaAs, the calibration of the nonlocal trap assisted tunneling models is illustrated in (b) by only varying the electron TAT tunneling mass of GaAs, followed by (c) where only the hole TAT tunneling mass of GaAs is varied, and lastly in (d) where the Huang-Rhys factor of GaAs is varied. The B2B tunneling masses for AlGaAs were set to 0.09 and 0.37 for the B2B framework, and set to 0.7 and 2.8 in AlGaAs for the TAT framework with S=5.6. The experimentally measured tunnel junction was grown and fabricated at the Université de Sherbrooke [119]n and measured at the University of Ottawa.

The aforementioned tunneling masses are constrained to values that are reasonably close to the density of states effective masses of electrons and holes for GaAs and AlGaAs. However, this does not necessarily have to be the case. This constraint is adopted simply to establish an order of magnitude to such as to restrict the parameter space. Figure 4-6 (b)-(d) illustrate the steps in calibrating the nonlocal TAT model where the the electron and hole tunneling masses ($m_t^{e,h}$) and the Huang-Rhys factor (S) are the fitting parameters for GaAs

and AlGaAs (note that these tunneling parameters are different from the nonlocal B2B tunneling masses). As any of these factors are decreased, the nonlocal TAT increases considerably, as can be observed by increases in the valley current. The optimal nonlocal TAT electron and hole tunneling masses are 0.5 and 2.0 respectively for GaAs, 0.7 and 2.8 for AlGaAs respectively, and S are 4.0 and 5.6 for GaAs and AlGaAs respectively. The values for the AlGaAs nonlocal TAT masses were not sensitive to the overall valley current and were therefore selected based on a 40% increase with respect to the GaAs values using typical effective mass interpolation schemes for AlGaAs [122].

However, it is important to note that multiple solutions exist to fit the simulated data to experiment, as illustrated in [23]. A distributed resistance of 2×10^{-5} $\Omega\cdot cm^2$ was added to improve the agreement with the experimental slope near the origin and the experimental tunneling peak voltage. The agreement between the simulated and experimental *J-V* curves for the optimal parameters is on the order of 25% in terms of the ratio of the absolute difference between the total areas of each curve with respect to the experimental area. It is interesting to note that the valley current of the measured *J-V* curve cannot be well fitted to an empirical formula representative of typical excess currents, such as [35]

$$J_{\text{excess}}(V) = J_V \exp(C[V - V_V]) \tag{4.3.17}$$

where J_V, C and V_V are empirical constants. Plotting the experimental curve on a semi-logarithmic scale (see Fig. 4-7) identifies a region of the exponent which contributes to the valley current (dashed oval), prior to the diffusion current (dashed rectangle). This complicates the optimization of the nonlocal TAT parameters, as theory predicts a single exponential contribution to the excess current [35].

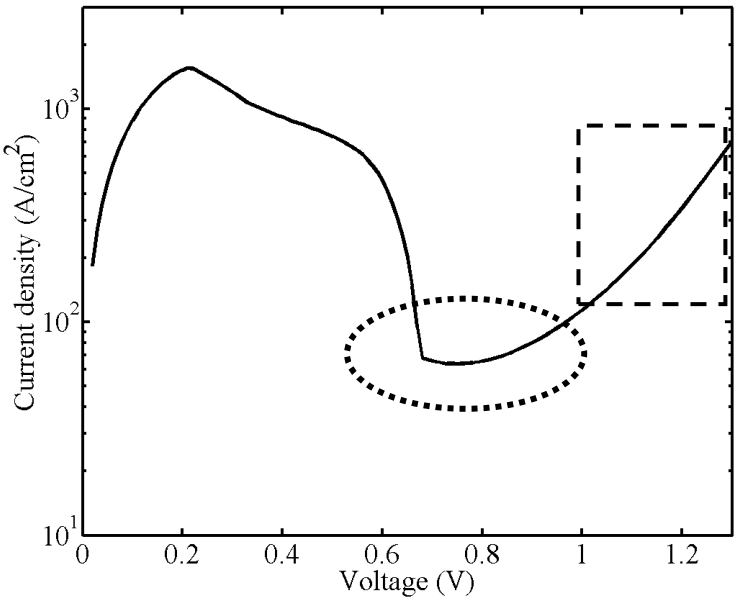

Figure 4-7. Experimental *J-V* curve of the AlGaAs/GaAs tunnel junction on a semi-log scale to outline the nonlinearity of the slope of the exponential in the excess current region as illustrated in the dashed oval. By nonlinearity, it is implied that a typical exponential, such as that outlined by the dashed square, has a linear slope on a semi-log scale.

The AlGaAs/GaAs material system is not the only one exploited for TJ use in multi-junction solar cells. Primarily because the middle sub-cell is composed of GaAs, a more desirable material system adopted in the top tunnel junction would be composed of a higher bandgap material. For this reason, the AlGaAs/AlGaAs and AlGaAs/InGaP material systems merit some study. However, the latter material system consisting of phosphides has been shown to require the highest effective doping to achieve the same resistance as AlGaAs/AlGaAs, AlGaAs/GaAs and GaAs/GaAs based TJ [20]. As a result, the material system consisting of AlGaAs/AlGaAs is investigated for concentrator applications in MJSC. The TJ structure of interest is outlined in Table 4-2, with the simulation results illustrated in Fig. 4-8a optimized through the same process as adopted earlier for the AlGaAs/GaAs TJ. However, since the grown TJ is an altogether different tunnel junction than the AlGaAs/GaAs TJ calibrated earlier, and is composed of AlGaAs with a different Al molar

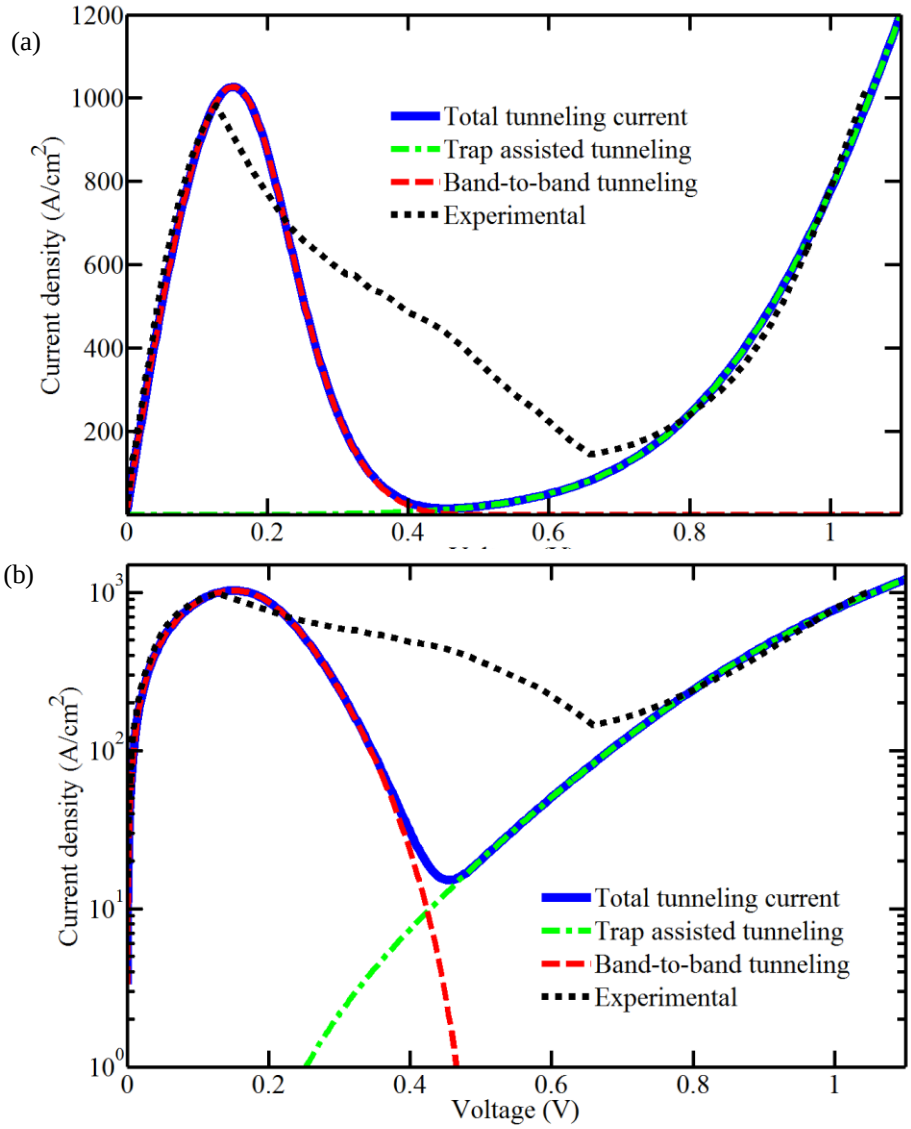

Figure 4-8. Simulation of the AlGaAs/AlGaAs tunnel junction whose structure is depicted in table 4-2 on a linear scale (a) and on a semi-log scale in (b) to outline the calibrated nonlocal band to band trap assisted tunneling models using the experimentally measured tunnel junction grown by Cyrium Technologies Inc. [21]. The region from 0.2 to 0.7 V is the negative differential resistance (NDR) region where the measurement setup is highly unstable.

fraction (x=0.3 for the former and x=0.15 for the latter), it is justifiable to re-calibrate the model parameters to fit the experimental data. Once again, it is important to note that multiple solutions exist to fit the simulated data to the four-probe measurement of the AlGaAs/AlGaAs TJ structure grown by Cyrium Technologies Inc. and measured at the University of Ottawa [20]. A good agreement between simulation and experiment justifies

the use of the nonlocal band-to-band and trap assisted tunneling models to explain the measured *J-V* characteristics.

The calibrated tunneling masses for $Al_{0.15}Ga_{0.85}As$ within the nonlocal B2B framework are 0.06 and 0.23 for electrons and holes respectively. Within the nonlocal TAT framework, the tunneling masses were set to 1.15 and 0.5 for electrons and holes respectively, and a Huang-Rhys factor of 5.67; these parameters were obtained through a genetic optimization routine which allowed all parameters to vary in order to minimize a residual error between the simulated and experimental data. Figure 4-8b illustrates the agreement of the simulated and experimental tunnel junction characteristics on a semi-log scale. However, it is highly intriguing that the best fit would require electron tunneling masses to be larger than the tunneling masses for holes, since electrons are typically more mobile than light or heavy holes in conduction processes. For a phonon-mediated process through traps, perhaps it could be conceivable that holes have stronger coupling to longitudinal phonons which mediate the process, thereby resulting in a lower tunneling mass with respect to electrons. Furthermore, it is conceivable that the energy levels of the traps coincide more optimally with the holes for the tunneling to occur, thereby facilitating this process further. The nonlocal B2B tunneling and nonlocal TAT models described above have given the most accurate simulation results in comparison to measured tunnel junction current – voltage characteristics [20],[23]. However, Jandieri *et. al.* have argued that resonant tunneling through defects is the dominant tunneling process in GaAs TJ's [123]-[124]. Although this process can contribute to the tunneling depending on the trap concentration near the TJ interface, the ideal process of band-to-band tunneling is considered as the dominant

tunneling process in this thesis. The nonlocal TAT models have also been used successfully to reproduce the valley currents [26].

Table 4-2. Tunnel junction structure used in the simulation based on a structure grown by Cyrium Technologies [21].

Layer	Material	Doping (cm^{-3})	Thickness (μm)
Cap	n-$Al_{0.15}Ga_{0.85}As$:C	2.25×10^{19}	0.05
p++ TJ	p- $Al_{0.15}Ga_{0.85}As$:C	4.5×10^{19}	0.2
n++ TJ	n- $Al_{0.15}Ga_{0.85}As$:Te	2.7×10^{19}	0.02
n+ buffer	n- $Al_{0.15}Ga_{0.85}As$:Te	1.35×10^{19}	0.05

4.2.2. Simulation Methods and Results for MJSC Sub-Cells and Full Structure

An example of a standard lattice matched multi-junction solar cell structure is illustrated in Fig. 4-9 and described in Table 4-3 (where TC, MC and BC represent top cell, middle cell and bottom cell respectively), which includes all of the relevant layers including the top and bottom tunnel junctions given in tables 4-2 and 4-1 respectively with thinner buffer layers; the ARC is omitted from Table 4-3 as it is discussed in more detail in section 4.2.4. The full device is 50 μm wide, which represents the smallest unit cell of the device, and includes a top contact that is 2.5 μm wide (5% shadowing loss), as illustrated in Fig. 4-9 with the Ge bottom sub-cell cut off since its thickness dwarfs the top and middle sub-cell layers. This section first outlines the simulation method for individual sub-cell characteristics (*J-V,* IQE and EQE) before optimizing the broadband ARC.

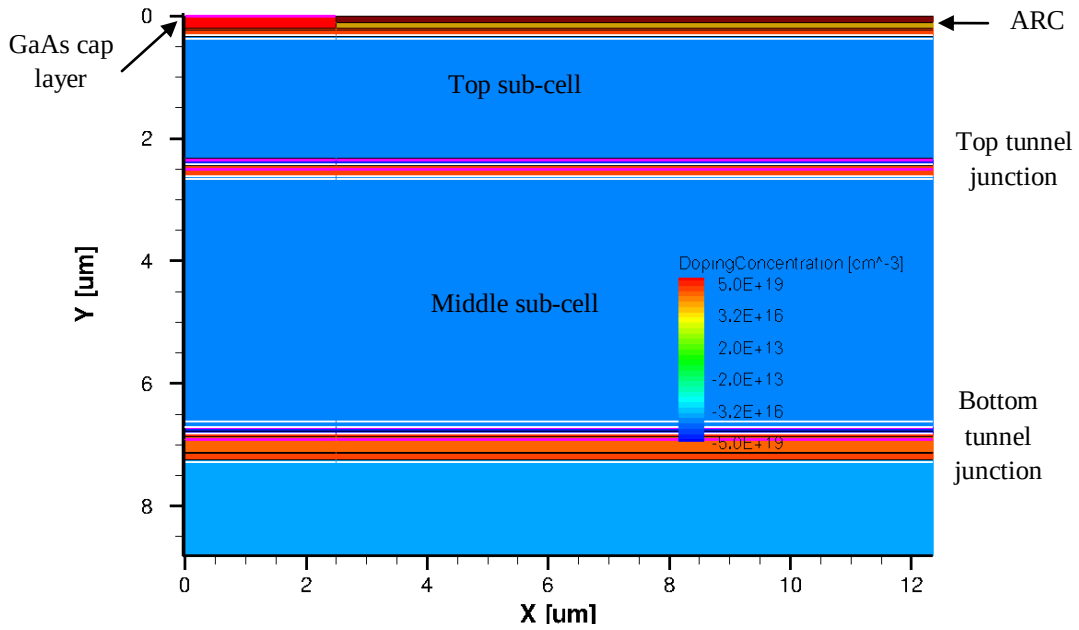

Figure 4-9. Simulated structure of the standard InGaP/InGaAs/Ge multi-junction solar cell which illustrates the highly doped GaAs cap to ensure an Ohmic contact, the ARC, the top sub-cell below the ARC, the top AlGaAs/InGaP tunnel junction followed by the middle sub-cell and the AlGaAs/GaAs bottom tunnel junction. The legend outlines the doping levels in the structure between 2×10^{13} cm^{-3} and 5×10^{19} cm^{-3} for *p*- and *n*-type.

Table 4-3. Standard multi-junction solar cell structure composed of InGaP/InGaAs/Ge.

Layer	Material	Doping (cm^{-3})	Thickness (µm)
Cap	n-GaAs	1×10^{19}	0.2
TC-Front surface	n-$Al_{0.51}In_{0.49}P$	1×10^{19}	0.03
TC-Emitter	n-$Ga_{0.51}In_{0.49}P$	3×10^{18}	0.1
TC-Base	p-$Ga_{0.51}In_{0.49}P$	5×10^{17}	1.5
TC-Back surface field	p-$(Al_{0.25}Ga_{0.75})_{0.51}In_{0.49}P$	1×10^{18}	0.03
Top-TJ buffer	p-$Al_{0.15}Ga_{0.85}As$	2.25×10^{19}	0.05
Top-TJ p++	p- $Al_{0.15}Ga_{0.85}As$	4.5×10^{20}	0.02
Top-TJ n++	n- $Al_{0.15}Ga_{0.85}As$	2.7×10^{19}	0.02
Top-TJ buffer	n- $Al_{0.15}Ga_{0.85}As$	1.35×10^{19}	0.05
MC-Front surface	n-$Ga_{0.51}In_{0.49}P$	5×10^{18}	0.02
MC-Emitter	n-$In_{0.01}Ga_{0.99}As$	5×10^{18}	0.1
MC-Base	p-$In_{0.01}Ga_{0.99}As$	5×10^{17}	4
MC-Back surface	p-$Ga_{0.51}In_{0.49}P$	1×10^{18}	0.1
Bottom-TJ buffer	p-$In_{0.01}Ga_{0.99}As$	4×10^{19}	0.05
Bottom -TJ p++	p-$Al_{0.3}Ga_{0.7}As$	4×10^{20}	0.05
Bottom -TJ n++	n-$In_{0.01}Ga_{0.99}As$	2×10^{19}	0.05
Bottom -TJ buffer	n-$In_{0.01}Ga_{0.99}As$	4×10^{18}	0.05
BC-Buffer	n-$In_{0.01}Ga_{0.99}As$	5×10^{18}	0.2
BC-Front Surface	n-$Ga_{0.51}In_{0.49}P$	5×10^{19}	0.02
BC-Emitter	n-Ge	1×10^{19}	0.1
BC-Base	p-Ge	2×10^{17}	170

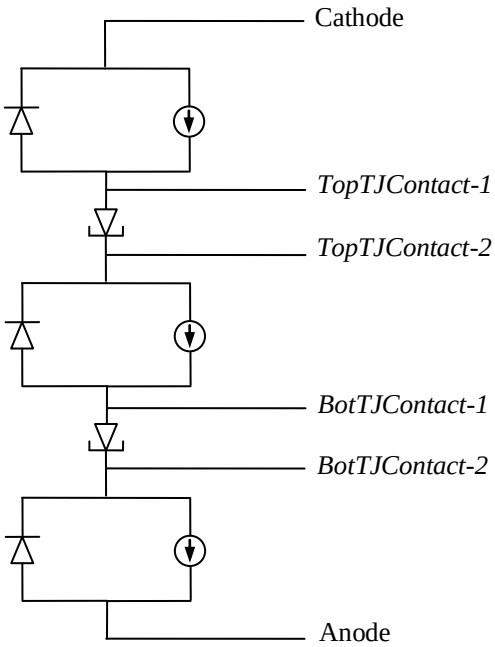

Figure 4-10. Equivalent circuit diagram of a multi-junction solar cell with virtual contacts implemented within the structure to probe the internal behaviour of individual sub-cells and tunnel junctions.

The sub-cells composing the full multi-junction solar cell can be isolated within the full structure using virtual contacts to give insight into individual *J-V* characteristics, which is extremely useful in optimizing the full MJSC device. Let us consider the structure outlined in Table 4-3 with a dual layered Si_3N_4/SiO_2 ARC, and a cathode and anode applied to the top and bottom parts of the cell respectively. Applying a virtual contact below the back surface field of the top sub-cell (before the top tunnel junction) allows for the isolation of the top sub-cell's *J-V* characteristics (note that a virtual contact in this case is optically transparent and obeys Kirchhoff's laws for current calculations). However, the behaviour of the top sub-cell can be simulated separately from the full device since the top sub-cell does not depend on the remaining parts of the structure and receives full illumination; this is therefore not particularly advantageous. On the other hand, if a virtual contact is placed above and below the middle sub-cell, then its *J-V* characteristics can be extracted from the

full structure after the top sub-cell filters out the incident illumination. This gives a strong advantage since the middle sub-cell characteristics depend heavily on the top sub-cell. Lastly, the probing of the bottom sub-cell can be accomplished by

isolating it through the implementation of a virtual contact below the middle sub-cell. Note that the tunnel junctions can also be isolated in a similar fashion. An equivalent circuit representing the implementation of these virtual contacts at all the relevant locations is illustrated in Fig. 4-10.

The initial biases at all of the contacts illustrated in Fig. 4-10 are set to 0 V. Once Poisson's equation is solved, the electron and hole quasi-Fermi levels are equal at all contacts. A transient simulation (see section 3.2.2.3) can then solve the electron and hole current-continuity equations coupled to the Poisson equation under illumination conditions, which ramps up the current flowing through the device to the quasi-equilibrium J_{sc} under no bias. Implementing a quasistationary command can then ramp up the voltage at any of the contacts for a typical voltage sweep, as discussed in Chapter 3. Doing this to a particular set of contacts allows for the simulation of an individual component within the full device, as illustrated in the following scenarios.

A forward voltage sweep across an *n-p* top sub-cell is performed when all the contacts below the top sub-cell are swept using a positive applied bias whilst maintaining a zero voltage at the top contact (cathode). However, this can be performed more trivially by performing a negative voltage ramp solely at the cathode (i.e. leaving the other contacts at 0 V) with the only difference being that the photogenerated current flows in the opposite direction at the cathode than under a positive bias. The current – voltage characteristics for the top sub-cell simulated using this methodology are illustrated in Fig. 4-11 under standard

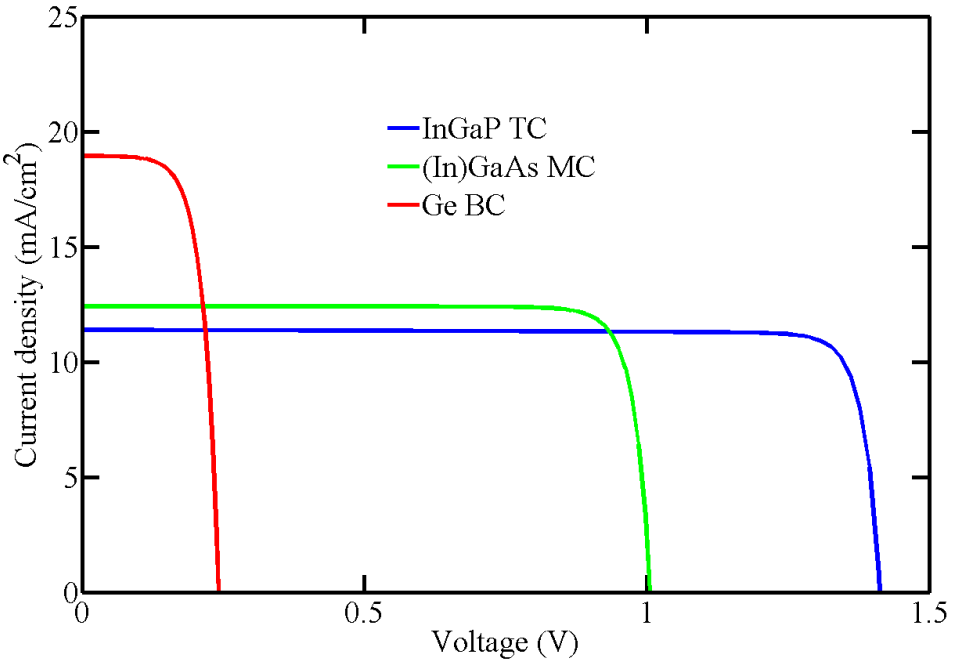

Figure 4-11. Simulated *J-V* characteristics of the individual top, middle and bottom sub-cells within the full device outlined in Table 4-3 under standard testing conditions and one sun illumination using the virtual contact approach, where the InGaP bandgap is 1.87 eV illustrating the current mismatch and the limitations of the detailed balance predictions.

testing conditions and one sun illumination (the current density is multiplied by (-1) based on the argument above). The bandgap of the InGaP adopted in this simulation is 1.87 eV based on the predictions from detailed balance (see Fig. 4-3). In this simulation, the thicknesses of the Si_3N_4/SiO_2 ARC are 0.04 μm and 0.05 μm.

A tunnel junction requires a reversed bias ramp since its polarity is reversed with respect to the sub-cells within the structure (i.e. *p-n* in order to connect the *n-p* sub-cells). In other words, during a forward sweep of the full device, the TJ are reversed biased. A voltage ramp of the TJ within the full device can be performed by either of two methods: 1) a simultaneous positive voltage ramp applied to both the cathode and the contact above the top TJ (*TopTJContact-1* in Fig. 4-10), or 2) a simultaneous negative voltage ramp at the contacts below the top TJ (*TopTJContact-2*, *BotTJContact-1* and *BotTJContact-2* and the anode). In either of the two scenarios, the voltages at all the other contacts must be set to

zero to maintain the operating point of all other devices at short circuit. Regardless of either approach, the final current propagating through the tunnel junction as a function of applied bias can be extracted through the sum of the cathode and *TopTJContact-1* currents based on Kirchhoff's law, or: $J_{TopTJ} = J_{TopTJContact-1} + J_{Cathode}$. The simulated current – voltage characteristics reproduce those illustrated in Fig. 4-8, except that a very small photocurrent flows through the TJ due to a very small amount of generation in the TJ layers.

The probing of the middle sub-cell is similar in analysis compared to the top tunnel junction since multiple contacts must be simultaneously biased to properly forward bias this sub-cell. Once again, two scenarios are possible: 1) negatively biasing all the contacts above the sub-cell (i.e. cathode, *TopTJContact-1* and *TopTJContact*-2), or 2) positively biasing all the contacts below the sub-cell (*BotTJContact*-1 and *BotTJContact*-2 as well as the anode). In each scenario, all contacts not being biased must be set to zero. The middle sub-cell *J-V* characteristics can then be extracted by summing up all the current densities as a function of voltage through the contacts above the middle sub-cell, or $J_{MC} = J_{TopTJContact-2} + J_{TopTJContact-1} + J_{Cathode}$. These are illustrated in Fig. 4-11 alongside those of the top sub-cell.

Similar to the top tunnel junction, the bottom tunnel junction must be reversed biased. The two scenarios are analogous to the top tunnel junction strategy: 1) positively bias the contacts above the tunnel junction or 2) negative bias the contacts below the tunnel junction. The final current density – voltage characteristics are extracted by summing up the current densities simulated at the contacts above the bottom tunnel junction, given as $J_{BotTJ} = J_{BotTJContact-1} + J_{TopTJContact-2} + J_{TopTJContact-1} + J_{Cathode}$. The simulation of this AlGaAs/GaAs TJ structure within the full MJSC corresponds to the simulated current

density – voltage characteristics displayed in Fig. 4-6, with the exception that a non-zero current density flows through the device at zero bias due to the photogeneration within the TJ.

The final scenario to extract the bottom sub-cell behaviour is quite straightforward and involves a positive bias applied to the anode whilst the remaining contacts above the sub-cell are set to 0 V. The simulated current density measured at the anode as a function of bias is thus representative of the bottom sub-cell. The simulated current density – voltage characteristics are illustrated in Fig. 4-11.

The sub-cell *J-V* characteristics appear to be limited by the current generated by the top sub-cell. If the current matching criterion is specific to the J_{sc}, then the top and middle sub-cells are not well current matched at J_{sc}. However, the optimization of the *FF* typically results in the middle sub-cell to have a slightly higher photocurrent than the limiting sub-cell in order for the sub-cells to be well current matched at the maximum power point (a topic not fully discussed here). The operating point of the full device current *J-V* characteristic is discussed in section 4.2.5.

4.2.3. External and Internal Quantum Efficiencies

The simulation method described above for probing the individual sub-cell *J-V* characteristics presents an optimal strategy for simulating the internal and external quantum efficiencies, since the J_{sc} can be extracted using the virtual contact approach. The internal quantum efficiency (IQE) can be computed according to equation (3.4.13), although integrating the optical generation for each sub-cell requires more intricacies within the Sentaurus Device code. On the other hand, a trivial alternative exists since one simulation can compute the EQE as well as the total reflectivity profile. The essential difference

between EQE and IQE is the reflectivity $R(\lambda)$, or in other words, the IQE can be expressed as a function of the EQE through the transmission $T(\lambda)$ as

$$IQE(\lambda) = \frac{EQE(\lambda)}{T(\lambda)} = \frac{EQE(\lambda)}{1-R(\lambda)}. \quad (4.3.18)$$

However, equation (4.3.18) must be modified to account for shading, since the simulated transmission (or reflection) is representative of the area of the cell that is not shadowed. The following modification accounts for this

$$IQE(\lambda) = \frac{EQE(\lambda)}{1-R(\lambda)\times(1-S)-S}. \quad (4.3.19)$$

where *S* represents the fraction of the cell area that is shadowed with respect to the total cell area. For this simulation, *S=0.05*. The distance between contact fingers is typically large enough (100 μm) that diffraction effects are not important. Figure 4-12 illustrates the simulated EQE and IQE of the InGaP/InGaAs/Ge multi-junction solar cell, once again adopting an InGaP bandgap of 1.87 eV. As expected, the IQE is larger in magnitude compared to the EQE. The oscillatory nature of the EQE matches with the patterns from the reflectivity profile.

Another method of simulating the EQE involves using an experimental-based approach which is similar to how the EQE is measured experimentally (since experimentalists cannot add "virtual" contacts within the structure). The approach uses three light emitting diodes (LED's) to controllably light bias each sub-cell with a single wavelength at a specific intensity to generate a controllable photocurrent in each sub-cell. For example, an LED at a wavelength of 600 nm would be quickly absorbed by the top sub-cell due to the high absorption coefficient of InGaP at this wavelength. For the middle sub-cell, an LED emitting at 800 nm is adequate, and lastly, a 1.1 μm LED for the bottom sub-cell. Decreasing the intensity of the LED for the target sub-cell thus limits the overall

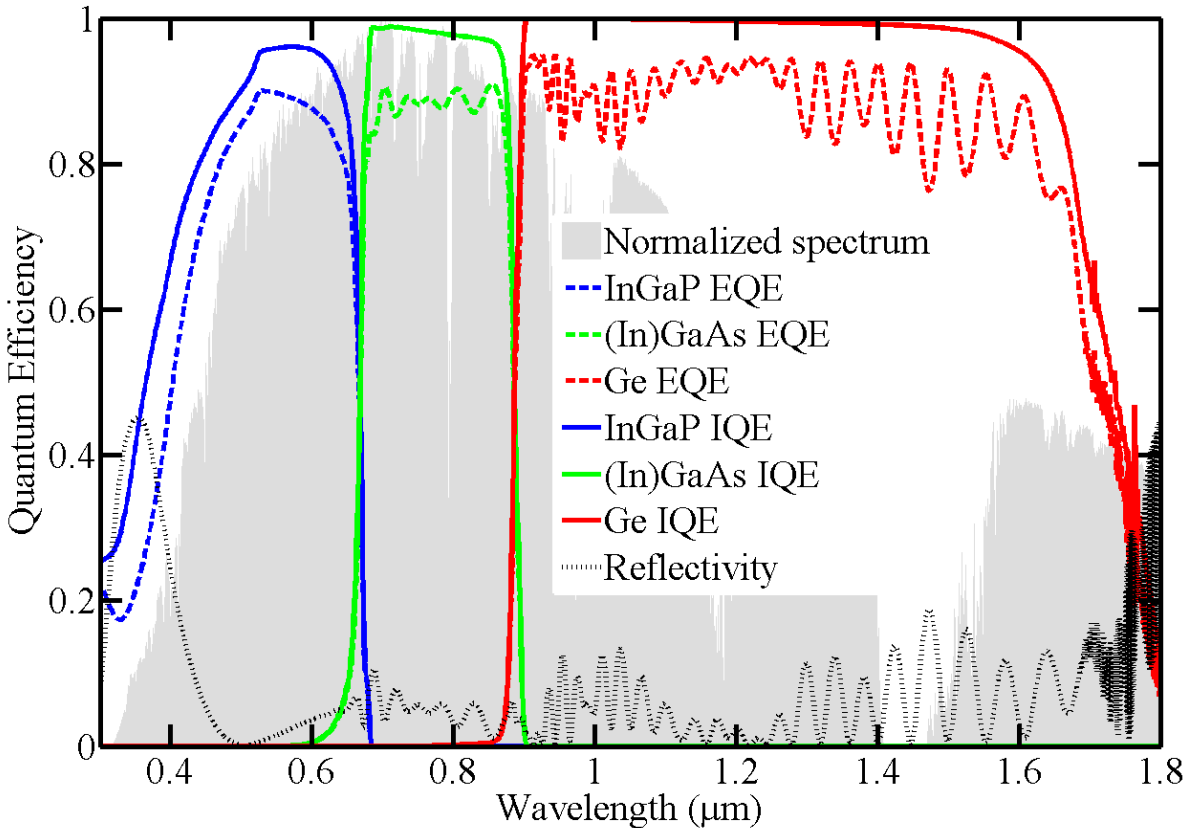

Figure 4-12. Simulated external and internal quantum efficiencies for the InGaP/InGaAs/Ge multi-junction solar cell based on Table 4-3 using an InGaP bandgap of 1.87 eV based on detailed balance predictions and a Si_3N_4/SiO_2 ARC. The normalized photon flux is also outlined to demonstrate the current potential of each sub-cell.

photocurrent of the entire device. Performing a quasistationary wavelength ramp using a fourth and final "tunable" LED thus yields the supplementary photocurrent due to this fourth LED. This technique, however, has the added complexities of internal biases due to the three light biases (i.e. each sub-cell may operate at a different voltage in order to produce the same photocurrent as the limiting sub-cell), which alter the operating point of each sub-cell [125]. For these reasons, the simpler approach is adopted in this section and the remaining EQE studies contained in this thesis.

4.2.4. Broadband Anti-Reflection Coatings

An important consideration in MJSC is the requirement for ARC designs that minimize reflectivity over a broad range of wavelengths, i.e. between 300 and 1850 nm.

Whereas chapter 3 addresses single layer ARC for single junction solar cells, a broadband ARC requires a minimum of two layers of materials with refractive indices appropriate for ARC applications (see section 3.4.3 of chapter 3). Note that a multi-layered ARC can also be used for single junction designs as these generally lower the overall reflectivity below that of a single layer design. This is illustrated in Fig. 4-13 which compares the reflectivity profiles of three ARC designs: 1) a single layer Si_3N_4 of thickness 200 nm, 2) a dual layered Si_3N_4/SiO_2 ARC of thicknesses 40 nm and 50 nm respectively, and 3) a dual layered MgF_2/TiO_x of thicknesses 60 nm and 40 nm respectively.

An optimization process of the aforementioned ARC designs can be performed quantitatively comparing the reflectivity profile of an ARC for applications in solar cells: the solar weighted reflectance (*SWR*) [126]. This parameter represents a quantification of the short circuit current density of a solar cell using an ARC relative to the short circuit current density with zero reflectivity, computed for a single junction solar cell as

$$SWR = 1 - \frac{J_{sc}}{J_{sc,R=0}} \ , \tag{4.3.20}$$

where J_{sc} is computed using

$$J_{sc} = q \int \frac{I(\lambda)}{E_{ph}(\lambda)} \cdot T(\lambda) \cdot IQE(\lambda) d\lambda \ \ , \tag{4.3.21}$$

where q is the elementary charge, I is the irradiance, E_{ph} is the photon energy, T is the ARC transmission, IQE is the internal quantum efficiency and λ is the wavelength. In equation (4.3.20), $J_{sc,R=0}$ is computed based on equation (4.3.24) with $T=1$ for all wavelengths. Based on equation (4.3.20), an ideal ARC will have a *SWR* of 0. However, equation (4.3.22) applies to single junction solar cells. For multi-junction solar cells, the short circuit current density needs a special type of calculation which examines the J_{sc} of each sub-cell to determine the minimum of these. As a result, equation (4.3.21) is modified as follows

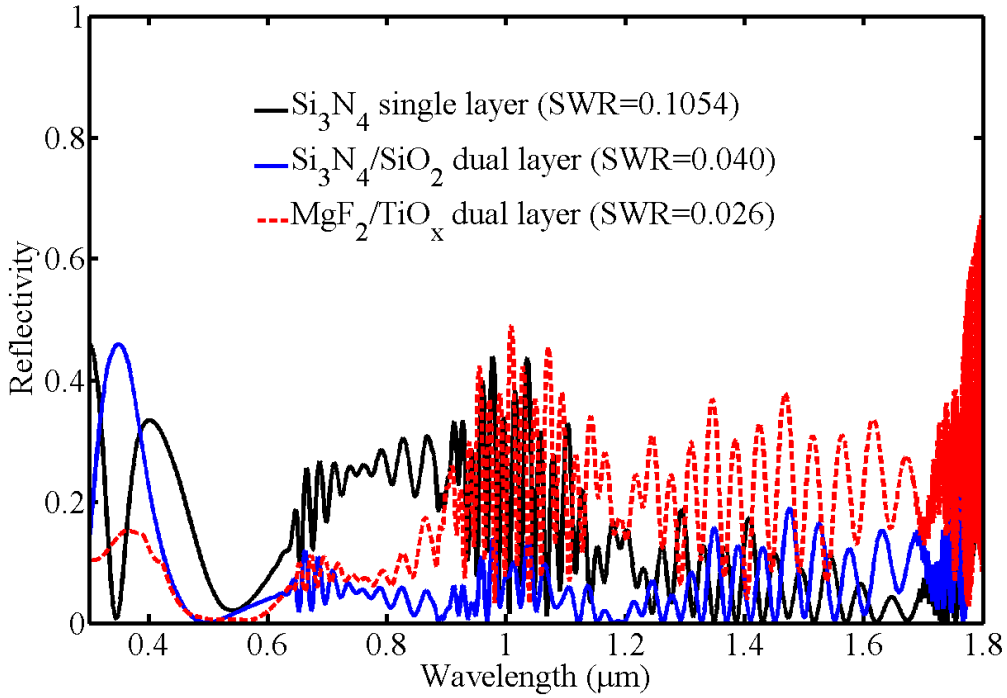

Figure 4-13. Comparison of reflectivities for three anti-reflection coatings: 1) a single layer of Si_3N_4 of thickness 200 nm, 2) a dual layered Si_3N_4/SiO_2 with thicknesses of 120 nm and 80 nm respectively, and 3) a MgF_2/TiO_x dual layered ARC with thicknesses of 60 nm and 40 nm respectively. The solar weighted reflectance (*SWR*) is given for each design.

$$J_{sc} = \min\left[q\int \frac{I(\lambda)}{E_{ph}(\lambda)} \cdot T(\lambda) \cdot IQE_N(\lambda) d\lambda\right]_{n=1}^{N} \tag{4.3.22}$$

where n represents the n^{th} sub-cell out of N sub-cells. Using equation (4.3.20) with equation (4.3.22), the *SWR* can be computed which gives a figure of merit for comparing various ARC designs. A key component of this calculation is the simulated *IQE*, which is illustrated for the default InGaP/InGaAs/Ge MJSC in Fig. 4-12. The results illustrated in Fig. 4-13 are based on minimizing the *SWR* by optimizing the thicknesses of the ARC layers. This was performed iteratively since it only involved 2 parameters. Note that this process keeps the MJSC structure fixed; otherwise the IQE would also change.

The corresponding J_{sc} for the sub-cells composing the default InGaP/InGaAs/Ge MJSC using the optimized ARC for the MgF_2/TiOx material system are 11.4 mA/cm^2, 13.4 mA/cm^2 and 22.1 mA/cm^2 for the top, middle and bottom sub-cells respectively. This is far

from current matched, and the minimum sub-cell J_{sc} is also far from maximized, which indicates that the MJSC device efficiency is not maximized by performing the optimization routine for the ARC described above (i.e. minimizing the *SWR*). Furthermore, these current mismatched sub-cells indicate that the ideal assumptions inherent to the detailed balance calculations (i.e. an ideal top sub-cell bandgap close to 1.87 eV) are incorrect when more realistic processes such as SRH, Auger and surface recombination are considered, along with the effects of a realistic ARC. In order to current match the MJSC device as well as maximize the J_{sc}, the ARC optimization process must be performed iteratively as a function of the InGaP bandgap, which requires the simulated IQE for an identical structure as a function of this material's bandgap. The optimization is therefore an iterative process between optimizing the ARC layers as a function of the InGaP bandgap.

Generating these data, however, requires the optical characteristics of InGaP as a function of bandgap. These can be obtained using a simple translation in energy of the extinction coefficient, whilst assuming the refractive index profile remains intact. Although this violates the Kramers-Kronig relation, the refractive index over the wavelength range which is translated does not vary significantly and is therefore a reasonable assumption. Such a method has been developed and reported previously [127] in an effort to study the effects of temperature on the external quantum efficiency of lattice matched MJSC, which required the InGaP and InGaAs optical characteristics as a function of temperature (or bandgap). The details of these calculations are discussed in section 4.3.2.2. For the moment, let's assume the optical characteristics of InGaP are known as a function of the material's bandgap such that the iterated process can be performed specifically for the Si_3N_4/SiO_2 ARC design. These ARC materials are used in this study since they have negligible absorption in

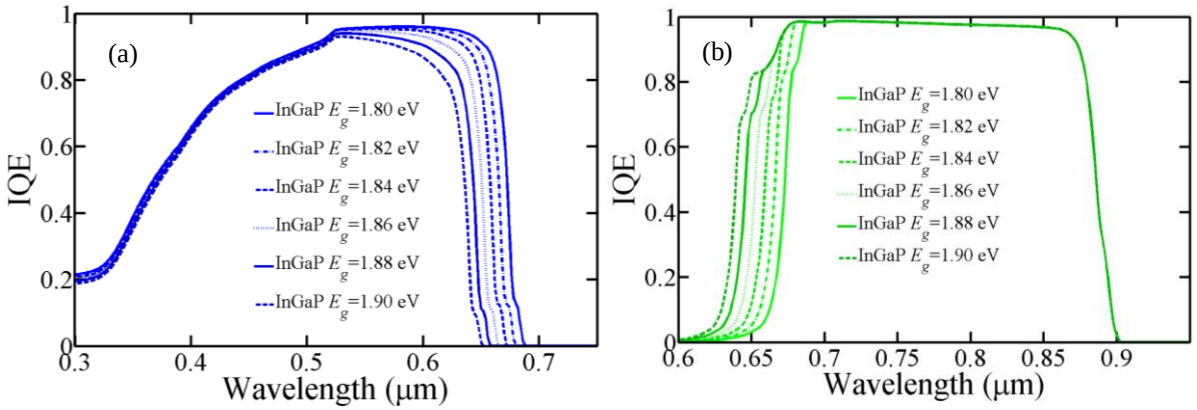

Figure 4-14. a) The simulated internal quantum efficiency of the InGaP top sub-cell as part of the lattice matched InGaP/InGaAs/Ge MJSC given by the structure in Table 4-3 for various InGaP bandgap. b) The simulated IQE of the InGaAs sub-cell for various InGaP bandgaps.

the UV region, whereas TiOx and MgF_2 can have non-negligible absorption in the same wavelength range.

The simulated IQE of the InGaP top sub-cell (TC) as a function of InGaP bandgap is illustrated in Fig. 4-14a where the extinction of the top sub-cell IQE shifts to shorter wavelengths (or higher energy) as the bandgap of the material increases. The resulting middle InGaAs sub-cell (MC) IQE is affected as well, as shown in Fig. 4-14b. The final IQE is then used to simulate the SWR as a function of InGaP bandgap. Furthermore, these calculations reveal the J_{sc} of each sub-cell, which allows the current matching potential of the ARC to be gauged based on the ratio of $J_{sc,\,top}/\,J_{sc,\,mid}$.

Figure 4-15a illustrates the effects of varying the ARC layer thicknesses on the simulated J_{sc} of the top and middle sub-cells for a top InGaP sub-cell bandgap of 1.84 eV using equations (4.3.23) and (4.3.25). This figure shows the high sensitivity of each sub-cell's J_{sc} to ARC design parameters, and that several combinations of ARC thicknesses result in current matched top and middle sub-cells. It is also apparent that both ARC layer thicknesses cannot be below certain threshold values. Figure 4-15b illustrates the variation of the SWR as a function of ARC thicknesses. Several local minima exist, which makes the

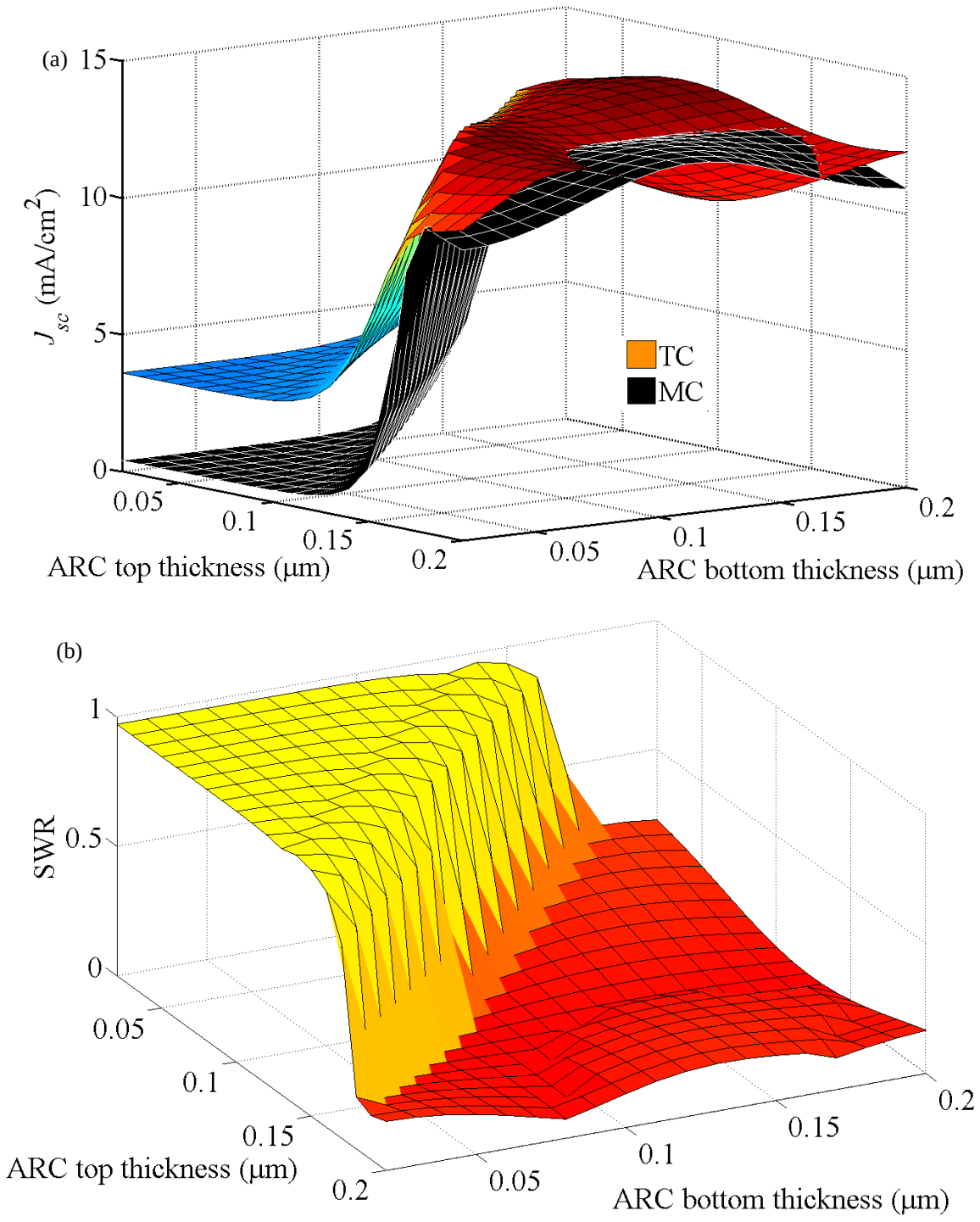

Figure 4-15. Surface contour plot of a) the calculated top and middle sub-cell short circuit current densities and b) the SWR, both as a function of the top (Si_3N_4) and bottom (SiO_2) ARC layer thicknesses to outline the nature of the optimization problem using the SWR minimization routine.

location of the global minimum difficult to find via an optimization algorithm such as those offered by the Optimizer tool in TCAD Sentaurus [128]. When comparing Figs. 4-15a and b, it becomes clear that the trends in SWR follow the trends of the limiting sub-cell J_{sc}. Note that this optimization process assumes the top sub-cell base thickness is fixed, since the IQE, which is highly dependent on this fixed parameter, is used as a fixed input in this methodology. Thus, performing this optimization process including the top sub-cell base thickness as another variable significantly increases the computational time. Since the goal of this specific exercise is the optimization of the MJSC design including the design of the ARC, another approach is required which diminishes the overall computational time involved and exploits one metric as a response to the optimization routine: maximizing the limiting sub-cell J_{sc}. Such an approach is described below.

The hypothesis in this optimization process is that maximizing the MJSC efficiency essentially comes down to maximizing the minimum sub-cell J_{sc} for a specific spectrum. In this optimization routine, the constraint of current matching is assumed to have a lower weight than maximizing the minimum sub-cell J_{sc}, which assumes the wasted current in a current mismatched MJSC does not significantly contribute to heating (which decreases the efficiency, as studied in section 4.3.2.2). This optimization process is performed using the genetic optimization routine [128], and makes use of the most influential parameters on the top and middle sub-cell J_{sc}'s: ARC thicknesses, the top sub-cell base thickness, and lastly, the InGaP bandgap. For each bandgap, three parameters are varied in order to maximize the J_{sc}, which makes visualizing the parameter space particularly difficult. The maximized J_{sc} achieved by varying the top sub-cell thickness and the ARC thicknesses is plotted as a function of InGaP bandgap in Fig. 4-16. Based on the use of a genetic optimization

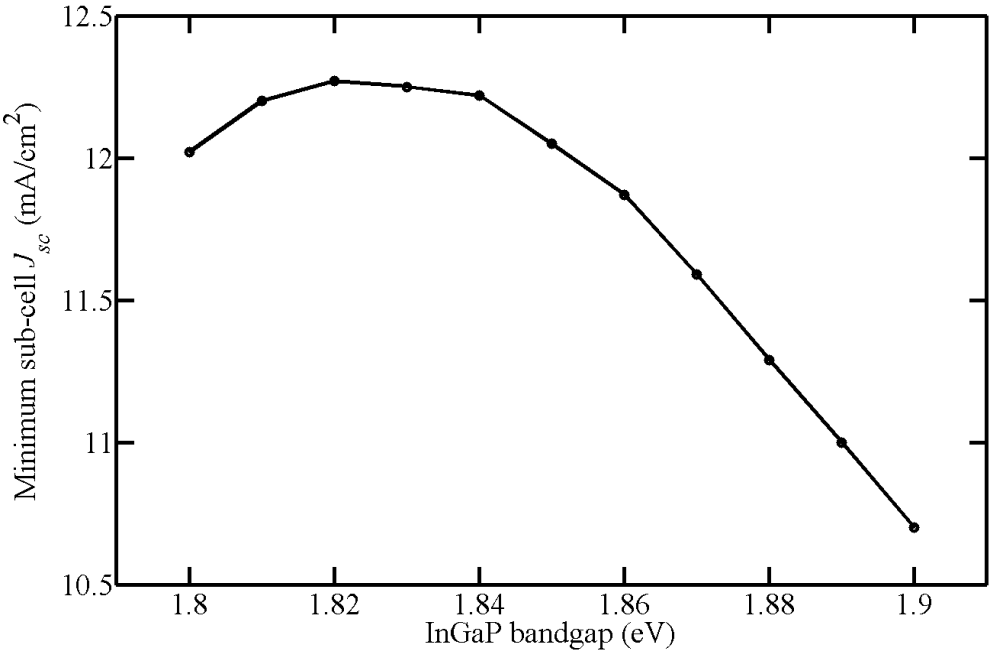

Figure 4-16. Simulated optimized sub-cell J_{sc} as a function of InGaP bandgap, where the sub-cell J_{sc} represents the minimum of the top and middle sub-cells in the simulated MJSC structure for an incident spectrum normalized to 900 W/m^2. For each InGaP bandgap, the ARC and top sub-cell thicknesses were varied to obtain a maximized minimum sub-cell J_{sc}.

algorithm to explore the multi-parameter surface, these results should represent the global maxima for each bandgap explored using the described input parameters. However, since the reported world record J_{sc}'s for similar structures are considerably larger (see Table 4-4), one should investigate the input material parameters further to approach the world record more closely. This suggests that the structure can be optimized further using better designs such as a top sub-cell *n-i-p* design or better material interface quality in the top sub-cell. With respect to maximizing the MJSC device efficiency, an increase in the bandgap of InGaP leads to an increase in V_{oc}. Thus, the largest GaInP bandgap that offers near maximal J_{sc} is expected to provide the highest device efficiency. For these reasons, a GaInP bandgap of 1.83 eV is chosen based on Fig. 4-16, along with the ARC and top sub-cell thicknesses that maximized the J_{sc} (given as 0.0794 and 0.0592 μm for the Si_3N_4/SiO_2 ARC and 1.624 μm for the top sub-cell base).

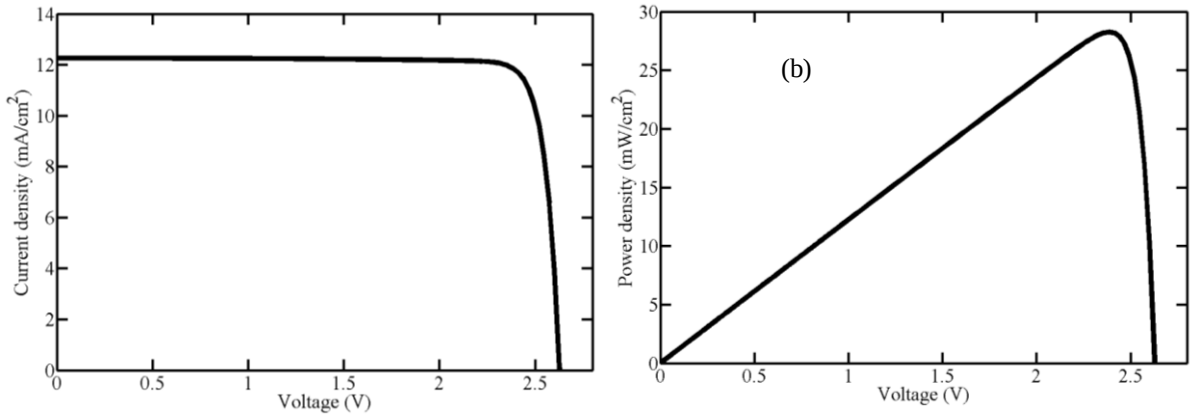

Figure 4-17. Simulated a) current density – voltage and b) power density – voltage characteristics for the InGaP/InGaAs/Ge multi-junction solar cell with a Si_3N_4/SiO_2 broadband anti-reflection coating optimized in section 4.2.4 at one sun intensity (900 W/m^2).

4.2.5. Simulation Results

The simulation of the full device current density – voltage and power density – voltage characteristics can be performed using a two terminal approach (i.e. no virtual contacts) based on the MJSC design optimized in the previous section. However, the complex nature of the device and the use of multiple physical models such as the nonlocal tunneling models for the tunnel junctions require significant computational time. For these reasons, two Sentaurus Device tools are used in this type of simulation. The first one targets the optical problem and generates an optical generation profile similar to that illustrated in Fig. 3-23. The resulting optical generation profile is then imported into the second Sentaurus Device simulation tool, where the transient simulation to solve for the J_{sc} is very important and can result in long simulation times (especially for high concentration simulations, as discussed in section 4.3). The physical solutions of this step (i.e. carrier concentrations and the energy potential throughout the structure) are then used to solve the set of semiconductor equations as a function of applied bias using a quasistationary command. The final simulated *J-V* and *P-V* results are shown in Fig. 4-17a and b respectively, with the corresponding *J-V* metrics

given in Table 4-4. These metrics are in agreement with similar types of devices such as a lattice matched InGaP/InGaAs/Ge MJSC [129] and a lattice mismatched InGaP/InGaAs/InGaAs MJSC [130], where the J_{sc} values reported in the literature were corrected for the illumination spectrum total power. It is important to note that several components of the structure have not been optimized in this thesis (such as the doping and thicknesses of the layers) since the parameter space involved is too large and is therefore extremely time consuming. Performing such an optimization process based on feedback from the growth and material characterization could improve the agreement with the *J-V* metrics. For example, the simulated magnitude of the top sub-cell EQE is smaller compared to the world record structure [130], which explains the discrepancy in J_{sc}. The V_{oc} could also be enhanced through graded doping layers (for example, a base layer that is divided into multiple layers with increasing doping) and improved crystal quality (leading to decreased recombination rates). For these reasons, the efficiency is under-estimated in these simulations. However, the fill factor is overestimated in part due to the perfect illumination uniformity in the simulation environment, whereas the measured results were most likely obtained using some degree of non-uniform illumination. Nevertheless, the goal of this chapter is not to reproduce the experimental results per say (since these are not available for known MJSC structures). Rather, the primary goal of this chapter is to describe the simulation methodology and simulation results of a lattice matched triple-junction solar cell. This latter component then serves to outline the general trends of a MJSC and to identify possible areas of improvement in order to obtain better agreement with the world record performance metrics. It becomes clear from Table 4-4, for example, that the MJSC photocurrent must be increased by ~7% to improve the agreement with world records.

Table 4-4. Simulated *J-V* metrics of the lattice matched (LM) MJSC compared to world record (WR) values published in the literature for a lattice matched (LM) MJSC and a lattice mismatched (LMM) MJSC, all of which are corrected for an incident spectrum of 900 W/m^2 at 25° C, where "*" implies the J_{sc} was corrected for the incident spectrum total power from 1000 W/m^2 to 900 W/m^2, with the V_{oc}, FF and efficiency remaining intact.

Device	J_{sc} (mA/cm^2)	V_{oc} (V)	Fill Factor (%)	Efficiency (%)
MJSC	12.3	2.628	87.2	31.3
LM-MJSC WR [129]	13.2*	2.691	86.0	32.1
LMM-MJSC WR [3],[130]	13.1*	3.015	85.5	37.5

4.3. Concentrated Illumination

4.3.1. Effects on Performance

The purpose of concentrating sunlight onto a small area of multi-junction solar cell originates from theoretical arguments that show the efficiency increasing logarithmically with concentration factor (defined as the geometrical area factor between the area of the optical components and the area of the device), which are briefly presented here. To a first approximation, the photocurrent generated by a solar cell scales linearly with the concentration factor X [105], or $J_{sc}(X) \approx XJ_{sc}(X=1)$. Furthermore, the dark current of the solar cell remains constant for a specific bias at a fixed temperature. A larger applied bias is therefore required to balance the photocurrent and reach open circuit voltage. Substituting the linearly increasing $J_{sc}(X)$ with XJ_{sc} and re-arranging equation (3.3.4) gives a first approximation on the behaviour of V_{oc} as a function of concentration,

$$V_{oc}(X) = \frac{nk_BT}{q} ln\left(\frac{XJ_{sc}}{J_0} + 1\right) \approx V_{oc}(X=1) + \frac{nk_BT}{q} ln(X) \qquad (4.4.1)$$

where n is the ideality factor and $V_{oc}(X = 1)$ is the V_{oc} at 1 sun illumination. Equation (4.4.1) indicates that the V_{oc} increases logarithmically as a function of concentration with a slope given by the ideality factor. Based on this first approximation, the power generated by the cell should increase as a function of concentration, assuming the fill factor and the temperature remain constant. However, the effects of increasing the minority carrier concentrations as a function of concentration results in increased levels of Auger recombination which changes the ideality factor and therefore affects the slope of the V_{oc} as a function of X. The effects of temperature on MJSC efficiency as a function of concentrated illumination is discussed in detail in the following section.

Figure 4-18 illustrates the idealized effect of concentration on the simulated *J-V* and *P-V* characteristics from 1 sun illumination to 3 suns illumination. The concentration is achieved by scaling the photogeneration rates by the concentration ratio. Another route is to scale up the illumination spectrum, although this requires Sentaurus Device to import unique spectra for each concentration. Figure 4-18 illustrate the linearity in scaling the J_{sc} with X as well as the logarithmic increase in V_{oc}, both of which are depicted in Figs. 4-19a and b respectively for a much larger range of concentrations (up to X=1000). Lastly, Fig. 4-19c and d illustrate the effects of the concentration on fill factor and efficiency of the MJSC device respectively. These results primarily outline the logarithmic nature of these metrics as a function of concentration, whereby the losses due to series resistance appear at high concentration. The topic of series resistance is discussed in more detail in the following section.The effects of *FF* as a function of concentration can be complex as it depends on the ideality factors of each sub-cell. For example, Auger recombination will become a more important mechanism for high carrier concentrations and thus impact the ideality factor of

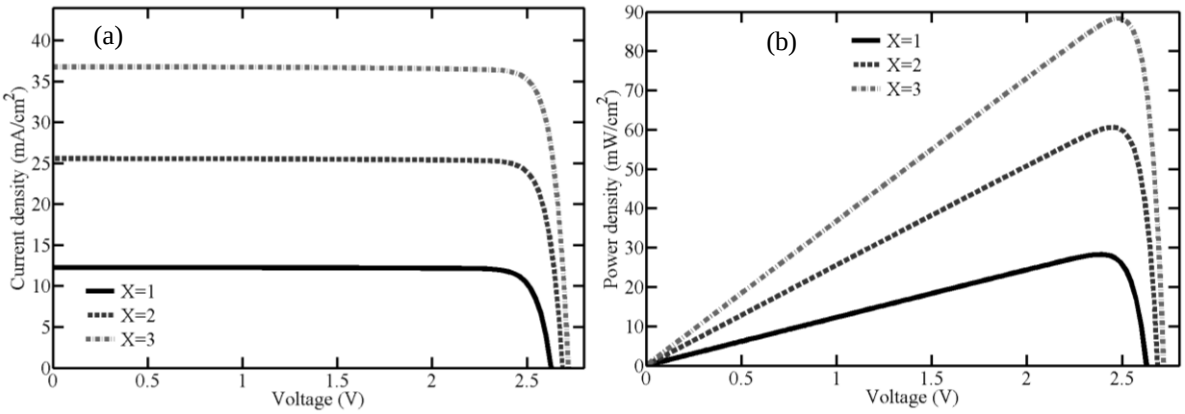

Figure 4-18. Simulated a) current density – voltage and b) power density – voltage characteristics for the optimized InGaP/InGaAs/Ge multi-junction solar cell one sun intensity (900 W/m^2), 2 suns intensity (1800 W/m^2) and 3 suns intensity (2700 W/m^2).

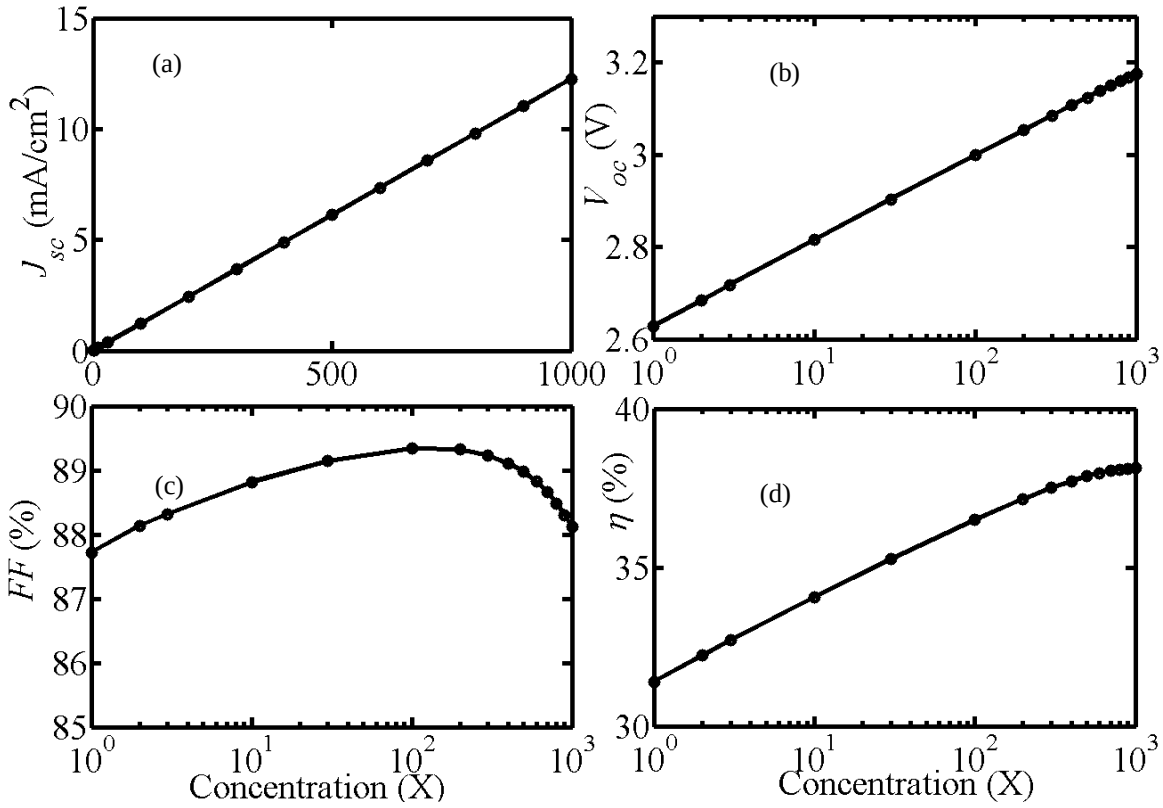

Figure 4-19. Simulated a) J_{sc} b) V_{oc}, c) fill factor (FF) and d) efficiency (η) as a function of concentration X.

each sub-cell differently depending on the magnitude of the radiative and SRH recombination rates. Furthermore, the ideality factor of the device will also affect the efficiency through the slope of the V_{oc} based on equation (4.4.1).

4.3.2. Limitations

4.3.2.1. Series Resistance

Since the photocurrent scales linearly with concentration, the effects of series resistance (R_s) on device performance can become important at high concentrations (X~500 or above), where the potential drops across the device, given as $J \cdot Area \cdot R_s$ increases linearly as a function of concentration. This can have quite an important effect on the fill factor, as seen in chapter 3. The effects of series resistance are outlined in Fig. 4-20 in terms of the J_{sc}, V_{oc}, FF and overall efficiency. Figure 4-20a illustrates that the photocurrent scales linearly with concentration, as expected based on the previous section. However, the J_{sc} becomes dependent on series resistance only at very high values of R_s, where the photocurrent becomes constant for X>200 as the resistance dominates the *J-V* characteristic (i.e. a straight line with negative slope from the V_{oc} to the J_{sc}; the linearity extends into the reverse bias regime). As a result, the J_{sc} becomes pinned by the V_{oc} and only increases with concentration based on the fact that V_{oc} increases logarithmically over X independently of R_s as shown in Fig. 4-20b. However, the fill factor and efficiency are highly dependent on series resistance as a function of concentration (Figs. 4-20c and d). This outlines the importance of minimizing series resistance in order to achieve the highest efficiency possible at the highest level of concentration achievable. A typical series resistance for a state-of-the-art MJSC for concentrator applications is on the order of 0.01 $\Omega \cdot cm^2$ [131].

It is important to note that the series resistance decreases as the contacts of the cell are made larger. However, as the contacts get larger, so are the shadowing losses. This introduces another optimization problem in that series resistance must be minimized whilst maximizing the surface area exposed to incident illumination by increasing the thickness

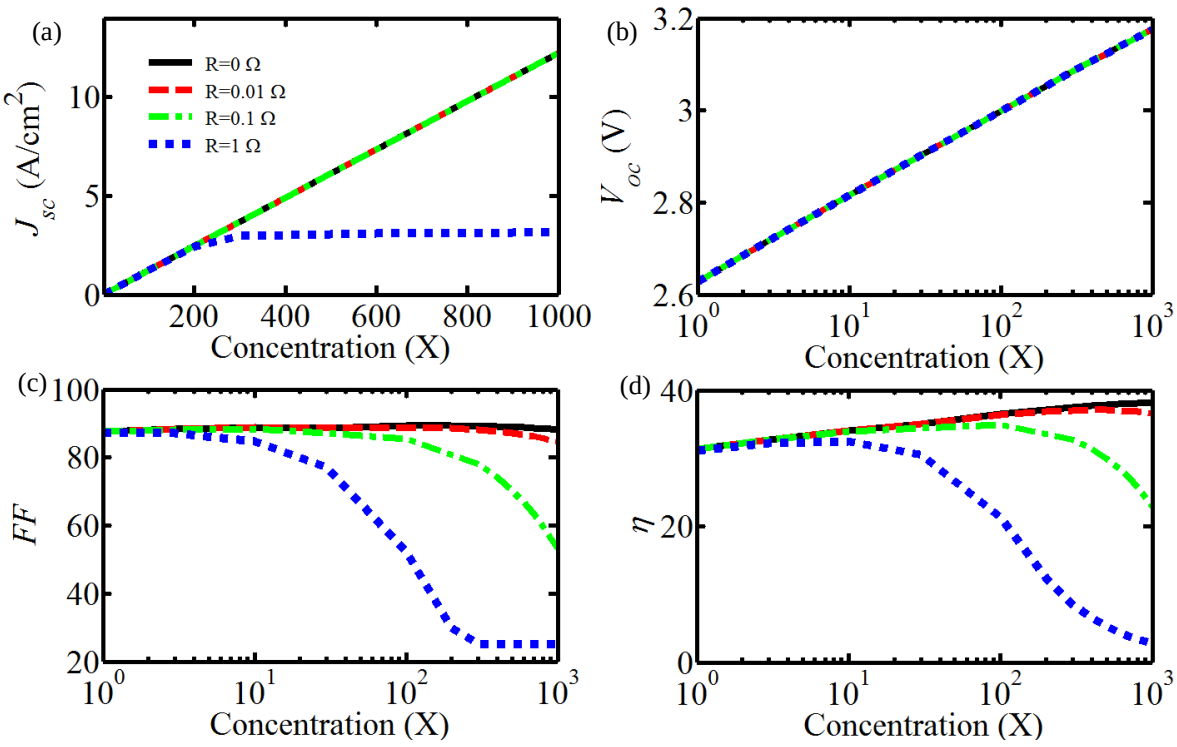

Figure 4-20. Simulated a) J_{sc}, b) V_{oc}, c) fill factor (*FF*) and d) efficiency (η) as a function of concentration X for various series resistances.

between metallic contacts on the surface of the cell. A work around to this problem is to increase the depth of the contacts into the cell, although this increases the requirement for high quality ohmic contacts since metal-semiconductor interfaces can have high concentrations of interface defect states. Furthermore, the effects of lateral resistance stemming from the top sub-cell emitter (and front surface field) can also have an effect at ultra-high levels of light concentration. It is therefore important to maximize the doping levels in the emitter and front surface field, while keeping in mind the increased levels of recombination that accompany the higher levels of doping. These are just another two important optimization problems in MJSC design.

4.3.2.2. Temperature Under Concentration

The amount of power incident on the cell under high concentration can be up to 9×10^4 W/m^2 for *X=1000*. This implies that for state-of-the-art MJSCs operating at an efficiency of

40%, 5.4×10^4 W/m^2 must be dissipated as heat. This heat can be highly problematic for MJSC performance under concentration, since it can drastically increase the operating temperature of the device to close to 100℃ above ambient [131] if an appropriate thermal paste is not used between the cell and the carrier (the carrier is the location of the installed PV device for current extraction along with a bypass diode for proper integration into a CPV system). An efficiency drop of close to 8% has been observed for a MJSC device operating under continuous concentration at 1000 suns without the thermal paste in comparison with thermal paste, solely due to the temperature effects [131]. This behaviour has also been modeled successfully using the TCAD Sentaurus models described above [127],[131]. This section investigates these effects in more detail.

As temperature increases, the most significant effect on semiconductors is the decrease in the bandgap of the material, described using the Varshni model [132] expressed as

$$E_g(T) \sim E_g(T=0) - \alpha \frac{T^2}{\beta + T} \ , \tag{4.4.3}$$

where α and β are material dependent quantities in units of eV/K and K respectively. Semiconductors such as GaAs have very well known temperature dependences [121], whereas quaternary materials have temperature parameters that range significantly such as those reported for AlGaInP [133],[134]. This temperature dependence is important to understanding the effects of temperature on MJSC performance, since the intrinsic carrier concentrations are inherently dependent on temperature

$$n_i^2 \sim \exp\left(-\frac{E_g}{k_B T}\right). \tag{4.4.2}$$

As the intrinsic carrier concentration increases, so does the dark current of the cell, which decreases the open circuit voltage. Furthermore, temperature has significant effects on the density of states, the Fermi level and carrier mobilities. TCAD Sentaurus implicitly

considers all of these aforementioned temperature dependences, with the exception of the extinction coefficient which is described below. As the bandgap decreases, the overall absorption increases and thus the photocurrent of the cell is expected to increase. However, in a multi-junction solar cell, the situation is more complex. The change in bandgap of the top sub-cell, which leads to an increase in its photocurrent, modifies the light spectra available for absorption in the lower lying sub-cells. This change in bandgap depends implicitly on the Varshni parameters. This point becomes clearer when studying the effects of temperature on the EQE of the device (see Fig. 4-22). Furthermore, the benefit of an increased photocurrent is typically dwarfed by the drop in V_{oc} [127].

In order to study the effects of temperature on MJSC performance under concentrated illumination, one must develop a method for determining the extinction coefficient of materials over temperature. This can be done using the Varshni relation given by equation (4.4.3). Since the absorption coefficient is directly proportional to the square root of the energy gap, then a modification of the absorption coefficient due to the temperature dependence of the energy gap can be expressed as going from $\alpha(E,T) \propto (E - E_g(T))^{1/2}$ to $\alpha(E,T) \rightarrow (E - E_g(T=0) + \alpha\frac{T^2}{\beta+T})^{1/2}$, which demonstrates the shift of the absorption edge to lower energies as temperature increases. The developed model first locates the energy at which the experimentally measured absorption coefficient experiences the largest slope (on a logarithmic scale). This energy represents the bandgap of the material to a first approximation. The difference between this bandgap (at a known temperature, typically 300 K) and the bandgap of the material at the target temperature (using the Varshni relation) can then be used to translate the entire absorption coefficient of the material as a function of energy. This works to a first approximation for CPV applications since the temperature

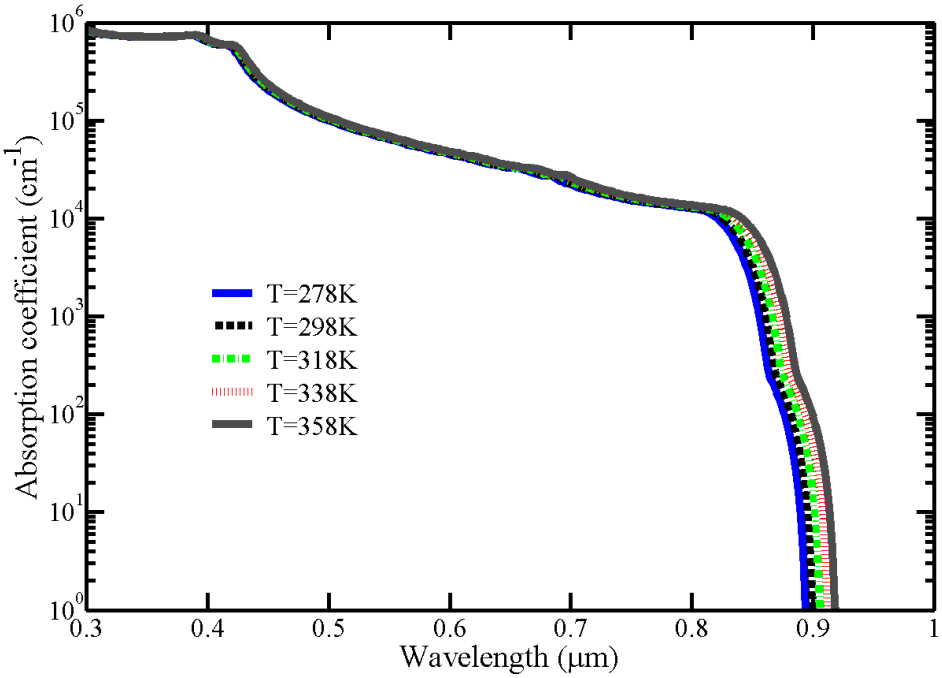

Figure 4-21. Absorption coefficient of GaAs over temperature using a simple Varshi-based absorption model.

changes, up to 100°C [131], limit the change in bandgap to ~50 meV for GaAs, which is a small energy translation at energies above the bandgap of the material. This can be seen in Fig. 4-21 which shows the variation of the absorption coefficient of GaAs using this model, where the data at 300 K originates from [44]. The variation in the absorption coefficient is very small for wavelengths shorter than 0.8 μm, which validates the use of such a model for CPV applications. The change in refractive index is assumed to be vary slowly in the range of wavelengths close to the bandgap where the shift in energy is most important. The Kramers-Kronig relationship should be used to model the corresponding change in refractive index.

Implementing this model for all the materials of interest using Varshni parameters obtained from the literature gives the simulated EQE profile as a function of temperature as illustrated in Fig. 4-22. As expected, the low energy EQE edge of each sub-cell shifts to

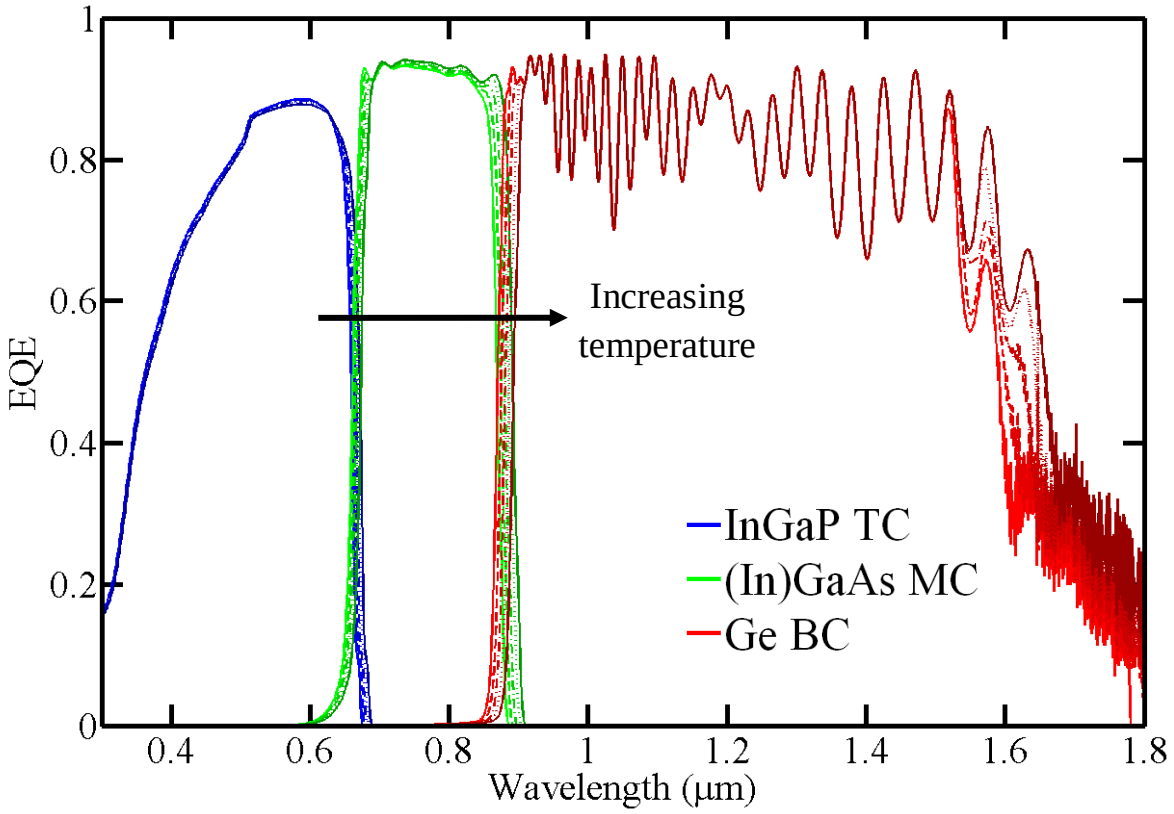

Figure 4-22. Simulated EQE of the standard lattice matched MJSC over temperature, where the band edges shift to longer wavelengths for increasing temperature. The EQE of the middle and bottom sub-cells shift to longer wavelength in both their short and long wavelength ranges as the temperature increases.

lower energies for increasing temperature. However, it is interesting to note that the increase in absorption range of the middle sub-cell is cancelled to some extent by the increase in absorption of the top sub-cell. As a result, the change in photocurrent of the full device over temperature depends on the interplay between the Varshni parameters of all materials. The magnitude of the EQE does not significantly change over temperature, predominantly due to the temperature independence of the minority carrier lifetimes. Further research is required to implement valid temperature dependence to carrier lifetimes.

Figure 4-23 illustrates how the various *J-V* metrics vary as a function of concentration for different operating temperatures. Performing this study for various temperatures is a method of gauging the performance drop as a function of concentration for different thermal

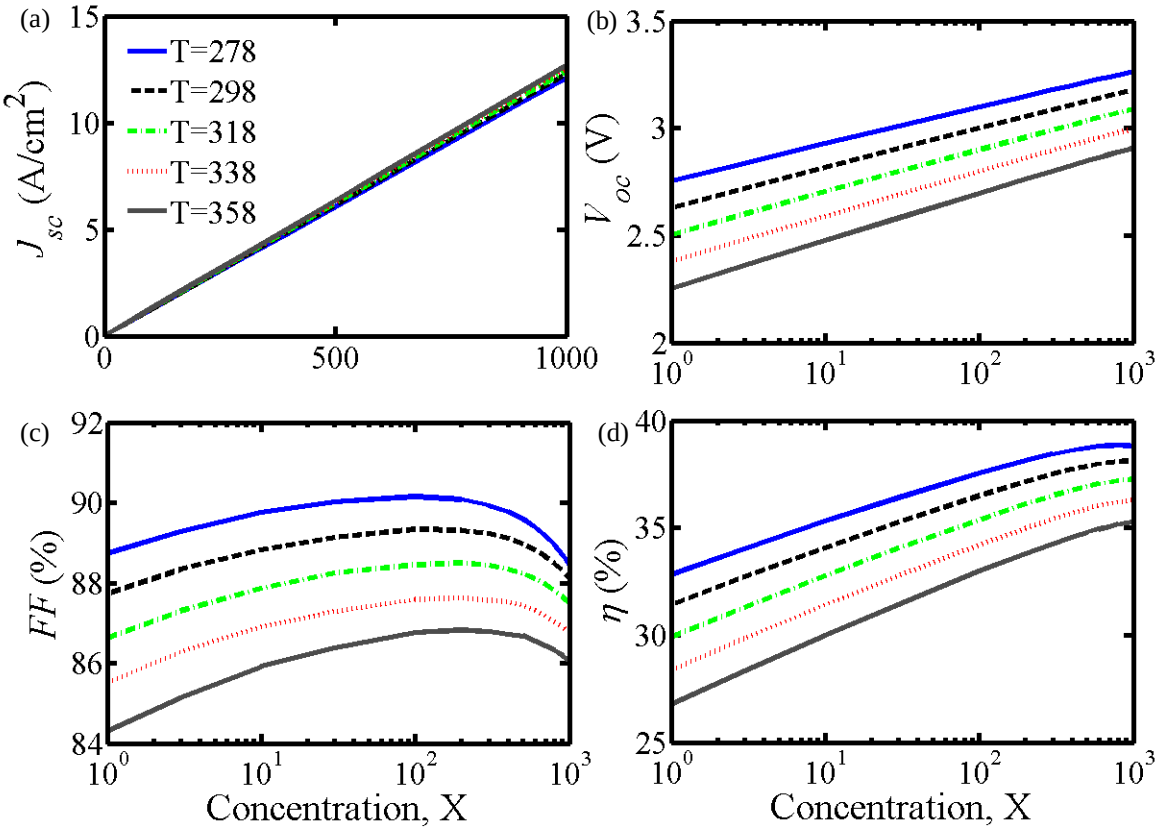

Figure 4-23. Simulated a) J_{sc}, b) V_{oc}, c) *FF* and d) efficiency (η) as a function of concentration for various temperatures. Note the photocurrent is on a linear concentration axis, whereas the other metrics are on a logarithmic axis.

management strategies of different efficiency. Figure 4-23a shows that the temperature has a very negligible impact on the MJSC J_{sc} as a function of concentration. However, Fig. 4-23b shows that the temperature has a pronounced effect on the V_{oc} as a function of concentration, which is reflected in the overall efficiency, as seen in Fig. 4-23d. The slope of V_{oc} as a function of X increases for increasing T due to equation (4.4.1); this is also reflected in the slope of efficiency as a function of X. Interestingly, the fill factor drops over the temperature range studied as a result of the drop in V_{oc}.

An important metric for the temperature dependence of a MJSC is the V_{oc} temperature coefficient, which has been studied theoretically [31],[127] as well as experimentally [5],[135],[136],[137], with typical values ranging between -4 and -7 mV/°C. Figure 4-24

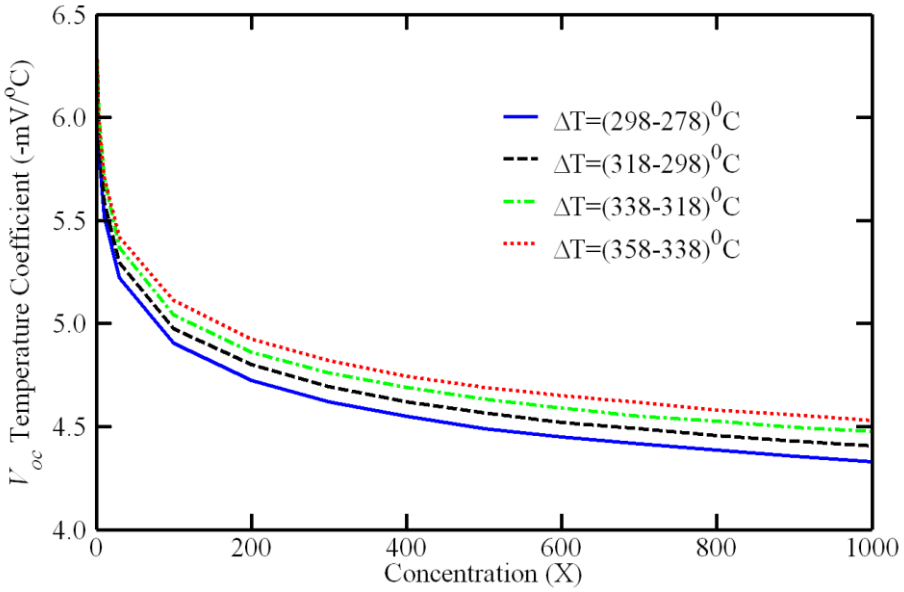

Figure 4-24. Simulated V_{oc} temperature coefficient as a function of temperature.

illustrates how the V_{oc} temperature coefficient changes as a function of concentration, and is in agreement with these studies. This demonstrates an important benefit of concentrated illumination on the open circuit voltage in that the drop in V_{oc} due to temperature is smaller at high concentration.

4.3.2.3. Tunnel Junction Limiting MJSC Performance

Tunnel junctions are essential in the successful operation of MJSCs under high concentration. Ideally, the J_{peak} is significantly higher than the J_{sc} of the solar cell such that the TJ's contribution to series resistance is minimal. As demonstrated in Fig. 4-19a, the J_{sc} of a MJSC scales linearly with concentration, which implies that specific conditions exist whereby the J_{sc} of the MJSC exceeds that of the TJ J_{peak}. This can occur if the TJ is performing poorly as a result of poor epitaxial growth, or if a MJSC is operated under levels of concentration well exceeding the targeted concentration range of operation [138]. In the regime where the TJ limits the performance of the device (i.e. the TJ limited regime), the behavior of the MJSC *J-V* characteristic has been shown to be considerably affected

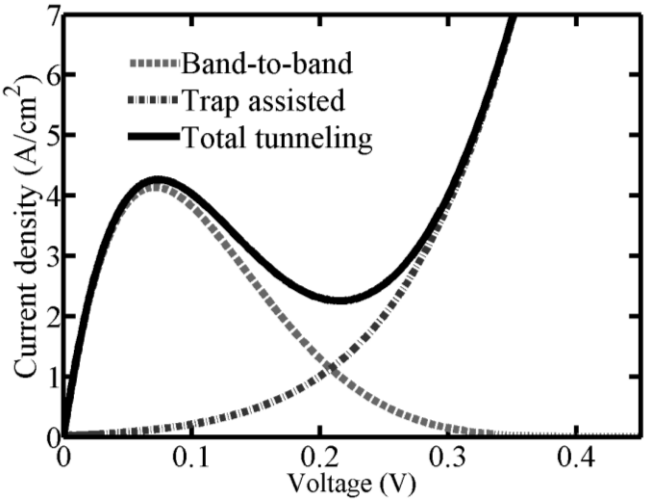

Figure 4-25. Simulated current density – voltage (*J-V*) characteristic of an AlGaAs/GaAs tunnel junction with contributions from the nonlocal band-to-band and trap assisted tunneling; the thermionic emission regime appears at voltages above 1.3 V. The design characteristics of this TJ are such that the J_{peak} is on the order of the J_{sc} at 500 suns illumination.

[138],[139],[140]. Such limitations greatly affect the efficiency as a function of concentration [108]. Although III-V semiconductor-based TJ have been reported with very high tunneling peaks > 1000 A/cm^2 with active doping levels on the order of 10^{20} cm^{-3} [20],[21],[141], designing TJ for MJSC applications for high light concentration involves the growth of tunnel junctions with the lowest practical and controllable levels of doping such as to achieve a minimal series resistance and maximal peak tunneling current densities [20]. The aspect of achieving such a minimum doping level becomes important when considering high volume manufacturing, where the epitaxial growth can be subjected to small fluctuations in the temperature distribution of the wafer due to the bow of the wafer as an example. This temperature distribution is important when considering the effects on dopant diffusion and how these are incorporated within the tunnel junction layers. Since the TJ characteristics vary greatly as a function of doping levels [20], such non-uniformities can lead to unintentional variations in doping throughout the TJ. A study is therefore required to demonstrate and quantify the effects of TJ-limited MJSC performance as a function of

concentration based on the main components of the TJ characteristics (J_{peak} and J_{valley}). This section of the thesis on TJ-limited MJSC is a summary of work published by the author [23].

The simulated *J-V* characteristics of an AlGaAs/GaAs tunnel junction are illustrated in Fig. 4-25 and correspond to a structure given in Table 4-1 with the exception that the *p++* doping level is reduced from 4×10^{20} cm^{-3} to 2.5×10^{19} cm^{-3} to decrease the peak tunneling current density for the purpose of studying the effects of a MJSC with a $J_{sc}(X) > J_{peak}$. The tunneling parameters for GaAs and AlGaAs are set to the same values chosen in section 4.2.1.3 (see Fig. 4-6 and 4-8), and to generate excess currents that would influence the operation of the MJSC *J-V* characteristic. A physical scenario representative of such a low J_{peak} could be realized if a high level of trap states exists within the TJ layers, while the B2B tunneling remains as the dominant mechanism contributing to J_{peak}. The AlGaAs/AlGaAs tunnel junction (see Table 4-2 and Fig. 4-8), is used as the top tunnel junction in the MJSC and does not limit the overall performance. The bottom tunnel junction, however, is studied for two cases: 1) the *p++* doping concentration is 4×10^{20} cm^{-3} based on [121] to represent the ideal case where $J_{peak} \sim 1600$ A/cm^2 >> $J_{sc}(X<1000)$, and 2) a *p++* doping level of 2.5×10^{19} cm^{-3} to lower the $J_{peak} \sim J_{sc}(X=500)$. In both scenarios, the full MJSC *J-V* characteristics are obtained by adding the individual characteristics of the sub-cells and the TJ together as devices connected in series (see Fig. 4-10). Forward and reverse biasing of the limiting TJ has been observed to result in a hysteresis [140] which arises from the NDR region. Identifying each as a separate *J-V* characteristic added to the remaining sub-cells can be handled realistically based on [21]. It is important to note that the numerical simulation environment (primiarly SDevice) has difficulty solving the system of equations for the full device when nonlocal TAT is considered in the TJs (reasons unknown; the source code is

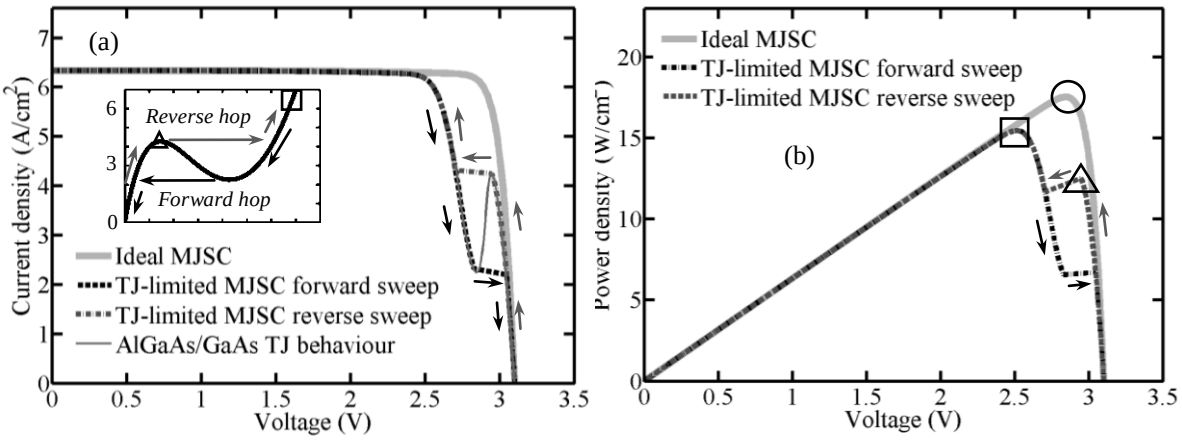

Figure 4-26. Simulated forward and reverse biased a) *J-V* and b) *P-V* characteristics of a standard InGaP/InGaAs/Ge MJSC at 300 K under the AM1.5D spectrum (900 W/cm^2) concentrated by a factor of 500 with and without limitations from the bottom AlGaAs/GaAs TJ (see Fig. 4-6 and inset plot). For the TJ limited MJSC, the TJ *J-V* characteristic is superimposed within the MJSC *J-V* curve. In both cases, the direction of the sweep is indicated by arrows. Three maximum power points (MPP) are illustrated in (b): the ideal (circle), forward sweep (square) and reverse sweep (triangle). The inset plot in (a) illustrates the hopping behaviour within the TJ *J-V* characteristic.

not available). General troubleshooting was unable to clarify this issue. Future work could emphasize the optimization of the SDevice code which struggles to find convergence due to the nonlocal TAT models as a recombination process. However, the virtual contact approach can solve the individual sub-cell and TJ components within the full device. As a result, the individual *J-V* characteristics can be added together in series to obtain the complete behavior representative of the full MJSC. It is assumed that the virtual contact approach provides an accurate depiction of the complete *J-V* characteristic based on the equivalent circuit diagram of Fig. 4-10.

The *J-V* and *P-V* characteristics of the MJSC at an intensity of 500 suns concentration at 300 K are illustrated in Fig. 4-26 without the limiting effects of the tunnel junctions ("Ideal MJSC"). The *J-V* metrics of this device include a J_{sc} of 6.34 A/cm^2, a V_{oc} of 3.10 V, a FF of 89.2% and an efficiency of 39.0%. When the p++ doping layer of the bottom AlGaAs/GaAs TJ is reduced to lower J_{peak} from 1600 A/cm^2 to just over 4 A/cm^2, the MJSC

performance enters the TJ-limited regime. Furthermore, the *J-V* characteristics become strongly dependent on the biasing because of the instability of the NDR region, as seen in Fig. 4-26a. A forward sweep of the MJSC (thus starting from its J_{sc}) dictates the tunnel junction to operate in the excess current region (i.e. at a current density of 6.4 A/cm^2). As the current density of the MJSC decreases from J_{sc} to its current density at its maximum power point (*MPP*), the operating point of the tunnel junction must *hop* from the J_{valley} in the excess current to the same current level within the band-to-band tunneling region, in agreement with [139]. This process is outlined in the inset of Fig. 4-26a. On the other hand, a reverse sweep of the MJSC results in the operating point of the TJ to lie in the direct B2B tunneling regime initially, until the current density of the MJSC surpasses the J_{peak}. Once this occurs, the operating point of the TJ once again *hops* to the excess current region, which offsets the voltage output of the device considerably, as seen in the reverse sweep illustrated in Fig. 4-26a and 4-26b. The directionalities of the forward and reverse sweeps are illustrated as black and grey arrows respectively. Different maximum power points for the ideal and TJ limited MJSCs are visible in Fig. 4-26b (outlined as a square for the **primary** *MPP* at the smallest voltage, a triangle to represent the **secondary** *MPP* only present in the reverse sweep, and a circle for the **ideal** *MPP*). The efficiency drop at 500 suns for the ideal and TJ limited MJSC is 5.5% absolute arising from a decrease of 12% absolute in fill factor.

Another way of understanding the corresponding voltage drop of the TJ-limited MJSC is through the simulated energy band diagrams at the two important operating points (J_{peak} in the B2B tunneling regime and the corresponding magnitude of J_{peak} in the excess current regime of the TJ), which are illustrated in Figs. 4-27a and 4-27b respectively. An optimal energy band alignment between the VB and CB of the p++ and n++ respectively is

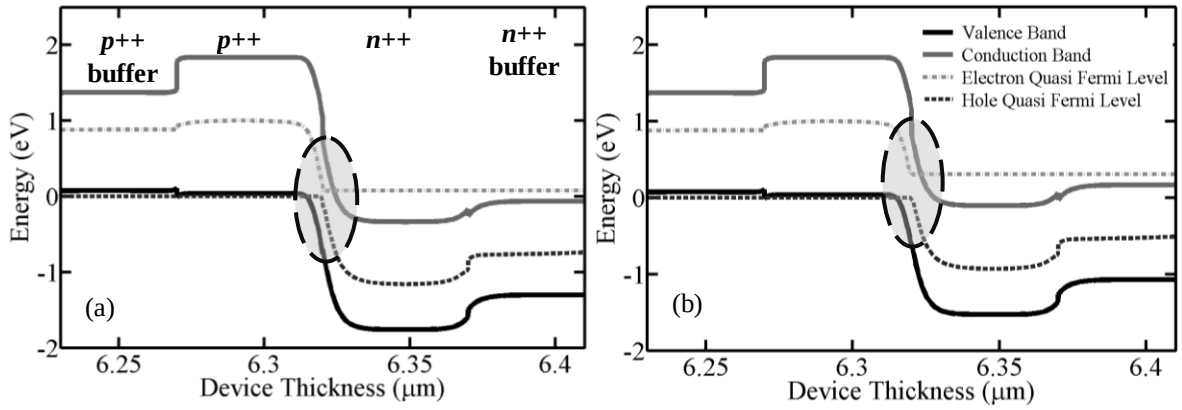

Figure 4-27. A close up of the simulated energy band diagram of the AlGaAs/GaAs TJ within the MJSC at a) J_{peak} within the direct tunneling regime, and b) J_{peak} in the excess current regime to outline the band alignment and misalignment at each operating point respectively, and the associated voltage drop. The difference in quasi-Fermi levels at the *p*++/*n*++ interface reveal the drop in voltage, as outlined by the dashed ovals.

observed in Fig. 4-27a, which corresponds to the direct band-to-band tunneling. On the other hand, Fig. 4-27b shows energy bands that are far from optimally aligned: carriers tunnel across the potential barrier primarily through trap assisted tunneling at a large applied voltage. When comparing Fig. 4-27b compared to 4-27a, one can observe the larger difference in carrier quasi-Fermi levels at the *p*++/*n*++ interface (as outlined by the dashed oval), which leads to an increase in the energy levels on the *n*-side of the TJ. Due to the constraint that the quasi-Fermi levels must be continuous across the full device, this leads to a decrease in potential energy difference between the bottom sub-cell and the middle sub-cell, which ultimately reduces the overall potential energy difference with the top sub-cell. This decrease in overall potential energy can be seen as a drop in voltage.

This study can be performed as a function of concentration for both the ideal, non-limiting TJ behavior as well as the TJ-limited MJSC regime to give insight into the trends in efficiency as a function of concentration. This is illustrated in Fig. 4-28a for three TJs with low, medium and high J_{peak} to explore the dependence of J_{peak} on the efficiency as a function of concentration. The corresponding TJ characteristics are illustrated in Fig. 4-28b. These TJ

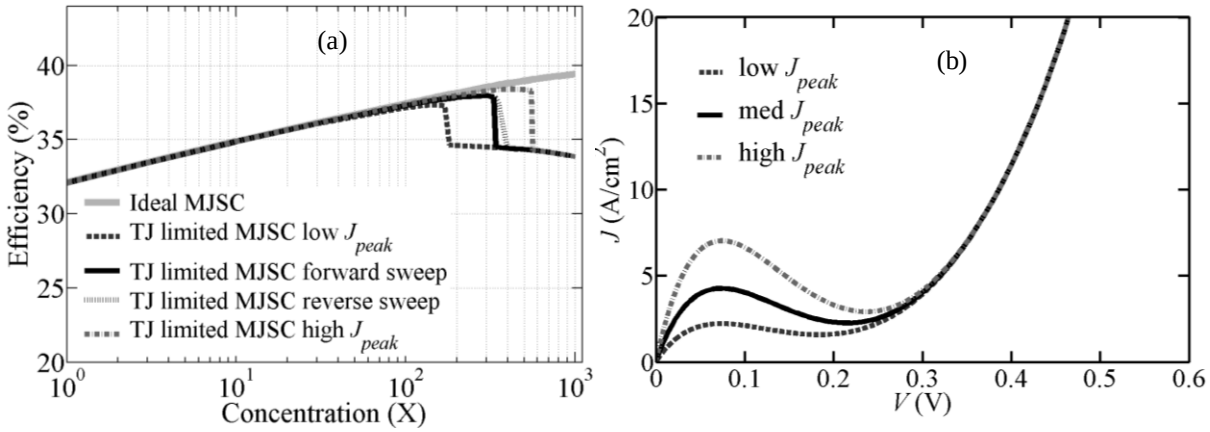

Figure 4-28. Simulated a) efficiency of the ideal and TJ limited MJSC over concentration for the three AlGaAs/GaAs TJs illustrated (b) for low, medium and high J_{peak} considerations, and b). For the medium J_{peak} scenario, the efficiency for forward and reverse sweeps is illustrated to show the effects of the hysteresis on the efficiency.

J_{peak}'s correspond to p++ doping levels of 2.25×10^{19} cm^{-3} and 2.75×10^{19} cm^{-3} respectively, although the J_{peak} was controlled simply by changing the electron tunneling masses in order to keep the same valley currents.. The ideal case (where the TJ J_{peak} >> $J_{sc}(X)$) shows the expected characteristics in efficiency as a function of concentration, similar to Fig. 4-19. However, when the TJ starts to limit the MJSC efficiency, the trend begins to deviate from the ideal case as the J_{sc} ramps up closer to the J_{peak} for a concentration approaching 100 suns. This deviation is initially small since the fill factor drops only slightly from the added series resistance from the limiting TJ. However, once the J_{sc} surpasses the J_{peak}, a significant drop in fill factor and thus efficiency is observed at a concentration close to 330 suns (based on the TJ with the medium J_{peak}). The hysteresis results in a different drop in efficiency for the forward and reverse sweeps (see Fig. 4-26). Interestingly, the drop is observed to be less severe in the reverse sweep scenario since the reverse has two *MPPs*, whereas the forward sweep only has one. Once the secondary *MPP* in the reverse sweep becomes smaller than the primary *MPP*, the efficiencies converge. This result outlines how a maximum power point tracker in a real concentrator system must be capable of differentiating between local

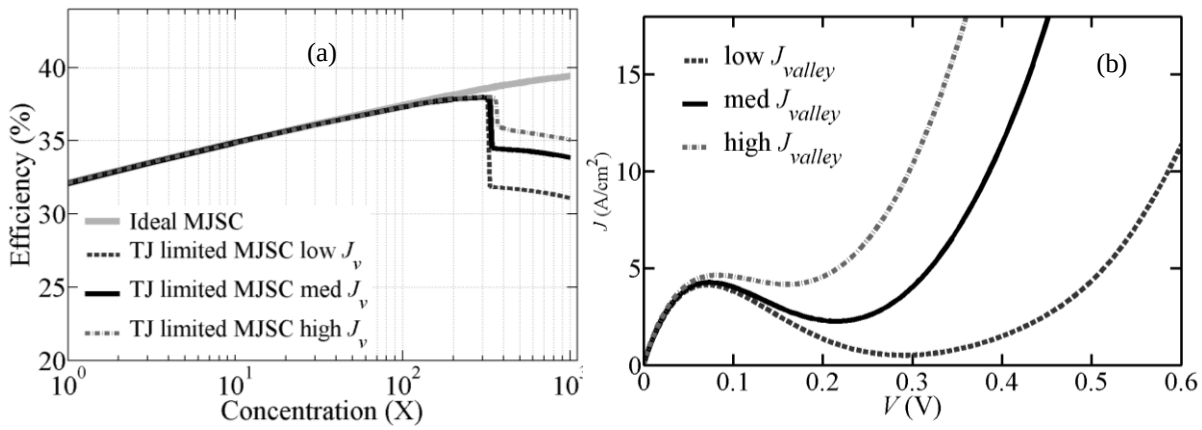

Figure 4-29. Simulated a) ideal and TJ limited MJSC efficiency over concentration for three AlGaAs/GaAs TJs illustrated in (b) for low, medium and high J_{valley} considerations.

power maxima in the TJ-limited MJSC regime.

As the AlGaAs/GaAs TJ peak tunneling current increases due to an equivalent p++ doping increase from 2.25×10^{19} cm^{-3} to 2.75×10^{19} cm^{-3}, the concentration required to show a drop in device efficiency increases from 170 suns to 550 suns; in other words, the drop in efficiency appears at a higher concentration for a TJ with a higher J_{peak}, as one would expect. Growing an AlGaAs/GaAs TJ which generates a $J_{peak} > J_{sc}$(X=1000) ~ 12.7 A/cm^2 requires a p++ doping level of at least 3.25×10^{19} cm^{-3} for a n++ doping level of 2×10^{19} cm^{-3}. Even at this doping, however, the MJSC will still experience a drop in fill factor compared to an ideal TJ, since the J_{peak} is comparable to J_{sc} at 1000 suns. Ideally, the TJ J_{peak} is significantly greater in magnitude compared to the J_{sc}, which requires a p++ doping level of 5×10^{19} cm^{-3} for this calibrated AlGaAs/GaAs TJ model.

The drop in efficiency for tunnel junctions of different valley currents but similar J_{peak} is illustrated in Fig. 4-29a, with the corresponding limitng TJ J-V characteristics shown in Fig. 4-29b for low, medium and high J_{valley}. A TJ with a high trap concentration within the active TJ layers would allow for an increase in J_{valley} without significantly affecting J_{peak}, assuming J_{peak} is dictated by the ideal B2B tunneling and not resonant tunneling through

defects. The question of whether resonant tunneling through defects would dominate ideal B2B tunneling merits further analysis, since both models are influenced by fitting parameters which have not been fully calibrated to experimental devices of varying trap and doping concentrations. The excess current of these three TJs is controlled using the Huang-Rhys factor because the trap concentration does not enter the formalism explicitly. In the case of a TJ with a low valley current (corresponding to a large Huang-Rhys factor of *S=8* for GaAs and *S=9* for AlGaAs), the drop in efficiency is highest compared to the TJs with medium (*S*=5.5 for GaAs and *S=8* for AlGaAs) and high J_{valley}*'s* (*S=5* for GaAs and *S=8* for AlGaAs). A lower J_{valley} results in a higher potential drop across the limiting tunnel junction, as seen in Fig. 4-29b. A 6% absolute drop in efficiency is observed for the TJ with a low J_{valley} when the J_{sc} initially surpasses that of the J_{peak}. This drop is reduced to 3.4% absolute for the TJ with the medium J_{valley}, and is further reduced to 1.9% absolute for the TJ with the high J_{valley}. A high J_{valley} is therefore important for MJSC limited by a TJ, as shown experimentally in [108]. Furthermore, larger trap concentrations within the TJ reduce the efficiency drop within the TJ limited MJSC regime. However, for MJSC grown with good TJ that do not limit the device performance, the excess current will have no effect on the device.

Chapter 5: Quantum Dot Enhanced Multi-Junction Solar Cells

The issues of current matching and optimizing device performance are a central issue in the photovoltaics community for advancing the performance of the state-of-the-art. It is worth noting that current matching at the short circuit current is not always necessarily the aim of MJSC designers, since it depends highly on the fill factor of each sub-cell; for more details, see [142]. Several approaches have been suggested in the literature such as metamorphic multi-junction solar cells (as discussed in Chapter 4) and alternative substrates such as silicon in an epitaxial configuration [143] or using a mechanical stacking approach [144]. However, the benefits of integrating bulk lattice mismatched materials (i.e. obtaining an ideal bandgap combination) are hindered by the complexities in the growth of high quality materials (such as the formation of dislocations and their effects at high concentration). A similar alternative to these strategies is embedding quantum structures in the limiting sub-cell's design to extend that sub-cell's absorption range. This allows device designers to increase the photocurrent in this sub-cell through a re-optimization of the top sub-cell, which allows for an overall increase in the full device photocurrent. However, these quantum structures must be optimized specifically to target sub-bandgap photons whilst minimizing any degradation effects.

A strong candidate for such quantum structures are $In_xGa_{1-x}As/GaAs$ quantum dots targeted for integration into the middle sub-cell of a triple InGaP/InGaAs/Ge solar cell. Prior

to modeling these quantum dots, however, a literature review is necessary to understand the growth of these structures, their optical characteristics, the carrier dynamics in the QD, and lastly, how QD compare to other structures such as quantum wells on photovoltaic performance. This literature review is summarized in section 5.1. This information and knowledge is then used to create a model of InAs QD in TCAD Sentaurus, a topic discussed in section 5.2. Section 5.3 focuses on simulations of the said triple junction solar cell enhanced with QD in terms of the EQE and *J-V* characteristics for different approaches to simulating the carrier dynamics. These simulation results are also compared to a similar commercially available product manufactured by Cyrium Technologies Inc. as a partial calibration. A study on the positioning of the QD layers within the middle sub-cell is also performed in section 5.4, and also considers differences in the background doping of the InGaAs spacer layers. Finally, section 5.5 discusses the optimization of the said triple junction solar cell based on varying the number of QD layers and the effects on the *J-V* metrics.

5.1. Literature Review on InAs/GaAs Quantum Dots and Wells

One of the most commonly used quantum dot (QD) systems for applications in III-V semiconductor devices is the InAs/GaAs QD system, mostly referred to as $In_xGa_{1-x}As/GaAs$ [51],[145],[146],[147],[148],[149],[150],[154],[156],[157],[158],[159],[164],[165],[166],[167],[168],[169],[170],[171],[173]. This material system exploits the Stranski-Krastanov self-assembly growth process. When a critical thickness of InAs is deposited on GaAs, the InAs layer undergoes a morphological transition from a quantum well (referred to as a wetting layer) to a quantum dot (a zero dimensional InAs island) as the strain present at the

InAs/GaAs interface relaxes; the wetting layer (WL), which is typically 1-2 monolayers in thickness, is omnipresent throughout this process and exhibits two-dimensional confinement properties. The high degree of control in InAs island size and shape leads to highly tunable photoluminescence peaks [148],[149],[150],[151]. The high crystal quality of these QD has been shown to result in ultra-sharp spectral lines, which clearly outlines the strong 0D characteristics arising from the QDs [51],[146],[148],[149],[150],[151]. The InAs/GaAs material system is therefore a combination of a weakly two-dimensional confining potential (the wetting layer) and a strongly zero-dimensional confining potential (the InAs islands, or QDs). Applications of these structures range from infrared lasers to photo-detectors to photovoltaic devices. This section is a summary of a literature review which focuses on the following topics with an emphasis on photovoltaics: a) optical and structural properties of these precise QD systems using specific growth techniques, b) the optical properties based on energy band structure calculations and absorption characteristics, c) radiative and non-radiative recombination lifetimes reported in the literature based on time resolved photoluminescence (TRPL), d) carrier dynamics (capture and escape times, as well as intra-band relaxation processes), e) the breakdown of thermionic emission in small quantum wells, f) discussions on IR photo-detectors made of QD and quantum wells (QWs),which serves as a comparison between the use of QD and QW for photovoltaic applications and leads to section g) which outlines some conclusions from this literature review.

5.1.1. Growth Techniques for the Refinement of Structural and Optical Properties of Nanostructures

5.1.1.1. InAs QD

Several papers have been published in the literature discussing the effects of a rapid thermal anneal and an indium flush technique on the structural and optical properties of InAs QDs grown using the Stranski-Krastanov growth process [146],[147],[148],[149],[150],[151]. The rapid thermal anneal is a post-growth thermal treatment that has been shown to cause a significant narrowing and blue-shift of the photoluminescence (PL) emission peaks of the QDs. The rapid thermal anneal treatment involves raising the substrate temperature to 700-900^{0}C. The effects appear to be agreed upon in the literature: the higher temperature causes an inter-diffusion between Ga and In atoms, such that the QDs become smaller and more disk shaped. The reduction in size causes an increase in confinement which increases the confined energy levels and therefore results in a blueshift of the PL emission. It has been shown that these blue-shifted peaks can be very close to the bulk GaAs energy gap [147]. However, annealing temperatures of greater than 850°C caused a disappearance of the QD (as observed from cross-section transmission electron microscopy) [146]. Interestingly, the PL peak was still present and shifted closer to the wetting layer peak. The authors claim that this structure is QW-like. Furthermore, annealing temperatures above 900^{0}C caused an increase in dislocation densities and resulted in a disappearance of the PL peak altogether, which implies two things: 1) the disappearance of the QD altogether, and 2) significant non-radiative recombination centers originating from the dislocations.

The indium flush technique, on the other hand, has been shown to give an extra degree of control over the size and shape of the QD without reducing any crystal quality [148],[149],[150],[151]. The step involves an interrupt during the growth of the GaAs capping layer above the InAs wetting layer. During this growth interrupt, the substrate temperature is raised rapidly to ~610°C to remove any indium content from the growth front. The temperature of the substrate is then brought down to approximately 515°C. This growth interrupt allows the QD to evolve to an equilibrium shape. Furthermore, the sizes of the QDs become more uniform, which causes a significant narrowing of the PL peak if measured from the ensemble of QDs. The reproducibility of this technique has been shown from sample to sample, where the QD energy levels shift in a predictable manner based on the depth of the indium flush and the final size of the dots [148]. An important aspect of implementing the indium flush technique is the successful growth of vertically uncorrelated stacks of up to 50 layers of InAs QD within a GaAs matrix with high quality [152], as displayed by state-filling spectroscopy measurements at liquid nitrogen temperature (T=77K) [149]. Furthermore, a minimum separation of ~8 nm of GaAs is required to minimize wave-function coupling between adjacent QD layers [149].

5.1.1.2. InGaAs QWs

In the case of AlGaAs/GaAs QW solar cells, the lattice matching of the two materials does not require any strain compensation strategies during the epitaxial growth. However, in the case of QWs composed of $In_xGa_{1-x}As$ embedded in a GaAs matrix, the lattice mismatch is important and specific strain compensation strategies are required to minimize strain relaxation processes such as the formation of dislocations [153]. Growing alternating tensile and compressively strained layers with specific alloy composition (ex: $GaAs_{0.91}P_{0.09}$) and

thicknesses is one method of doing this, which involves meticulous optimization of the growth parameters. A publication by Fraunhofer ISE has shown these strain compensation layers allow for the growth of up to 50 high quality QW layers in a GaAs solar cell [30]. Although this study focused on the successful calibration of the simulated external quantum efficiency to experimental measurements, which is indicative of accurately simulating the J_{sc} of their solar cell, no current – voltage characteristics were reported. It is therefore difficult to explore the added benefits of increasing the photocurrent of this QW solar cell when the expected degradation of the open circuit voltage is not reported.

5.1.2. Optical Properties of QD: Band Structure and Corresponding Absorption Properties

5.1.2.1. Band structure

In order to study the optical properties of a QD system, i.e. the energies at which the QDs emit and absorb, one needs to study the energy band structure of the QD with strain considerations. Two central papers address the energy band structure of InAs QD within a GaAs matrix [51],[154] in significant detail. Korkusinski and Hawrylak [154] discuss the simulation of the electronic structure of vertically stacked self-assembled quantum disks with considerations of strain assuming the effective mass approximation, and discuss the effects of strain on the potential barriers present in the conduction and valence band at the interface of the QD as well as the electronic energy levels. They use an exact diagonalization technique to solve the large Hamiltonian matrices involved using the 8-band **k·p** method. Bruno Riel [51] was able to extract conduction and valence band offsets with strain considerations, the bandgap of the QD at T=77K, and the electron effective mass. In his paper, he derives the energy levels of QD grown under the Stranski-Krastanov growth

process based on sizes achievable with an indium flush and with strain considerations. These band offsets and the bandgap of the QD are used in section 5.2.1 to determine the absorption characteristics of the QD in the developed model.

Popescu, Bester and Zunger [155] focuses on the energy band and energy level configurations with considerations of QD dimensions under strain in the presence of a wetting layer. In this paper, the authors adopt an atomistic pseudopotential approach for the band structure calculation. The shape of the potential barrier is obtained by allowing the strain around each atom to relax such as to minimize the strain energy using a generalized valence force field functional. Once the pseudopotential and relaxed positions of each atom are obtained, the authors solve the single-particle Schrödinger equation with spin-orbit coupling to study the energy levels and wavefunctions of electrons and holes. The authors study the most important carrier transitions in the system, which are of vital importance in studying the absorption spectrum of InAs QD (see Figure 1 of [155]). These include both interband transitions between energy levels with the same quantum number, intraband transitions from confined states within the QD to strain induced localized states (SILS), and cross transitions between a WL state and a QD confined state. The authors conclude that cross-level transitions can be ignored as they fall within the bulk (or continuum) transitions of GaAs. In essence, this paper discusses the **optical coupling** between the WL and QD, and serves as a strong guideline in evaluating the important contributions to the absorption coefficient in the later developed model discussed in section 5.2.1.

5.1.2.2. Absorption properties

Popescu [155] brings great insight into the various carrier transitions that are important in this QD system. However, these transitions must be related to an absorption

profile for the material system. One paper discusses an analytical approach to deriving the absorption profile of semiconductor QDs, written by Ferreria and Alves [52]. The authors use the effective mass approximation for the envelope wavefunction of the carriers, and based on an infinite potential, they solve Schrödinger's equation in three-dimensions for the energy levels. They then obtain an analytical equation for the absorption coefficient representing a size distribution of spherical shaped QDs. An important assumption in these analytical approximations is that the Coulombic interactions of the carriers are deemed insignificant due to the small dot size and the small mixing of heavy and light-hole bands. By applying a Gaussian spread to the sizes of the QD, they derive an analytical absorption coefficient which they study as a function of size and shape of the QDs. This approach is adopted in this study as a template to use the energy levels resulting from a lens shaped QD, which depend on size, shape and strain considerations (the latter being based on CBO, VBO and effective masses based on Riel's paper [51]). An analytical absorption coefficient is then derived taking into account the density of QD per layer, as discussed in section 5.2.1.

An important parameter in dictating the magnitude of the absorption is the optical matrix element for each transition between allowed energy levels, which is analogous to the oscillator strength of the transition. This matrix is a measure of the overlap between the wavefunctions of the states involved in the transition. Initially, one would expect this to be zero due to the orthogonality of the electron and hole wavefunctions in the conduction and valence bands. However, the optical matrix element involves the derivative of the wavefunction with respect to the carrier momentum (or k-vector) which renders the element non-zero. The value of this optical matrix element requires significantly complex calculations (i.e. solving for the wavefunctions of each energy level with strain

considerations), and is highly dependent on the size of the QD, the shape of the energy bands due to strain, as well as the magnitude of the electric field (which warps the wavefunctions). The results of a paper by Johansen *et* al [156] can be used to extrapolate the optical matrix element based on the sizes of dots we are interested in. However, COMSOL simulations are used to compute these based on the aforementioned dependences. A good review of the optical matrix element's dependence on quantum dot parameters (ex: height) is the paper by A. D. Andreev and E. P. O'Reilly [157].

Another important aspect of the absorption of InAs/GaAs QD systems is the contribution from the wetting layer. The WL acts as a weakly confining two-dimensional potential, or a quantum well, and is typically on the order of 1-2 monolayers (ML) thick; this corresponds to a thickness on the order of 2 times the interatomic spacing of the relaxed InAs atoms, which should correspond to twice the lattice constant of the substrate (GaAs): $2\times5.65\text{Å} \approx 1.1$ nm. This WL gives rise to confined energy levels and therefore resonance energies in absorption. A similar derivation to the QD absorption characteristics is performed considering the density of states of a QW (a step function expressed as the Heaviside function). An analytical approximation is used to compute the confined energy levels in a finite potential square well, and integrated over a Gaussian spread in energy levels to account for thermal broadening. The final result for the analytical expression is an error function, which is discussed in section 5.2.1.

5.1.3. Recombination Lifetimes

5.1.3.1. Radiative

As seen in chapters 3 and 4, radiative and non-radiative recombination lifetimes of minority carriers are crucial parameters for solar cell device operation. The radiative

lifetimes of ground state interband transitions in InAs QD have been reported in the literature for various temperatures using time-resolved photoluminescence, which shows an extremely fast increase in PL intensity on the order of pico-seconds, followed by an exponential decay. Fitting this exponential decay to a time decay rate gives rise to a radiative decay rate which has been reported throughout the literature to be on the order of 1 ns or less. For solar cell applications, a reference from the literature which points to a radiative lifetime of 1 ns is adopted in this study [156]. This reference also points to a non-radiative decay rate of 0.11 ns^{-1}, or a non-radiative recombination lifetime of ~9 ns. As a comparison, another study conducted on the exciton dynamics in $In_{0.2}Ga_{0.8}As$/GaAs QW heterostructures demonstrates room temperature measurements of radiative recombination lifetimes of 10^3 ns and in another similar QW system, 10^4 ns [158]. However, these long lifetimes would be dominated by the QD lifetimes, which is why the 1 ns lifetime is adopted in these studies.

5.1.3.2. Non-Radiative

The non-radiative lifetime of carriers in InAs QD within a GaAs matrix is studied in [159], which concludes a non-radiative recombination rate of 10^8 s^{-1}, or a non-radiative recombination lifetime of 10 ns. Since the result from this paper is in agreement with Johansen *et al.* [156], a non-radiative recombination lifetime of 10 ns is adopted in this thesis. Interestingly, the study conducted on InGaAs/GaAs QW heterostructures show non-radiative recombination lifetimes on the order of 40 ns (with no AlGaAs barrier materials) to 0.1 ns (with AlGaAs barrier materials) [158]. These barrier materials thus appear to increase the concentration of non-radiative recombination centres at the interface between the barrier material and the QW, which drastically reduces carrier lifetimes. Ramey and Khoie [59]

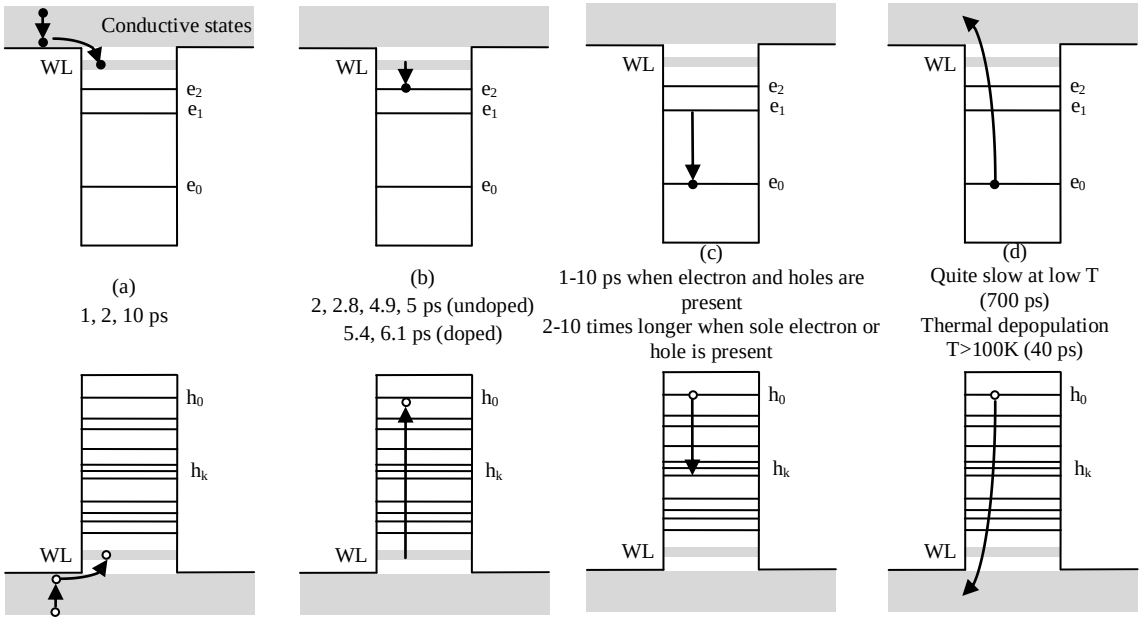

Figure 5-1. Different relaxation processes in InAs/GaAs QD: a) Carrier capture by the wetting layer from the barrier, b) transition from the confined energy levels of the wetting layer to the second excited state of the QD (e_2), c) relaxation between excited state to ground state within the QD (e_1 to e_0) via Auger scattering, i.e. from the P orbital to the S orbital, and d) thermal escape from the ground state (e_0) of the QD to the bulk states. This plot is adopted from [159].

conclude that non-radiative recombination processes dominate at room temperature, and therefore neglect radiative recombination in the well; they refer to a paper by Gurioli *et al.* [160]. This further indicates that the strain compensation strategies aimed at QW solar cells have an important drawback as these layers, if not properly optimized, can significantly degrade solar cell operation.

5.1.4. Carrier Dynamics

The carrier dynamics in InAs/GaAs QD systems are highly complex, since they depend on a number of important parameters such as temperature and the number of confined energy levels, the latter depending on QD size and the strain present in the system. Based on a literature review, most studies consider fairly large QD (15 nm width by 10 nm height) such that they contain more than 4 confined energy levels for electrons and holes

respectively. Due to the larger mass of the heavy hole compared to the electron (see Cusack *et al.* who predict a heavy hole effective mass of $m_h^*=0.59m_e$, whereas the electron effective mass is $m_e^*=0.063m_e$ [161]), and the smaller confinement strength of the potential, the heavy hole energy levels are much closer together than the electronic levels in the conduction band [162]. This is represented schematically in Fig. 5-1, which is also adopted from Figure 1 of [162]. This paper gives a very good overview of the various processes that are outlined in Fig. 5-1, which are: a) carrier thermalization within the barrier (sub-picoseconds), and subsequently carrier to wetting layer carrier capture (~2 ps), b) carrier capture from the wetting layer into the QD (undoped QD: 2, 2.8, 4.9 and 5 ps as measured experimentally, and for doped QD: 5.4 and 6 ps), c) relaxation of excited carriers within the dot (central issue of the paper, discussed in more detail in the next paragraph), and d) thermal escape of carriers from the dot.

The central topic of Narvaez *et al.* [162] is the relaxation mechanisms corresponding to case c) of Fig. 5-1: intraband relaxation within the QD between the P (n>1) and S (n=1) orbitals. If the QD has an electron and hole present in the CB and VB respectively, the dominant relaxation mechanism is Auger relaxation via electron-hole scattering. Since this process is temperature independent (the rate-limiting step is the electron relaxation), the electron-hole scattering can take place efficiently and quickly, on the order of 1-10 ps. The results of this theoretical paper are in agreement with experimental results [160]. Otherwise, the relaxation of a carrier within the dot occurs through carrier-phonon scattering. This occurs on a very short time period for holes since the hole energy levels are closely spaced such that acoustic phonons satisfy the conservation of energy in the scattering process, even at low temperatures.

Modulation doped QD, or populating the QD with a specific type of carrier by growing a highly doped layer of GaAs adjacent to the QD material, is another interesting avenue for controlling the relaxation mechanisms in the QD [163],[164],[165],[166]. The methodology of these papers is of interest to understanding carrier dynamics, so let's take a moment to describe this here. A tunable laser is typically used in these studies composed of Ti:sapphire (wavelength range: 700-1040 nm) which can be used to probe the GaAs barrier, the wetting layer or the QD energy levels. The photoluminescence (PL) rise time upon illumination is of interest in these studies, and the analysis depends predominantly on the laser wavelength. For example, the photo-excitation of carriers at ~800 nm implies carriers are generated in the GaAs barriers, and must therefore be transported to the WL before being captured, relaxing and subsequently photoluminescing in the QD. For a lasing wavelength of ~870 nm, the carriers are excited into the WL, and from this point, relax to the confined energy levels of the QD before finally recombining via photon emission. Lastly, photo-excitation at ~960 nm probes the QD transition, whereby carriers relax to the ground state and finally recombine radiatively. Of course, there is non-radiative recombination taking place, but this process does not contribute to the photoluminescence.

In these studies, *p*-type modulation doping of the QD was shown to enhance the QD hole population at room temperature, which enhanced the electron-hole scattering rates that acted as the dominant intra-dot relaxation process. The *n*-type modulation doping scenario also showed enhanced relaxation times. In all cases, undoped QD layers had the longest relaxation times since electron-hole scattering was not as effective. Note that this process is not the same as carrier capture by the WL (process b) in Fig. 5-1, which shows longer capture times for doped QD. In all of these papers, no temperature dependence on the carrier

relaxation time was found, since the energy level spacing was large compared to the bulk GaAs longitudinal optical (LO) phonon energy. One of these studies concluded that the modulation doping of QD also increased non-radiative recombination centres [163]. A study conducted by Morris *et al.* [166] demonstrated that the undoped InAs QD PL rise time was dependent on excitation energy. The authors therefore argued that the dominant relaxation process was also Auger scattering. Furthermore, an interesting study conducted on the electron capture cross-sections of InAs/GaAs quantum dots [167] concluded that this cross-section was 3-4 orders of magnitude larger than the actual size of the QD. This implies that the carriers can also be captured by the wetting layer, and subsequently captured by the QD on a fast time scale.

Another study, however, obtained different conclusions [168] where the dominant relaxation process in doped QD was temperature dependent, which implies the rate-limiting step involved carrier-phonon scattering. The QDs involved in this study had confined energy states for the electron (e_1-e_0) with energy separations on the order of the LO phonon energy in bulk GaAs (~30 meV), whereas the previous papers had energy differences that were large compared to the LO phonon energy. As a result, the decay time did vary as a function of temperature. Furthermore, the decay time was found to be independent on excitation density, which implies carrier-carrier scattering was not important in the carrier dynamics.

Lastly, and most importantly for photovoltaic applications, is the thermal depopulation of carriers from the confined energy states into the bulk continuous states. A paper by Urayama *et al.* [169] claims that when temperature increases, the re-emission and non-radiative recombination play a more important role in the carrier dynamics. Electron-hole scattering can be important at lower temperatures (shown by a dependence on excitation

power), but at higher temperatures, the data suggest that carriers are easily escaping the confinement level, which results in escape times decreasing from several hundred picoseconds to a few tens of picoseconds. A second paper by M. De. Giorgi *et al.* [170] claims that at room temperature, double LO phonon interaction becomes the dominant relaxation mechanism, and occurs on timescales of 3-4 picoseconds, whereas the escape time decreases from 700 ps to 40 ps from 4 to 300 K. Thermal depopulation occurs at T>100 K according to [169],[170], although Heitz *et al*. argue that this occurs closer to 200 K [171].

The analysis of the aforementioned papers on the general mechanisms of carrier capture and escape in the InAs/GaAs QD system depends highly on the size and shape of the QD, the temperature of the system and modulation doping. Irrespectively, we can safely assume that the capture rate is on the order of 1-10 ps, and the escape time on the order of tens of picoseconds.

5.1.5. Thermionic Emission Theory for Quantum Structures

One paper addresses the use of bulk thermionic emission theory to describe the escape current from quantum wells [53]. The authors adopt a formulation of the thermionic emission current density to describe the lifetime of carriers to escape based on the QW size. They compare these results to a quantum mechanical formulation of the escape current density (which they relate to a lifetime). The comparison is good for larger QW widths, but does not compare wells for small QW widths (< 10 nm) where the escape time is underestimated using bulk thermionic emission theory. They also study the escape time as a function of indium mole fraction composing the QW, which is correlated with its depth. Again, the thermionic emission fails for shallow depths (or small indium mole fractions).

This paper is relevant to modeling the escape of carriers using bulk thermionic emission theory, since effective band offsets can scale the escape lifetimes of carriers within the QD/QW system; this topic is discussed in more detail in section 5.2.2. It is worth mentioning at this point that a paper by Fafard *et al.* [172] justifies this approximation for thermionic emission currents in and out of the QDs with an activation energy equivalent to the difference in energy between the barrier bandgap and the peak of the QD emission. This approach is adopted as described in section 5.2, and further justified in Appendix C-3.

5.1.6. QD and QW Device Characteristics

A paper published by Liu *et al.* [152] discusses the growth and fabrication of a quantum dot infrared photo-detector based on the indium flush technique for InAs QDs. In this paper, they demonstrate a successful photo-detector device consisting of 50 layers of QD with a high level of photo-responsivity to wavelengths intended for the QD structures. Referencing a paper published by Ryzhii *et al.* [173] on the theory of QD photo-detectors, the authors argue that zero-dimensional confinement results in lower dark currents, which for solar cells, implies larger open circuit voltages compared to QW systems. This low dark current is a result of the zero density of states between the continuum states and the quantized energy levels of the QD. Furthermore, the QD states may already be occupied by previously captured or photo-injected carriers. A second advantage of QD over QW photo-detectors is a reduced capture rate of electrons into the QD confined energy levels compared to QWs.

5.1.7. Literature Review Conclusions

The absorption characteristics of the InAs/GaAs QD system can be tailored with a high level of control using the rapid thermal anneal and indium flush technique for

manipulating the energy levels via control of the shape and size of the QDs. This is an advantage over QWs which require meticulous control over the strain compensation strategies of growing alternating tensile and compressively strained layers of specific thickness and composition. Furthermore, these strain-compensation layers can also introduce non-radiative recombination centres which further reduce the benefits of adding nanostructures. As for recombination lifetimes, the radiative lifetime can dominate in high crystal quality QD, whereas non-radiative recombination typically dominates in QW structures.

As for carrier dynamics, photons of energy greater than the bandgap of GaAs generates carriers that can be captured first by the WL from the GaAs barrier material on the order of 1-2 ps, and subsequently captured by the QD on a a timescale of 1-10 ps. Carriers then experience either radiative or non-radiative recombination, or escape through carrier-optical phonon scattering. Generally, carriers escape readily from the WL and QD states via phonon interaction at room temperature, since thermal depopulation occurs above 100 - 200 K. This justifies the proposed approach of modeling the QD as one effective medium with one confinement potential dictating the escape of carriers from the lowest energy of QD.

Table 5-1. Summary of QD and QW solar cell properties.

Property	InAs/GaAs QD	InGaAs/GaAs QW
Strain	Stranski-Krastanov growth process & indium flush/rapid thermal anneal	Alternating layers of barrier materials
Optical tunability	Indium flush/ rapid thermal anneal gives reproducible control over energy levels	Controlled by the depth of the QW, but depends on strain management
Recombination	Radiative (1 ns) Non-radiative (10 ns)	Radiative (10^3-10^4 ns) Non-radiative (0.1 – 40 ns)
Carrier capture	δ-like density of states minimizes carrier capture, which reduces dark current.	Very fast carrier capture and intraband relaxation due to non-zero density of states.

Carrier capture is typically smaller in QD devices compared to QW devices, which is one important advantage of QD. However, the InAs/GaAs system of interest incorporates both a QW and a QD, which gives rise to absorption characteristics and carrier dynamics representative of both structures. Advantageously, no strain management strategies are required in this material system as the indium flush technique allows for the growth of high crystal quality of up to 50 layers or more of InAs QD within a GaAs matrix. A summary of QD and QW solar cell properties that are relevant to the successful device performance is given in Table 5-1.

5.2. Modeling a QD Enhanced Multi-Junction Solar Cell

An effective medium approach is adopted to model the QD and WL material system, which reflects the results published in [174]. Figure 5-2a shows an example of the geometry of an InAs QD and the accompanying WL, and Fig. 5-2b is a schematic of the energy band alignment in a typical InAs/GaAs quantum dot system. It also shows the quantized energy levels and their corresponding wavefunctions. The wavefunction of the WL is present throughout the complete volume of the InAs including the QD; in comparison, the wavefunction of the QD exists primarily within the volume of the QD. However, the energy levels are not degenerate. The strain arising from the lattice mismatched InAs/GaAs interface results in band bending at the conduction and valence bands [51],[154]. Fermi's Golden Rule is used to derive an analytical expression for the absorption coefficient for both the QD and the WL, as described in sections 2.5 and 5.2.1, where numerical simulations in COMSOL Multiphysics are used to solve the energy levels based on strain and size considerations. Section 5.2.2 discusses the important carrier scattering processes occurring within a real InAs/GaAs QD system in terms of carrier capture into the bound states of the

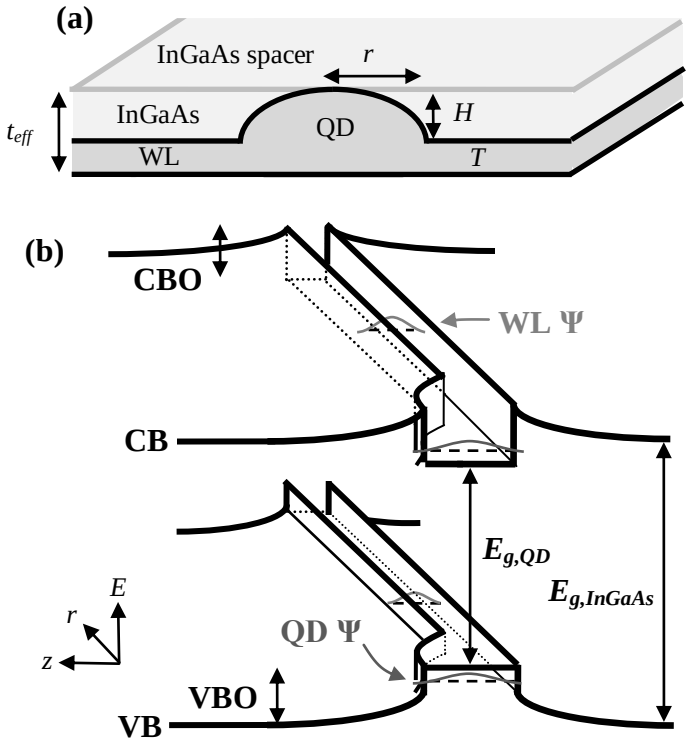

Figure 5-2. a) Geometry of the effective medium which includes the InAs wetting layer (WL) and quantum dot (QD). b) Approximate energy band alignment in an InAs/InGaAs heterostructure showing the QD and WL energy levels and wavefunctions (Ψ) within the confined potentials given by the CBO and VBO. $E_{g,InGaAs}$ and $E_{g,QD}$ are the bandgaps of bulk InGaAs and the QD respectively. Taken from [174].

WL/QD and carrier escape. A first approximation to mimicking carrier escape and capture is discussed using effective band offsets within bulk thermionic emission theory. This approximation can be justified within the framework of supplementary equations to the current-continuity equations which explicitly consider carrier escape and capture (discussed in Appendix C-3). Section 5.2.3 summarizes the recombination lifetimes adopted within the effective medium, and finally, section 5.3 discusses the simulated external quantum efficiency and *J-V* characteristics.

5.2.1. Quantum Dot and Quantum Well Absorption

The energy levels in the lens shaped InAs QD are computed by solving Schrödinger's equation in the one-band effective mass approximation using the finite element solver

COMSOL under no electric field [48]. In these simulations, we assume a CBO and a VBO that are specific to the material system under study [51,154], and that are temperature independent [175]. On the other hand, the QD material bandgap ($E_{g,QD}$) is assumed to have a temperature dependence following the Varshni relationship [176]. The absorption coefficient is then obtained by using Fermi's Golden rule and by applying a Gaussian distribution of QD energy levels [52] (see appendix C-1 for the full derivation). The final absorption coefficient as a function of energy is given by the following expression

$$\bar{\alpha}_{QD}(\hbar\omega) = \frac{2A}{\sqrt{2\pi}\xi\pi r^2 H} \cdot \sum_{m=0}^{\infty} \frac{M_{QD}^2 2(l+1)}{E_{QD,l}} \cdot e^{-\frac{\left(\frac{\hbar\omega}{E_{QD,l}}-1\right)^2}{2\xi^2}} \tag{5.1.1}$$

where $\bar{\alpha}_{QD}$ is the absorption coefficient of an ensemble of QD as a function of photon energy ħω, r and H are the mean radius and height of the QD respectively, ξ is the relative standard deviation of the QD energy level, the degeneracy of the energy levels is given by 2(l+1) based on cylindrical symmetry considerations and spin, A is a coefficient given as

$$A = \frac{\pi e^2 \hbar |P_{cv}|^2}{cn\varepsilon_0 m_0^2 \hbar\omega} \tag{5.1.2}$$

where m_o is the electron mass, n is the real component of the refractive index of the material, ε_o is the dielectric permittivity of free space, e is the electronic charge, c is the speed of light, and $\hbar$ is the reduced Planck's constant. In equation (5.1.1), the ground state energy transition in the lens shaped QD is given as $E_{QD,l}$ for the l^{th} eigenstate. The optical matrix element, in the case of the QD, is given by the square of the overlap integral between the electron and hole envelope functions and is expressed as $M_{QD}^2 = |\langle \Psi_e | \Psi_h \rangle|^2$. This integral is obtained numerically from the finite element simulation of the confined wavefunctions using COMSOL. The bulk InAs momentum matrix element, defined using the Kane energy

parameter, is $E_P = \frac{2|P_{cv}|^2}{m_0} = 22.2$ eV [177]. Important values for parameters used in the COMSOL simulations are given in Table 5-2.

The InAs wetting layer is also an important component of the overall absorption coefficient, and contributes significantly to the external quantum efficiency response around 900 nm (see Fig. 5-3). A similar derivation (see appendix C-2) yields the final absorption coefficient and takes the form

$$\bar{\alpha}_{WL} = A\frac{\mu}{2\pi\hbar^2 T}\sum_l M_{WL}^2\left(1 - \mathrm{erf}\left(\frac{\left(1-\frac{\hbar\omega}{E_{WL,l}}\right)}{\sqrt{2\xi^2}}\right)\right) \tag{5.1.3}$$

where μ is the reduced effective mass of the carriers, T is the mean thickness of the quantum well, and E_{WL} is the energy transition in the WL corresponding to the l^{th} eigenstate. The optical matrix element of the WL, M_{WL}, is dependent on the light polarization direction and the wave vector of the electrons and holes involved in the transition. For transitions occurring at the subband edges, using unpolarized light that is propagating in a direction normal to the surface, the electron – heavy hole momentum matrix element is calculated to be $M_{WL}^2 = 1.5 \cdot |\langle\Psi_e|\Psi_h\rangle|^2$ [178].

The effective medium absorption characteristic is then given as a weighted superposition of the contributions from transitions occurring within each of the QD and WL medium, the continuum states above the confinement potentials, and lastly, the bulk InGaAs surrounding the InAs. This is expressed as

$$\bar{\alpha}_{total} = F_{QD}\cdot\bar{\alpha}_{QD} + F_{WL}\cdot\bar{\alpha}_{WL} + F_{InAs}\cdot\bar{\alpha}_{InAs} + F_{InGaAs}\cdot\bar{\alpha}_{InGaAs} \tag{5.1.4}$$

where the factors F_{QD}, F_{WL}, F_{InAs} and F_{InGaAs}take into account the weighted volume of the QD, the WL, the unbound continuum states above the QD and WL, and the bulk InGaAs, as shown in Fig. 5-2a. The unbound states above the confined energy levels of the WL are

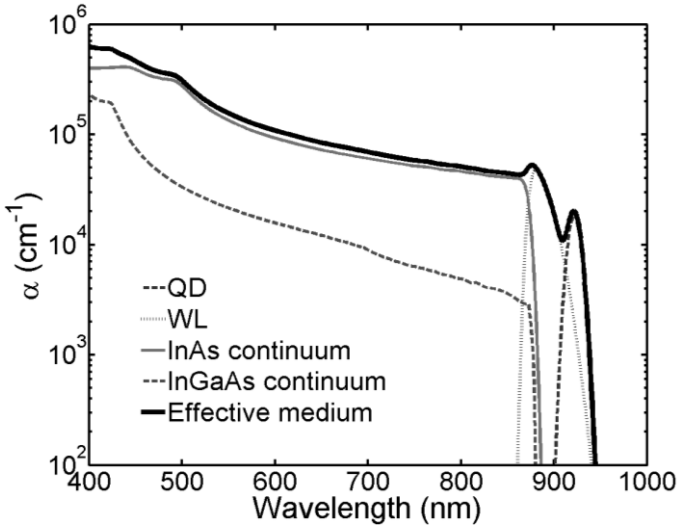

Figure 5-3. The absorption coefficient contributions from the bound states of the QD and WL, the continuum states of above the confined potential (InAs) and finally, bulk InGaAs. Only one confined energy level exists in each of the QD and WL. Taken from [174].

approximated as bulk InAs [44]. The complete absorption coefficient at room temperature for the effective medium is shown in Fig. 5-3. This formalism does not consider any interband transitions between the QD and WL energy states, as these are expected to be negligible compared to bulk absorption [155]. The mean radius and height of the ensemble of simulated QDs are taken to be r=5.2 nm and H=0.6 nm, and the mean thickness of the simulated WL is T=1.11 nm (approximately 2 monolayers). Based on these sizes, only the first confined energy level is present for both the WL and the QD. The quasi-bound energy level transitions at higher energies are not seen since they are within the continuum. The average ground state energy level, positioned ~60 meV below the bandgap of bulk InGaAs at room temperature, is in agreement with energy levels attainable using the indium flush technique and/or composition adjustments/intermixing [147]. The QD and WL dimensions that lead to this average ground state energy gives an effective medium thickness of t_{eff}=1.71 nm. The total thickness of the intrinsic InGaAs spacer layer is taken to be 8.3 nm such that the coupling of wavefunctions from adjacent QD layers is negligible [149]. A density of 125

QD/μm^2 is used in the calculation, which is comparable to other values published in the literature [149]. The magnitude of the QD absorption coefficient is in agreement with more sophisticated calculation methods as reported in [179]. The refractive index of the QD effective medium is assumed to correspond to InAs. Within the effective medium approach, the QD layers are assumed to absorb within a linear regime. This is justified based on the low current densities in a MJSC for concentrations up to 1000 suns (~14 A/cm^2) which is far from saturating the QD energy levels.

Table 5-2. Parameters adopted for COMSOL and Sentaurus absorption coefficient calculations.

Parameter	Value	Reference
CBO (meV)	580	[51]
VBO (meV)	360	[51]
$E_{g,QD}=E_{g,WL}$ ***(meV) at T=77K***	749	[51],[154]
Electron effective mass, m_e^*	$0.053m_o$	[154]
Heavy hole effective mass, m_h^*	$0.341m_o$	[180]
$\|\langle\Psi_e\|\Psi_h\rangle\|^2$ **(QD)**	0.74	-
$\|\langle\Psi_e\|\Psi_h\rangle\|^2$ **(WL)**	0.90	-

5.2.2. Carrier Dynamics

In order for carriers to contribute to the photocurrent of the device, they must first escape from the bound states of the nanostructures into the unbound states. The dominant process for this escape is carrier-optical phonon scattering at room temperature [169]. However, the reverse process – carrier capture – also takes place whereby unbound carriers are captured by the WL, a process on the picosecond time scale, and then subsequently captured by the QD on sub-picosecond time scales [162]. Describing these processes accurately requires a supplementary set of continuity equations for bound electrons and

holes which explicitly considers carrier capture and escape. This therefore introduces separate quasi-Fermi levels for the bound and unbound states [59]. The continuity equations that take these into account for electrons, hereafter referred to as the quantum well scattering formalism, are

$$\frac{dn_u}{dt} = G_u - U_u + \frac{n_b}{\tau_{esc}} - \frac{n_u}{\tau_{cap}} + \frac{1}{q}\nabla \cdot J = 0, \tag{5.1.5}$$

$$\frac{dn_b}{dt} = G_b - U_b - \frac{n_b}{\tau_{esc}} + \frac{n_u}{\tau_{cap}} = 0, \tag{5.1.6}$$

where u and b denote unbound and bound terms respectively, n is the free carrier concentration, G is the generation term, U is the recombination term, and τ_{esc} and τ_{cap} are the escape and capture lifetimes respectively. These equations assume a single transition between continuum (or unbound) states and the confined (or bound) state, where it is assumed the exchange of carriers within the WL and QD states is on a shorter time scale (picoseconds) than carrier recombination (radiative and non-radiative occur on the nanosecond timescale).

5.2.2.1. Effective Band Offset Model

Equation (5.1.6) essentially states that a quasi-equilibrium is reached when the net carrier capture rate (capture minus escape) is balanced by the net recombination rate (generation minus recombination). As a result, the net capture rate in equation (5.1.5) is equivalent to the QD net recombination given in equation (5.1.6). This allows for a simplification of the carrier dynamics in the continuity equations within the effective medium based on three approximations. First, the unbound generation rate can be coupled to the generation rate from bound states by considering one generation term arising from the total absorption coefficient in the effective medium (see Fig. 5-3). Second, the unbound recombination rate can be coupled to the bound recombination rate using one recombination

term based on one effective carrier lifetime, as described in section 5.2.3 below. Based on these two approximations, equation (5.1.5) can be rewritten as

$$\frac{dn_{u,b}}{dt} = G_{u,b} - U_{u,b} + \frac{1}{q}\nabla \cdot J = 0. \quad (5.1.7)$$

However, equation (5.1.7) assumes all carriers are generated in the continuum states of the effective medium, and that all carriers in the effective medium are subject to one effective minority carrier lifetime. A third approximation balances these over-estimations: introducing effective band offsets at the interface of the QD and GaAs results in bulk thermionic emission theory which mimics carrier escape and capture by generating supplementary terms from the $^1/_q \nabla \cdot J$ term of equation (5.1.5). It is important to note that introducing bulk thermionic emission ignores quantization effects within the effective medium, and assumes bulk density of states (see Fig. 5-4a). Although these terms mimic carrier capture and escape phenomena, the use of bulk density of states [181] assumes all carriers are captured (which therefore over-estimates the capture rates). The escape rates, on the other hand, depend on the potential barrier at this interface, and are exponentially scalable using the CBO and VBO for electrons and holes respectively, since $J \propto \exp(-\Delta E/kT)$. An escape lifetime can be derived from the gradient of the thermionic emission current density at the interface (see appendix B). These effective band offsets can be related to the activation energy for photoluminescence quenching in the InAs/InGaAs QD system, which was measured as close to the energy difference between the GaAs band edge and the ground state QD transition [172]. As a result, the third approximation of using bulk thermionic emission without quantization effects adopts band offsets for the effective medium such that the CBO and VBO sum to 56 meV (the energy difference between the QD ground state (920 nm) and the bandgap of bulk InGaAs (885 nm)). The weighting of the CBO to VBO is taken as 3:1 based

on the simulated electron and hole eigenenergies as obtained using COMSOL. This represents a worst case scenario since all carriers are captured. The voltage drop is therefore expected to be over-estimated in this scenario, which is hereafter referred to as the 56 meV band offset case. Ideally, QD layers in the active region of a solar cell do not capture carriers from adjacent barrier materials, and thus do not contribute additional recombination processes arising from the capture of carriers. Therefore, removing these effective band offsets represents an ideal case, hereafter referred to as 0 meV. Tunneling between adjacent QD layers and band bending are not considered explicitly in the model since the wavefunction overlap between adjacent QD is minimal. The effective band offset model is a heuristic approach to modeling the carrier dynamics in and out of a quantum well.

A calculation of the QD, WL and bulk CB density of states (*DOS*) is carried out in order to compare to bulk CB effective density of states (N_c). This serves as an estimate of the errors in modeling the QD effective medium using a bulk CB effective density of states (which is how it is performed in Sentaurus) to the more realistic approach which uses the *DOS* explicitly for the QD, WL and continuum states separately (which cannot be performed in Sentaurus). Figure 5-4 illustrates an example energy level configuration for a QD/WL system with bulk states beginning at 0.58 eV above the CB (which is set to 0 eV), where the QDs have three bound energy levels (0.38, 0.42 and 0.5 eV within the confinement potential), and the WL has a single energy level starting at 0.4 eV. Realistically, the excited states of the QD fall within the WL energies and therefore are dominated by the WL DOS. For this particular calculation, the energy levels of the QD system are computed using analytical equations from [51] for QD of radius 18 nm and height of 2.7 nm, and a WL thickness of 2 nm. These dimensions were chosen to clearly outline the separation of the

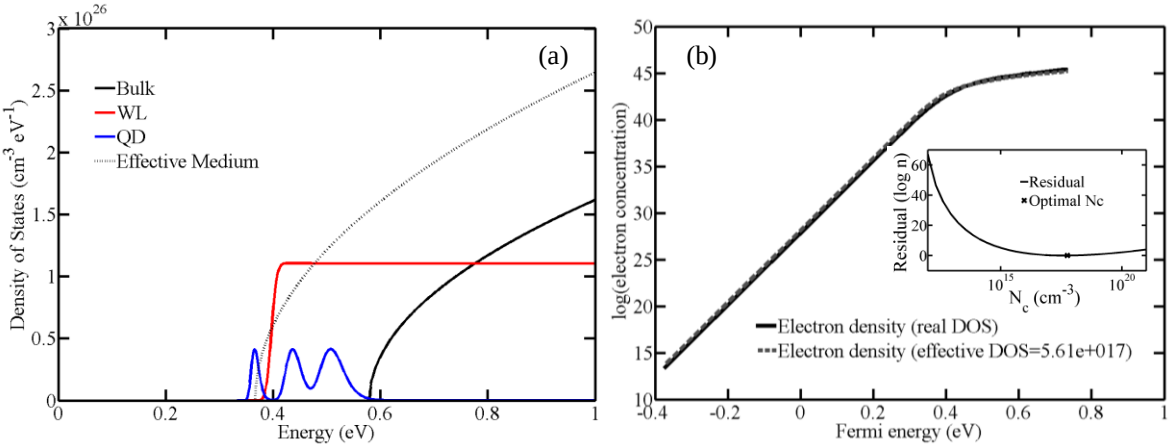

Figure 5-4. a) Simulated energy levels and density of states of the QD, WL (or QW) and bulk as a function of energy above the CB (at 0 eV) using a QD radius of 18 nm and a height of 5.2 nm with a WL thickness of 2 nm, and compared to the effective medium DOS, which is just the spacer InGaAs's DOS, b) the log (base 10) of the electron concentration as a function of Fermi energy computed using the DOS (shown in a). It is computed using equation (2.2.2), and compared to the electron concentration predicted by equation (2.2.7) using the best fit effective conduction band DOS of 3.3×10^{14} cm^{-3}. The inset plot shows the residual of equations (2.2.2) and (2.2.7) each integrated over all Fermi energies as a function of effective DOS. The optimal N_c from this inset plot is used in b.

QD, WL and bulk energy levels and are not representative of the energy levels and dimensions used in the actual device simulations. It is important to note that the COMSOL simulations of energy level dependences on QD and WL dimensions are quite different than the analytical equations from [51] (which assume disk shaped QD). Since the effective medium approach models the effects of the QD from the first confined energy level of QD, the effective DOS N_c is assumed to start at this energy level (0.38 eV) in order to compare to the actual DOS of the QD/WL system. The DOS of the InAs/GaAs system is computed according to equations (2.6.4) for the WL and (2.6.7) for the QD, while equation (2.6.4) is for the continuum states. It is important to note that within this study, the bulk CB energy level is not the same energy level as the CB of the InGaAs spacer, since strain from the lattice mismatched InAs/GaAs interface results in "wings" above the conduction band of InGaAs [155].

Figure 5-4b illustrates the calculation of the carrier concentration as a function of Fermi level for both the joint DOS scenario and the best fit effective DOS to compare the resulting predictions of carrier concentrations. The best fit to the effective DOS is deemed to minimize the residual error between the actual carrier concentrations arising from a joint DOS and the carrier concentration computed from the effective DOS. In other words, the residual represents the integrated difference between equations (2.2.2) and (2.2.7) over all Fermi levels. The inset of Fig. 5-4b shows that this best fit effective DOS is N_c=5.6×10^{17} cm^{-3}. The best fit appears quite broad as a function of N_c due to the logarithmic nature of the residual. The best fit effective density of states slightly over-estimates the electron concentration when the Fermi level is below the CB of the QD system (i.e. at 0.58 eV). This is due to the relatively low QD DOS compared to bulk DOS, since the former is described by a delta function. However, the effective DOS under-estimates the electron concentration for a Fermi energy above the QD system's CB, since the bulk DOS adds to the WL DOS and surpasses the effective medium's effective DOS. This outlines that an effective DOS can model the joint DOS of the QD, WL and bulk states to a reasonable level of accuracy within the effective band offset model. Furthermore, as the lowest energy level of the QD system gets closer to the bulk CB, the best fit effective DOS gets closer to the bulk DOS of the spacer material (for GaAs, N_c=4.7×10^{17} cm^{-3}), which therefore justifies the use of a bulk DOS to model a QD/WL system, but only to first approximation. The error will ultimately reside in the simulated quasi-Fermi level using the effective DOS, which for a specific carrier concentration, will be on the order of a few meV according to Fig. 5-4b.

5.2.2.2. *Quantum Well Scattering Formalism*

A more realistic approximation to considering carrier capture and escape is to adopt the supplementary continuity equations (equations 5.1.5 and 5.1.6) to describe the interaction of bound and unbound carrier populations in a quantum well, i.e. to adopt the quantum well scattering formalism explicitly. Within this formalism, a one-dimensional Schrödinger solver computes the bound energy level within the effective medium based on the confinement in the conduction and valence bands as well as the carrier effective masses. The subbands are solved independently assuming the electron, light and heavy holes are decoupled (see pp. 905-907 of [65] for the wavefunction ansatz and transcendental equations for the eigenmodes). The carrier scattering rates between unbound and bound energy levels can thus be computed using a specific scattering time for electrons and holes (see equations 2.6.16 and 2.6.17 in chapter 2) where the scattering processes are treated as elastic. The effects of an energy level introduced by the QD are modeled as traps which are located 42 meV below the conduction band according to a Gaussian distribution with a deviation of 0.007 eV (based on the absorption model described in section 5.2.1); these traps are modeled as acceptor traps which are uncharged when unoccupied and charged when occupied by an electron. Another Gaussian distribution of donor level traps is positioned 14 meV above the valence band also according to a Gaussian distribution with the same deviation. Each distribution of traps has a trap density related to the density of QDs within the volume of the effective medium (i.e. a QD density of 1.25×10^{10} cm^{-2} corresponds to a trap density of 7.4×10^{16} cm^{-3} for an effective medium thickness of 1.71 nm as described previously based on the dimensions of the QD and WL). The formalism describing the contribution of traps to the overall SRH recombination is discussed in section 5.2.3, where a trap cross-section of

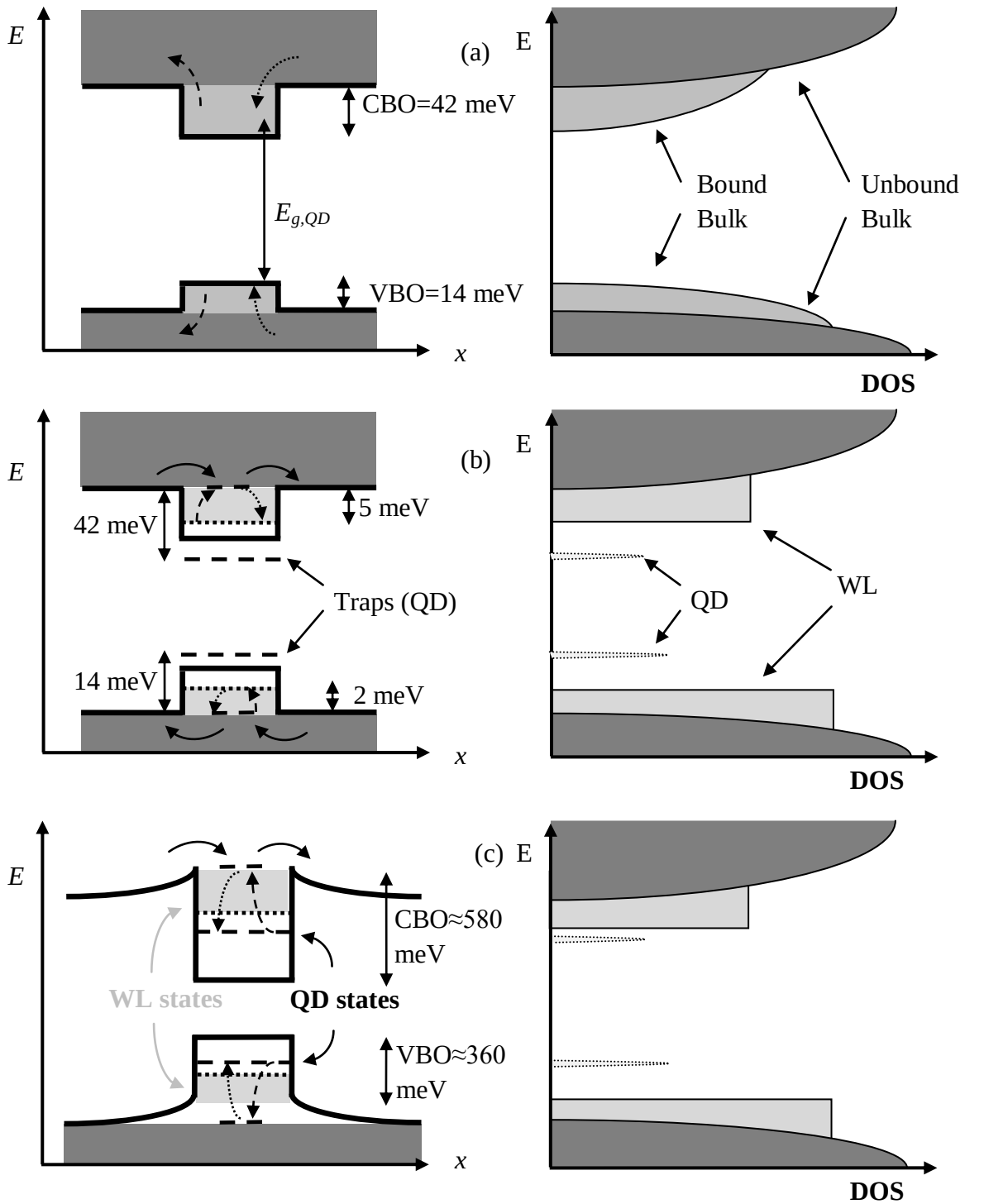

Figure 5-5. Schematic energy band diagram (left) and density of states (right) of the effective medium a) within the effective band offset model for mimicking carrier escape and capture using thermionic emission theory coupled to bulk density of states with a CBO and VBO summing to 56 meV, b) for the quantum well scattering formalism with traps where explicit carrier escape and capture rates dictate carrier exchange in and out of the quantum well, and the CBO and VBO give rise to WL energy levels (dotted lines) that results in an electron to hole transition energy of 7 meV less than that of InGaAs bulk; the trap states represent the QD energy levels (dashed lines) that are 42 meV below the CB and 14 meV above the VB (similar to scenario a), and c) based on the literature review with strained energy band structure and confined WL and QD energy levels.

1×10^{-13} cm^2 is adopted although the results of [167] indicate a cross-section of 1×10^{-11} cm^2, which is 2 orders of magnitude larger than the actual sizes of the QD using deep level trap spectroscopy coupled to capacitance versus voltage data. The trap degeneracy is 2 to account for spin. Figure 5-5 summarizes the different approaches to model the carrier dynamics within the effective medium, where (a) illustrates the effective band offset model, (b) illustrates the quantum well scattering formalism with traps, and (c) represents the most accurate and realistic approach to the carrier dynamics in an InAs/GaAs QD system based on strain dependent band bending (i.e. the "wings"), the depth of the confinement potential, etc. Furthermore, the density of states for each scenario is illustrated on the right to gain an understanding of the inadequacies of the two models compared to (c). For scenario (b), the CBO and VBO are set such that the energy level of the quantum well is 5 meV below the CB and 2 meV above the VB in accordance with COMSOL simulations using the 1.1 nm thick wetting layer. It also indicates that this WL is indeed a weakly confining quantum well. The VB DOS for the WL and QD are depicted as larger in magnitude than the CB DOS due to the larger hole effective mass [180].

It is noteworthy to mention that the band offsets are significantly different than those reported in the literature specifically for this material system (i.e. 42 and 14 meV compared to 580 and 360 meV), since the former are ideal band offsets with no strain considerations, whereas the latter are realistic band offsets which take into account wings in the conduction band at the interfaces due to strain [51],[154].

5.2.3. Recombination in the QD Effective Medium

The QD minority carrier lifetimes in the effective medium are described using radiative (τ_R = 1 ns [156]) and non-radiative (τ_{NR} = 10 ns [159]) recombination lifetimes

based on time-resolved photoluminescence studies performed on this particular QD system. Since this is an effective medium approach, the final lifetimes are a weighted sum of the QD and GaAs bulk recombination lifetimes (assuming carriers captured by the WL are subsequently captured by the QD). This weighted sum is based on the volume of the WL and QD with respect to the bulk in a single QD unit cell. For the effective band offset model, this approximation fits in the $U_{u,b}$ recombination term of equation (5.1.7) representing two populations of carriers experiencing two different lifetimes.

The introduction of traps (associated to scenario (b) of Fig. 5-5) establishes a supplementary recombination mechanism with its own unique minority carrier lifetime which depends on the concentration of traps, the trap cross-section, and the thermal velocities of the carriers. The final rate for this process is similar to the typical SRH formalism outlined in section 2.4.3 and given by

$$R_{net}^{SRH} = \frac{N_o v_{th}^n v_{th}^p \sigma_n \sigma_p \left(np - \gamma_n \gamma_p n_i^2\right)}{v_{th}^n \sigma_n \left(n + {}^{n_t}/_{g_n}\right) + v_{th}^p \sigma_p \left(p + {}^{p_t}/_{p_n}\right)} \tag{5.1.8}$$

where N_o is the trap concentration, v_{th}^n and v_{th}^n are the electron and hole thermal velocities respectively, σ_n and σ_p are the trap cross-sectional areas, and g_n and g_p are the trap degeneracies. The occupancy of all specified traps is determined for all processes, such as the capture of an electron from the conduction band being treated separately from the capture of an electron from the valence band. The effective lifetime can be described as $\tau = \frac{1}{N_o v_{th}^n \sigma_n}$. For more details, see page 412 of [65].

5.3. Simulating the QD Enhanced MJSC

5.3.1. Structure

The structure of the final device is given below in Table 5-3, and is similar to that given in Table 4-6 of a typical MJSC in Chapter 4. The dual-layered ARC in this structure is composed of Si_3N_4/SiO_2 of thicknesses 90 and 60 nm. The middle sub-cell's intrinsic region consists of alternating layers of the InAs QD effective medium (thickness 1.7 nm) and InGaAs spacer (8.3 nm), so 100 layers of QD results in a total intrinsic thickness of 1 μm. This structure is simulated in terms of the external quantum efficiency in an attempt to fit the simulated EQE to that of the experimentally measured EQE of a first generation Cyrium Technologies Inc. quantum dot enhanced cell (QDEC). Assuming the model of the QD effective medium is reasonable, the remaining fitting factors are primarily the number of QD layers and the background intrinsic doping in order to limit the parameter space. Note that the quantum well scattering formalism introduces more fitting parameters. It is worth noting that the use of ideal material parameters to describe AlInP, InGaP, InGaAs, AlGaAs and Ge typically results in high responsivities (EQE>0.9). For these reasons, surface recombination velocities are introduced at various interfaces of the full structure (such as the TC front surface field interface with the TC emitter, or the BC buffer layer with the front surface field in the BC). This method is useful in improving the agreement in simulated and experimental EQE. This modulates the effective recombination lifetime near this interface by introducing an SRH mechanism. Realistically, this represents a finite volume near the interface of the structure where the crystal quality might decrease upon the change in atomic compositions (such as Al substitution for Ga at the FSF/EM interface of the TC). Once more, without the

complete layer structure (i.e. grown doping levels and layer thicknesses), it becomes nearly impossible to perfectly fit the EQE to experiment.

Table 5-3. QD enhanced multi-junction solar cell structure composed of InGaP/InGaAs/Ge.

Layer	Material	Doping (cm^{-3})	Thickness (μm)
Cap	n-GaAs	1×10^{19}	0.2
TC-Front surface field	n-$Al_{0.51}In_{0.49}P$	5×10^{19}	0.03
TC-Emitter	n-$Ga_{0.51}In_{0.49}P$	5×10^{18}	0.1
TC-Base	p-$Ga_{0.51}In_{0.49}P$	1×10^{17}	0.4-1 (variable)
TC-Back surface field	p-$(Al_{0.25}Ga_{0.75})_{0.51}In_{0.49}P$	1×10^{18}	0.12
Top-TJ buffer	p-$Al_{0.15}Ga_{0.85}As$	2.25×10^{19}	0.005
Top-TJ p++	p- $Al_{0.15}Ga_{0.85}As$	4.5×10^{20}	0.02
Top-TJ n++	n- $Al_{0.15}Ga_{0.85}As$	2.7×10^{19}	0.02
Top-TJ buffer	n- $Al_{0.15}Ga_{0.85}As$	1.35×10^{19}	0.005
MC-Front surface field	n-$Ga_{0.51}In_{0.49}P$	5×10^{18}	0.03
MC-Emitter	n-$In_{0.01}Ga_{0.99}As$	1×10^{18}	0.05
MC-Intrinsic/InAs QD	p-$In_{0.01}Ga_{0.99}As$/InAs QD	5×10^{15}	0.65-1.25 (variable)
MC-Base	p-$In_{0.01}Ga_{0.99}As$	5×10^{17}	3-4.25
MC-Back surface field	p-$Ga_{0.51}In_{0.49}P$	1×10^{19}	0.1
Bottom-TJ buffer	p-$In_{0.01}Ga_{0.99}As$	4×10^{19}	0.05
Bottom -TJ p++	p-$Al_{0.3}Ga_{0.7}As$	4×10^{20}	0.05
Bottom -TJ n++	n-$In_{0.01}Ga_{0.99}As$	2×10^{19}	0.05
Bottom -TJ buffer	n-$In_{0.01}Ga_{0.99}As$	4×10^{18}	0.05
BC-Buffer	n-$In_{0.01}Ga_{0.99}As$	5×10^{18}	0.2
BC-Front Surface Field	n-$Ga_{0.51}In_{0.49}P$	5×10^{19}	0.02
BC-Emitter	n-Ge	1×10^{19}	0.1
BC-Base	p-Ge	2×10^{17}	170

5.3.2. Effective Band Offset Model

5.3.2.1. External Quantum Efficiency

The top, middle and bottom sub-cell external quantum efficiency (EQE) simulations, performed similar to those in Chapter 4, are compared to room temperature measurements of a CyriumQDEC in Fig. 5-6, where effective band offsets are adopted to mimic carrier escape and capture. Layer type, thicknesses, and doping concentrations are estimated based

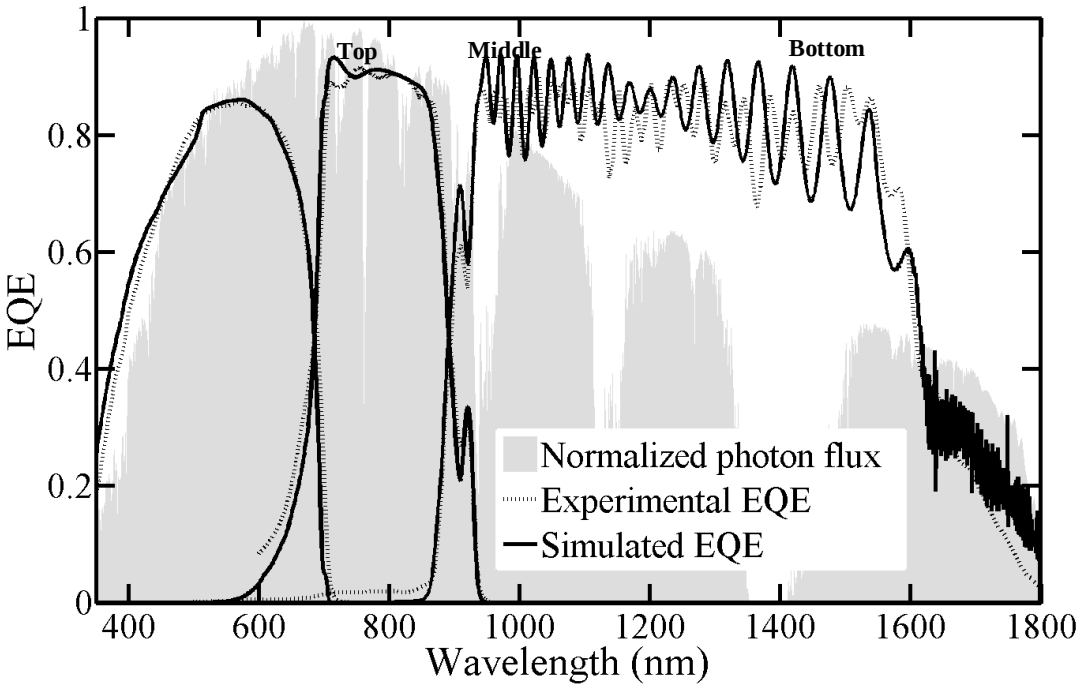

Figure 5-6. Simulated external quantum efficiency (EQE) of a QD enhanced MJSC with 130 layers of 56 meV band offset QDs compared to experimental measurements on a Cyrium QDEC.

on typical designs reported in the literature [127],[131], as the real structure of the Cyrium cell is unknown. The middle InGaAs sub-cell structure is assumed to have an *n-i-p* configuration with the InAs QD layers positioned in the intrinsic region based on an experimental study conducted by Zhou *et al.* on single junction GaAs solar cells with InAs QD [12]. The effects of QD positioning are verified in the next section (5.3.4). The middle sub-cell has additional dependences that are important solely for simulating the EQE, namely the number of alternating QD and InGaAs layers (hereafter the number of QD layers), the background doping level of the intrinsic InGaAs matrix, the QD density per layer and the effective band offsets at the InAs/InGaAs interface. All of these affect the level of response of the sub-cell. For the specific parameters studied (a background *p*-doping of 5×10^{15} cm^{-3} coupled to 56 meV of band offsets), 130 layers of QD layers were required to simulate a similar QD response to the experimental measurements at 920 nm. Integrating the

EQE over the spectrum to compute J_{sc} (according to equation 3.3.3) leads to an underestimation of 1.2% and 1.4% for the top and middle sub-cells respectively, and over-estimated by 0.6% for the bottom sub-cell compared to the J_{sc} computed using the experimental EQE. The nature of the errors in fitting the EQE of the middle and bottom cells is due in part to differences in ARC and also refractive indices, but also etalon effects, which are nearly impossible to reproduce without the correct layer structure. In short, Figure 5-6 serves as a demonstration that incorporating QD in the middle sub-cell allows for a redistribution of photons (and therefore photocurrent) from the Ge bottom sub-cell without significant degradation effects to the remaining middle sub-cell EQE. It also serves as a preliminary calibration of the model to a commercially available quantum dot enhanced triple junction solar cell.

5.3.2.2. Current – Voltage Characteristics

Four structures are investigated in this section to explore the performance boost of a MJSC with QD located in the intrinsic region of the middle sub-cell. The top and bottom sub-cells of all three structures correspond to those described in Table 5-3, with the exception that the top sub-cell base thickness is optimized in each case to current match the top two sub-cells. An alternative method of current matching the MJSC is optimizing the top sub-cell bandgap (which is accomplished in reality via ordering of InGaP during crystal growth). This would, however, influence the photovoltage of the simulated device and render the comparison more complex. The middle InGaAs sub-cell in the first control structure [1-Control *n-p*] is a simple *n-p* sub-cell with a 4.25 µm thick base. The second control [2-Control *n-i-p*] has a reduced base thickness (3 µm) such that a 1.3 µm thick *p*-type intrinsic layer of background doping (5×10^{15} cm^{-3}) can be used to expand the depletion

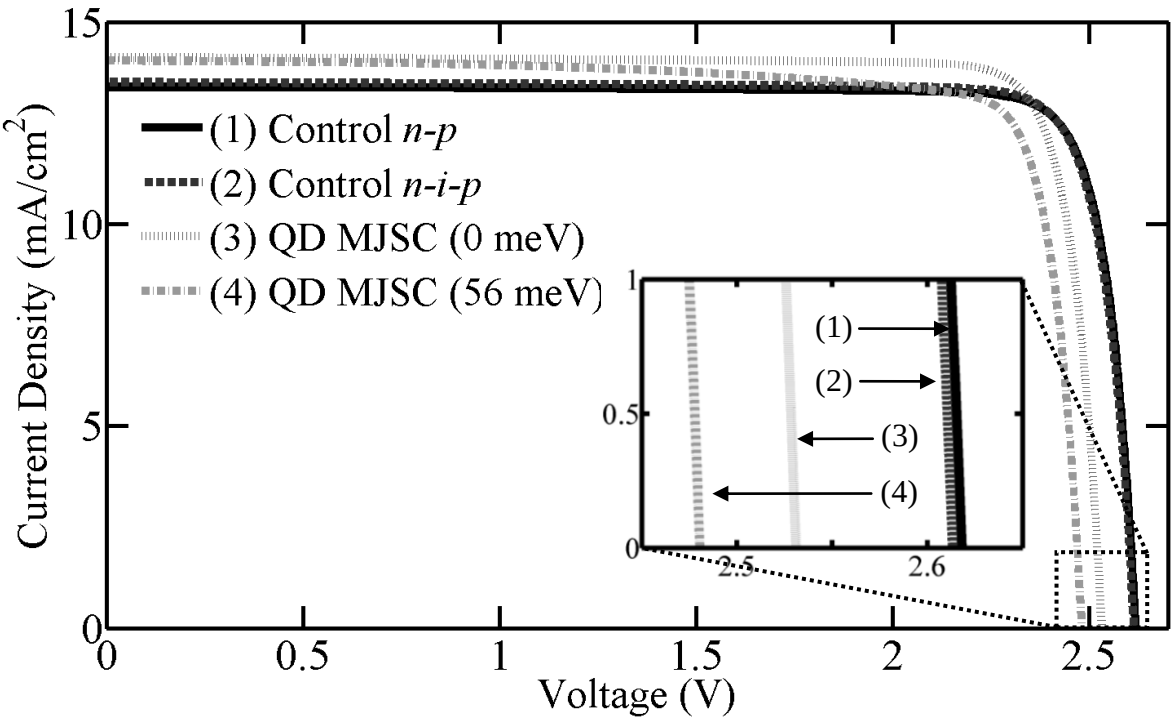

Figure 5-7. Simulated *J-V* curves of four MJSC structures with (1) an *n-p* middle sub-cell without QD, (2) *n-i-p* middle sub-cell without QD, (3) *n-i-p* sub-cell with 130 layers of QD (0 meV band offset) and (4) *n-i-p* sub-cell with 130 layers of QD (56 meV effective band offsets). Inset plot shows a close-up of the V_{oc}.

region. The base thickness is reduced in this structure to ensure similar bulk absorption throughout all structures. The third case [3-QD (0 meV)] introduces 130 layers of QD in the intrinsic region (preserving the total intrinsic layer thickness), where the effective medium describing the QD only considers the absorption characteristics and recombination lifetimes described in section 5.2.2 and 5.2.3. The fourth case [4-QD (56 meV)] builds on the third by taking into account carrier escape and capture according to bulk thermionic emission theory described in section 5.2.2.1, implemented by adding 56 meV of effective band offsets. The simulated current – voltage characteristics of the four cases under one sun illumination (1 kW/m^2) using the AM1.5D spectrum at 300 K are shown in Fig. 5-7, with the characteristics summarized in Table 5-4. For comparison, we include measured *J-V* metrics of a Cyrium QDEC cell under a class-AAA solar simulator corrected for spectral mismatch.

Table 5-4. Summary of simulated solar cell characteristics under 1 sun illumination (1 kW/m^2, AM1.5D) at 300 K according to the effective band offset model.

Structure	J_{sc} (mA/cm^2)	V_{oc} (V)	FF	η (%)
1-Control *n-p*	13.39	2.62	87.3	30.6
2-Control *n-i-p*	13.51	2.61	87.0	30.7
3-QD (0 meV)	14.09	2.53	87.1	31.1
4-QD (56 meV)	**14.04**	**2.48**	**83.6**	**29.1**
5-Experimental	14.15	2.47	83.2	29.1

The first control structure, which has no QDs and no intrinsic region, shows typical MJSC characteristics reported in the literature [183]. The second control demonstrates an important effect originating from widening the depletion region of the middle sub-cell: a 0.4% relative drop in V_{oc} predominantly due to the increased Shockley-Read-Hall (SRH) recombination rates. This effect leads to a decrease in fill factor but an overall increase in overall efficiency of 0.1% absolute due to the increased photocurrent of the cell. The third structure (with QD layers described only by absorption and recombination lifetimes) shows a 5% increase in J_{sc} compared to the first control structure due to contributions from the QD, WL and InAs continuum, and shows a 3.4 % drop in V_{oc}. This voltage drop occurs in part due to the widened depletion region as observed by comparing the two controls, but also due to the decreased carrier lifetimes introduced by the effective medium. The fourth structure (which considers the effective band offsets and thus mimics the effects of carrier escape and capture) has a similar increase in J_{sc}, but a 5.3% degradation in V_{oc} relative to the *n-p* control structure. This drop arises due to the implementation of the 56 meV band offsets which contribute supplementary recombination terms in equation (5.1.7) based on the thermionic emission approximation of carrier capture and escape rates. Introducing effective band offsets therefore degrades the photovoltage with little to no effect on the photocurrent. A study on the voltage dependence of the recombination currents on a similar QD enhanced MJSC structure is given in [184]. The simulated J_{sc}, V_{oc}, *FF* and efficiency are in excellent

agreement with values measured in-lab. The drop in *FF* due to the introduction of band offsets is primarily a result of the current mismatch between the top and middle sub-cells, since the 100% carrier capture into the potential confinements of the effective medium renders it as more difficult for carriers to escape and contribute to the middle sub-cell photocurrent. An increase in photocurrent, however, is still obtained through the addition of these QD/WL nanostructures. This results in the middle sub-cell limiting the current of the device by 2%, in agreement with the experimental EQE of the QD enhanced MJSC, which indicates the middle sub-cell is also the current limiting sub-cell.

The increase in photocurrent in a QD enhanced cell is thus explained by the increased absorption from the nanostructures, whereas the decrease in open circuit voltage is explained in part by increased recombination and also a decreased effective bandgap within the middle sub-cell. The addition of 130 layers of QD within the framework of the effective band offset model shows a 5% boost in the short circuit density, along with a 5.3% degradation of the open circuit voltage relative to a control structure. The overall efficiency of the QD enhanced cell is lower than the control *n-p* structure by just over 1% absolute at 1 sun illumination. It is important to note that this drop in open circuit voltage in the 56 meV band offset scenario represents a worst case for this specific solar cell structure, since the effective density of states of the effective medium implies a lower quasi-Fermi energy level is required to generate the same carrier concentration in comparison to a true QD/WL structure (and from Chapter 4, a lower quasi-Fermi level implies a lower V_{oc}). As a result, a reduced density of states would increase the quasi-Fermi level required to generate the same carrier concentration, and thus one would expect an increase in V_{oc}. This hypothesis is tested in the next section where the quantum well scattering formalism is implemented in the simulation.

One last comment regarding the effective band offset model: the effect of increasing the band offsets beyond 56 meV drastically affects the open circuit voltage but also decreases the short circuit current density. These results are not shown here since the effective band offset model is a first approximation to modeling the carrier dynamics in QD solar cells.

The data published in a nearly identical study [174] provide different results than this thesis since the material parameters adopted in the work reported here have been revamped through a collaborative project involving Cyrium Technologies Inc., the University of Ottawa and l'Université de Sherbrooke. These differences in material properties have a significant impact on the conclusions, namely that the structure studied in this section of the thesis has a lower performance than the control structure, whereas the results in the publication show the opposite.

5.3.3. Quantum Well Scattering Formalism

5.3.3.1. Quantum Efficiency

Figure 5-8a illustrates the same QD enhanced MJSC as shown in Fig. 5-6 but with 65 layers of QD in the middle sub-cell since only 65 layers are required to match the QD peak at 920 nm. The characteristics from the top and bottom sub-cells are identical (in terms of layer thicknesses and doping levels). The main differences in this simulation compared to results from Fig. 5-6 are the implementation of the quantum well scattering equations to describe the carrier dynamics in the effective medium to account for the carrier dynamics in the wetting layer, and the introduction of traps to describe the QD ground state energy levels. It is important to note the conduction and valence band offsets within this framework are not the same as the 56 meV effective band offset scenario, since the energy levels solved by Sentaurus' Schrödinger solver need to match those corresponding to the wetting layer

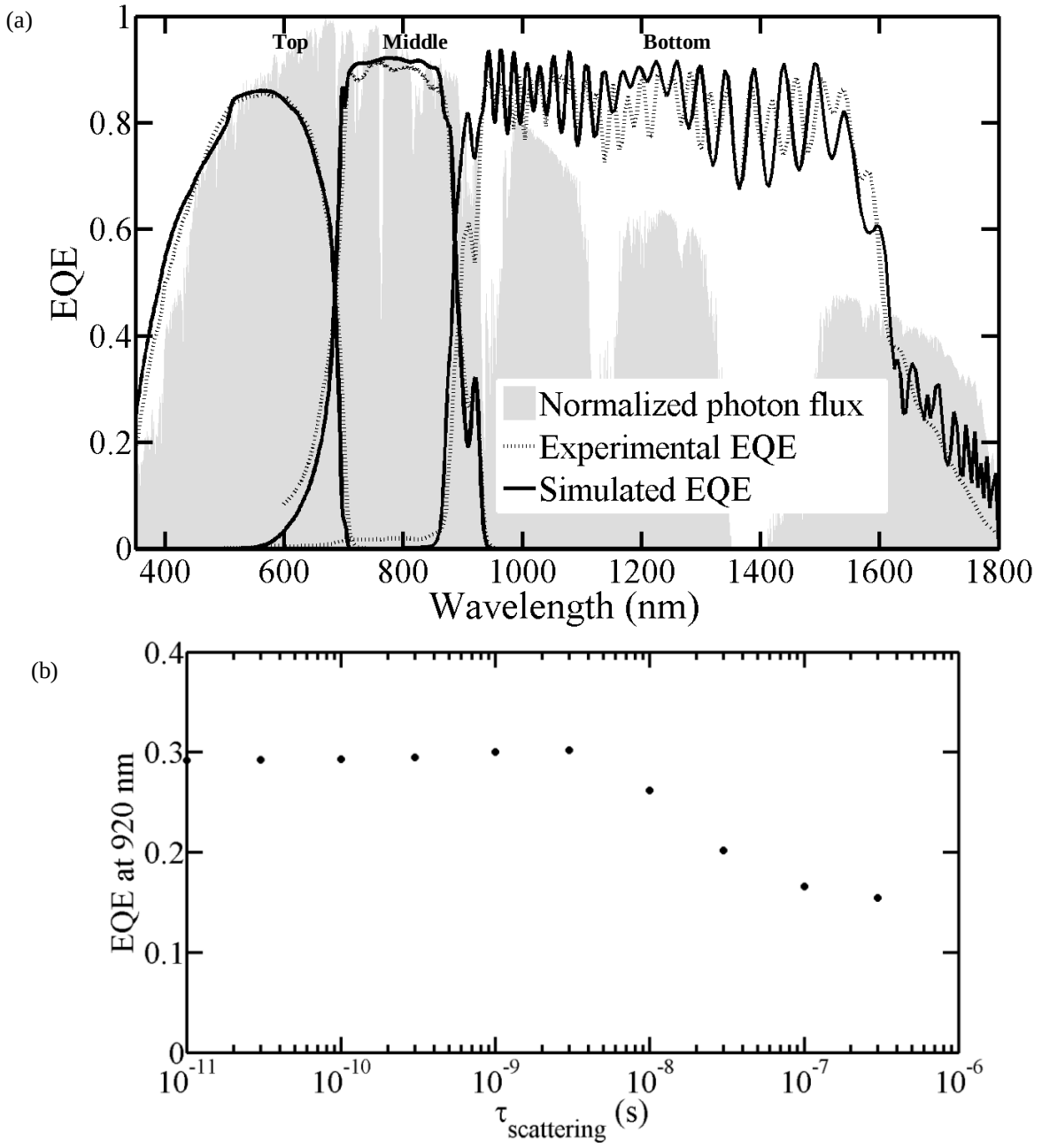

Figure 5-8. a) Simulated external quantum efficiency (EQE) of a QD enhanced MJSC with 65 layers of QDs described using the quantum well scattering formalism and compared to experimental measurements on a Cyrium QDEC and b) dependence of the EQE at 920 nm as a function of carrier scattering time.

energy levels. The band offsets were set with the similar CBO to VBO ratio used in the effective band offset approach.

The fact that less QD layers were considered to reproduce the same EQE response as the effective band offset model implies that the bulk thermionic emission approximations under-estimated the escape rates and over-estimated the capture rates of bound to unbound and unbound to bound carrier populations respectively. Interestingly, the scattering time for electrons and holes (which are set to the same value) has no effect on the magnitude of the quantum efficiency for wavelengths targeted for the nanostructures when $\tau_{scat}^{e,h} < \tau_{SRH}^{e,h}$, where $\tau_{SRH}^{e,h}$ is the SRH minority carrier lifetime. However, when the scattering time becomes longer than the SRH lifetime, the EQE response diminishes according to the results illustrated in Fig. 5-8b where the electron and hole scattering times were kept the same. This result implies that carriers easily escape for scattering times shorter than the average recombination lifetime in the effective medium. For increasing operating temperatures, carrier-phonon scattering would dominate further, which would reduce the scattering time and therefore maximize the escape of carriers out of the confinements.

The magnitude of the EQE in the wavelength range of 730 to 880 nm increased noticeably relative to Fig. 5-6 (the EQE was greater than 95%) since the generation corresponding to the total absorption coefficient of the effective medium is only considered in the continuity equations describing the unbound carrier populations. In other words, there is no generation term in the continuity equation (5.1.6) describing the bound carrier populations. As a result, the generation is over-estimated in the simulation. This is a limitation of the laser physics module (which allows for the introduction of the quantum well transport equations in Sentaurus Device), since laser physics does not consider optical generation. In order to obtain a better agreement between simulated and experimental EQE, the bulk contribution to the effective medium absorption coefficient was scaled down (i.e.

for wavelengths shorter than 880 nm as contributed by InAs and GaAs), which resulted in Fig. 5-8a. Note that the QD and WL contributions remained intact in the absorption coefficient. This scaled absorption could hypothetically be due to over-estimated absorption contributions from bulk GaAs and InAs as developed in section 5.2.1 which could originate from the strained InAs energy band structure. This scaled absorption coefficient contribution is assumed for the remainder of the studies using the QW scattering formalism. However, this foreshadows an inadequacy in the model in simulating optical generation whilst considering scattering processes within the quantum well. It is important to note that this limitation in the compatibility between the optical generation and laser modules rendered the quantum efficiency simulations as non-trivial. An optical generation profile needed to be simulated and exported for each wavelength and imported into the Sentaurus Device tool to simulate the transport equations. As such, a single quantum efficiency simulation was extremely time consuming (24 hours for a 1 nm resolution), since it involved two Sentaurus Device tools for each wavelength. Previously, a single Sentaurus Device tool could simulate the quantum efficiency of the QD enhanced MJSC over all wavelengths. An improved model is proposed in section 5.3.4 to overcome this inadequacy.

5.3.3.2. Current – Voltage Characteristics

The same structure giving rise to the EQE illustrated in Fig. 5-8a is simulated in terms of *J-V* characteristics, with the results presented in Fig. 5-9 and summarized in Table 5-4. These are compared to the performance of the effective band offset scenario with 130 QD layers, and of the two control structures (*n-p* and *n-i-p*) with the *n-i-p* structure incorporating an intrinsic thickness corresponding to 65 layers of QD (i.e. 0.65 μm). The in-plane carrier mobilities of the wetting layer are set to 1000 and 100 cm^2/Vs for electrons and

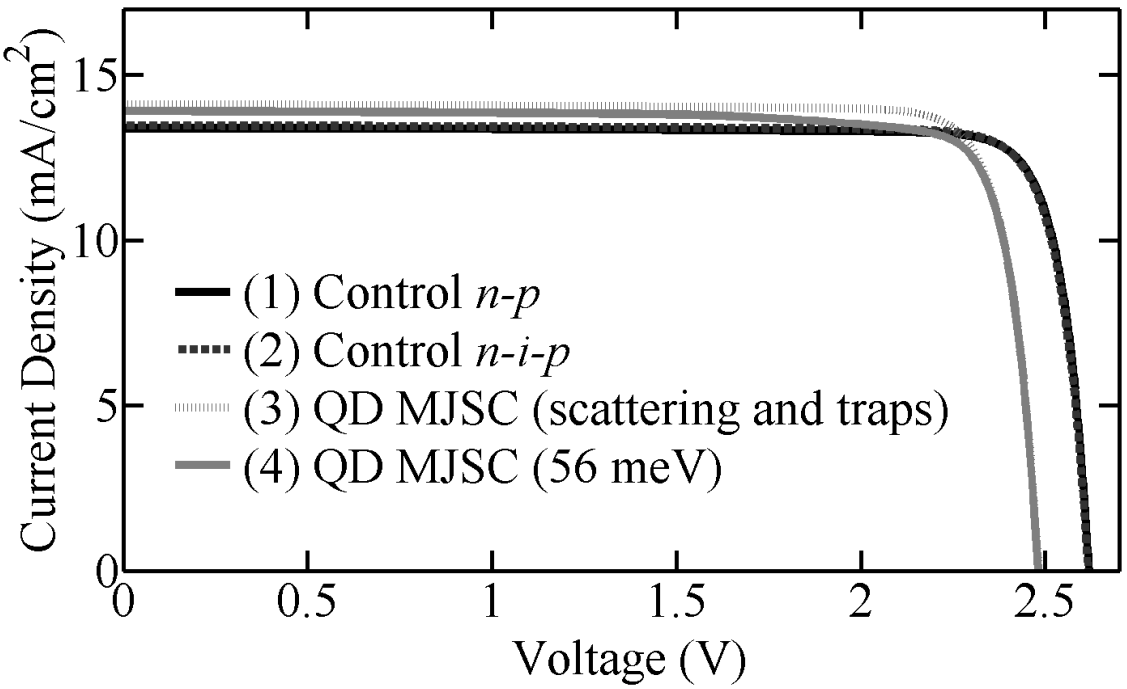

Figure 5-9. Simulated *J-V* curves of the QD enhanced MJSC structures with 65 layers of QD using the quantum well scattering formalism for a scattering time of 1×10^{-12} s at and compared to two control structures (*n-p* and *n-i-p* with an intrinsic thickness of 0.65 µm) and lastly to the QD enhanced MJSC with 130 layers of QD modeled using the 56 meV effective band offsets.

holes respectively. Varying these mobilities has little effect on the simulated performance due to the high level of illumination uniformity and the low level of shadowing. As expected, the control structures have the largest V_{oc} and the lowest J_{sc}. Interestingly, the V_{oc} for the QD MJSC modeled using the QW scattering formalism with traps is nearly equal to the V_{oc} corresponding to the QD MJSC modeled using effective band offsets (although it is 0.1% relatively higher). The comparable V_{oc} predicted by both models indicates the drop in quasi-Fermi level separation from the introduction of lower bandgap semiconductor heterostructures is similar, even though the band offsets adopted in each simulation are quite different. This also indicates the minority carrier lifetimes are central in determining the resulting V_{oc} of the structure. The simulated *FF* is considerably larger than the effective band offset scenario as well as the measured data (see Table 5-4) predominantly due to the

increased escape rates coupled to decreased capture rates of the effective medium, which generated a larger J_{sc} in the middle sub-cell and thus less limitation on the photocurrent of the device. This partially justifies the hypothesis that the effective band offset model was a worst case scenario, as all carriers were captured. The final device efficiency of the QD enhanced MJSC is lower than the control structures by 0.4% absolute primarily due to the low V_{oc}. Further improvements on device performance could be obtained using longer minority carrier lifetimes in the effective medium.

Table 5-5. Summary of simulated QD enhanced MJSC characteristics under 1 sun illumination (1 kW/m^2, AM1.5D) at 300 K corresponding to Fig. 5-9 for various QD models.

Model	J_{sc} (mA/cm^2)	V_{oc} (V)	FF	η (%)
Control *n-p*	13.39	2.62	87.3	30.6
Control *n-i-p* (*i*-0.65 µm)	13.47	2.62	87.0	30.6
Effective BO (130 layers)	14.04	2.48	83.6	29.1
Quantum Well Scattering Formalism With Traps (65 layers)	**14.11**	**2.48**	**86.3**	**30.2**

5.3.4. Performance Optimization of QD Enhanced MJSC

So far, the studies on QD enhanced MJSC have relied on structures that have been partially calibrated to the experimental EQE of a First Generation Cyrium QDEC. The next study of this thesis focuses on maximizing the performance of a QD enhanced MJSC by optimizing the number of layers of QD in the middle sub-cell for a fixed background doping of 5×10^{15} cm^{-3}, assuming no formation of threading dislocations (i.e. ideal growth conditions). The quantum well scattering models are adopted once again with the same parameters as in the previous section, even though the scaling of the bulk contributions of

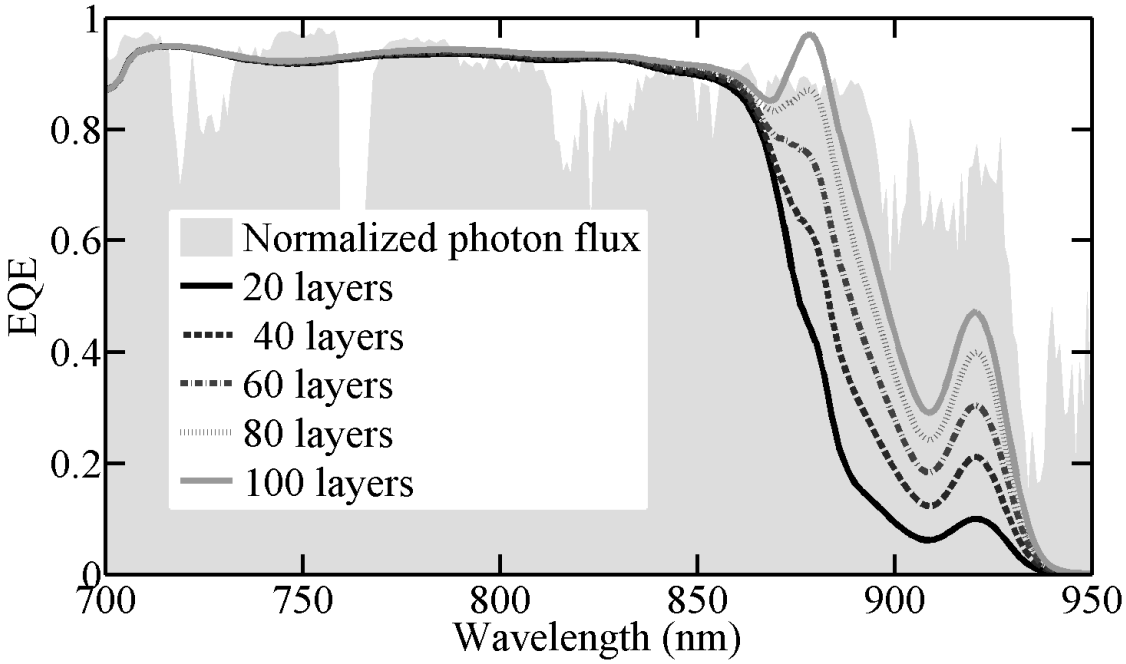

Figure 5-10. Simulated external quantum efficiency curves of a QD enhanced MJSC with increasing number of layers of QD in the intrinsic region of the middle sub-cell where the QD are described using the QW scattering formalism with scattering times of 1 ps for electrons and holes respectively. The contribution from the WL and QD show linear increases in EQE magnitude, and leads to an unphysical

the effective medium absorption coefficient was required to obtain reasonable agreement in the EQE. Figure 5-10 illustrates the effects of increasing the number of QD layers on the simulated EQE of the device. As expected, the magnitude of the EQE response for wavelengths targeted by the nanostructures increases as a function of QD layers. The increase in magnitude of the EQE is nearly linear with the number of QD layers up to 100 layers, since the addition of QD layers are within (for the first 60) and very near (for 60-100) the depletion region and experience a near 100% carrier collection probability. However, the simulation of 120 QD layers demonstrates the final breakdown of the QW scattering formalism as a model to describe the exchange of carriers between bound and unbound states: the simulated EQE goes beyond unity in the wavelength range absorbed by the WL by upwards of 1% absolute. A plausible reason for this unphysical result is the unsatisfactory solution to the coupled set of continuity equations (i.e. the set describing the

bound and unbound populations) as a result of no generation in the bound continuity equation. It is inherently linked to the previous inadequacy in the model whereby the absorption was scaled down.

Due to unphysical nature of the results, the performance optimization cannot be performed using the QW scattering formalism. Instead, an improved model is proposed consisting of the effective band offset model to describe the effects of the WL and a Gaussian distribution of traps to describe the QD ground state. This new improved model is hereafter referred to as the effective band offset model with traps. The trap cross-section is set to 10^{-13} cm^2 since this best represents the cross-section of the QD and since carriers are all captured by the effective medium's confinements. This improved model consists of an ideal scenario (0 meV), as well as a worst case scenario of 56 meV whereby the WL is modeled as having states existing all the way to the ground state of the QD. Such a physical scenario is representative of the absorption coefficient depicted in Fig. 5-3, where a significant amount of overlap exists between the WL and QD contributions to the absorption, which is due to their respective size distributions. Moreover, four additional effective band offsets are explored as scenarios in-between the ideal and the worst case to explore the effects of strain management at the InAs/GaAs interface which affect the wings in the energy bands (see Fig. 5-5c on the left). The scenario consisting of 6.7 meV of band offsets corresponds to the WL energy levels as predicted by the COMSOL Multiphysics simulations which gave rise to the absorption illustrated in Fig. 5-3. The other three scenarios consist of the effective band offsets as outlined in Table 5-6. Fig. 5-11 illustrates the effects of increased QD layers for these scenarios on the device EQE and performance metrics as compared to a control MJSC where the intrinsic thickness of the *n-i-p* middle sub-

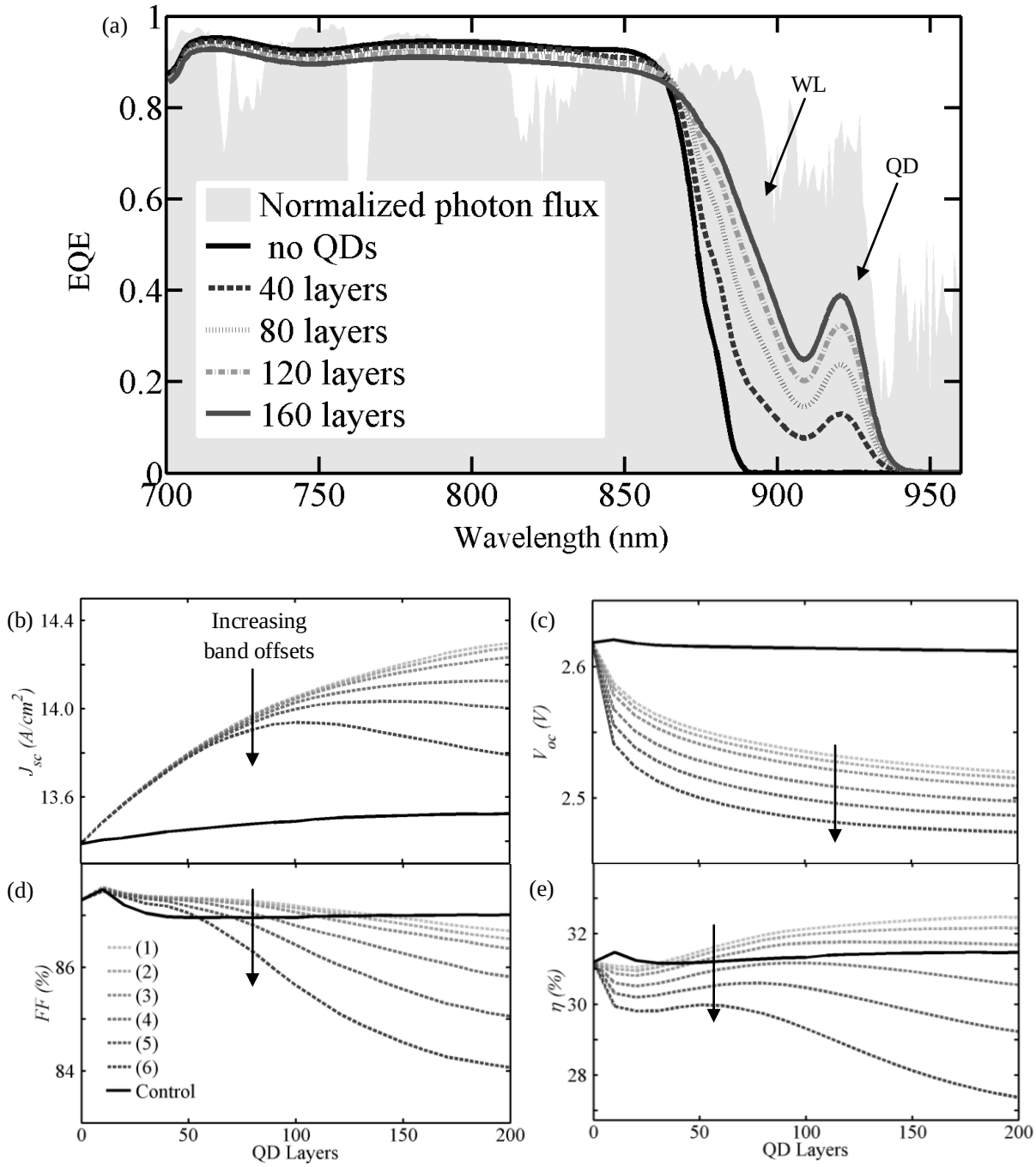

Figure 5-11. a) Increase in responsivity of the middle sub-cell in terms of EQE due to the addition of QD layers for band offsets given by scenario (2). b) J_{sc}, c) V_{oc}, d) *FF* and e) efficiency as a function of QD layers for QD enhanced MJSC described using effective band offset scenarios (1)-(6) as summarized in Table 5-6, and compared to a control MJSC structure which has an intrinsic region thickness increasing by 10 nm for each QD layer added.

Table 5-6. Summary of effective band offset scenarios explored during the optimization study of the QD enhanced MJSC as a function of QD layers.

Scenario	*CBO (meV)*	*VBO (meV)*	Total (meV)
1	0	0	0
2	5	1.7	6.7
3	10	3.4	13.4
4	20	6.8	26.8
5	30	10.2	40.2
6	42	14	56

cell increases for increasing number of QD layers (10 nm per QD layer). These results are also reported in [185]. For each number of QD layers studied within the MJSC, the device is current matched by optimizing the top sub-cell base thickness for a fixed bandgap, since changing the top sub-cell bandgap would render the analysis more complex. Figure 5-11a illustrates the EQE for increasing number of QD layers in the middle sub-cell wavelengthcarrier collection as these additional layers are placed further from the active region of the cell. For similar reasons, the EQE in the wavelength range of 700-850 nm decreases for

increasing number of layers, as carriers generated by these wavelengths outside the depletion region have a lower carrier collection probability. Furthermore, carriers generated in the base must be transported across all of the QD layers (some outside and others inside the depletion region), which also affects the carrier collection probability. However, the increase in the EQE in the 880-940 nm is more important than the drop in EQE in the range of 700-850 nm based on the photon flux for those wavelength ranges. This is confirmed in Fig. 5-11b which illustrates the J_{sc} as a function of QD layers. Note that the J_{sc}'s increase begins to stabilize around 120 layers. Each of the 6 scenarios generates the same photocurrents up to 60 layers of QDs. After this, the benefits of more QD layers depend

inherently on the magnitude of the band offsets, since these added QD layers are positioned outside the depletion region and thus contribute less to the photocurrent if the band offsets are greater than 13.4 meV. The control illustrates the small benefits of adding an intrinsic region to the middle sub-cell, whereby the increased depletion region thickness increases carrier collection probability.

Figure 5-11c illustrates the trend in V_{oc} as a function of QD layers. A steep decrease in V_{oc} is observed for the introduction of 10 QD layers. Interestingly, the V_{oc} stabilizes as the number of QD layers increases, where each band offset scenario illustrates a different *effective* V_{oc} for increasing QD layers. Each scenario thus represents a different *effective* bandgap for the middle sub-cell which ultimately depends on the number of QD layers. The addition of an intrinsic region without QDs does not show a strong influence in V_{oc}, as outlined by the control structure. Figure 5-11d illustrates the fill factor, where the *FF* generally decreases for increasing number of QD layers. Initially, an increase in *FF* is observed for up to 10 layers, although it decreases beyond 20 layers. This initial increase of 0.2% absolute is due to the 0.8% relative increase in photocurrent compared to the 3% relative drop in open circuit voltage. The eventual decrease becomes more pronounced for larger band offsets since the QD layers are positioned outside the depletion region and effectively decreases the diffusion length of carriers in these regions. This is a drawback of introducing an intrinsic layer with reduced carrier lifetimes in the middle sub-cell. The control *FF* remains reasonably constant over the entire range of intrinsic thicknesses studied primarily due to the long diffusion lengths of carriers in intrinsic InGaAs. Lastly, the efficiency of the QD enhanced MJSC illustrates the complex nature of this optimization problem, whereby the benefits of increased photocurrent must be balanced by the drop in

open circuit voltage and drop in fill factor to result in an absolute boost in efficiency over the control structure. A decrease in efficiency is observed for up to 20 layers of QD for all band offset scenarios since the drop in V_{oc} is more significant than the drop in J_{sc}. On the other hand, an overall boost in efficiency is obtained relative to the control structure for the ideal (0 meV) scenario with more than 30 layers of QDs, the 6.7 meV scenario for more than 37 layers and the 13.4 meV scenario for more than 47 layers. However, effective band offsets greater than 27 meV do not illustrate an overall boost in efficiency. The benefits of adding QDs to a MJSC are thus clearly demonstrated based on the set of material and model input parameters via this study. However, the results depend inherently on the magnitude of the confinements, the minority carrier lifetimes and the overall boost in photocurrent.

5.3.5. Performance of QD Enhanced MJSC as a function of concentration

A QD enhanced MJSC is intended for concentrated illumination applications of up to 1000 times concentration and beyond. Figure 5-12 illustrates the effects of concentrated illumination on the performance of the QD enhanced MJSC using the new improved model using effective band offsets coupled to trap distributions; the effective band offsets are 0 meV and 56 meV. Each structure consists of 110 QD layers rather than 130 layers since the 6.7 meV band offset scenario is adopted to most accurately represent the energy levels of the WL, and only 110 layers are required to match the peak at 920 nm in this scenario. These results are compared to the QW scattering formalism describing 65 QD layers, even though this model was shown to have failed for greater than 120 layers of QDs. The trends are also compared to control structures with both *n-p* and *n-i-p* middle sub-cell configurations where the *p*-type intrinsic doping for all the structures is kept fixed at 5×10^{15} cm^{-3}. Each structure is

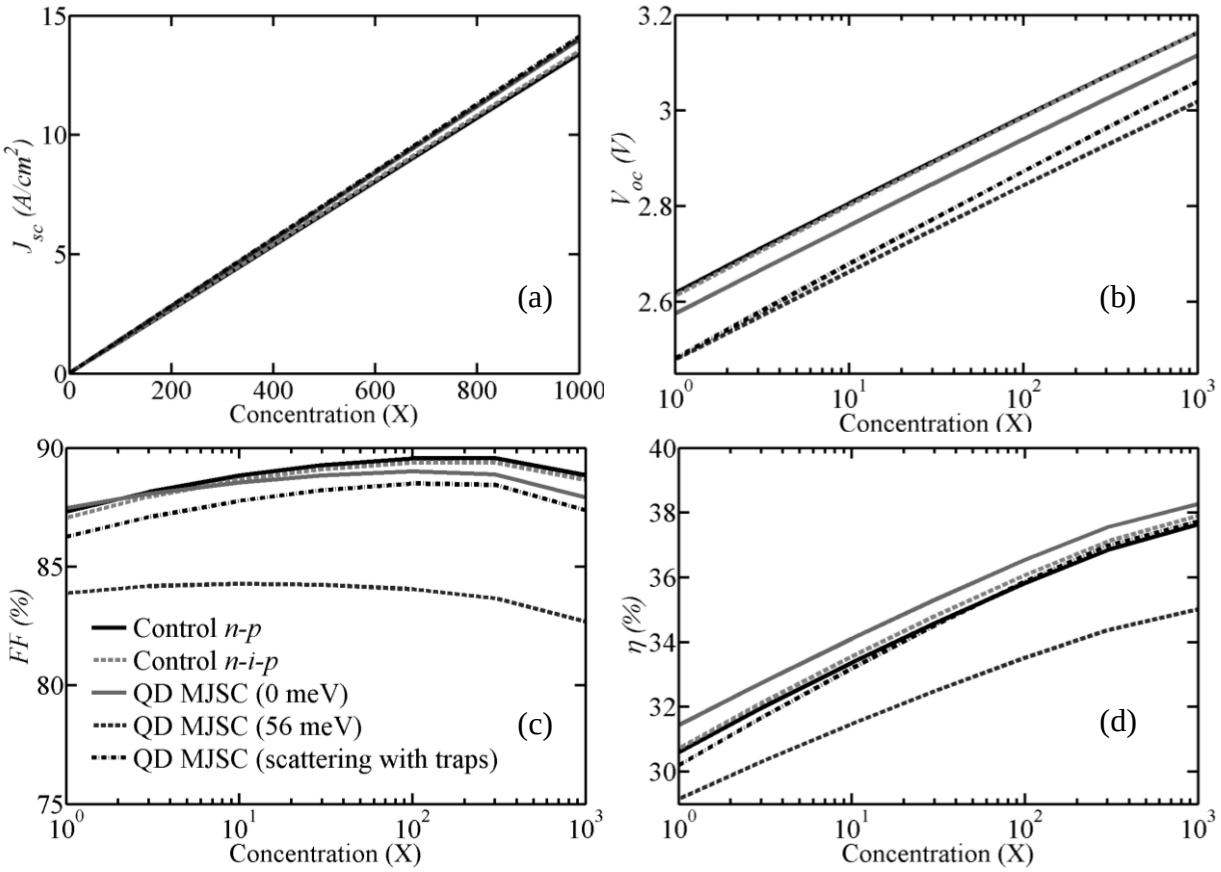

Figure 5-12. Simulated *J-V* metrics (J_{sc}, V_{oc}, FF and η) of a QD enhanced MJSC as a function of concentration for a control structures (*n-p* and *n-i-p* for the middle sub-cell) and the QD enhanced MJSC described using the new improved effective band offset approach (0 meV and 56 meV) with traps to model the QD ground state, and lastly, a QD enhanced MJSC structure as described using the QW scattering

optimized for current matching using strictly the top sub-cell base thickness. The effects of the concentrating optics on the spectrum are ignored (i.e. an optical transfer function of unity). These simulations are performed at room temperature primarily because devices intended for CPV are measured under STC.

Figure 5-12a outlines two different subsets of data for the J_{sc} as a function of concentration: one set with a higher photocurrent, corresponding to the QD enhanced MJSCs, and the other set with a lower photocurrent, corresponding to the control structures. These two subsets are expected simply based on the higher photocurrent of the QD MJSC in comparison to the control structures. Although not easily observed, the 0 meV band offset

scenario is virtually identical to the QD MJSC described using the QW scattering formalism with traps. The linearity in the J_{sc} as a function of concentration is still maintained, as expected.

Figure 5-12b illustrates the logarithmic behaviour of the V_{oc} as a function of concentration, similar to Fig. 4-19. Within this plot, the structures with the largest V_{oc} correspond to the control structures simply due to the higher bandgap of the middle sub-cell. The structure with the lowest V_{oc} corresponds to the QD MJSC described using 56 meV of effective band offsets, which is also an expected result since this is the worst case scenario. The ideal QD MJSC described using 0 meV of effective band offsets has the highest V_{oc} of the three QD MJSC structures, and is lower than the control structures due to the lower minority carrier lifetimes of the QD effective medium. Interestingly, the QD MJSC described using the QW scattering formalism with traps has a V_{oc} in agreement with the effective band offset (56 meV) with traps at low concentrations, and reaches a V_{oc} very similar to that corresponding to the ideal 0 meV band offset scenario at high light concentration. It thus demonstrates the largest slope out of all the structures, which indicates it has the highest ideality factor (see equation 4.4.1). However, this result should not be treated as an actual expectation from a QD enhanced MJSC since the recombination taking place within the effective medium depends on the adequate solution of the continuity equations, which is in doubt based on the unphysical results reported earlier. The slope of V_{oc} as a function of concentration for the effective band offset scenarios and the control structures are similar (i.e. parallel), which indicates the recombination processes are similar in the middle sub-cell.

Figure 5-12c illustrates the trends in *FF* as a function of concentration, whereby the highest *FF*s correspond to the control structures, and the lowest corresponds to the QD MJSC described using 56 meV of effective band offsets with traps. This latter observation confirms the worst case scenario for this model, and is considerably lower than the larger band offset scenarios since the middle sub-cell is current limiting the device by 2% with respect to the top sub-cell's photocurrent. This 2% current mismatch arises out of the constant top sub-cell thickness for each of the 6 band offset scenarios to allow for a better comparison. As a result, the other scenarios exhibit a more even current sharing scheme between the top and middle sub-cells since the band offsets do not significantly degrade the photocurrent of the middle sub-cell. The *FF* corresponding to the ideal 0 meV band offset is initially in agreement with the control structures, but decreases more so as a function of concentration in comparison to the control structures. The *FF* of the structure modeled using the QW scattering formalism with traps is in between the control structures and the worst case scenario. The roll-off of the *FF* at concentrations above 300 is due to the added contact resistance of 0.01 Ω that is typical of MJSC for concentrator applications [131].

Lastly, Figure 5-12d outlines the overall cell efficiency as a function of concentration. This demonstrates that the ideal 0 meV band offset scenario has the highest efficiency over all concentrations due to its minimal voltage drop and maximal photocurrent compared to the other structures. It reaches an efficiency of 38% at 1000 suns. In a close second is the control MJSC with an *n-i-p* middle sub-cell with an efficiency of 37.8% at 1000 suns. The QD MJSC described using the QW scattering formalism with traps has a very comparable efficiency of 37.7%, and the control MJSC with the *n-p* middle sub-cell has an efficiency of 37.6%. Lastly, the QD MJSC described using 56 meV of band offsets

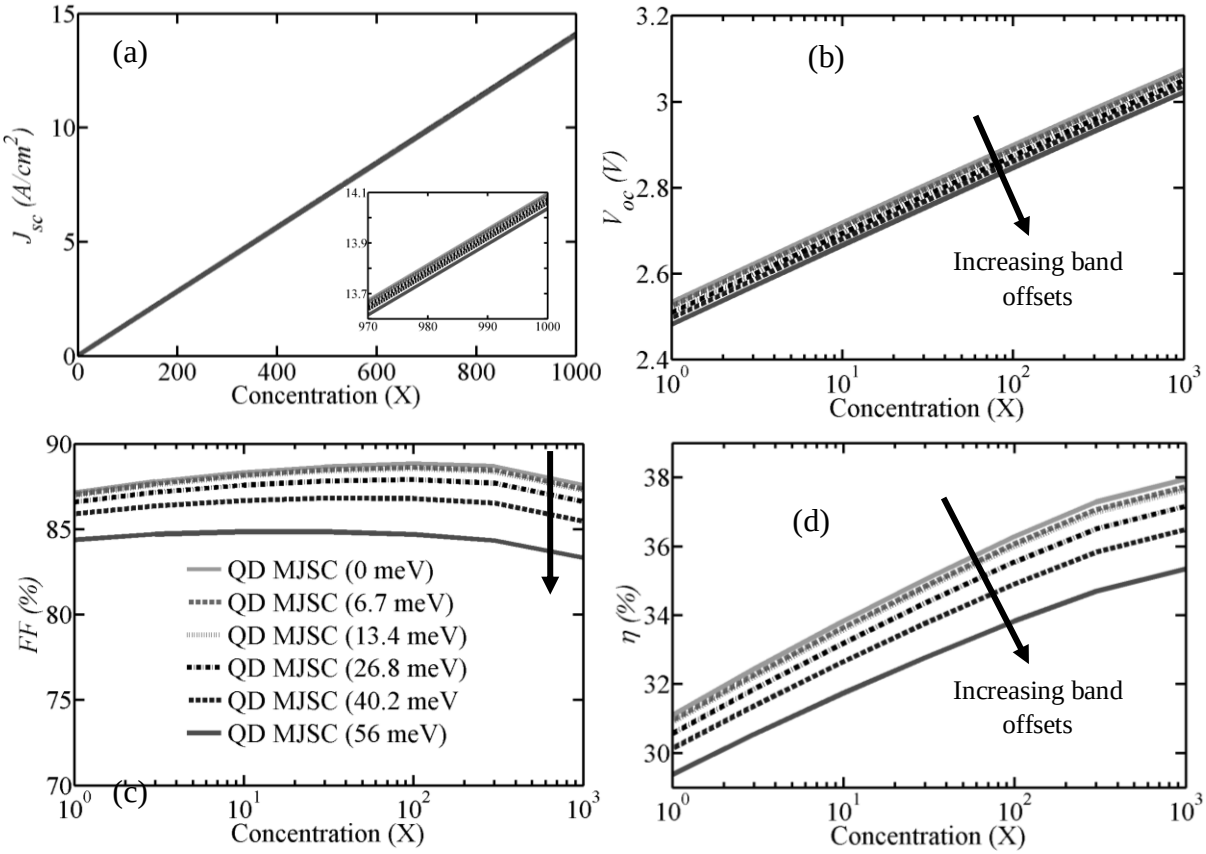

Figure 5-13 Simulated *J-V* metrics (J_{sc}, V_{oc}, FF and η) of a QD enhanced MJSC as a function of concentration for the QD enhanced MJSC described using the effective band offset with traps using the 6 scenarios outlined in Table 5-6, namely (1) 0 meV of effective band offsets, (2) 6.7 meV, (3) 13.4 meV, (4) 26.8 meV, (5) 40.2 meV and (6) 56 meV.

comes in as the worst performing device at 1000 suns with an efficiency of 35.0%. This is appreciably lower than the predictions from the other models primarily due to the low fill factor arising from the middle sub-cell limiting the current of the device. This significant drop in efficiency thus emphasizes the importance of the magnitude of the band offsets in the design of the QDs and of the device as a whole.

Varying the band offsets (i.e. adopting the band offsets of scenarios (2)-(5) from Table 5-6 generates *J-V* metrics in between those obtained using the ideal scenario (1) with 0 meV and worst case scenario (2) with 56 meV of band offsets. These data are illustrated in Fig. 5-13 as a function of concentration and are summarized in [186]. Figure 5-13a shows

nearly identical photocurrents versus concentration, although the inset plot illustrates that the 0 meV band offset scenario predicts the highest photocurrent compared to the 56 meV scenario. The open circuit voltage versus concentration illustrates the trend of decreasing V_{oc} for increasing band offsets, which is expected based on decreased carrier escape and therefore increased recombination rates. Increasing band offsets naturally leads to a decrease in efficiency, where the 6.7 meV band offset scenario illustrates an efficiency very comparable to the ideal scenario of 0 meV as the confinement potentials of the effective medium do not lead to a severe drop in open circuit voltage nor in fill factor. These results are very important for MJSC enhanced with QDs in that their performance benefits become clear when investigating high concentration applications. One can propose, hypothetically, that these structures would be even better performing at concentrations exceeding 1000 suns assuming series resistances can be reduced to below 0.01 Ω cm^{-2}.

5.3.6. Positioning and Doping of the QD Layers within the InGaAs Sub-cell

A theoretical study is conducted on the effects of varying the position of the QD layers on the simulated current – voltage characteristics [187]. This serves as a verification of the model to explain the experimental results of QDs positioned in a single junction solar cell as reported by Zhou *et al*. [12] from a theoretical standpoint. These studies are conducted by simulating the *J-V* characteristics of the QD enhanced MJSC with and without QD in the various layers of the middle sub-cell, namely the emitter, the intrinsic region and the base. The effective band offset approach with traps is used to model the effective medium according to scenario (2) from Table 5-6 (i.e. band offsets of 6.7 meV), as this is the most relevant scenario since the band offsets represent the simulated WL energy level and the QD

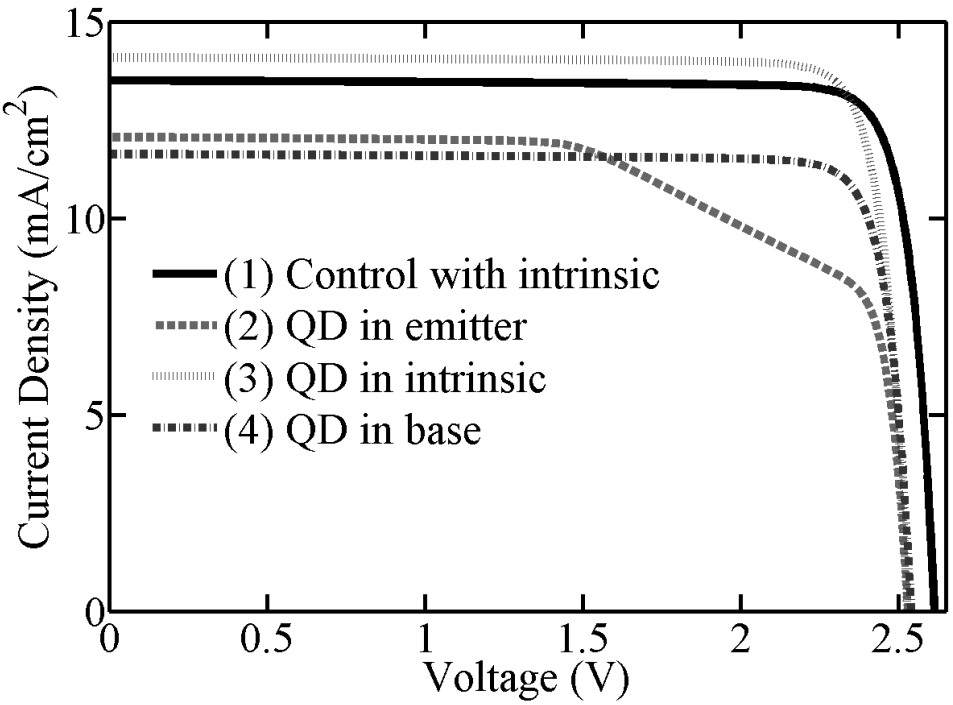

Figure 5-14. Simulated *J-V* curves of the QD enhanced MJSC structures with 110 layers of QD using the effective band offset approach (6.7 meV) with traps where the QD are positioned in the a) emitter, b) intrinsic region, and c) base. These results are compared to a control structure (*n-i-p* in the middle sub-cell with an intrinsic thickness of 1.1 µm).

ground state is modeled using the trap distribution. The energy band diagrams at equilibrium are then used to study the properties of the simulated *J-V* curves.

Figure 5-14 illustrates the *J-V* results for a control MJSC with no QD layers labelled as structure (1), and three QD enhanced MJSC where the QD are positioned in the emitter, labelled structure (2), in the intrinsic region, labelled structure (3), and lastly, in the base, labelled as structure (4). The *J-V* metrics are summarized in Table 5-7. Structure (3) demonstrates the highest efficiency, since the carrier collection probability is highest when

Table 5-7. Summary of simulated QD enhanced MJSC characteristics under 1 sun illumination (1 kW/m^2, AM1.5D) at 300 K corresponding to Fig. 5-14.

	Structure	J_{sc} (mA/cm^2)	V_{oc} (V)	FF	η (%)
(1)	**Control (no QDs)**	13.47	2.62	87.0	30.6
(2)	**QDs in the emitter**	12.06	2.53	64.9	19.8
(3)	**QDs in the intrinsic**	**14.09**	**2.53**	**87.1**	**31.0**
(4)	**QDs in the base**	11.63	2.54	87.0	25.7

the QD layers were positioned in the depletion region. The control structure (1) comes in as the second highest efficiency, followed by structure (4) then structure (2) where the QD layers are positioned in the base and the emitter respectively. Placing the QD layers in the emitter and base significantly degrades the performance of the overall MJSC by reducing the carrier collection probability for carriers generated in the QD layers. When QD layers are positioned in the emitter, a strong reduction in the fill factor is observed, which indicates that an irregularity in the energy band diagram is most likely present. The trends illustrated in Fig. 5-14 are in qualitative agreement with the results found by Zhou *et al*., although reverse diode characteristics were not reproduced in this simulation. Note that Zhou *et al.* [12] investigated the positioning of QD layers in a single junction solar cell, whereas this study focuses on a triple junction solar cell.

To gain a better understanding of the effects of QD layers on the *J-V* characteristics, one must study the energy band diagram for each structure. Note that each energy band diagram will have subtle differences in the top sub-cell thickness due to current matching considerations, i.e. the top sub-cell base thickness is optimized for maximum efficiency in each structure. The energy band diagram of the control structure at J_{sc} and at an applied bias of $V=2.3\ V$ are shown in Fig. 5-15a, which show typical MJSC features of a *n-p* top InGaP sub-cell connected to an AlGaAs/GaAs tunnel junction followed by an InGaAs *n-i-p* sub-cell. The energy band diagram for QD layers positioned in the intrinsic region of the *n-i-p* middle sub-cell, illustrated in Fig. 5-15b at J_{sc} and at $V=2.3\ V$, are different from the control in that the intrinsic region contains lower bandgap structures (see inset plot of Fig. 5-5b). This explains the drop in V_{oc}, in combination with the lower minority carrier lifetimes in the

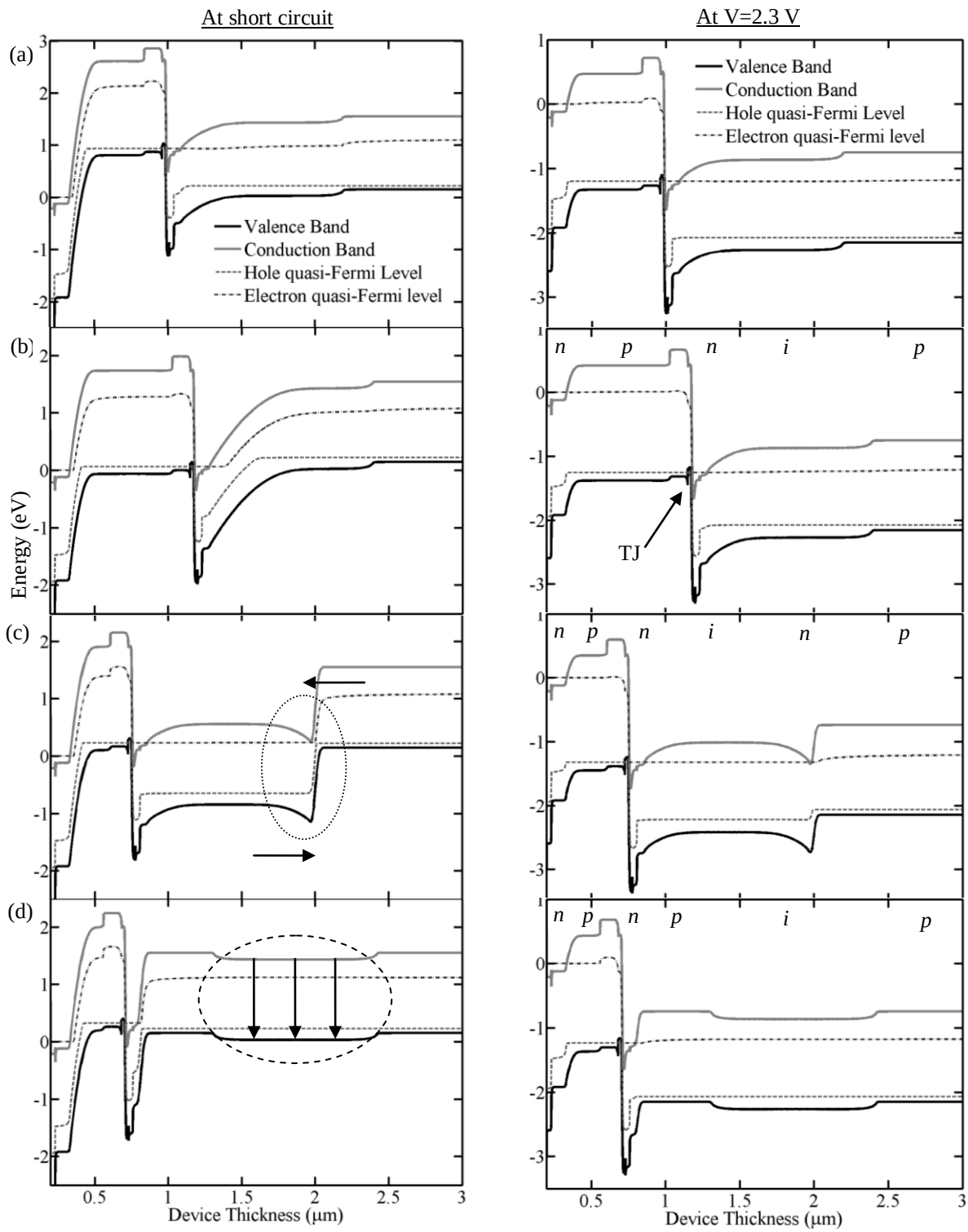

Figure 5-15. Simulated energy band diagrams of four structures at equilibrium and at an applied bias of V=2.3 V: (a) a control MJSC structure with no QD in the *n-i-p* middle sub-cell, and three QD enhanced MJSC structures each with 110 layers of QD using 6.7 meV of effective band offsets with traps, where the QD are positioned in b) the intrinsic region with an inset showing the potential confinements, c) the emitter, and d) the base. The QD layers in the emitter of the middle sub-cell produce potential barriers near the active region (marked by a dotted oval). On the other hand, QD layers positioned in the base produce a region of lower potential energy (dashed oval) where carriers generated in these layers experience lower carrier collection probabilities.

effective medium. However, the overall J_{sc} is higher in this structure due to the absorption of the QDs in the 880-920 nm range.

When the QDs are positioned in the emitter of the middle sub-cell, a significant drop in fill factor is observed in Fig. 5-14. Consequently, some irregularity should be present in the energy band diagram of this cell. Figure 5-15c shows that adding QD layers of *p*-type background doping in the emitter creates a potential barrier for the minority carriers, as highlighted by the dotted oval and the arrows corresponding to the direction of minority carrier flow. The potential barrier introduced into the structure forms as a result of the *p*-type background doping of the intrinsic and QD layers that are located between two *n*-type layers. This potential barrier also manifests itself in the decreased open circuit voltage observed in Fig. 5-14 and reported in Table 5-7 in comparison to the control. The energy band diagram at the applied bias also shows this potential barrier, where carriers will get trapped in the region of low potential within the ’epletion region (i.e. between the base and the QD layers) and thus have a lower collection probability. This also explains the decreased photocurrent for this specific structure relative to the QD MJSC with QDs positioned in the intrinsic region.

Lastly, Fig. 5-15d illustrates the energy band diagram for QD positioned in the base. Since there is no intrinsic region adjacent to the nitter and base, the depletion region is not widened, and the photocurrent is therefore considerably lower than the other reported structures. Furthermore, the lower doping level of the intrinsic InGaAs and QD layers relative to the base doping level produces a region of lower energy for the minority carriers (outlined with a dashed oval in Fig. 5-15d). As a result, carriers generated in the QD experience a lower carrier collection probability, thereby lowering the photocurrent of the

cell below the J_{sc} of an *n-i-p* cell with no QDs. The rates of radiative and non-radiative recombination of minority carriers in this region increase significantly. However, the open circuit voltage is larger than the structures (1)-(3) since the depletion region is drastically reduced in volume, and therefore the overall SRH recombination of the sub-cell is reduced.

The focus is then applied on studying the effects of the doping level of the InGaAs spacer layers and of the QD on the overall efficiency of the device. The QD layers are positioned in the intrinsic region of the middle sub-cell and are modeled using the effective band offset with traps according to scenario (2) with 6.7 meV of band offsets. The results are illustrated in Fig. 5-16 in terms of a) simulated *J-V* characteristics of a QD enhanced MJSC with 110 QD layers for various levels of intrinsic background doping, followed by the *J-V* metrics in (b)-(e). The J_{sc} begins to decrease only slightly for higher levels of doping since the depletion region is diminished. This implies that some of the QD layers are positioned outside the depletion region due to its reduced width, and thus carriers generated in these layers have a decreased carrier collection probability. Increased levels of doping also affect the V_{oc}, since the SRH recombination rates are decreased once again due to the reduced depletion region. Increasing the intrinsic background doping leads to increased fill factors and efficiencies, primarily due to the increase in V_{oc}. For the intrinsic level of 3×10^{16} cm^{-3}, an overall 1 sun efficiency of 31.3% was achieved, which is higher than the control performance reported in Table 5-7.

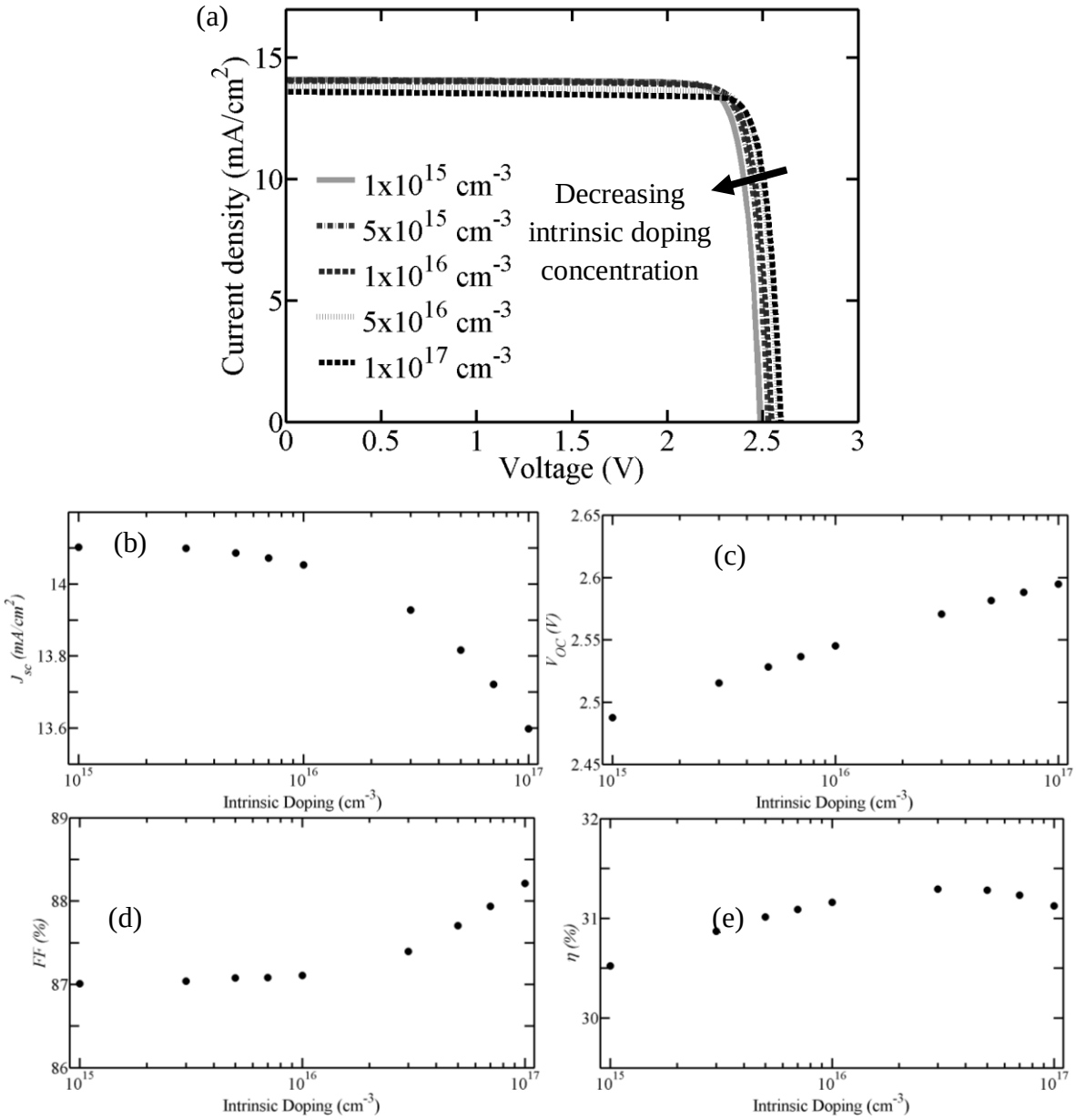

Figure 5-16. a) Simulated *J-V* curves of a QD enhanced MJSC with 110 layers of QD as a function of intrinsic doping level for the InGaAs spacer and the QD layers. The QD are described using 6.7 meV of effective band offset with traps. The *J-V* metrics are then given as a function of intrinsic background doping for b) J_{sc}, c) V_{oc}, d) FF and e) efficiency.

5.4. Conclusions & Limitations of the Models

The simulation results presented in this chapter outline the benefits of integrating InAs QD in the middle sub-cell of a lattice matched triple junction solar cell composed of InGaP/InGaAs/Ge for concentrator photovoltaic applications. The simulated device performance was reported and discussed under standard testing conditions and as a function of concentration. These simulations were also compared to control structures without QD layers. Although experimental data from known test structures is lacking in this thesis primarily due to the costs and complexities in the growth of such devices, the results can be generalized as follows. The addition of QDs to the middle sub-cell of a MJSC allows for an increase in photocurrent over a control structure. The enhanced efficiency depends strongly on the resulting drop in open circuit voltage. Thus, the higher performance of the QD MJSC over the control structures lacking QDs arises primarily due to the higher overall photocurrent with respect to the control. Integrating QDs thus effectively tunes the bandgap of the middle sub-cell depending on the ground state optical transitions in the QD. The degree of varying the effective bandgap of the middle sub-cell also depends implicitly on the number of layers of QDs and their proximity to the depletion region. The role of the QDs in improving the total photocurrent of the device was complimentary to the tunable bandgap of the top InGaP sub-cell using ordering effects by varying crystal growth conditions. However, the introduction of the lower bandgap structures coupled to shorter minority carrier lifetimes resulted in a reduced open circuit voltage contribution from the middle sub-cell, which is an expected trade-off. The net result on efficiency is therefore an optimization problem between improving the overall current without significantly degrading the open circuit voltage and fill factor for increasing the number of QD layers. The introduction of

InAs QD thus represents a method of bandgap engineering the middle sub-cell, where the crystal quality of the said QDs is vitally important to the improvements in device performance. Thus, under the assumption that these QDs can be grown in a high quality crystalline InGaAs matrix, this material system presents an excellent opportunity to improve triple junction solar cells by introducing a highly controllable and reproducible method of sharing currents between the top InGaP, middle InGaAs and bottom Ge sub-cells.

However, the models developed in this thesis are limited in a few noteworthy manners. First and most importantly is the lack of calibration of these models to experimental data of known structures. The validity of the developed models depends inherently on their ability to predict and reproduce phenomena of MJSCs, and thus merits further investigation. However, the models developed can be tested to known devices as they become available from advanced research groups. Another important limitation of the models is the incompatibility of the laser physics modules (responsible for the QW scattering formalism) and the optical generation modules in Sentaurus Device. This forced two assumptions in the development of an effective medium for the InAs/GaAs QD system using the effective band offsets: 1) coupling the generation terms between bound and unbound carrier populations, and 2) coupling the recombination lifetimes between these populations. When quantum well scattering equations were implemented to describe the carrier dynamics in and out of the potential confinements of the nanostructures, this led to the over-estimation of the generation in the simulated external quantum efficiency, which was corrected by scaling the bulk contribution to the effective medium's absorption coefficient. This was perhaps a foreshadowing of the unphysical nature of the model when simulating more than 120 layers of QD, whereby the EQE exceeded unity. This is an

inherent limitation within the TCAD Sentaurus environment, which can only be modified from within the internal Sentaurus Device code simply by including a generation term originating specifically from the bound energy levels of the nanostructures. Based on these findings, the most heuristically sound model to describe a QD MJSC thus combines the effective band offset approach explicitly for the wetting layer, and the Gaussian distribution of traps for the QD states above and below the valence and conduction bands respectively. This approach targets the effects of the InAs wetting layer behaving as a QW with respect to the carrier dynamics by using effective band offsets to mimic carrier escape and capture by the potential energy barriers of the WL based on the WL energy levels (in this case, 5 meV below the conduction band and 1.7 meV above the valence band). Varying the levels of effective band offsets therefore simulates the effects of strain in the bandstructure of the WL from the GaAs matrix (i.e. the effects of "wings" in the conduction band). The error in using the effective band offset stems from the difference between two-dimensinoal density of states rather than bulk three-dimensinoal effective bulk density of states, although this was shown to be within reasonable error. The traps corresponding to the QD energy levels mimic the localization of the carrier wavefunctions, although this component to the model relies on the thermal depopulation of carriers from these trap states at 300 K.

Secondly, the absorption coefficient calculation depends implicitly on the energy levels, which were computed using COMSOL externally from Sentaurus. The interconnectivity of these models could be improved by developing c++ code to compute energy band structures of strained quantum dots with dependences on the quantum dot geometry. The calculation of the resulting ground state and higher excited energy transitions can then be performed and coupled to the calculation of the extinction coefficient of the

material using the developed analytical absorption models. An example of a similar feat is Tomić *et al*. [179] for intermediate band applications. Once this is developed, exploring the effects of various QD geometries on device performance can be performed more trivially.

Third, the models developed in both chapters 4 and 5 do not include the effects of photon recycling, an effect where radiative recombination processes result in a continuously iterative process of absorption followed by carrier dynamics followed by radiative recombination, until either the carrier is collected at the contacts or a non-radiative recombination process occurs. The difficulty in modeling the effects of photon recycling includes an iterative calculation of the optical generation coupled to radiative recombination rates. This would result in the emission of photons that would be re-absorbed by the sub-cell and thus iteratively contribute to the generation term. A method has been proposed in the literature [188], which can be adapted to modeling multi-junction solar cells.

Future modeling work without test structures can focus on exploring the effects of concentrations exceeding 1000 suns, exploring the effects of elevated operating temperatures, and considering optical transfer function effects as simulated using, for example, Zemax (an optical design software made by Radiant Zemax, Redmond, WA, USA), or experimentally measured optical transfer functions. Other studies such as the effects of different QD geometries (and therefore different energy level configurations on absorption and carrier dynamics) on device performance can also be performed. However, the developed QD effective medium models need further validation and calibration, which can only be performed using experimental data from known test structures. This becomes the most significant component of the future work, and should be performed using single junction solar cells with and without QDs before progressing to more complex devices such

as a QD MJSC. On this note, a doctoral student from the University of Sherbrooke (Jihene Zribi) just completed the characterization of single junction solar cells composed of GaAs with InAs QDs for experimental characterization. However, the analysis of her results were not particularly clear due to irregularities in the current – voltage characteristics, although some very nice external quantum efficiency measurements were performed for QDs of different geometries. Unfortunately the overlap between this experimental work and this thesis were minimal. Another possible topic for future work is studying the effects of energy band structure using TCAD Sentaurus and including strain effects to model the bands at the InAs/InGaAs interface internally to Sentaurus rather than using COMSOL.

Chapter 6: Conclusions & Future Work

This thesis introduces the important concepts in modeling multi-junction solar cells in order to investigate the modeling of an InGaP/InGaAs/Ge triple junction solar cell enhanced with InAs/GaAs QD nanostructures within the middle InGaAs sub-cell. First, the semiconductor physics and basic material properties of semiconductors were introduced in chapter 2, including basic physics of quantum structures such as quantum dots and wells. The discussion then progressed to the analysis of a *p-n* junction and the simulation of single junction solar cells using TCAD Sentaurus in chapter 3, which required the introduction of the material properties for group III-V semiconductors AlInP, GaInP, AlGaAs, GaAs, group IV semiconductors Ge and Si, and lastly the I-III-VI_2 semiconductor compound Cu(In,Ga)Se_2. Chapter 4 then focused on modeling and simulating multi-junction solar cells composed of the group III-V semiconductors by first introducing detailed balance predictions, then simulating the behavior of tunnel junctions, before simulating the performance of a fully interconnected MJSC system composed of sub-cells, tunnel junctions and a broadband anti-reflection coating. These were then simulated under concentrated illumination, at elevated temperatures, and within the regime of tunnel junction limiting performance. The central topic of this thesis was discussed in chapter 5 on bandgap engineering a triple junction InGaP/InGaAs/Ge solar cell using InAs/GaAs QDs within the middle sub-cell. The QDs were modeled as an effective medium which included absorption characteristics to model the generation of electron-hole pairs in the nanostructures, realistic recombination lifetimes as reported in the literature, and lastly, carrier-carrier and carrier-

phonon scattering dynamics, all of which fit into the current-continuity equations of the device simulator. An initial structure was studied and partially calibrated to the measured EQE of a First Generation QDEC device manufactured by Cyrium Technologies. The following simulated solar cell *J-V* metrics were obtained: a J_{sc} of 14.1 mA/cm^2, a V_{oc} of 2.48 V, a fill factor of 83.6% and an overall efficiency of 29.1% under standard testing conditions; these results were in good agreement with the measured performance of the commercially available device, even though the device structure was not known. A methodology for optimizing the QD MJSC performance involved the parameter space including background intrinsic doping and the number of QD layers under the assumption of a specific QD geometry to dictate the bound energy levels of the nanostructures. Simulations carried out for increasing levels of concentrated illumination revealed that a QD MJSC can exceed the performance of a lattice matched control structure by as much as 1% absolute. This indicates that bandgap engineering lattice matched MJSC using InAs/GaAs QDs can be a viable method of enhancing the performance of MJSC for CPV applications, as long as the minority carrier lifetimes are not significantly degraded due to the introduction of nanostructures within the InGaAs matrix. Growing and fabricating devices in which the lattice mismatch between InAs and InGaAs must be controlled using appropriate temperature and growth optimization is a difficult challenge. Modeling and simulation of these devices can assist in device design only with thoroughly calibrated models, which is a topic of future work for the author during postdoctoral studies.

The modeling methods discussed and developed in this thesis agglomerate into a detailed optimization routine with respect to the large parameter space relevant in maximizing multi-junction solar cell device performance under concentrated illumination

conditions with realistic temperature considerations. The effects of optical transfer functions from typical concentrator systems can be studied through these said methods. The general simulation methods of MJSC can also be adapted to model various other material systems, such as the closely linked lattice mismatched material system of InGaP/InGaAs/$In_{0.3}Ga_{0.7}As$, a dilute nitride based InGaP/InGaAs/InGaAsN triple junction or InGaP/InGaAs/InGaAsN/Ge quadruple junction cell, or an $Al_xGa_{1-x}As/Al_xGa_{1-x}As$/Ge system where the molar fraction of the top $Al_xGa_{1-x}As$ sub-cell is larger than the middle $Al_xGa_{1-x}As$ structure for optimal bandgap management.

Furthermore, the specific focus of this study – integrating nanostructures in the middle sub-cell of a MJSC – introduces the possibility of exploring the integration of QDs in another sub-cell such as one composed of the dilute nitride in a triple or quadruple junction configuration. This could lead to an extra degree of controlling the distribution of currents in each sub-cell, and therefore enhance the ability of current matching a triple or quadruple junction device for different climates which experience different incident spectra as compared to the standard AM1.5D adopted in this thesis. In other words, these modeling and simulation methods can be generalized to bandgap engineer any sub-cell of a MJSC. As the growth of high quality self-assembled nanostructures becomes more feasible in other material systems, it should be possible to achieve more optimal (effective) bandgap combinations which lead to enhanced MJSC efficiencies at high concentration.

Future research and development of multi-junction solar cells are targeting quadruple junction cells, where a leading candidate material is a dilute nitride to form the third sub-cell of an InGaP/InGaAs/InGaAsN/Ge configuration. However, the dilute nitride material typically has reduced material quality due to the clustering of N atoms in the material, which

reduces carrier mobilities and lifetimes, both of which reduce minority carrier diffusion lengths. This introduces difficulties in achieving a high enough short circuit current in the dilute nitride based sub-cell so as to not limit the overall photocurrent of the device. The problem of typically low fill factors in this sub-cell also compounds the problem. The modeling and simulation of dilute nitride sub-cells would assist in designing the next generation of multi-junction solar cells, where the concepts of enhancing the photocurrent of this sub-cell by integrating appropriately grown QD in the depletion region could be explored using the methods and models developed in this thesis.

References

[1] A. Yoshida, T. Agui, N. Katsuya, K. Murasawa, H. Juso, K. Sasaki, T. Takamoto. "Development of InGaP/GaAs/InGaAs inverted triple junction solar cells for concentrator application," Proceeding from the *21st International Photovoltaic Science and Engineering Conference (PVSEC-21)*, Fukuoka, Japan 2011.

[2] www.sj-solar.com.

[3] M. A. Green, K. Emery, Y. Hishikawa, W. Warta, E. D. Dunlop. "Solar Cell Efficiency Tables (version 40)," *Progress in Photovoltaics: Research and Applications* **20**(5), 606-614, 2012. DOI: 10.1002/pip.2267

[4] R. R. King, D. C. Law, K. M. Edmondson, C. M. Fetzer, G. S. Kinsey, H. Yoon, R. A. Sherif, N. H. Karam. "40% efficient metamorphic GaInP/GaInAs/Ge multijunction solar cells," *Applied Physics Letters* **90**, 183516-1 – 183516-3, 2007. DOI: dx.doi.org/10.1063/1.2734507.

[5] J. F. Geisz, A. Duda, R. M. France, D. J. Friedman, I. Garcia, W. Olavarria, J. M. Olson, M. A Steiner, J. S. Ward, M. Young. "Optimization of 3-junction inverted metamorphic solar cells for high-temperature and high-concentration operation," *AIP Conference Proceedings*, **1477**, 44-48, 2012. DOI: dx.doi.org/10.1063/1.4753830.

[6] W. Guter, J. Schone, S. P. Philipps, M. Steiner, G. Siefer, A. Wekkeli, E. Welser, E. Oliva, A. W. Bett, F. Dimroth. "Current-matched triple-junction solar cell reaching 41.1% conversion efficiency under concentrated sunlight," *Applied Physics Letters* **94**, 223504-1 – 223504-3, 2009. DOI: dx.doi.org/10.1063/1.3148341.

[7] F. Dimroth, W. Guter, J. Schone, E. Welser, M. Steiner, E. Oliva, A. Wekkeli, G. Siefer, S. P. Philipps, A. W. Bett. "Metamorphic GaInP/GaInAs/Ge Triple-Junction Solar Cells with >41% Efficiency," Proceeding from the *34th IEEE Photovoltaic Specialists Conference* (PVSC), Philadelphia, PA, USA, 7-12 June 2009, 001038-001042. DOI: 10.1109/PVSC.2009.5411199.

[8] J. F. Geisz, S. Kurts, M. W. Wanlass, J. S. Ward, A. Duda, D. J. Friedman, J. M. Olson, W. E. McMahon, T. E. Moriarty, J. T. Kiehl. "High-efficiency GaInP/GaAs/InGaAs triple-junction solar cells grown inverted with a metamorphic bottom junction," *Applied Physics Letters* **91**, 023502-1 – 023502-3, 2007. DOI: dx.doi.org/10.1063/1.2753729.

[9] R.R. King, P. Chiu, C.M. Fetzer, R.K. Jones. "Energy Production from High-Efficiency 5-Junction Concentrator Solar Cells," Proceeding from the *27th European Photovoltaic and Solar Energy Conference (EU-PVSEC)*, Frankfurt, Germany, September 24-28, 2012, 156-159. DOI: 10.4229/27thEUPVSEC2012-1BO.12.5.

[10] V. Aroutiounian, S. Petrosyan, A. Khachatryan, and K. Touryan. "Quantum dot solar cells," *Journal of Applied Physics* **89(4)**, 2268-2271, 2001. DOI: dx.doi.org/10.1063/1.1339210.

[11] G. Wei, K.-T. Shiu, N. C. Giebink and S. R. Forrest. "Thermodynamic limits of quantum photovoltaic cell efficiency," *Applied Physics Letters* **91**, 223507-1 – 223507-3, 2007. DOI: dx.doi.org/10.1063/1.2817753.

[12] D. Zhou, P. E. Vullum, G. Sharma, S. F. Thomassen, R. Holmestad, T. W. Reenaas, B. O. Fimland. "Positioning effects on quantum dot solar cells grown by molecular

beam epitaxy," *Applied Physics Letters* **96**(8), 083108-1 – 083108-3, 2010. DOI: dx.doi.org/10.1063/1.3309411.

[13] R. B. Laghumavarapu, M. El-Emawy, N. Nuntawong, A. Moscho, L. F. Lester, D. L. Huffaker. "Improved device performance of InAs/GaAs quantum dot solar cells with GaP strain compensation layers," *Applied Physics Letters* **91**, 243115-1 – 243115-3, 2007. DOI: dx.doi.org/10.1063/1.2816904.

[14] D. Guimard, R. Morihara, D. Bordel, K. Tanabe, Y. Wakayama, M. Nishioka, Y. Arakawa. "Fabrication of InAs/GaAs quantum dot solar cells with enhanced photocurrent and without degradation of open circuit voltage," *Applied Physics Letters* **96**(20), 203507-1 – 203507-3, 2010. DOI: dx.doi.org/10.1063/1.3427392.

[15] C. G. Bailey, D. V. Forbes, R. P. Raffaelle, S. M. Hubbard. "Near 1 V open circuit voltage InAs/GaAs quantum dot solar cells," *Applied Physics Letters* **98**, 163105-1 – 163105-3, 2011. DOI: dx.doi.org/10.1063/1.3580765.

[16] K. A. Sablon, J. W. Little, V. Mitin, A. Sergeev, N. Vagidov, K. Reinhardt. "Strong enhancement of solar cell efficiency due to quantum dots with built-in charge," *Nanoletters*, **11**, 2311-2317, 2011. DOI: 10.1021/nl200543v.

[17] C. Kerestes, S. Polly, D. Forbes, C. Bailey, S. M. Hubbard, J. Spann, P. Patel, P. Sharps. "Investigation of quantum dot enhanced triple junction solar cells," Proceeding from the *37th IEEE Photovoltaic Specialists Conference* (PVSC), Seattle, WA, USA, 19-24 June 2011, 000127-000132. DOI: 10.1109/PVSC.2011.6185860.

[18] Cyrium patent, US7,863,516.

[19] A. Luque & S. Hegedus. (2005) *Handbook of Photovoltaic Science and Engineering, First Edition*. Hoboken, NJ, USA: John Wiley & Sons Ltd. Chapter 9.6.3.2, p. 387, 2003*;* Chapter 9.5.8.3, p. 376.

[20] J. F. Wheeldon, C. E. Valdivia, A. W. Walker, G. Kolhatkar, A. Jaouad, A. Turala, B. Riel, D. Masson, N. Puetz, S. Fafard, R. Arès, V. Aimez, T. J. Hall, K. Hinzer. "Performance comparison of AlGaAs, GaAs and InGaP tunnel junctions for concentrated multi-junction solar cells," *Progress in Photovoltaics: Research and Applications* **19**, 442-452, 2011. DOI: 10.1002/pip.1056.

[21] G. Kolhatkar, J. F. Wheeldon, C. E. Valdivia, A. W. Walker, S. Fafard, A. Turala, A. Jaouad, R. Arès, V. Aimez, and K. Hinzer. "Current-voltage measurements within the negative differential resistance region of AlGaAs/AlGaAs tunnel junctions for high concentration photovoltaic," *International Journal of Nanoscience*, **11**(4), 1240014-1 – 1230014-6, 2012. DOI: 10.1142/S0219581X12400145.

[22] M. Hermle, G. Letay, S. P. Philipps and A. W. Bett. "Numerical simulation of tunnel diodes for multi-junction solar cells," *Progress in Photovoltaics: Research and Applications* **16**, 409-418, 2008. DOI: 10.1002/pip.824.

[23] A. W. Walker, O. Thériault, M. Wilkins, J. F. Wheeldon, K. Hinzer. "Tunnel-Junction-Limited Multijunction Solar Cell Performance Over Concentration," *IEEE Journal of selected topics in quantum electronics: Numerical Simulation of Optoelectronic Devices* 19(5), 4000508-1 – 4000508-8, 2013. DOI: 10.1109/JSTQE.2013.2258140.

[24] B. Galiana, C. Algora and I. Rey-Stolle. "Explanation for the dark I–V curve of III–V concentrator solar cells," *Progress in Photovoltaics: Research and Applications* **16**, 331-338, 2008. DOI: 10.1002/pip.805.

[25] M. Steiner, W. Guter, G. Peharz, S. P. Philipps, F. Dimroth and A. W. Bett. "A validated SPICE network simulation study on improving tunnel diodes by introducing lateral conduction layers," *Progress in Photovoltaics: Research and Applications* **20**, 273-283, 2012. DOI: 10.1002/pip.805.

[26] M. Baudrit and C. Algora. "Tunnel Diode Modeling, Including Nonlocal Trap-Assisted Tunneling: A Focus on III–V Multijunction Solar Cell Simulation," *IEEE Transaction On Electron Devices* **10** (10), 2564-2571, 2010. DOI: 10.1109/TED.2010.2061771.

[27] Z. Q. Li and S. Li. "Sophisticated models replicate the effects of tunnel junctions," *Compound Semiconductor Magazine* **13** (6), 29-31, 2007.

[28] A. W. Walker, J. Wheeldon, C. E. Valdivia, G. Kolhatkar, K. Hinzer. "Simulation, modeling and comparison of III-V tunnel junction designs for high efficiency metamorphic multi-junction solar cells," *Proceedings of SPIE* **7750**, 77502X-1 – 77502X-9, 2010. DOI: 10.1117/12.872882.

[29] J. F. Wheeldon, C. E. Valdivia, A. Walker, G. Kolhatkar, D. Masson, B. Riel, S. Fafard, A. Jaouad, A. Turula, R. Arès, V. Aimez, T. J. Hall, K. Hinzer. "GaAs, AlGaAs and InGaP tunnel junctions for multi-junction solar cells under concentration: Resistance Study," AIP Conference Proceeding **1277**, 28-31, 2010. DOI: doi:http://dx.doi.org/10.1063/1.3509213.

[30] P. Kailuweit, R. Kellenbenz, S. P. Philipps, W. Guter, A. W. Bett and F. Dimroth. "Numerical simulation and modeling of GaAs quantum-well solar cells," *Journal of Applied Physics* **107**, 064317-1 – 064317-6, 2010. DOI: dx.doi.org/10.1063/1.3354055

[31] A. Ben Or, P. Fuss-Kailuweit, S.P. Philipps, U. Fiedeler, S. Essig, E. Oliva, F. Dimroth, A.W. Bett. "Numerical Simulation and Modeling of GaInP Solar Cells," Conference proceeding from the *27th European Photovoltaic Solar Energy Conference and Exhibition*, Frankfurt, Germany, September 24-28 2012, 150-155. DOI: 10.4229/27thEUPVSEC2012-1BO.12.4.

[32] N. W. Ashcroft and N. D. Mermin. (1976) *Solid State Physics*. Dumfries, NC, USA: Hold, Rinehart and Winston. Chapter 4; chapter 10.

[33] S. L. Chuang. (1995) *Physics of Optoelectronic Devices.* Hoboken, NJ, USA: John Wiley & Sons. Chapter 4.

[34] J. E. Cunningham, T. H. Chiu, G. Timp, E. Agyekum, and W. T. Tsang. "Shallow donors in very pure GaAs grown by gas source molecular beam epitaxy," *Applied Physics Letters* **53**, 1285-1287, 1988. DOI: dx.doi.org/10.1063/1.99999.

[35] S. M. Sze and K. K. Ng. *Physics of Semiconductor Devices*. Hoboken, NJ, USA: John Wiley & Sons, Inc. 2007.

[36] Sentaurus Device User Guide, Version G-2012.06. (2012) Mountain View, CA, USA : Synopsys Inc.

[37] J. Nelson. (2003) *The Physics of Solar Cells.* London, UK: Imperial College Press. p. 102.

[38] K. Domen, M. Kondo, N. Tanahashi. (1992) *Gallium Arsenide and Related Compounds*. Institute of Physics Conference Series, Bristol and Philadelphia, PA, USA, **129**, 447-452.

[39] J. Nelson. (2003) *The Physics of Solar Cells.* London, UK: Imperial College Press. pp. 169-170.

[40] M. S. Lundstrom, "Device-Related Material Properties of Heavily Doped Gallium Arsenide", *Solid-State Electronics* **33**(6), 693-704, 1990. DOI: http://dx.doi.org/10.1016/0038-1101(90)90182-E.

[41] G. B. Lush, "A Study of Minority Carrier Lifetime versus Doping Concentration in n type GaAs grown by Metalorganic Chemical Vapor Deposition", *Journal of Applied Physics* **72**, 1436-1442, 1992. DOI: dx.doi.org/10.1063/1.351704.

[42] M. Levenshtein, S. Rumyantsev, M. Shur. (1996) *Handbook series on semiconductor parameters, Vol. I.* Hackensack, NJ: World Scientific.

[43] J. Nelson. (2003) *The Physics of Solar Cells.* London, UK: Imperial College Press, p. 83.

[44] S. Adachi. (1999) *Optical constants of crystalline and amorphous semiconductors: numerical data and graphical information*. New York, NY, USA: Springer, 1st edition.

[45] M.I. Alonso, M. Garriga, C.A. Durante Rincon, E. Hernandez, M. Leon. "Optical functions of chalcopyrite CuGaxIn1−xSe2 alloys," *Applied Physics A* **74**, 659-664, 2002. DOI: 10.1007/s003390100931.

[46] M. A. Green. "Optical Properties of Intrinsic Silicon at 300 K", *Progress in Photovoltaics: Research and Applications* **3**, 189-192, 1995. DOI: 10.1002/pip.4670030303.

[47] Simone Montanari. (2005) *Fabrication and characterization of planar Gunn diodes for Monolithic Microwave Integrated Circuits.* Doctorate Thesis from RWTH-Aachen University, Aachen, Germany. Figure obtained from website: http://gorgia.no-ip.com/phd/html/thesis/phd_html/node4.html, accessed August 13, 2012. Courtesy of Simone Montanari.

[48] R. V. N. Melnik and M. Willatzen. "Bandstructures of conical quantum dots with wetting layers," *Nanotechnology* **15**, 1-8, 2004. DOI: 10.1088/0957-4484/15/1/001.

[49] B. I. Barker, G. H. Rayborn, J. W. Ioup, G. E. Ioup. "Approximating the finite square well with an infinite well: Energies and eigenfunctions," *American Journal of Physics* **59**(11), 1038-1042, 1991. DOI: dx.doi.org/10.1119/1.16644.

[50] D. L. Argonstein, C. R. Stroud Jr. "General series solution for finite square-well energy levels for use in wave-packet studies," *American Journal of Physics* **68**(10), 943-949, 2000. DOI: dx.doi.org/10.1119/1.1285868.

[51] B. J. Riel. "An introduction to self-assembled quantum dots," *American Journal of Physics* **76**(8), 750-757, 2008. DOI: dx.doi.org/10.1119/1.2907856.

[52] D. L. Ferrerra and J. L. A. Alves. "The effects of shape and size nonuniformity on the absorption spectrum of semiconductor quantum dots," *Nanotechnology* **15**, pp. 975-981, 2004. DOI: 10.1088/0957-4484/15/8/019.

[53] C. Tsai, L. F. Eastman, Y. Lo, C. Tsai. "Breakdown of thermionic emission theory for quantum wells," *Applied Physics Letters* **65**, 469-471, 1994. DOI: dx.doi.org/10.1063/1.112339.

[54] G. A. Baraff. "Semiclassical description of electron transport in semiconductor quantum-well devices," *Physical Review B* **55**(16), 10745-10753, 1997. DOI: 10.1103/PhysRevB.55.10745. G. A. Baraff. "Model for the effect of finite phase-coherence length on resonant transmission and capture by quantum wells," *Physical Review B* **58**(20), 13799-13810, 1998. DOI: 10.1103/PhysRevB.58.13799.

[55] M. Grupen and K. Hess. "Simulation of carrier transport and nonlinearities in quantum-well laser diodes," *IEEE Journal of Quantum Electronics* **34**(1), 120-140, 1998. DOI: 10.1109/3.655016.

[56] M. A. Alam, M. S. Hybertsen, R. K. Smith and G. E. Baraff. "Simulation of semiconductor quantum well lasers," *IEEE Transactions on Electron Devices* **47**(10), 1917-1925, 2000. DOI: 10.1109/16.870572.

[57] B. Witzigmann, A. Witzig and W. Fichtner. "A multidimensional laser simulator for edge-emitters including quantum carrier capture," *IEEE Transactions on Electron Devices* **47**(10), 1926-2000, 2000. DOI: 10.1109/16.870574.

[58] W. W. Chow and S. W. Koch. "Theory of semiconductor quantum dot laser dynamics," *IEEE Journal of Quantum Electronics* **41**(4), 495-505, 2005. DOI: 10.1109/JQE.2005.843948.

[59] S. M. Ramey and R. Khoie. "Modeling of multiple-quantum-well solar cells including capture, escape and recombination of photoexcited carriers in quantum wells," *IEEE Journal of Quantum Electronics* **50**(5), 1179-1188, 2003. DOI: 10.1109/TED.2003.813475.

[60] J. Nelson. (2003) *The Physics of Solar Cells*. London, UK: Imperial College Press, p. 151.

[61] A. W. Walker, J. F. Wheeldon, G. Arbez, K. Hinzer. *Understanding Synopsys Sentaurus by simulating a P-N junction*. CMC Microsystems Application Note, available online [http://sunlab.site.uottawa.ca/research/Content/AppNote_Simulation_w_Sentaurus_Feb2011.pdf]

[62] Mesh Generation Tools User Guide, Version A-2007.12 (2007) Mountain View, California: Synopsys, Inc.; Sentaurus Structure Editor User Guide, Version A-2007.12 (2007). Mountain View, California: Synopsys, Inc.

[63] Epi/Matpar User Guide, Version April 2008. (2008) Mountain View, California: Synopsys, Inc.

[64] R. E. Bank, D. J. Rose, and W. Fichtner, "Numerical Methods for Semiconductor Device Simulation," *IEEE Transactions on Electron Devices* **ED-30**(9), 1031–1041, 1983. DOI: 10.1109/T-ED.1983.21257.

[65] Sentaurus Device User Guide, Version D-2010.03. (2010) Mountain View, California: Synsopsy, Inc. Chapter 37 (Nonlinear solvers).

[66] R. S. Varga. (1962) *Matrix Iterative Analysis.* Englewood Cliffs, NJ, USA: Prentice-Hall.

[67] E. M. Buturla, P. E. Cottrell, B. M. Grossman, K. A. Salsburg. "Finite-Element Analysis of Semiconductor Devices: The FIELDAY Program," *IBM Journal of Research and Development* **25**(4), 218–231, 1981.

[68] R. E. Bank and D. J. Rose. "Global Approximate Newton Methods," *Numerical Mathematics* **37**, 279-295, 1981. DOI: 10.1007/BF01398257.

[69] S. Selberherr. (1984) *Analysis and Simulation of Semiconductor Devices*. New York, NY, USA: Springer Vienna. DOI: 10.1007/978-3-7091-8752-4.

[70] J. Nelson. (2003) *The Physics of Solar Cells*. London, UK: Imperial College Press, p. 10.

[71] J. Nelson. (2003) *The Physics of Solar Cells*. London, UK: Imperial College Press, p. 7.

[72] L. C. Hirst and N. J. Ekins-Daukes. "Fundamental losses in solar cells," *Progress in Photovoltaics: Research and Applications* **19**, 286-293, 2011. DOI: 10.1002/pip.1024.

[73] B. M. Kayes, H. Nie, R. Twist, S. G. Spruytte, R. Reinhardt, I. C. Kizilyalli, G. S. Higashi. "27.6% conversion efficiency, a new record for single-junction solar cells under 1 sun illumination," Proceedings of the *37th IEEE Photovoltaic Specialists Conference*, Seattle, WA, USA, 19-24 June 2011, 000004-000008. DOI: 10.1109/PVSC.2011.6185831.

[74] ASTM G173-03, 2008, "Standard Tables for Reference Solar Spectral Irradiances: Direct Normal and Hemispherical on 37° Tilted Surface," *ASTM International*, West Conshohocken, PA, 2003. DOI: 10.1520/G0173-03R08.

[75] S. Adachi. "GaAs, AlAs, and $Al_xGa_{1-x}AsB$: Material parameters for use in research and device applications," *Journal of Applied Physics* **58**(3), R1-R29, 1985. DOI: dx.doi.org/10.1063/1.336070

[76] T. Bååk. "Silicon oxynitride; a material for GRIN optics," *Applied Optics* **21**, 1069-1072, 1982. DOI: dx.doi.org/10.1364/AO.21.001069.

[77] G. Ghosh. "Dispersion-equation coefficients for the refractive index and birefringence of calcite and quartz crystals," *Optical Communications* **163**, 95-102, 1999. DOI: dx.doi.org/10.1016/S0030-4018(99)00091-7.

[78] E. D. Palik. (1998) *Handbook of Optical Constants of Solids, Vol. II*. San Diego, CA, USA: Elsevier, Part II, Chapter 36.

[79] E. D. Palik. (1998) *Handbook of Optical Constants of Solids, Vol. II*. San Diego, CA, USA: Elsevier, Chapter 45.

[80] Refractive Index Database http://refractiveindex.info. Retrieved July 6th, 2012.

[81] H. Morkoç, Ü. Özgür. *Zinc Oxide: Fundamentals, Materials and Device Technology*. Hoboken, NJ, USA: John Wiley & Sons, p. 190, 2009.

[82] D. Palik. "*Handbook of Optical Constants of Solids, Vol. II*," Elsevier, Part II, Chapter 24, 1998.

[83] Refractive Index Database http://refractiveindex.info. Retrieved July 12th, 2012; H. Kato, S. Adachi, H. Nakanishi, K. Ohtsuka. "Optical Properties of $(Al_xGa_{1-x})_{0.5}In_{0.5}P$ Quaternary Alloys," *Japan Journal of Applied Physics* **33**, 186-192, 1994. DOI: 10.1143/JJAP.33.186.

[84] E. D. Palik. (1998) *Handbook of Optical Constants of Solids, Vol. II*. San Diego, CA, USA: Elsevier, Part II, Chapter 15.

[85] E. D. Palik. (1998) *Handbook of Optical Constants of Solids, Vol. II*. San Diego, CA, USA: Elsevier, Part II, Chapter 17.

[86] G. Masetti, M. Severi, S. Solmi. "Modeling of carrier mobility against carrier concentration in arsenic-, phosphorus-, and boron-doped silicon," *IEEE Transactions on Electron Devices* **ED-30**(7), 764-769, 1983. DOI: 10.1109/T-ED.1983.21207.

[87] Y. Ohba, M. Ishikawa, H. Sugawara, M. Yamamoto, T. Nakanisi. "Growth of high-quality InGaAlP epilayers by MOCVD using methyl metalorganics and their application to visible semiconductors lasers," *Journal of Crystal Growth*, **77**(1-3), 374-379, 1986. DOI: dx.doi.org/10.1016/0022-0248(86)90326-X.

[88] M. Sotoodeh, A. H. Khalid, A. A. Rezazadeh. "Empirical low-field mobility model for III–V compounds applicable in device simulation codes," *Journal of Applied Physics* **87**(6) 2890-2900, 2000. DOI: dx.doi.org/10.1063/1.372274.

[89] V. Palankovski, R. Quay. (2004) *Analysis and Simulation of Heterostructure Devices.* New York, NY, USA: Springer-Verlag/Wien.

[90] D. J. Schroeder, J. L. Hernandez, G. D. Berry & A. A. Rockett. "Hole transport and doping states in epitaxial $CuIn_{1-x}Ga_xSe_2$," *Journal of Applied Physics* **83**, 1519-1526, 1998. DOI: 10.1063/1.366860.

[91] Sentaurus Device User Guide, Version D-2010.03. (2010) Mountain View, California: Synsopsy, Inc. Part 2, Chapter 13, Table 67.

[92] M. Levenshtein, S. Rumyantsev, M. Shur. (1996) *Handbook series on semiconductor parameters, Vol. I*. Hackensack, NJ: World Scientific.

[93] W. Gerlach, H. Schlangenotto, and H. Maeder, Phys. "On the radiative recombination rate in silicon," *Physica Status Solidi A* **13**(1), 277-283, 1972. DOI: 10.1002/pssa.2210130129.

[94] U. Strauss, W. W. Rühle, H. J. Queisser, K. Nakano, A. Ishibashi, "Band-to-band recombination in $Ga_{0.5}In_{0.5}P$," *Journal of Applied Physics* **75**, 8204-8206, 1994. DOI: 10.1063/1.356522.

[95] N. M. Haegel, S. E. Williams, C. L. Frenzen, C. Scandrett. "Minority carrier lifetime variations associated with misfit dislocation networks in heteroepitaxial GaInP," *Semiconductor Science and Technology* **25**, 055017, 2010. DOI: 10.1088/0268-1242/25/5/055017.

[96] H. Yoon, K. M. Edmondson, G. S. Kinsey, R. R. King, P. Hebert, R. K. Ahrenkiel "Minority Carrier Lifetime and Radiation Damage Coefficients of Germanium", Proceeding from the *33rd Photovoltaics Specialist Conference (PVSC-33)*, January 3-7, 2005, 842-845. DOI: 10.1109/PVSC.2005.1488264.

[97] S. Shirakata and T. Nakada. "Photoluminescence and time-resolved photoluminescence in Cu(In,Ga)Se2 thin films and solar cells," *Physica Status Solidi C* **6**(5), 1059-1062, 2009. DOI: 10.1002/pssc.200881164.

[98] J. Nelson. (2003) *The Physics of Solar Cells*. London, UK: Imperial College Press. Chapter 7.4.3; Simulation of a 2D planar monocrystalline silicon solar-cell with transfer matrix method, Version intended for TCAD Sentaurus D-2010.03-SP1, Mountain View, California: Synopsys, Inc., 2010.

[99] J. M. Olson, D. J. Friedman, S. Kurtz. (2005) *High-Efficiency III-V Multi-Junction Solar Cells*, Chapter 9.6.3 of Handbook of Photovoltaic Science and Engineering, edited by A. Luque, S. Hegedus. Hoboken, NJ, USA: John Wiley & Sons; T. Agui, T. Takamoto and M. Kaneiwa, "Investigation on AlGaInP Solar Cells for Current Matched Multijunction Cells", Proceeding from the *3rd World Conference on Photovotlaic Energy Conversion*, May 11-18, Osaka, Japan, 2003.

[100] D. J. Friedman and J. M. Olson. "Analysis of Ge junctions for GaInP/GaAs/Ge three-junction solar cells," *Progress in Photovoltaics: Research and Applications* **9**(3), 179-189, 2001. DOI: 10.1002/pip.365; N.E. Posthuma, G. Flamand and J. Poortmans. "Development of stand-alone Germanium Solar Cells for Application in Space using Spin-on Diffusants," Proceeding from the *3rd World Conference on Photovoltaic Energy Conversion*, May 11-18, Osaka, Japan, 2003, 777-780.

[101] J. Nelson. (2003) The Physics of Solar Cells. London, UK: Imperial College Press. Chapter 8.6; P. Jackson, D. Hariskos, E. Lotter, S. Paetel, R. Wuerz, R. Menner, W. Wischmann, M. Powalla. "New world record efficiency for Cu(In,Ga)Se-2 thin-film

solar cells beyond 20%," Progress *in Photovoltaics: Research and Applications* **19** (7), 894-891, 2011. DOI: 10.1002/pip.1078.

[102] W. Shafarman & L. Stolt. (2005) *Cu(InGa)Se_2 Solar Cells*, Chapter 13 of Handbook of Photovoltaic Science and Engineering, edited by A. Luque, S. Hegedus. Hoboken, NJ, USA: John Wiley & Sons.

[103] W. Shockley and H. J. Queisser. "Detailed Balance Limit of Efficiency of p-n Junction Solar Cells," *Journal of Applied Physics*, **32**(3), 510-519, 1961. DOI: dx.doi.org/10.1063/1.1736034.

[104] G. Letay, A. W. Bett. "EtaOpt – a program for calculating limiting efficiency and optimum bandgap structure for multi-bandgap solar cells and TPV cells," 17th European Photovoltaics Solar Energy Conference, Munich, Germany, October 22-26, 2001, 178-181.

[105] J. Nelson. (2003) *The Physics of Solar Cells*. London, UK: Imperial College Press, p. 151.

[106] J. M. Olson, S. R. Kurtz, A. E. Kibbler and P. Faine. "A 27.3% efficient $Ga_{0.5}In_{0.5}$/GaAs tandem solar cell," *Applied Physics Letters* **57**(7), 623-625, 1990. DOI: dx.doi.org/10.1063/1.102717.

[107] M. A. Green, K. Emery, Y. Hishikawa, W. Warta. "Solar Cell Efficiency Tables (version 36)," *Progress in Photovoltaics: Research and Applications* **18**(5), 346-352, 2010. DOI: 10.1002/pip.1021; M. Ohmori, T. Takamoto, E. Ikeda, H. Kurita. "High efficiency InGaP/GaAs tandem solar cells," *Techical Digest, International PVSEC-9*, Miyasaki, Japan, November 1996, 525–528.

[108] M. Yang, T. Takamoto, E. Ikeda, H. Kurita and M. Yamaguchi. "Investigation of High-Efficiency InGaP/GaAs Tandem Solar Cells under Concentration Operation," *Japan Journal of Applied Physics* **37**(7B), L836-L838, 1998. DOI: 10.1143/JJAP.37.L836.

[109] A. W. Bett, F. Dimroth, W. Guter, R. Hoheisel, E. Oliva, S. P. Philipps, J. Schone, G. Siefer, M. Steiner, A. Wekkeli, E. Welser, M. Meusel, W. Kostler, G. Strobl. "Highest efficiency multi-junction solar cell for terrestrial and space applications," Proceeding from the *24th European Photovoltaic Solar Energy Conference and Exhibit*, Hamburg, Germany,Sept. 2009, pp. 1-6.

[110] T. Gessmann and E. F. Schubert. "High-efficiency AlGaInP light-emitting diodes for solid-state lighting applications," *Journal of Applied Physics* **95**(5), 2203-2216, 2004. DOI: dx.doi.org/10.1063/1.1643786.

[111] A. Banerjee, T. Su, D. Beglau, G. Pietka, F. Liu, G. DeMaggio, S. Almutawalli, B. Yan, G. Yue, J. Yang, S. Guha. "High efficiency, multi-junction nc-Si:h based solar cells at high deposition rate," *IEEE Journal of Photovoltaics* **2**(2), 99-103, 2012. DOI: 10.1109/JPHOTOV.2011.2180892.

[112] E. O. Kane. "Theory of Tunneling," *Journal of Applied Physics* **32**, 83-91, 1961. DOI: dx.doi.org/10.1063/1.1735965.

[113] A. Schenk, "A Model for the Field and Temperature Dependence of Shockley–Read–Hall Lifetimes in Silicon," *Solid-State Electronics* **35**(11), 1585–1596, 1992. DOI: dx.doi.org/10.1016/0038-1101(92)90184-E.

[114] G. A. M. Hurkx, D. B. M. Klaassen, and M. P. G. Knuvers, "A New Recombination Model for Device Simulation Including Tunneling," *IEEE Transactions on Electron Devices* **39**(2), 331–338, 1992. DOI: 10.1109/16.121690.

[115] M. Ieong, P. M. Solomon, S.E. Laux, H.-S. P.Wong, D. Chidambarrao. "Comparison of Comparison of Raised and Schottky Source/Drain MOSFETs Using a Novel Tunneling Contact Model," *IEDM Technical Digest*, San Fransisco, CA, USA, 733-736, December 1998. DOI: 10.1109/IEDM.1998.746461.

[116] F. Li, S. P . Mudanai, Y.-Y. Fan, L. F. Register, S. K. Banerjee. "Compact Model of MOSFET Electron Tunneling Current through Ultrathin SiO_2 and High-k Gate Stacks," in *Device Research Conference*, Salt Lake City, UT, USA, 47–48, June 2003.

[117] L. F. Register, E. Rosenbaum, K. Yang. "Analytic model for direct tunneling current in polycrystalline silicon-gate metal–oxide–semiconductor devices," *Applied Physics Letters* **74**, 457-459, 1999. DOI: dx.doi.org/10.1063/1.123060.

[118] U. Woggon, E. Lu¨thgens, H. Wenisch and D. Hommel. "Probing the electron–LO-phonon interaction of a single impurity state in a semiconductor," *Physical Review B*, **63**, 073205-1 – 073205-4, 2001. DOI: 10.1103/PhysRevB.63.073205.

[119] L. Wang, J. M. L. Figueiredo, C. N. Ironside, E. Wasige. "DC characterization of tunnel diodes under stable non-oscillatory circuit conditions," *IEEE Transactions on Electron Devices* **58**(2), 343-347, 2011. DOI: 10.1109/TED.2010.2091507.

[120] N. Suzuki, T. Anan, H. Hatakeyama, M. Tsuji. "Low resistance tunnel junctions with type-II heterostructures," *Applied Physics Letters* **88**, 231103-1 – 231103-3, 2006. DOI: dx.doi.org/10.1063/1.2210082; H. Sugiura, C. Amano, A. Yamamoto, M. Yamaguchi. "Double Heterostructure GaAs Tunnel Junction for a AlGaAs/GaAs Tandem Solar Cell," *Japan Journal of Applied Physics* **27**, 269–72, 1988. DOI: 10.1143/JJAP.27.269.

[121] B. Paquette , M. DeVita , G. Kolhatkar , A. Turala , A. Boucherif, J. F. Wheeldon , A. W. Walker , O. Thériault , K. Hinzer , C. E. Valdivia, S. G. Wallace , S. Fafard , V. Aimez and R. Arès. "Chemical Beam Epitaxy Growth of AlGaAs/GaAs Tunnel Junctions using Trimethyl Aluminum for Multijunction Solar Cells," Abstract accepted for an oral presentation at the *9th International Conference on Concentrating Photovoltaic Systems (CPV-9)*, Miyazaki, Japan, April 15-17, 2013.

[122] NSM database: http://www.ioffe.rssi.ru/SVA/NSM/Semicond/, accessed on October 15, 2012.

[123] K. Jandieri, S. D. Baranovskii, O. Rubel, W. Stolz, F. Gebhard, W. Guter, M. Hermle, A. W. Bett. "Resonant electron tunneling through defects in GaAs tunnel diodes," *Journal of Applied Physics* **104**, 094506-1 – 094506-7, 2008. DOI: dx.doi.org/10.1063/1.3013886.

[124] K. Jandieri, S. D. Baranovskii, W. Stolz, F. Gebhard, W. Guter, M. Hermle, A. W. Bett. "Fluctuations of the Peak Current of Tunnel Diodes in Multi-Junction Solar Cells," *Journal of Physics D: Applied Physics* **42**, 155101-1 – 155101-8, 2009. DOI: 10.1088/0022-3727/42/15/155101.

[125] M. Meusel, C. Baur, G. Letay, A. W. Bett, W. Warta, E. Fernandez. "Spectral Response Measurements of Monolithic GaInP/Ga(In)As/Ge Triple-Junction Solar Cells: Measurement Artifacts and their Explanation," *Progress in Photovoltaics: Research and Applications* **11**, 499-514, 2003. DOI: 10.1002/pip.514.

[126] C. E. Valdivia, E. Desfonds, D. Masson, S. Fafard, A. Carlson, J. Cook, T. J. Hall, K. Hinzer. "Optimization of antireflection coating design for multi-junction solar cells

and concentrator systems," *Proceedings of SPIE* **7099**, 709915-1 – 709915-10, 2008. DOI: 10.1117/12.807675.

[127] A. W. Walker, J. F. Wheeldon, O. Theriault, M. Yandt, K. Hinzer. "Temperature Dependent External Quantum Efficiency Simulations and Experimental Measurement of Lattice Matched Quantum Dot Enhanced Multi-Junction Solar Cells," Proc. from the *37th IEEE Photovoltaic Specialist Conference* (*PVSC*-37), Seattle, WA, USA, June 2011.

[128] Optimizer User Guide, Version G-2012.06, Synopsys Inc.

[129] M. A. Green, K. Emery, Y. Hishikawa, W. Warta, and E. D. Dunlop, "Solar cell efficiency tables (version 38)," *Progress Photovoltaics: Research and Applications*, 19, 565–572, 2011. DOI: 10.1002/pip.1150.

[130] D. Yoshida, T. Agui, N. Katsuya, K. Murasawa, H. Juso, K. Sasaki, T. Takamoto. "Development of InGaP/GaAs/InGaAs inverted triple junction solar cells for concentrator application," Proceeding from the *21st International Photovoltaic Science and Engineering Conference* (PVSEC-21), Fukuoka, Japan, 2011.

[131] J. F. Wheeldon, A. W. Walker, C. E. Valdivia, S. Chow, O. Theriault, R. Beal, M. Yandt, F. Proulx, D. Masson, B. Riel, D. McMeekin, N. Puetz, S. G. Wallace, V. Aimez, R. Ares, T. J. Hall, S. Fafard, K. Hinzer. "Efficiency measurements and simulations of GaInP/InGaAs/Ge quantum dot solar cells at up to 1000-suns under flash and continuous concentration," *AIP Conference Proceeding* **1407**, 220-223, 2011. DOI: dx.doi.org/10.1063/1.3658331.

[132] Y. P. Varshni. "Temperature dependence of the energy gap in semiconductors," *Physica*, **34**(1), 149-154, 1967. DOI: dx.doi.org/10.1016/0031-8914(67)90062-6.

[133] C. Soubervielle-Montalvo, I.C. Hernández, M. Sheldon, A. Gorbatchev, A.G. Rodríguez, F. de Anda, L. Zamora-Peredo, V.H. Méndez-García. "P-cracker cell temperature effects on the optical properties of AlGaInP:Be layers grown by SSMBE," *Journal of Crystal Growth* **301-302**, 84-87, 2007. DOI: dx.doi.org/10.1016/j.jcrysgro.2006.11.293.

[134] C. Soubervielle-Montalvo, V. Mishournyi, I. C. Hernández, V. H. Méndez-García. "Temperature dependence of photoluminescence oxygen-related deep levels in $Al_{0.2}Ga_{0.3}In_{0.5}P$:Be grown by solid source molecular beam epitaxy," *Journal of Vacuum Science and Technology B* **26**(3), 1089-1092, 2008. DOI: 10.1116/1.2891250.

[135] G. S. Kinsey, P. Hebert, K. E. Barbour, D. D. Krut, H. L. Cotal, R. A. Sherif. "Concentrator multijunction solar cell characteristics under variable intensity and temperature," *Progress in Photovoltaics: Research and Applications* **16**, 503-508, 2008. DOI: 10.1002/pip.834.

[136] K. Nishioka, T. Sueto, M. Uchida, Y. Ota. "Detailed analysis of temperature characteristics of an InGaP/InGaAs/Ge triple-junction solar cell," *Journal of Electronic Materials* **39**(6), 704-708, 2010. DOI: 10.1007/s11664-010-1171-y.

[137] G. A. Landis, D. J. Belgiovane, D. A. Scheiman. "Temperature coefficient of multijunction space solar cells as a function of concentration," Proceeding of the *37th IEEE Photovoltaic Specialist Conference (PVSC)*, Seattle, WA, USA, June 19-24, 2011. DOI: 10.1109/PVSC.2011.6186260.

[138] F. Dimroth, R. Beckert, M. Meusel, U. Schubert, A. W. Bett. "Metamorphic $Ga_yIn_{1-y}P/Ga_{1-x}In_xAs$ Tandem Solar Cells for Space and for Terrestial Concentrator

Applications at C>1000 Suns," *Progress in Photovoltaics: Research and Applications* **9**, 165-178, 2001. DOI: 10.1002/pip.362.

[139] V. M. Andreev, E. A. Ionova, V. R. Larionov, V. D. Rumyantsev, M. Z. Shvarts, G. Glenn. "Tunnel Diode Revealing Peculiarities at *I-V* Measurements in Multijunction III-V Solar Cells," Proceeding from the *4th World Conference on Photovoltaic Energy Conversion* **1**, 799-802, Waikoloa, Hawaii, USA, May 2006. DOI: 10.1109/WCPEC.2006.279577.

[140] J. M. Gordon, E. A Katz, W. Tassew, D. Feuermann. "Photovoltaic hysteresis and its ramifications for concentrator solar cell design and diagnostics," *Applied Physics Letters* **86**, 073508-1 – 073508-3, 2005. DOI: dx.doi.org/10.1063/1.1862776.

[141] E. Garcia, I. Rey-Stolle, C. Algora. "Performance analysis of AlGaAs/GaAs tunnel junctions for ultra-high concentration photovoltaics," *Journal of Physics D: Applied Physics* **45**, 045101-1 – 045101-8, 2012. DOI: 10.1088/0022-3727/45/4/045101.

[142] S. R. Kurtz, P. Faine, J. M. Olson. "Modeling of two junction series connected tandem solar cells using top-cell thickness as an adjustable parameter," *Journal of Applied Physics* **68**(4), 1890-1895, 1990. DOI: dx.doi.org/10.1063/1.347177.

[143] M. Wilkins, A. Boucherif, R. Beal, J. E. Haysom, J. F. Wheeldon, V. Aimez, R. Arès, T. J. Hall, K. Hinzer. "Multijunction Solar Cells using Silicon Bottom Subcell and Porous Silicon Compliant Membrane," *IEEE Journal of Photovoltaics* **3**(3), 1125-1131, 2013. DOI: 10.1109/JPHOTOV.2013.2261931.

[144] J. Yang, D. Cheong, J. Rideout, S. Tavakoli, R. Kleiman. "Silicon-based multi-junction solar cell with 19.7% efficiency at 1-sun using areal current matching for 2-terminal operation," Proceeding from the 37th *IEEE Photovoltaics Specialist Conference (PVSC)*, 19-24 June 2011, Seatle, WA, USA, 001019-001024. DOI: 10.1109/PVSC.2011.6186125.

[145] J. P. McCaffrey, M. D. Robertson, P. J. Poole, B. J. Riel, S. Fafard. "Interpretation and modeling of buried InAs quantum dots on GaAs and InP substrates," *Journal of Applied Physics* **90**(4), 1784-1787, 2001. DOI: dx.doi.org/10.1063/1.1384861.

[146] S. J. Xu, X. C. Wang, S. J. Chua, C. H. Wang, W. J. Fan, J. Jiang, X. G. Xie. "Effects of rapid thermal annealing on structure and luminescence of self-assembled InAs/GaAs quantum dots," *Applied Physics Letters* **72**, 3335-3337, 1998. DOI: dx.doi.org/10.1063/1.121595.

[147] S. Fafard, K. Hinzer, C. N. Allen. "Semiconductor quantum dot nanostructures and their roles in the future of photonics," *Brazilian Journal of Physics* **34**(2B), 2004.

[148] Z. R.Wasilewski, S. Fafard, J. P. McCaffrey. "Size and shape engineering of vertically stacked self-assembled quantum dots," *Journal of Crystal Growth* **201/202**, 1131-1135, 1999. DOI: dx.doi.org/10.1016/S0022-0248(98)01539-5.

[149] S. Fafard, Z. R. Wasilewski, C. Ni. Allen, D. Picard, M. Spanner, J. P. McCaffrey, P. G. Piva. "Manipulating the energy levels of semiconductor quantum dots," *Physical Review B* **59**(23), 15368-15373, 1999. DOI: 10.1103/PhysRevB.59.15368.

[150] S. Fafard, Z. R. Wasilewski, C. Ni. Allen, K. Hinzer, J. P. McCaffrey and Y. Feng. "Lasing in quantum-dot ensembles with sharp adjustable electronic shells," *Applied Physics Letters* **75**(7), 986-988, 1999. DOI: dx.doi.org/10.1063/1.124253.

[151] S. Fafard, C. Ni. Allen. "Intermixing in quantum-dot ensembles with sharp adjustable shells," *Applied Physics Letters* **75**(16), 2374-2376, 1999. DOI: dx.doi.org/10.1063/1.125019.

[152] H. C. Liu, M. Gao, J. McCaffrey, Z. R. Wasilewski and S. Fafard. "Quantum dot infrared photodetectors," *Applied Physics Letters* **78**(1), 79-81, 2001. DOI: dx.doi.org/10.1063/1.1337649.

[153] N. J. Ekins-Daukes, D. B. Bushnell, J. P. Connolly, K. W. J. Barnham, M. Mazzer, J. S. Roberts, G. Hill, R. Airey. "Strain-balanced quantum well solar cells," *Physica E* **14**, 132-135, 2002. DOI: dx.doi.org/10.1016/S1386-9477(02)00378-8.

[154] M. Korkusinski and P. Hawrylak. "Electronic structure of vertically stacked self-assembled quantum disks," *Physical Review B* **63**, 195311-1 – 195311-7, 2001. DOI: 10.1103/PhysRevB.63.195311.

[155] V. Popescu, G. Bester and A. Zunger. "Coexistence and coupling of zero-dimensional, two-dimensional, and continuum resonances in nanostructures," *Physical Review B* **80**, 045327-1 – 045327-12, 2009. DOI: 10.1103/PhysRevB.80.045327.

[156] J. Johansen, S. Stobbe, I. S. Nikolaev, T. Lund-Hansen, P. T. Kristensen, J. M. Hvam, W. L. Vos and P. Lodahl. "Size dependence of the wavefunction of self-assembled InAs quantum dots from time-resolved optical measurements," *Physical Review B* **77**, 073303-1 – 073303-4, 2008. DOI: 10.1103/PhysRevB.77.073303.

[157] A. D. Andreev, E. P. O'Reilly. "Optical matrix element in InAs/GaAs quantum dots : Dependence on quantum dot parameters," *Applied Physics Letters* **87**, 213106-1 – 213106-3, 2005. DOI: dx.doi.org/10.1063/1.2130378.

[158] G. Bacher, C. Hardmann, H. Schweizer, T. Held, G. Mahler, H. Nickel. "Exciton dynamics in $In_xGa_{1-x}As/GaAs$ quantum-well heterostructures: Competition between capture and thermal emission," *Physical Review B* **47**(15), 9545-9555, 1993. DOI: 10.1103/PhysRevB.47.9545.

[159] D. G. Deppe, D. L. Huffaker, S. Csutak, Z. Zou, G. Park, O. B. Shchekin. "Spontaneous emission and threshold characteristics of 1.3-micron InGaAs-GaAs quantum-dot GaAs-based lasers," *IEEE Journal of Quantum Electronics* **35**(8), 1238-1246, 1999. DOI: 10.1109/3.777226.

[160] M. Gurioli, A. Vinatteri, M. Colocci, C. Deparis, J. Massies, G. Neu, A. Bosacchi, S. Franchi. "Temperature dependence of the radiative and nonradiative recombination in GaAs/AlGaAs quantum-well structures," *Physical Review B* **44**, 3115-3124, 1991. DOI: 10.1103/PhysRevB.44.3115.

[161] M. A. Cusack, P. R. Briddon, M. Jaros. "Absorption spectra and optical transitions in InAs/GaAs self-assembled quantum dots," *Physical Review B* **57**(7), 4047-4050, 1997. DOI: 10.1103/PhysRevB.56.4047.

[162] G. A. Narvaez, G. Bester and Alex Zunger. "Carrier relaxation mechanisms in self-assembled (In,Ga)As/GaAs quantum dots: Efficient P to S Auger relaxation of electrons," *Physical Review B* **74**, 075403-1 – 075403-7, 2006. DOI: 10.1103/PhysRevB.74.075403.

[163] J. Siegert, S. Marcinkevicius, Q. X. Zhao. "Carrier dynamics in modulation-doped InAs/GaAs quantum dots," *Physical Review B* **72**, 085316-1 – 085316-7, 2005. DOI: 10.1103/PhysRevB.72.085316.

[164] K. Gundogdu, K. C. Hall, T. F. Boggess, D. G. Deppe, O. B. Shchekin. "Ultrafast electron capture into p-modulation-doped quantum dots," *Applied Physics Letters* **85**, 4570-4572, 2004. DOI: dx.doi.org/10.1063/1.1815371.

[165] K. W. Sun, A. Kechiantz, B. C. Lee, C. P. Lee. "Ultrafast carrier capture and relaxation in modulation-doped InAs quantum dots," *Applied Physics Letters* **88**, 163117-1 – 163117-3, 2006. DOI: 10.1063/1.2197309.

[166] D. Morris, N. Perret, S. Fafard. "Carrier energy relaxation by means of Auger processes in InAs/GaAs self-assembled quantum dots," *Applied Physics Letters* **75**(23), 3593-3595, 1999. DOI: dx.doi.org/10.1063/1.125398.

[167] O. Engstrom, M. Kaniewska, Y. Fu, J. Piscator, M. Malmkvist. "Electron capture cross sections of InAs/GaAs quantum dots," *Applied Physics Letters* **85**, 2908-2910, 2004. DOI: 10.1063/1.1802377.

[168] M. Wesseli, C. Ruppert, S. Trumm, H. J. Krenner, J. J. Finley and M. Betz. "Nonequilibrium carrier dynamics in self-assembled InGaAs quantum dots," *Physica Status Solidi* **243**(10), 2217-2223, 2006. DOI: 10.1002/pssb.200668006.

[169] J. Urayama, T. B. Norris, H. Jiang, J. Sing, P. Bhattacharya. "Temperature-dependent carrier dynamics in self-assembled InGaAs quantum dots," *Applied Physics Letters* **80**, 2162-2164, 2002. DOI: dx.doi.org/10.1063/1.1462860.

[170] M. De Giorgi, C. Lingk, G. Von Plessen, J. Feldmann, S. De Rinaldis, et al. "Capture and thermal re-emission of carriers in long-wavelength InGaAs/GaAs quantum dots," *Applied Physics Letters* **79**, 3968-3970, 2001. DOI: dx.doi.org/10.1063/1.1421235.

[171] R. Heitz, I. Mukhametzanov, H. Born, M. Grundmann, A. Hoffman, A. Madhukar, D. Bimberg. "Hot carrier relaxation in InAs/GaAs quantum dots," *Physica B* **272**, 8-11, 1999. DOI: dx.doi.org/10.1016/S0921-4526(99)00366-X.

[172] S. Farfard, S. Raymond, G. Wang, R. Leon, D. Leonaerd, S. Charbonneau, J. L. Merz, P. M. Petroff, J. E. Bowers. "Temperature effects on the radiative recombination in self-assembled quantum dots," *Surface Science* **361/362**, 778-782, 1996. DOI: 10.1016/0039-6028(96)00532-8.

[173] V. Ryzhii. "The theory of quantum-dot infrared phototransistors," *Semiconductor Science and Technology* **11**, 759-765, 1996. DOI: 10.1088/0268-1242/11/5/018.

[174] A. W. Walker, O. Thériault, J. F. Wheeldon, K. Hinzer. "The effects of absorption and recombination on quantum dot multi-junction solar cell efficiency," *IEEE Journal of Photovoltaics* **3**(3), 1118-1124, 2013. DOI: 10.1109/JPHOTOV.2013.2257920.

[175] R. Teissier, D. Sicault, J. C. Harmand, G. Ungaro, G. Le Roux, and L. Largeau. "Temperature-dependent valence band offset and band-gap energies of pseudomorphic GaAsSb on GaAs," *Journal of Applied Physics* **89**(10), 5473-5477, 2001. DOI: dx.doi.org/10.1063/1.1365061.

[176] J. X. Chen, A. Markus, A. Fiore, U. Oesterle, R. P. Stanley, J. F. Carlin, R. Houdré, M. Ilegems, L. Lazzarini, L. Nasi, M. T. Todaro, E. Piscopiello, R. Cingolani, M. Catalano, J. Katcki, and J. Ratajczak. "Tuning InAs/GaAs quantum dot properties under Stranski-Krastanov growth mode for 1.3 μm applications," *Journal of Applied Physics* **91**(10), 6710-6716, 2002. DOI: dx.doi.org/10.1063/1.1476069.

[177] J. Davies. (1997) *The physics of low-dimensional semiconductors*. Cambridge, UK: Cambridge University Press.

[178] C.-S. Chang and S. L. Chuang. "Universal curves for optical-matrix elements of strained quantum wells," *Applied Physics Letters* **66**(7), 795-797, 1995. DOI: dx.doi.org/10.1063/1.114191.

[179] S. Tomić, T. S. Jones, and N. M. Harrison. "Absorption characteristics of a quantum dot array induced intermediate band: Implications for solar cell design," *Applied Physics Letters* **93** (26), 263105-1 – 263105-3, 2008. DOI: dx.doi.org/10.1063/1.3058716.

[180] M. Grundmann, O. Stier, D. Bimberg. "InAs/GaAs pyramidal quantum dots: Strain distribution, optical phonons and electronic structure," *Physical Review B* **52**(16), 11969-11981, 1995. DOI: 10.1103/PhysRevB.52.11969; M. Califano, P. Harrison. "Presentation and experimental validation of a single-band, constant-potential model for self-assembled InAs/GaAs quantum dots," *Physical Review B* **61**(16), 10959-10965, 2000. DOI: 10.1103/PhysRevB.61.10959.

[181] D. Schroeder. (1994) *Modelling of Interface Carrier Transport for Device Simulation*. New York, NY, USA: Springer Vienna.

[182] O. Theriault, Ph.D. Thesis, unpublished, University of Ottawa, Ottawa, Canada.

[183] R.R. King, A. Boca, W. Hong, X.-Q. Liu, D. Bhusari, D. Larrabee, K.M. Edmondson, D.C. Law, C.M. Fetzer, S. Mesropian, N.H. Karam. "Band-gap-engineered architectures for high-efficiency multijunction concentrator solar cells," Proceeding from the *24th European Photovoltaic Science and Energy Conference and Exhibit*, Hamburg, Germany, 21-25 Sep. 2009.

[184] O. Thériault, A. W. Walker, J. F. Wheeldon, K. Hinzer. "The Effect of Quantum Dot Layers on the Efficiency of Multijunction Solar Cells under Concentration," *AIP Conference Proceedings* **1477**, 20-23, 2012. DOI: doi:http://dx.doi.org/10.1063/1.4753824.

[185] A. W. Walker, O. Thériault, J. F. Wheeldon, K. Hinzer. "The Dependence of Multi-Junction Solar Cell Performance on the Number of Quantum Dot Layers," Submitted to *IEEE Journal of Quantum Electronics*, September 2013.

[186] A. W. Walker, O. Thériault, J. F. Wheeldon, K. Hinzer. "Carrier dynamics in quantum dot enhanced multi-junction solar cells under high concentration" Submitted to *IEE Journal of Photovoltaics*, July 2013.

[187] A. W. Walker, O. Thériault, J. F. Wheeldon, K. Hinzer. "Positioning and doping effects of quantum dot multi-junction solar cells," Submitted to *Progress in Photovoltaics: Research and Applications*, August 2013.

[188] G. Letay, M. Hermle, A. W. Bett. "Simulating single-junction GaAs solar cells including photon recycling," *Progress in Photovoltaics: Research and Applications* **14**, p. 683-696, 2006. DOI: 10.1002/pip.699.

[189] BP Statistical Review of World Energy. Published June 2012, accessed July 31st 2012: bp.com/statisticalreview.

[190] Solarbuzz research and analysis. Linked accessed on July 31st, 2012: http://www.solarbuzz.com/facts-and-figures/retail-price-environment/module-prices.

[191] Gross world product from the CIA's *The World Factbook*. Link accessed on July 15th 2012: https://www.cia.gov/library/publications/the-world-factbook/geos/xx.html.

[192] D. V. Schroeder. (1999) *An introduction to thermal physics*. Boston, MA, USA: Addison Wesley Longman. p. 123; p. 302-303.

[193] Reuters article entitled 'Google plans new mirror for cheaper solar power', 2009. Link accessed July 23rd 2012: http://www.reuters.com/article/2009/09/11/us-summit-google-idUSTRE58867I20090911

[194] Reference 126: Table I.

[195] M. A. Green, K. Emery, Y. Hishikawa, W. Warta, E. W. Dunlop. "Solar cell efficiency tables (version 41)," *Progress in Photovoltaics: Research and Applications* **21**, 1-11, 2013. DOI: 10.1002/pip.2352.
[196] Thermal energy storage Wikipedia article, accessed July 20th 2012: http://en.wikipedia.org/wiki/Thermal_energy_storage.
[197] Desertec Foundation. Link accessed July 23rd 2012: http://www.desertec.org.
[198] J. Nelson. (2003) *The Physics of Solar Cells*. London, UK: Imperial College Press. Chapter 3.
[199]

Appendix A

A-1. A Motivating Argument for Solar Energy Generation

The sun has been shining for billions of years and is expected to shine for another 5 billion years approximately before it engulfs the Earth as it transforms into a red giant. As a result, we can expect the sun to shine at a constant illumination for the next century to a pretty good approximation. The intensity output of the sun on a sunny cloudless day is on the order of 1 kW/m^2 at an air mass value of 1.5 (which implies a declination angle of 45^o and represents the atmospheric conditions found in the city of Ottawa). If we assume a solar cell efficiency of 15%, which is typical of today's average commercial silicon solar cell performance, then a 1 m^2 area covered by this type of solar cell would produce on the order of 150 W. On the other hand, the Earth consumes on the order of 474 exajoules (474×10^{18} J) in one year [189] which represents approximately 1.5×10^{13} Whr. Simple mathematics shows that this type of power can be supplied by ~1×10^5 km^2 of land dedicated to 15% efficient silicon solar cells (this calculation does not consider temperature effects, cloud cover, degradation of performance over time, etc). At first sight, this appears to be quite a large area. However, this only represents 1% of the area of the Sahara desert! Of course, a project involving 1×10^5 km^2 of solar cell coverage represents an obscene capital investment. Today, Silicon solar cells cost ~0.7$/W [190], which would result in a total capital investment on the order of $10 trillion, which is actually ~15% of the world's gross domestic product from

2011 [191]. However, considering that it could supply the Earth's energy demands for every second of all daylight hours, this figure really puts today's energy crisis into context.

A-2. Comparing Concentrating Solar Power to Concentrating Photovoltaics

Solar energy can be converted into electrical power through either of two methods: photovoltaics (PV) and concentrated solar thermal power (CSP). The domain of photovoltaics, or the generation of electrical power (voltage) from solar radiation (photo), is a wide field of academic research and industrial level technological development. It is grounded on how light interacts with inorganic semiconductor materials such as Silicon or Gallium Arsenide (organic solar cells also exist), and typically deals with complex material systems, their interactions, and sophisticated growth and fabrication techniques to form larger more advanced electrical systems. Reading this thesis will exemplify the level of complexity involved in the research and development of photovoltaic devices. On the other hand, CSP, simply put, relies on concentrating a large area of sunlight onto a small area where the concentrated light is converted to heat, which then drives a heat engine. The key to CSP is achieving the highest temperature possible, since the maximum possible theoretical efficiency is highly dependent on this temperature. Since CSP is based on a simpler process, one can explore the theoretical maximum efficiencies of these types of systems to give the reader some numbers to consider throughout this thesis. The following argument considers Carnot's principle of heat engines [192] as well as assumptions on solar. Consider an ideal system with a perfect collection capacity (in terms of absorption and therefore emission, so $\alpha = \epsilon = 1$) operating a temperature T, the efficiency of the actual receiver system is described as:

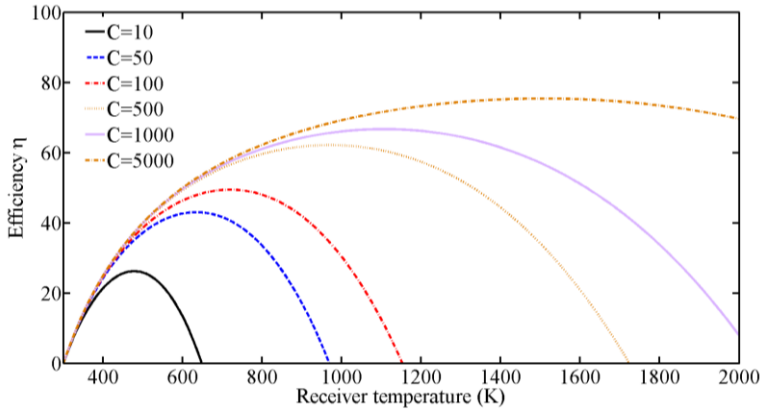

Figure A-1. Theoretical CSP efficiency as a function of receiver temperature for various concentration ratios based on equation (1).

$$\eta_{receiver} = \frac{Q_{absorbed} - Q_{emitted}}{Q_{total}} \tag{A.1.1}$$

Where Q_{total} represents the total heat incident on the receiver given by $Q_{total} = C \cdot P_{sun} \cdot \eta_{optics}$, P_{sun} is the total incident power (given as the intensity, typically 1000 W/m^2, times the collection area), C is the concentration factor of the incident solar power which is based on the optics involved in the system, η_{optics} is the efficiency of these concentrating optics, $Q_{absorbed}$ represents the absorbed total heat flux, or $Q_{absorbed} = \alpha Q_{total}$, and lastly, $Q_{emitted} = Area \cdot \epsilon \cdot \sigma \cdot T_H^4$ is the total emitted heat based on radiative losses (perfect black body radiator according to the Stefan-Boltzmann law), where σ is the Stefan-Boltzmann constant and T_H is the temperature of the heat source (or receiver). The overall efficiency of the system can be expressed as the product of the receiver efficiency with the Carnot efficiency (ideal scenario: $\eta_{Carnot} = 1 - {}^{T}/_{T_H}$ where T is the heat sink temperature) gives

$$\eta = \eta_{receiver} \cdot \eta_{Carnot} = \left(1 - \frac{\sigma \cdot T_H^4}{C \cdot I_{sun}}\right)\left(1 - {}^{T}/_{T_H}\right) \tag{A.1.2}$$

Figure A-1 illustrates the overall efficiency of a CSP system based on equation (1) above as a function of the receiver temperature, which predicts efficiencies greater than 60% for concentrations upwards of 500 and receiver temperatures on the order of 1000 K. Although

concentrations above 500 are currently achievable, these predicted efficiencies assume perfect absorption and emission amongst other ideal parameters, all of which are not realistic. Although not shown, the efficiency of a CSP system without any concentration (C=1) is on the order of 3%. The purpose of introducing a short theoretical investigation of CSP efficiencies is to first give an idea of what is theoretically possible with CSP, but secondly to give the reader a figure of merit for an eventual comparison to ideal photovoltaic device efficiencies. Since CSP is considered an inexpensive alternative energy source (costs estimated at 12-18 ¢/kWh based on numbers released in 2009 [193]), these theoretical efficiencies under concentration are a good comparison metric for state-of-the-art PV device efficiencies. The current world record efficiency for a photovoltaic device is 37.9% under standard testing conditions [194], and 44.4% under concentrated illumination of ~942 suns at a cell temperature of 25^0C [195].

Both CSP and PV require minimal cloud cover for maximum incident light, and both suffer in energy storage capabilities, although this latter issue is different for both methods due to their inherent differences in how each generates its electricity. For example, photovoltaics generate electricity directly via direct current, or if coupled with an inverter to produce alternating current; therefore the primary source of energy storage would be batteries which are expensive and can be toxic. In CSP, on the other hand, sunlight is first used to generate heat, which is then used to generate electricity via a heat engine; as a result, some energy can be stored away directly as heat through large insulated barriers or phase-change materials [196]. Current research and development in CSP focuses in part on improving solar collection methods and capacities, which include parabolic troughs, Fresnel reflectors, Stirling dishes and large power towers, and in part on energy storage

technologies. The motivation for larger and larger scales is based on the theoretical results illustrated in Fig. 1.1.2, which show that the larger collection capacities, and therefore receiver temperatures, the larger the efficiencies, and most importantly, the larger the return on investment (ROI) on the land area. For more details on CSP, there exists a very interesting and inspiring international scale project involving both CSP and PV, along with a combination of hydro, wind and biomass, called the DESERTEC project [197]. The project originated in Germany and its primary goals are to exploit the Saharan deserts for solar energy and to distribute it across Europe, the Middle East and North Africa. Some of the most difficult challenges of this project include the unification of governments and companies in all these countries as well as the energy distribution to all of the countries involved using very large scale transmission lines. The main technology considered within this project is CSP, since the technology exists and can be implemented on a large scale within the next decade. The domain of photovoltaics, on the other hand, represents a considerably small portion of the energy production. It is my hope that advancements in the field of photovoltaics over the next few years could lead to a larger contribution in terms of energy production within the DESERTEC project, as well as any future desert-exploiting project around the world.

Appendix B

Example Sentaurus Device code to simulate a simple *p+p-n-n+* junction in the dark and under illumination. The italics in each section represent code, with % acting as a comment on each line. Extra features for the simulation of multi-junction solar cells, namely tunnel junctions, are also included in the last sections.

B-1. Files Section

```
Files (
% Input
    Grid = "nX_grid_msh.tdr"
    Parameter = @mpr@ % SDevice automatically locates files containing npar/mpr.par
#if [string compare @light@ "on"] == 0
    IlluminationSpecturm="../spectra/am15d/am1-5d-1000wcm2.txt"
    OpticalGenerationOutput = "n@node@_OptGen"
#endif
% Output
    Plot = "@tdr@" %  spatially resolved solutions to specified variables in .tdr format
    Current = "@plt@"% output of electrical data at the specified contacts in .plt format
    Output = "@log@"% output log files containing input data, iterative output, etc
)
```

See Table 146 of [65] for more details.

B-2. Electrode Section

```
Electrode (
    {name="cathode" Voltage=0 resist=0}
    {name="anode" Voltage=0}
}
```

See Table 167 of [65] for more details on the options available for initial conditions at the contacts.

B-3. Global Physics Section

```
Physics {
    AreaFactor=<@1e11/wtot@> % to convert to mA/cm^2, see sidenode
    Fermi
    Temperature=@temp@
    Recombination (
        SRH (DopingDep)
        Auger
        Radiative
    )
    ThermionicEmission
    HeteroInterface
    Mobility (DopingDep)
    Optics (
        OpticalGeneration (
            QuantumYield = 1
            ComputeFromSpectrum
            # ComputeFromMonoChromaticSource % for EQE
        )
        Excitation (
            Theta = 0 % normal incidence
            Polarization = 0.5 % half TM, half TE
            # Wavelength = @wstart@ % parameter for EQE
            # Intensity = @intensity@ % parameter for EQE
        Window (
            #if [string compare @dimension@ "2d"] == 0
                Origin = (@wfrontc@, -1, 0)
                OriginAnchor = West
                Line ( Dx = @<wtot-wfrontc>@ )
            #elif [string compare @dimension@ "1d"] == 0
                Origin = (0, -1, 0)
                OriginAnchor = West
                Line ( Dx = @wtot@ )
            #endif
        )
        OpticalSolver (
            TMM (
                LayerStackExtraction (
                    Position = (@<wtot/2>@, -1, 0)
                    Mode = Elementwise # or Regionwise
                )*End of LayerStackExtraction
            ) *end of TMM
        ) *end of OpticalSolver
```

```
    ) *end of Optics

    Physics (materialInterface="AlGaAs/GaAs") {
        Recombination (SurfaceSRH)
    }
} *end of Physics
```

The area factor in this case is obtained as follows. The area factor requires the third dimension of the device, that is *@wtot@*. Then, to convert the units from A to A/cm^2, one must divide by the cross-sectional area, that is *@wtot@* squared. However, the variable *wtot* is in microns, and thus one must divide by 10^{-8}. Lastly, to convert from A to mA requires a factor of 10^3. As a result, the overall area factor is given as $\frac{wtot \cdot 10^3}{wtot \cdot wtot \cdot 10^{-8}} = \frac{10^{11}}{wtot}$. See Table 182 of [63] for more details on what Physics commands are available.

An EQE simulation will compute the optical generation profile from a monochromatic source, whereby a specific excitation wavelength and intensity would be required, and are typically given as a variable defined in the workbench. Simulations of current – voltage characteristics as a function of concentration can be performed either of two ways. Either the spectrum is scaled by the concentration factor, or the optical generation profile is scaled by the concentration factor. The latter method is more convenient by defining two Sentaurus Device simulations: the first to compute the optical generation profile, which feeds into the second to simulate the current – voltage characteristics with a scaled profile. This method is more convenient since scaling the spectrum must be performed externally from Sentaurus to generate a unique spectrum file.

B-4. Output Section

```
Plot {
```

```
    xMoleFraction Doping DonorConcentration AcceptorConcentration
    eEffectiveStateDensity hEffectiveStateDensity EffectiveIntrinsicDensity
    IntrinsicDensity
    eDensity hDensity SpaceCharge
    eQuasiFermiPotential hQuasiFermiPotential BandGap ConductionBandEnergy
    ValenceBandEnergy ElectronAffinity
    ElectricField ElectricField/vector ElectrostaticPotential
    eLifetime hLifetime SRH Auger TotalRecombination SurfaceRecombination
    RadiativeRecombination eSRHRecombination hSRHRecombination
    tSRHRecombination
    eCurrent/Vector hCurrent/Vector current/vector
    eMobility hMobility eVelocity hVelocity
    OpticalIntensity
    OpticalGeneration
    RefractiveIndexRealVertexComponent0
    RefractiveIndexImagVertexComponent0
}
```

See Table 263 of [65] for more options on the types of datasets available for output, grouped under scalar, tensorial, vector datasets.

B-5. Math Section

```
Math {
    Transient=BE % or TRBDF
    Extrapolate
    Derivatives
    RelErrControl
    Digits=5
    Iterations=25
    Notdamped=100
    Method=Super
    ErrRef(electron) = 1E0
    ErrRef(hole) = 1E0
    -MetalConductivity
    Number_of_Threads = maximum
    ExitOnFailure
    CNormPrint
    BreakCriteria {
        Current (Contact = "cathode" minval = -1e-3)
    }
}
```

where a break criteria can be set to only simulate until past the open circuit voltage in a current – voltage simulation. CNormPrint outputs the vertex with the largest residual errors for each iteration and allows for enhanced tracking of convergence issues. The *Super* method is the numerical methods adopted for solving the matrix multiplication involved in the TMM. For more details on the available keywords in the *Math* section, see Table 170 of [65].

B-6. Solve Section

```
Solve {
        Poisson
        Transient (
                InitialStep=0.1  MaxStep=0.1  MinStep=0.01  Increment=1.5
                Decrement=1.2)
                {Coupled {Poisson Electron Hole}}
        )
        Quasistationary (
                InitialStep=0.1  MaxStep=0.1  MinStep=0.01  Increment=1.5
                Decrement=1.2)
                Goal { Name="anode" Voltage=2.0}
        ) {Coupled {Poisson Electron Hole}}
}
```

Exporting the energy band diagrams and plot data at a specific voltage requires multiple quasistationary commands interrupted by the following command:

Plot (FilePrefix = "n@node@_Banddgm_*V*") ,

where the *V* should be specific to the voltage or level of perturbation which is associated with the plot variables. The Tecplot command file must import the appropriate file.

B-7. Tunnel Junctions

The addition of a tunnel junction requires two components: 1) activating the tunneling models at the appropriate interface, and 2) defining a nonlocal mesh

applicable to the interface. The first component is achieved by the following section within the global *Physics* section:

```
eBarrierTuneling "TJ_NLM"(
    BandToBand
    TwoBand
}
hBarrierTuneling "TJ_NLM"(
    BandToBand
    TwoBand
}
```

The definition of a nonlocal mesh must be in the global *Math* section, for example:

```
Math {
    NonLocal "TJ_NLM" (
        RegionInterface = "TJp/TJn"
        Length = 15e-7 # in cm
        Permeation = 15e-7 # in cm
}
```

The specification of nonlocal trap assisted tunneling is more trivial, since it does not require a nonlocal mesh. The keywords must be activated for a specific material layer, as illustrated below

```
Physics (Region="TJn") {
    Recombination (
        SRH(
            NonLocalPath (
                Lifetime=Schenk % or Hurkx
                Fermi % or –Fermi
                TwoBand % or -TwoBand

        )
    )
}
```

The expressions are analogous for the *p*-type layer of the TJ. Including the Fermi statistics typically leads to convergence issues. The tunneling masses must be specified in the material properties of the TJ layers.

Appendix C

C-1. Detailed Derivation of QD Absorption Coefficient

A common method of defining the absorption coefficient, $\alpha(\hbar\omega)$, is through the Beer-Lambert law: $I(x) = I_o e^{-\alpha x}$, where *I(x)* and I_o are the incident intensity at a depth of *x* and at a depth of *x=0*. In other words, $-\alpha I = \frac{\partial I}{\partial x}$. However, a derivation of the absorption coefficient related to quantum dots (QDs) must depend rigorously on the density of states in the valence and conduction bands, which depend highly on the material of interest. For these reasons, the derivation is based on Fermi's Golden Rule. In this scenario, the rate of electronic transitions from an initial state *i* to a final state *f* occurring due to absorption of a photon of energy E, $W_{i\to f}$, is of interest. The challenge is thus to relate $W_{i\to f}$ to the ratio of energy removed from an incident beam of photons per unit time per unit volume. This derivation is based on [198].

The energy of an incident beam of photons can be described as an electromagnetic wave consisting of an electric field component

$$E(x,t) = \mathrm{Re}\left[\vec{E}(x)e^{-i\omega t}\right] = \frac{1}{2}\left[\vec{E}(x)e^{-i\omega t} + \vec{E}^{*}(x)e^{i\omega t}\right] \qquad \text{(C.1.1)}$$

where the electric field takes the form of a plane wave given as $\vec{E}(x) = E_o e^{-i(\vec{q}\cdot\vec{x})}$. The average energy density of an electromagnetic (EM) wave can be expressed simply as $U_{EM} = \frac{n^2\epsilon_o}{2}|E_o|^2$ where *n* is the refractive index of the material and ϵ_o is the permittivity of free space. The intensity of a beam of EM radiation can thus be expressed as the speed of the

wave multiplied by its energy density, $I = \frac{c}{n} U_{EM} = \frac{cn\epsilon_o}{2}|E_o|^2$. The last key relation is how the electronic transition rate can be related to the rate at which the EM field is losing energy to the material absorbing it, which is expressed as

$$\frac{\partial U_{EM}}{\partial t} = -E_{\text{ph}} \times W_{i\to f}(E), \tag{C.1.2}$$

where the dependence of the transition rate $W_{i\to f}$ on the photon energy $E_{\text{ph}} = \hbar\omega$ is considered. For a plane wave, the rate at which an EM wave loses energy as a function of time is equal to the rate at which the intensity of this wave diminishes as a function of distance, or $\frac{\partial U_{EM}}{\partial t} = \frac{\partial I}{\partial x}$ [198]. Using $-\alpha I = \frac{\partial I}{\partial x}$ as a starting point, one can thus express the absorption coefficient generally as

$$\alpha = \frac{2\hbar\omega}{cn\epsilon_o|E_o|^2} \cdot W_{i\to f}(E). \tag{C.1.3}$$

The remaining task is then deriving the transition rate $W_{i\to f}(E)$ based on Fermi's Golden Rule. The transition rate is related to the transition probability of an electron in an initial state $|i\rangle$ at energy E_i to a final empty state $|f\rangle$ at energy E_f under a perturbed Hamiltonian H' based on

$$W_{i\to f}(E) = \frac{2\pi}{\hbar}|\langle f|H'|i\rangle|^2 . \tag{C.1.4}$$

The full Hamiltonian is given by

$$\begin{aligned} H &= \frac{1}{2m}\left(\hat{p} + e\vec{A}\right)^2 + V(r) \\ &= H_o + \frac{e}{m}\hat{p}\cdot\vec{A} + \frac{1}{2m}e^2A^2 \end{aligned} \tag{C.1.5}$$

where $\vec{A}$ is the vector potential of the EM wave given as $\vec{E} = -\frac{\partial\vec{A}}{\partial x}$, $\hat{p}$ is simply the momentum operator and $V(\vec{r})$ is the atomic potential felt by the carriers; thus the typical Hamiltonian $H_o = \frac{\hat{P}^2}{2m} + V(\vec{r})$ is recovered. The last term of the last equation can be ignored

since A^2 is negligible, which gives a perturbed Hamiltonian of $H' = \frac{e}{m}\vec{P}\cdot\vec{A}$. The full transition rate can thus be expressed as a summation of all final states,

$$W_{i\to f}(E) = \frac{2\pi}{\hbar}\sum_f |\langle f|H'|i\rangle|^2$$

$$= \frac{e^2}{m^2}\sum_f \left|\langle f|\hat{p}\cdot\vec{A}|i\rangle\right|^2, \qquad \text{(C.1.6)}$$

where it is assumed the valence band is effectively full and the conduction band is empty (probability of having a filled state in the valence band is ~1, while the probability of having an empty state in the conduction band is ~0). The initial and final state wavefunctions can be expressed as Bloch functions respectively

$$|i\rangle = u_v(\vec{r})e^{i\overrightarrow{k_v}\cdot\vec{r}}e^{-i^{E_v t}/\hbar}, \qquad |f\rangle = u_c(\vec{r})e^{i\overrightarrow{k_c}\cdot\vec{r}}e^{-i^{E_c t}/\hbar}. \qquad \text{(C.1.7)}$$

The vector potential $\vec{A}$, defined as the time derivative of the electric field, can be expressed as

$$\vec{A} = \frac{E_o}{-2i\omega}\left[e^{i(\vec{q}\cdot\vec{r}-\omega t)} - e^{-i(\vec{q}\cdot\vec{r}-\omega t)}\right], \qquad \text{(C.1.8)}$$

where $\vec{q}$ is the photon momentum for a photon angular frequency ω. As a result, the overlap integral between the final and initial states due a perturbed Hamiltonian can be expressed as

$$\left|\langle f|\hat{p}\cdot\vec{A}|i\rangle\right|^2 = \frac{|E_o|^2}{4\omega^2}\left|\int u_c^* e^{i(\vec{q}-\vec{k}_c)\cdot\vec{r}}\,\hat{e}\cdot\hat{p}\,u_v e^{i\vec{k}_v\cdot\vec{r}}dr^3\right|^2, \qquad \text{(C.1.9)}$$

where $\hat{e}$ represents the polarization unit vector. The integration over time inside the matrix element will involve conservation of energy

$$\int e^{\frac{iE_c t}{\hbar}}e^{-i\omega t}e^{-\frac{iE_v t}{\hbar}}dt \to \delta(E_c - E_v - \hbar\omega), \qquad \text{(C.1.10)}$$

The application of the momentum operator $\hat{p}$ gives two components, the latter of which is zero due to orthogonality of the Bloch function. Hence, $\hat{p}$ will only be applied on the Bloch

function u_v. Furthermore, one can integrate over a single unit cell of unit vector $\vec{R}_j$, as expressed by

$$\left|\langle f|\hat{p}\cdot\vec{A}|i\rangle\right|^2 = \frac{|E_o|^2}{4\omega^2}\left|\sum_j e^{i(\vec{q}-\vec{k}_c+\vec{k}_v)\cdot\vec{R}_j}\int u_c^* e^{i(\vec{q}-\vec{k}_c)\cdot\vec{r}}\,\hat{e}\cdot\hat{p}\,u_v e^{i\vec{k}_v\cdot\vec{r}}dr^3\right|^2, \qquad \text{(C.1.11)}$$

which can be simplified using

$$\sum_j e^{i(\vec{q}-\vec{k}_c-\vec{k}_v)\cdot\vec{R}_j} = \delta\left(q-\vec{k}_c+\vec{k}_v\right) \approx \delta\left(-\vec{k}_c+\vec{k}_v\right), \qquad \text{(C.1.12)}$$

where the photon momentum q is assumed to be negligible compared to the carrier momentum. This renders the overlap integral as

$$\left|\langle f|\hat{p}\cdot\vec{A}|i\rangle\right|^2 = \frac{|E_o|^2}{4\omega^2}|P_{cv}|^2\,, \qquad \text{(C.1.13)}$$

where $|P_{cv}|^2$ is typically referred to as the momentum matrix element and is given as

$$|P_{cv}|^2 = \left|\int u_c^*(\vec{k}_c)\hat{e}\cdot\hat{p}\,u_v(-\vec{k}_v)dr^3\right|^2 = |\langle u_c|\hat{e}\cdot\hat{p}|u_v\rangle|^2. \qquad \text{(C.1.14)}$$

However, this momentum matrix element assumes no carrier confinement, i.e. the wavefunctions of the carriers are described solely by the Bloch function of the lattice. In a quantum structure, the carrier wavefunctions are modulated by the envelope function due to the confinement potential. As a result, the carrier wavefunction is more accurately described as

$$|i\rangle = |u_v\rangle|n\rangle\,, \qquad |f\rangle = |u_c\rangle|m\rangle \qquad \text{(C.1.15)}$$

where $|n\rangle$ and $|m\rangle$ are the envelope functions of the initial and final states respectively. The momentum matrix element thus becomes

$$|P_{cv}|^2 \equiv |\langle m|\langle u_c|\hat{e}\cdot\hat{p}|u_v\rangle|n\rangle|^2 \qquad \text{(C.1.16)}$$

$$|P_{cv}|^2 = |\langle m|n\rangle|^2|\langle u_c|\hat{e}\cdot\hat{p}|u_v\rangle|^2 + |\langle u_c|u_v\rangle|^2|\langle m|\hat{e}\cdot\hat{p}|n\rangle|. \qquad \text{(C.1.17)}$$

However, the Bloch functions in the valence and conduction bands are orthogonal, which reduces the optical matrix element as

$$|P_{cv}|^2 = |\langle m|n\rangle|^2 |\langle u_c|\hat{e}\cdot\hat{p}|u_v\rangle|^2. \quad \text{(C.1.18)}$$

At this stage in the derivation, it becomes useful to differentiate between the bulk momentum matrix element and the quantum structure's momentum matrix element. We therefore introduce the optical matrix element $|M_{cv}|^2 = |\langle m|n\rangle|^2$ such that

$$|P_{cv}|^2 = |M_{cv}|^2 |\langle u_c|\hat{e}\cdot\hat{p}|u_v\rangle|^2 = |M_{cv}|^2 |P_{cv}^{bulk}|^2. \quad \text{(C.1.19)}$$

The final absorption coefficient can thus be simplified to

$$\alpha(\hbar\omega) = \frac{\pi e^2 \hbar |P_{cv}^{bulk}|^2}{cn\epsilon_o m^2 E_{ph}} \sum_{i,f} |M_{cv}|^2 \delta\left(E_c(\vec{k}_c) - E_v(\vec{k}_v) - \hbar\omega\right). \quad \text{(C.1.20)}$$

The above formulation of the absorption coefficient is general for any material (i.e. bulk and quantum structures), since in bulk, the overlap between envelope functions approaches unity, or $|M_{cv}|^2 = 1$. This derivation is similar to that performed by Nelson [198], although with different units. The next step is to replace the summation over all initial and final states *i* and *f* with an integral over all *k* space. This introduces the density of states of carriers in the conduction and valence bands $g_c(\vec{k}_c)$ and $g_v(\vec{k}_v)$ respectively.

However, rather than integrating over all *k*-space, one can replace the density of states in the conduction and valence bands with a joint density of states which implicitly considers the *k*-dependence of the carriers within the bound energy levels of the QD. The joint density of states for a QD is given as

$$jDOS_{QD}(E) = \frac{1}{V_{QD}} \sum_{n=0}^{\infty} \left|M_{cv}^{QD}\right|^2 g_s\, \delta\left(E - E_{g,QD} - E_{n,QD}\right), \quad \text{(C.1.21)}$$

where g_s is the spin degeneracy factor, V_{QD} is the volume of the QD, $E_{g,QD}$ is the bandgap of the QD (which corresponds to $E_c - E_v$) and $E_{n,QD}$ contains the necessary information of the n^{th} quantized energy levels in both conduction and valence bands (i.e. the n^{th} bound electron

energy level from the conduction band, $E_{e,QD}$, and the n^{th} bound hole energy level from the valence band, $E_{h,QD}$). The absorption coefficient of a single QD thus takes the form

$$\alpha_{QD}(E = \hbar\omega) = A_\alpha \int \delta\big(E - E_{cv}(\vec{k})\big) jDOS_{QD}(E) dE_{cv}, \qquad \text{(C.1.22)}$$

where $A_\alpha = \frac{\pi e^2 \hbar |P_{cv}^{bulk}|^2}{cn\epsilon_o m^2 E_{ph}}$, $\left|M_{cv}^{QD}\right|^2$ is expressed explicitly for a QD, and where $E_{cv}(\vec{k})$ represents the energy levels between the valence and conduction bands of the material involved in the optical transition, which depend on $\vec{k}$ implicitly. For a QD, the optical transitions correspond to discrete transitions between bound states, i.e. $E_{g,QD} + E_n$, and thus the joint density of states can be reduced to a summation over the bound energy levels of the QD, as given by

$$\alpha_{QD}(E = \hbar\omega) = \frac{A_\alpha}{V_{QD}} \sum_{n=0}^{\infty} \left|M_{cv}^{QD}\right|^2 g_s \, \delta\big(E - E_{g,QD} - E_{n,QD}\big). \quad \text{(C.1.23)}$$

This formalism depends implicitly on the electron and hole eigenenergies of the QD, $E_{n,QD}$, and the QD bandgap $E_{g,QD}$. These energy levels can be computed analytically, such as [15],[52] or using COMSOL based on [49], where the dimensions of the QD dictate the energy levels based on appropriate carrier effective masses and conduction and valence band offsets. Simulations conducted in COMSOL also reveal the bound wavefunctions, which thus reveals the optical matrix element $|M_{cv}|^2$. This last equation is in agreement with equation (12) of [52].

One can then associate the absorption coefficient of a single QD to an average absorption coefficient representative of a distribution of QD sizes. If the probability function for the distribution of dot sizes, $P(r)$ is known (where the QD are described solely by a radius *r*, i.e. spherical shaped QD), then this average absorption coefficient for a population of QD takes the form [52]

$$\bar{\alpha}_{QD} = \int_0^\infty P(r)\alpha_{QD}dr. \quad \text{(C.1.24)}$$

An alternative to this is to consider the broadening of the energy levels as a function of energy due to the distribution in QD dimensions. However, the derivation of an absorption coefficient for a more generalized QD, i.e. a QD of any shape, cannot be derived for a simple distribution in QD radii. For example, a population of lens shaped QD can vary in both radius and height. We are therefore interested in an average absorption coefficient representative of a population of QD sizes where the population in sizes effectively results in a broadening of the energy levels of the QDs. Thus, rather than integrating over possible QD radii, as done in [52], we integrate over a distribution of energy levels. The distribution of energy levels can be expressed as

$$P(E) = \frac{1}{\sqrt{2\pi}\xi\bar{E}_{QD}^n}\exp\left(-\frac{\left(E-\bar{E}_{QD}^n\right)^2}{2\xi^2}\right), \quad \text{(C.1.25)}$$

where $\bar{E}_{QD}^n$ is the mean of the full optical transition energy in the QD (given by the sum of the QD bandgap and the n^{th} electron and hole eigenenergies) and ξ is the relative standard deviation of this optical transition energy. Thus, the average absorption coefficient can be computed as

$$\bar{\alpha}_{QD} = \int_0^\infty P(E)\alpha_{QD}dE \quad \text{(C.1.26)}$$

$$= \frac{1}{\sqrt{2\pi}\xi}\frac{A_\alpha}{V_{QD}\bar{E}_{QD}^n}\sum_{n=0}^\infty\left|M_{cv}^{QD}\right|^2 g_s\int_0^\infty \exp\left(-\frac{\left(E-E_{QD}^n\right)^2}{2\xi^2}\right)\delta\left(E-E_{QD}^n\right)dE, \quad \text{(C.1.27)}$$

where $E_{QD}^n = E_{g,QD} + E_{QD,n}$. The δ-function essentially reduces the integral and thus the entire equation to

$$\bar{\alpha}_{QD} = \frac{1}{\sqrt{2\pi}\xi}\frac{A_\alpha}{V_{QD}\bar{E}_{QD}^n}\sum_{n=0}^\infty\left|M_{cv}^{QD}\right|^2 g_s\exp\left(-\frac{\left(E-\bar{E}_{QD}^n\right)^2}{2\xi^2}\right). \quad \text{(C.1.28)}$$

This last equation marks the final absorption coefficient of a distribution of QD sizes, where V_{QD} considers the average dimensions of the QD which gives rise to the eigenenergies E_{QD}^{n}. The spin degeneracy g_s also depends on the shape of the QD. For lens shaped QDs, the absorption coefficient takes the form as that reported in [174].

C-2. Detailed Derivation of QW Absorption Coefficient

The derivation of the wetting layer (WL) absorption coefficient begins with equation (C.1.20) and also adopts the joint density of states but for a quantum well (QW), as given by

$$jDOS_{QW}(E) = \frac{1}{L_{QW}}\frac{\mu}{\pi\hbar^2}\sum_{n=0}^{\infty}\Theta\left(E - E_{g,QW} - E_{n,QW}\right), \qquad \text{(C.2.1)}$$

where μ represents the reduced effective mass of the carriers, given as $\frac{1}{\mu} = \frac{1}{m_e^*} + \frac{1}{m_h^*}$, L_{QW} is the confinement depth of the QW, i.e. its thickness, $E_{g,QW}$ is the bandgap of the QW, $E_{n,QW}$ represents the n^{th} bound electron and hole eigenenergies in the QW, and Θ represents the Heaviside function. Using this joint density of states coupled to the results from equation (B.1.13), one can express the absorption coefficient of a QW as

$$\alpha_{QW}(E = \hbar\omega) = \frac{A_\alpha}{L_{QW}}\frac{\mu}{\pi\hbar^2}\sum_{n=0}^{\infty}\left|M_{cv}^{QW}\right|^2\Theta\left(E - E_{g,QW} - E_{n,QW}\right), \qquad \text{(C.2.2)}$$

where the optical matrix element is considered for the QW. Once again, this overlap integral can be extracted from COMSOL simulations. In a very similar fashion to the previous section, the QW also abides by a distribution in size (i.e. thickness). It is worth noting at this point that the distribution in thickness is significantly more rigid for the InAs/GaAs QD system, since the WL is on the order of 2 monolayers (MLs) in thickness. The thickness thus ranges between 1 and 2 MLs, with a mean thickness closer to 2 MLs. Thus we are interested

in integrating equation (B.2.2) over a distribution of energy levels corresponding to the QW eigenenergy to determine the average absorption coefficient of the WL

$$\bar{\alpha}_{WL} = \int_0^\infty P(E)\alpha_{WL}dE \tag{C.2.3}$$

where the distribution in energy is identical to equation (C.1.17) but for the mean eigenenergies of the QW, as given by

$$P(E) = \frac{1}{\sqrt{2\pi}\xi\bar{E}_{QW}^n}\exp\left(-\frac{\left(E-\bar{E}_{QW}^n\right)^2}{2\xi^2}\right), \tag{C.2.4}$$

We are therefore interested in analytically solving the following integral

$$\bar{\alpha}_{WL} = \frac{A_\alpha}{\sqrt{2\pi}\xi L_{QW}\bar{E}_{QW}^n}\frac{\mu}{\pi\hbar^2}\sum_{n=0}^\infty\left|M_{cv}^{QW}\right|^2\int_0^\infty\exp\left(-\frac{\left(E-\bar{E}_{QW}^n\right)^2}{2\xi^2}\right)\Theta\left(E-\bar{E}_{QW}^n\right)dE, \tag{C.2.5}$$

where $\bar{E}_{QW}^n = E_{g,QW} + E_{n,QW}$ corresponds to the mean optical energy transition involved in the QW. The integral itself is straightforward since the Heaviside function essentially changes the limits of the integral from $[0,\infty]$ to $\left[\bar{E}_{QW}^n,\infty\right]$ (since for $E = \left[0,\bar{E}_{QW}^n\right]$ results in a zero integral). As a result, the integral is that of a simple exponential function, which results in an error function, as given by

$$\bar{\alpha}_{WL} = \frac{A_\alpha}{\sqrt{2\pi}\xi L_{QW}\bar{E}_{QW}^n}\frac{\mu}{\pi\hbar^2}\sum_{n=0}^\infty\left|M_{cv}^{QW}\right|^2\left[\xi\bar{E}_{QW}^n\frac{\sqrt{2\pi}}{2}\mathrm{erf}\left(\frac{E-\bar{E}_{QW}^n}{\sqrt{2}\xi}\right)\right]_{\bar{E}_{QW}^n}^\infty, \tag{C.2.6}$$

which, after evaluating the limits of the argument of the error function and simplifying, gives

$$\bar{\alpha}_{WL} = \frac{A_\alpha}{2L_{QW}}\frac{\mu}{\pi\hbar^2}\sum_{n=0}^\infty\left|M_{cv}^{QW}\right|^2\left[1-\mathrm{erf}\left(\frac{E-\bar{E}_{QW}^n}{\sqrt{2}\xi}\right)\right]. \tag{C.2.7}$$

Equation (C.2.7) is the final equation that is in agreement with that used in [174].

C-3. Approximating Carrier Escape and Capture using Bulk Thermionic Emission

When thermionic emission (TE) is introduced at an interface, such as that depicted in Fig. C-1 in the effective band offset model of a quantum dot, the current densities getting in and out of the potential well are given as

$$J_{in}^{TE} = 2q\left[n_{QD}v_{QD} - \frac{m_{QD}}{m_b}n_b v_b \exp\left(\frac{\Delta E_c}{kT}\right)\right] \quad \text{(C.3.1)}$$

$$J_{out}^{TE} = 2q\left[n_b v_b - \frac{m_b}{m_{QD}}n_{QD} v_{QD} \exp\left(-\frac{\Delta E_c}{kT}\right)\right] \quad \text{(C.3.2)}$$

where n_b and n_{QD} are the carrier concentrations in the barrier and in the QD respectively, m_b and m_{QD} are the carrier effective masses in the barrier and QD materials respectively, v_b and v_{QD} are the thermal velocities of carriers in the barrier and in the QD respectively, where the velocity can be expressed as $v = \sqrt{\frac{kT}{2\pi m}}$, and ΔE_c is the potential barrier between the barrier and QD materials [65]. These carrier densities in and out of the potential fall into the carrier continuity equation, given as

$$\frac{dn}{dt} = G - U + \frac{1}{q}\nabla \cdot J = 0 \quad \text{(C.3.3)}$$

where G and U are the generation and recombination terms respectively. At the barrier/QD material interface, the gradient in the thermionic emission current density fits into equation (C.3.3) to provide supplementary terms, which should mimic carrier escape and capture for J_{in}^{TE} and J_{out}^{TE} respectively. Thus the goal of this exercise is to use equations (C.3.1) and

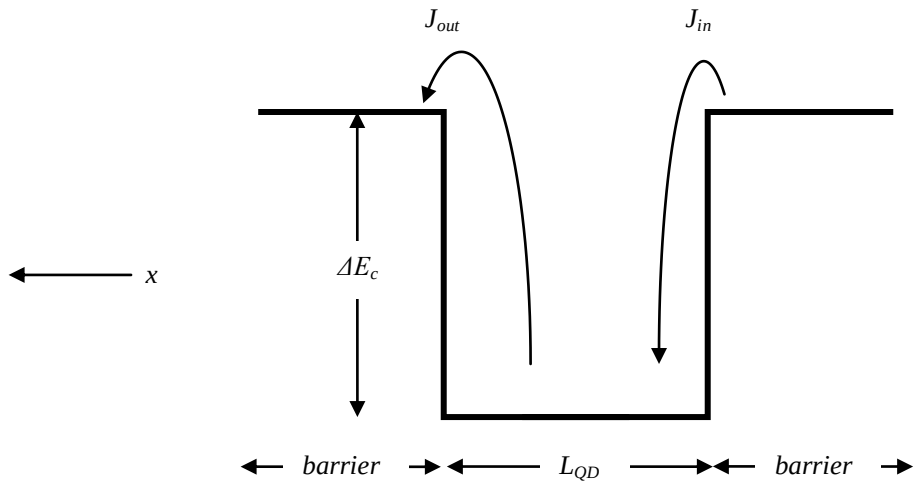

Figure C-1. Schematic energy band diagram of the QD potential (of thickness L_{QD}) surrounded by barrier layers to demonstrate the current densities in and out of the potential due to thermionic emission.

(C.3.2) into equation (C.3.3) to arrive at the following equation

$$\frac{dn}{dt} = G - U + \frac{n_{QD}}{\tau_{esc}} - \frac{n_b}{\tau_{cap}} + \frac{1}{q}\nabla \cdot J = 0 \qquad \text{(C.3.4)}$$

where τ_{esc} and τ_{cap} are the carrier escape and capture lifetimes of the carriers.

It is assumed in this derivation (for simplicity) that the gradient in current density is only important along one direction (say the *x*-direction). As a result, the gradient in J can be expressed as

$$\frac{dJ}{dx} \approx \frac{\Delta J}{\Delta x} = \frac{J_{in}^{TE} - J_{out}^{TE}}{L_{QD}} \qquad \text{(C.3.5)}$$

$$\frac{dJ}{dx} \approx \frac{2q\left[n_{QD}v_{QD} - n_b v_b - \frac{m_{QD}}{m_b} n_b v_b \exp\left(\frac{\Delta E_c}{kT}\right) + \frac{m_b}{m_{QD}} n_{QD} v_{QD} \exp\left(-\frac{\Delta E_c}{kT}\right)\right]}{L_{QD}} \qquad \text{(C.3.6)}$$

$$\frac{dJ}{dx} \approx \frac{2q}{L_{QD}}\left[n_{QD}v_{QD}\left(1 + \frac{m_b}{m_{QD}}\exp\left(-\frac{\Delta E_c}{kT}\right)\right) - n_b v_b\left(1 + \frac{m_{QD}}{m_b}\exp\left(\frac{\Delta E_c}{kT}\right)\right)\right] \qquad \text{(C.3.7)}$$

$$\frac{dJ}{dx} \approx \frac{2qn_{QD}v_{QD}}{L_{QD}}\left(1+\frac{m_b}{m_{QD}}\exp\left(-\frac{\Delta E_c}{kT}\right)\right)-\frac{2qn_bv_b}{L_{QD}}\left(1+\frac{m_{QD}}{m_b}\exp\left(\frac{\Delta E_c}{kT}\right)\right) \quad \text{(C.3.8)}$$

$$\frac{dJ}{dx} \approx q\left(\frac{n_{QD}}{\tau_{esc}^{TE}}-\frac{n_b}{\tau_{cap}^{TE}}\right) \quad \text{(C.3.9)}$$

where the thermionic emission approximated escape and capture lifetimes are given as

$$\frac{1}{\tau_{esc}^{TE}}=\frac{2v_{QD}}{L_{QD}}\left(1+\frac{m_b}{m_{QD}}\exp\left(-\frac{\Delta E_c}{kT}\right)\right), \qquad \frac{1}{\tau_{cap}^{TE}}=\frac{2v_b}{L_{QD}}\left(1+\frac{m_{QD}}{m_b}\exp\left(\frac{\Delta E_c}{kT}\right)\right). \quad \text{(C.3.10)}$$

One can thus compare inserting equations (C.3.9) and (C.3.10) back into the continuity equation to give the result of equation (C.3.4).

It is possible to compute approximate carrier escape and capture lifetime based on typical thermal velocities and effective masses. For values outlined in Table C-1, this yields τ_{esc}^{TE}~6.55 fs and τ_{cap}^{TE}~0.84 fs for electrons, which are extremely fast compared to values reported in the literature (on the picosecond time scale). This thus confirms that although bulk thermionic emission can mimic carrier escape and capture, it over-estimates these rates. Keep in mind the conduction band offset is 56 meV to consider just the electron capture and escape times within the framework of the effective band offset model.

Table C-1. Parameters used to compute carrier escape and capture lifetimes using equations (C.3.10).

Parameter	Value
$\boldsymbol{m_b}$	0.063 m_o
$\boldsymbol{v_b}$	1.07 ×10^5 m/s
$\boldsymbol{m_{QD}}$	0.053m_o
$\boldsymbol{v_{QD}}$	1.17×10^5 m/s
$\boldsymbol{\Delta E_c}$	0.06 eV